A Single-Frequency Impedance Diagnostic for State of Health Determination in Li-ion 4P1S Battery Packs

Brett M. Huhman

Dissertation submitted to the faculty of the Virginia Polytechnic Institute and State University in partial fulfillment of the requirements for the degree of

Doctor of Philosophy
In
Electrical Engineering

Lamine Mili, Chair
Willem G. Odendaal
Amir Zaghloul
David Wetz
Virgilio Centeno
Alan Brown

November 3, 2017
Falls Church, VA

Keywords: Pulsed Power, Electrochemical Impedance Spectroscopy, EIS, Computed Tomography, Battery, $LiFePO_4$

A Single-Frequency Impedance Diagnostic for State of Health Determination in Li-ion 4P1S Battery Packs

Brett M. Huhman

ABSTRACT

State-of-Health (SoH), a specified measure of stability, is a critical parameter for determining the safe operating area of a battery cell and battery packs to avoid abuse and prevent failure and accidents. A series of experiments were performed to evaluate the performance of a 4P1S battery array using electrochemical impedance spectroscopy to identify key frequencies that may describe battery state of health at any state of charge. Using a large sample number of cells, the state of health frequency, f_{SoH}, for these $LiFePO_4$ 26650 cells is found to be 158 Hz. Four experiments were performed to evaluate the lifetime in different configurations: single-cell at 1C (2.6A), single-cell at 10C (26A), four cells in parallel at 10C (ideal match), and four cells in parallel (manufacturer match). The lifetime for each experiment set degraded substantially, with the final parallel series reaching end of life at 400 cycles, a 75.32% reduction in life compared to operating solo. Analysis of the f_{SoH} data for these cells revealed a change in imaginary impedance at the critical frequency that corresponded to changes in the capacity and current data, supporting the development of a single-frequency diagnostic tool. An electrochemical model of the battery was generated, and it indicated the anode material was aging faster than the SEI layer, the opposite of normal cell degradation. A post-mortem analysis of cells from three configurations (baseline, single-cell, and parallel-cell) supported the modeling, as physical damage to the copper current collector in the anode was visible in the parallel-connected cell.

A Single-Frequency Impedance Diagnostic for State of Health Determination in Li-ion 4P1S Battery Packs

Brett M. Huhman

GENERAL AUDIENCE ABSTRACT

Lithium-ion batteries are used in a large number of applications, from cellular phones to laptops and electric vehicles. In low power devices, such as a laptop, these batteries can be relatively stable if the associated circuitry is designed properly. However, as the amount of power required from the battery increases, the possibility of an internal battery fault will also increase. The ability to determine the stability of the battery for military applications such as laser weapon systems, electromagnetic railguns or commercial systems such as electric vehicles or industrial-scale micro-grids becomes critical to prevent catastrophic events such as fires. Additionally, the ability to determine the battery State-of-Health (SoH), a specified measure of stability, will enable advance warning of a failing battery to optimize the logistics chain in an operational system. A battery marked as “bad” can be scheduled for replacement before a failure actually occurs. This dissertation has designed a series of experiments that establishes the technology to detect these internals faults, and applies them to a scaled battery system that represents a much larger system. When batteries are placed in parallel and discharged at very high currents, typical of the military applications, the lifetime for the cells was reduced by 75% when compared to batteries discharged under the same conditions by themselves. A post-mortem analysis of cells from three different conditions (uncycled, single-cell, parallel-cell) reveals physical damage to the internal electrodes that indicates a high level of internal destruction occurs at high currents when in parallel arrays.

Dedication & Acknowledgements

"Be glad of life…
Because it gives you the chance
To love and to work and to play…
And to look up at the stars."
- Henry Van Dyke

This dissertation would not have been possible without the support and guidance of my family. First, I would like to thank my wife Heather for her endless support through several years of first (seemingly) endless take-home exams and homework, then the arduous process of performing research and interpreting the results. I would also like to thank my in-laws Bill and Terry Pugh for their invaluable help in allowing me to find time to continue to push through the PhD process. My parents, Mike and Carol Huhman, have always supported me throughout my entire life and I'm extremely grateful. Finally, I'd like to dedicate this work to my daughter, Aurora. May this be a reminder that you can do anything you want to do, if you put in the hard work.

I would like to also thank my advisor, Dr. Lamine Mili, for first accepting me into the Virginia Tech Graduate Program, and then for pushing me to explore new avenues of research. I would also like to acknowledge the support of the entire Plasma Physics Division at the U.S. Naval Research Laboratory (NRL), but in particular Dr. T. Mehlhorn, Dr. J. Schumer, Dr. J. Neri, and Dr. C. Carney without whom I would never have started this process. In the NRL Chemistry Division I would never have started this topic without Dr. C. Love. I would like to thank the U.S. Office of Naval Research for their financial support, in particular Mr. R. Ellis and Dr. J. Heinzel. I would also like to thank the Edison Memorial Training Program at NRL for giving me a vehicle to pursue this opportunity.

I would also like to thank the Spacecraft Engineering Divison at NRL for the use of their thermal chamber and MACCOR cycler, as well as the NRL Laboratory for Autonomous Systems Research (LASR). I would also like to thank Mr. C. Berry and Mr. T. Kijowski for their superb technical assistance helping me fabricate various widgets. Finally, I would like to thank my PhD Committee Members Dr. W. G. Odendaal, Dr. A. Zaghloul, Dr. D. Wetz, Dr. V. Centeno, and Dr. A. Brown for their invaluable insights in the PhD process.

Contents

List of Figures

List of Tables

List of Abbreviations

4P1S .....A battery arrangement with four cells in parallel (4P) and one in series (1S)

C-rate,C.....Rate at which a battery is discharged relative to its theoretical maximum

CC .....Constant current

CPE .....Constant phase element

CV .....Constant voltage

CT .....Computed tomography

EIS.....Electrochemical Impedance Spectroscopy

EOL.....End of life

ESR .....Equivalent series resistance

f_{SOH}.....State of health frequency

LFP.....Lithium iron phosphate ($LiFePO_4$) battery

Li-ion.....Lithium-ion battery

NIMH.....Nickel-metal hydride battery

NRL.....U.S. Naval Research Laboratory

SEI.....Solid electrolyte interface

SoC.....State of charge

SoH .....State of health

VRLA.....Valve-regulated lead-acid battery

Z'.....Real impedance

Z'' .....Imaginary impedance

ZARC.....Modeling construct consisting of a CPE element in parallel with a resistor

Chapter 1

Introduction

The US Navy is currently developing a host of electrical systems that rely on high pulsed power for their operation. In pulsed power supplies, energy is slowly, over several milliseconds to several seconds in most cases, transferred from an energy dense prime power supply into some intermediate power dense storage device, which is then able to release the energy in the form of a high peak to average power pulse to the load. In a laboratory setting, grid-tied power supplies are often used as the prime power supply. Aboard a mobile platform, the necessary power must be carried with the pulsed power system, which will have a limited lifetime and performance envelope. In recent years, lithium-ion batteries have emerged as a key component to the development of compact, portable pulsed-power devices due to both their high energy density as well as their high power density. In the vast majority of pulsed power systems, the intermediate energy storage device is a large capacitor that is charged at a relatively slow rate prior to the rapid discharge of high current into the load under test. This method has the advantage of always allowing us to know whether the input energy magnitude and quality are suitable for the application. A limited power supply requires care in the system design to ensure sufficient power is available to be delivered to the capacitive load.

Unlike many battery-driven loads, such as electric vehicles, pulsed power systems require high-power along with high-energy, meaning that in most cases, power cells are being considered rather than energy cells. In order to meet both the power requirements, multiple cells will be

connected in series to generate a sufficient potential to drive the load. In order to meet the capacity requirements, cells are paralleled. Oversizing the battery by putting more cells in parallel than are needed will reduce the current supplied by each cell and will increase their lifetime. Here, it is assumed that each parallel cell equally shares the current demanded by the load, though in most cases the manner in which the batteries are paralleled prevents verification that this current sharing does occur. In the Navy's applications, size and weight are critical; so oversizing of the battery is unlikely, meaning that each cell will be pushed to supply as much power as the manufacturer allows. Uneven current sharing under these conditions may become problematic and can push cells beyond their limits. Research is necessary to determine whether cells connected in parallel will share current evenly. Imbalance may potentially cause cells to prematurely fail within the pack due to excessive heat and cycling. Even if the cells do share current evenly at the beginning of their useful life, it is likely that they will age at an uneven rate due to differences in construction, materials, and location in the array caused by thermal effects. A cell with higher internal source impedance (ESR) will discharge a portion of its useful energy as heat rather than to the load. The additional thermal load on the array may also contribute to the aggregate aging of the parallel array. Conversely, a cell that has a lower ESR than the others in an array will source more current than expected. The low ESR cell will reach end of life prematurely, forcing the remaining cells to source more current than designed.

The lithium iron phosphate, $LiFePO_4$, chemistry features high rate capability with extremely flat discharge plateau and rapid lithiation/delithiation kinetics and is commonly selected for pulsed-power applicants. The chemistry is resistant to the typical thermal runaway conditions associated with lithium batteries, as the PO_4 is a stronger bond than CoO_2, preventing the generation of O_2 when exposed to excessive levels of thermal energy. However, the proximity of the reaction potential to the oxidation of the copper current collector can create a copper metal short if exposed to a slight overdischarge or voltage slip [1]. Another safety issue is the possibility of lithium plating at the graphite anode when overcharged, resulting in an internal lithium-generated short. The assembly of battery packs with many cells in parallel and in series requires complex wiring and battery management systems to ensure operation inside established safety envelopes. When one considers that a modest pulsed power system can include thousands, and

possibly even tens of thousands, of cells, the need to understand and accurately predict cell behavior is an economic and safety necessity.

1.1 Literature Review

1.1.1 Single-point Impedance Diagnostic

Given the potentially significant number of batteries installed in a deployed system, a simplified diagnostic would simultaneously increase safety and reduce costs. In support of that hypothesis, one may call on the work reported in [2-4] on 18650 $LiCoO_2$ cells, which demonstrated that a single-point impedance diagnostic may be identified for assessing battery health as related to safety and stability. That work, however, aimed at overcharging, not cycling, the tested cells for damage analysis. Furthermore, it was carried out on $LiCoO_2$ cells, not the LFP cells that this work is based upon. Nevertheless, it appears that the proposed single-point impedance method is effective due to the sensitivity of the EIS diagnostic to the solid electrolyte interface (SEI) in the battery. A properly formed SEI layer on the surface of the negative and positive electrodes protects against continuous electrolyte decomposition of those surfaces [5]. In contrast to [3, 4], in this experiment the cells are cycled, particularly at high C rates; as a result, the SEI will degrade and the protection is diminished or negated entirely, leading various effects from capacity fade to power fade and potentially destructive dendrite growth [6, 7]. The impedance associated with the SEI is in the 100 – 1000 Hz range of the electrochemical impedance spectrum for lithium batteries [8-14]. A C rate is defined as the rate at which a battery is discharged relative to its theoretical maximum capacity. For this work, 1 C = 2.6 AH and 10 C = 26 AH.

The impedance response can be split into real and imaginary components, but only the imaginary response provides the information of interest. The physical processes associated with the region of interest, 100 Hz – 1 kHz, are attributed to the anode [15-19], with an emphasis on the SEI layer. This association has been made via deconvolution of the Nyquist plot data through implementation of an equivalent circuit model [4] It has been established in [4] that abuse to a lithium-ion battery through various means, such as over-charging, over-discharge, and thermal abuse, will irreversibly affect SEI impedance. As a cell ages, the SEI layer impedance will change

to reflect measurable characteristics of the battery in circuit, specifically the loss of capacity and the loss of power [20].

1.1.2 Battery-driven Pulsed Power

The use of batteries to drive pulsed power is not new, however a review of the available literature has yielded few useful examples. In [21-24], sealed lead-acid (SLA) batteries were the preferred chemistry, as the now-common lithium ion battery was not available commercially until 1991 [25]. Oman in [21, 22] compared a bank of SLA cells to superconducting magnetic energy storage devices, which at that time was an emerging technology. Cornette in [24] proposed using SLA cells to directly drive an electromagnetic launcher system. The direct-drive (no intermediary DC-DC converter) connected to the pulsed power capacitor, and the energy was limited to only 27 kJ per capacitor (84 mF at 800 V). Chaudhari in [26] demonstrated some work with an unspecified chemistry (noted as “dry cell” in the text), to charge a 300-kV pulsed power system. The energy in that system was on a relatively small scale, 108 J. Verma in [27] used unspecified rechargeable batteries in concert with a Flyback converter to charge a 1 nF capacitor to 100 kV in 250 ms, for a total stored energy of 4 J. Allen in [28, 29] was the first to demonstrate repetitive rapid capacitor charging with SLA batteries on a 30-kJ capacitor bank. Finally, Holt in [30] used lithium polymer cells to charge a 50 μF capacitor to 5 kV in 500 ms, for a total stored energy of 625 J.

Over the past several years, the U.S. Naval Research Laboratory (NRL) has been developing a battery-powered pulsed power system that is designed to charge sixteen 60-kJ capacitors in approximately five seconds [31-35], which requires discharging the cells at 10C. In this system, each capacitor bank is connected to 12 battery packs comprised of 16 cells in series. During capacitor charging, they will be all connected in series for a 600 V input to the DC-DC converter that charges the 5-kV capacitor. Each battery discharges for four seconds, has a two second wait period, and repeats for a maximum of 50 pulses. The NRL research complements my work by investigating the changes in the effective lifetime of the batteries under the test conditions in the laboratory, as well as developing diagnostic technologies that serve as health monitoring to prevent battery incidents and provide advance warning when a battery is reaching end of life.

1.1.3 Pulsed Discharge Cycling of a Li-ion Battery

Few papers were found in the literature search connecting high C-rate pulsed discharge as a variable impacting the cycle life of any lithium-based battery. Wetz, et al. in [36] provided an analysis of different electrochemical energy storage devices that could be used for pulsed power loads. The focus was on determining the most appropriate energy storage type that had the highest power density and could be repeatedly pulse discharged at high C rates. Li-ion batteries were determined to be the most likely candidate, and some data was shown that indicates operation at a high C-rate does decrease the expected lifetime of the cell. The data presented, however, was at a constant rate and did not use pulse discharge. Based on [36] and some others, there is sufficient documentation in the literature for constant current discharge to eliminate the need for that aspect of battery performance to be evaluated for this work.

Another paper by Wetz, et al. [37] discharged a battery of similar chemistry and form factor to this work was discharged at a constant 10C rate with a 5 sec on/1 sec off profile until the cell voltage reached 2.5 V for one set, and 2.0 V for another. Unlike this work, the cells were recharged at 3.5C to simulate installation in a pulsed power system that requires rapid turn-around for operation. The authors found that discharging the cell to 2.0 V results in accelerated aging compared to the 2.5 V cell. They also concluded that the combination of high-rate charge and discharge induces higher thermal and mechanical stresses that are likely to cause cracking of the electrodes. This work uses 1C recharge to focus any damages observed on the discharge only, as well as adding additional cells to provide statistical depth not shown in this work.

Shrestha in [38] developed a test plan that evaluated three nickel-cobalt-aluminum-oxide Li-ion batteries at 1C, pulsed high C, and continuous high C rates to evaluate the impact of high rate cycling on these cells. Shrestha concluded that continuous operation in either the pulsed or continuous modes results in an increased lithium loss rate versus 1C operation. Additional testing performed on LFP cells with a 26650 form factor lead the author to conclude that the LFP chemistry showed an increase in electrolyte resistance and charge transfer resistance. Shrestha specifically used the EIS diagnostic as an integral part of testing to evaluate the battery performance, which replicates this work in that respect.

Chen, et al. in [39] did use a Saft VL8V battery (propriety chemistry) to pulse discharge a single cell into a load with a current of up to 1.7 kA for 5 ms. While this shows that some Li-ion chemistries can handle high discharge currents, neither a lifetime study nor a continuous pulse discharge was used to determine the long-term viability of this performance metric.

Ning, et al. in [40] performed high rate discharge cycling on a Sony 18650 Li-ion battery at ambient temperature. The experiment used three cells that were charged at the same rate but discharged at 1C, 2C, and 3C. After 300 cycles, capacity loss of 9.5%, 13.2%, and 16.9% were observed for the 1C, 2C, and 3C variables rates, respectively. The capacity was measured every 50 cycles with 1 A constant current discharge. This is interesting to see that even a modest power discharge of 3C is showing a significant decrease in cycle life. However, this study is minimally applicable to this work as it uses a different cell chemistry and form factor. Additionally, each test level was only used for one call, and cannot be considered a conclusive study of cell behavior.

While it was not at high C rates, Willard in [41] performed a pulsed discharge test on lithium polymer batteries, which were specifically designed for high energy applications. The pulse discharge profile varied between 1C, 0.5C, and 0C on each cell in 30 second increments, with an average discharge level of 0.5C. A separate test series used a constant discharge rate of 0.5C and C. The pulsed current test series was observed to degrade at a slower rate than the constant discharge cells. Williard concluded that the rest period between discharges in the pulse testing allowed the battery to recover and maintain a more stable electrochemical equilibrium. This paper seems to indicate that large rest periods between pulses may enhance the lifetime of the cells, however it was at relatively low discharge rates and a different chemistry than this work.

1.1.4 Performance of Batteries in Parallel Array

Relatively few papers were found to describe the operation of a parallel cell array. Of the nine results, three were of high interest. Gong et al. [42] carried out experimentation on automotive lithium cells to investigate and model series-parallel arrays. Unlike my work, they studied cells that had been previously used so that each of them was at a different SoH with varying level of capacity fade on them, and SoH is defined as a measured of remaining useful life. The results presented appear to confirm the hypothesis that when cells of varying impedance are mixed within a parallel connection of cells, there is significant variation in the current sourced by each that

follows the SoH of the cells. Published in April 2015, the authors of [42] state “few studies about parallel-connected battery packs have been done.” Based on this paper, there appears to be a knowledge gap that needs to be filled.

Gogoana et al. [43] demonstrated that a 20% variation in the internal resistance of two identical cells connected in parallel can lead to a 40% reduction in cycle life, when compared to two cells of similar internal resistance connected in the same manner. The experiment consisted in cycling the cells at 4.5C; [43] is in contrast to this work where the cells are cycled at 10C. Higher C rates are of interest to us because it leads to higher heat generation, which in turn leads to premature cell degradation. At such rates, even small variation in current sharing may induce significant variation in the heat generation and further exacerbate uneven cell aging.

Simulation results presented by Feng et al. [44] suggested the possibility of thermal runaway when asymmetry is developed between cells connected in parallel. Unfortunately, these results were not backed up by any measured data, and therefore were not conclusive. By contrast, in this experiment all of the cells stand are instrumented and carefully monitored for excessive thermal excursions.

A paper on load sharing by Han-Sik et al. [45] uses lead-acid batteries to study the electrical dynamics of a system. The authors discuss circulating currents between the batteries in the array, but they do not show any data supporting this assertion. They present the idea of controlled impedance at the output of each battery adjusted as needed by a microcontroller to maintain equal division of current. The paper suggests switches and resistors, which would be very lossy with high power cells. One may suggest that instead a MOSFET in linear mode would be a better choice, as the gate voltage can be precisely controlled via the microcontroller and the response time would be relatively fast. The system would require relatively high voltages, however, to accommodate the voltage drop across the MOSFET.

Of the four remaining battery discharge papers ([46-49]), only [46] was of any real interest. The authors looked only at cells with different capacities, instead of internal impedance mismatches. It appears the circuit model matches very well with measured data, but is on the highly complex edge of the modeling spectrum.

1.1.5 Battery Aging Phenomenon

Two papers were identified for background information on the construction of lithium-ion batteries. An overview of the cell design is given in [50], with a detailed description of electrolytes and anode structures. An overview of specific electrolytes is discussed in [15]. This work is very detailed, describing not only the common base solution but also additives to modify performance. Basic battery background knowledge was found in [9, 50-52].

In the electrochemistry regime, some useful data on capacity fade and aging is found in [20]. Specifically, "capacity fade can result from loss of lithium ions through electrolyte decomposition reactions and solid electrolyte interphase (SEI) formation, loss of active electrode material or a combination of the two." It also states that the cell impedance growth can be attributed to the loss of contact within the porous electrodes, loss of active electrode material, formation of resistive surface films, or impaired mass transport. The remainder of the paper is rather useful in the description of EIS scans with $LiFePO_4$ material; however, it is limited to only sections of the electrode and not the battery as a system.

Several papers on EIS were reviewed [54-61], and were useful for background information on EIS spectra and aging studies using EIS. The only paper that discusses the use of EIS with parallel cells is [53]. This paper uses on-the-fly EIS scans to determine the state of health for a battery pack in a portable defibrillator. This is also the only work seen that discusses limiting the frequency band to only the areas seen to vary monotonically with the battery state of charge. A general collection of data and explanations of regions can be found in [15-19]. In particular, [19] has a model variant that was used as a basis for the model created in this work. Several of the references found in [16] and [18] were also used to form a scientific basis for the correlation of the data measured and the electrochemical model.

1.1.6 Determination of Battery Temperature with EIS

The management of the internal temperature of a cell is a critical parameter for lithium-ion batteries, and the importance of thermal management increases with the number of cells in the system. Manufacturer defects and foreign objects in the cells can lead to serious conditions such as internal shorts or artificially increase the ohmic heating of the battery [62-66]. Overheating to

very high temperatures (130-200°C) can result in exothermic reactions like thermal runaway in $LiCoO_2$ chemistries, or destructive events like the vaporization of electrolyte followed by cell venting, and potential fires. Low temperatures can cause problems as well, in particular with recharge below freezing. The mass transport limitation in an increasingly viscous electrolyte as the temperature drops causes the precipitation of lithium from solution in to metallic lithium, which can collect into regions called dendrites. A dendrite can electrically connect the anode and the cathode internally, which results in a permanent short [3].

Traditionally, as was done with this work, thermocouples are used to measure the surface temperature of each cell. As a gross determination of cell performance this method is adequate, as during low C rates (1C and below), the cell can be assumed to be a homogenous structure. However, at higher C rates, the propagation delay between the core of the battery and the surface is sufficiently long that any damaging thermal event is beyond the point of recovery by the time the surface of the battery has reached the critical temperature limit. Prior research has shown that a discrepancy of nearly 50°C can be measured between the core and surface temperatures [3].

Two approaches exist to monitor the internal battery temperature. Forgez, et al. in [67] physically inserted thermocouples into a cell and developed a complementary thermal model. While useful in laboratory, it is entirely impractical for a large-scale battery installation. The other approach was described by Spinner, et al. [3], where EIS was used for a single 18650 $LiCoO_2$ cell to derive a critical thermal frequency that is sensitive to temperature changes. A frequency of 300 Hz was determined to be the critical frequency for that battery using their analysis method.

1.2 Research Objectives

Research has been performed on $LiFePO_4$ (LFP) cells with a 26650 form factor (26 mm x 65 mm) using a load profile identical to that utilized to charge a pulsed power device at NRL [35]. The objective of this work is to carry out some experimentation on a sample of controlled cells to test the hypothesis that changes in a single-point impedance value can be correlated to cell aging when 26650 $LiFePO_4$ cells are cycled using a standard, non-abusive, pulsed discharge profile in both single-cell and parallel-cell configurations. Another hypothesis that has been tested involves the aging of cells as a function of cycle in a parallel array. The hypothesis states that four cells

that have been filtered using equivalent series resistance (ESR), capacity, and overlapping EIS spectra will share current evenly when cycled using a standard, non-abusive, pulsed discharge profile, which will be referred to as the baseline parallel array. A corollary to that hypothesis is that four cells cycled in parallel under the same conditions but with only ESR and capacity filtering will not share current evenly. The cells in the baseline parallel array should age at approximately the same rate, while the other array should age at an irregular rate, which will cause an uneven increase in equivalent series resistance (ESR), which in turn imbalances the parallel cell discharge and causes premature aging of the parallel group when compared to the lifetime of a single cell. The development of a diagnostic that can detect electrochemical changes in a group of cells connected in parallel would be a significant step forward in the safe deployment of large-scale, high-power batteries in both U.S. Navy ships and other applications such as micro-grids, where instantaneous high power is required for specified periods of time.

1.3 Summary and Achievements

A series of experiments were carried out to characterize individual 26650 LFP cells. The impedance response as a function of state of charge (SoC) was measured and lifetime data was collected when they were cycled at 10C and 1C. An algorithm has been established that extracts the perturbation frequency (f_{SoH}) where the system response has been found to be invariant to cell state of charge. A second algorithm was created that found a critical frequency where the imaginary impedance response was invariant to state of charge but sensitive to temperature. Using the f_{SoH}, the electrochemical changes in a separate group of cells were tracked as a function of cycle, which is the first documented use of this type of diagnostic for both LFP cell chemistry and the 26650 form-factor in the single-cell state.

For the first time in published literature, a testbed was designed to evaluate the primary hypothesis of current sharing in identical batteries in a 4P1S array, which is defined as four cells in parallel (4P) and one in series (1S). Using the electrochemical impedance spectroscopy (EIS) diagnostic, an array was constructed with virtually identical cells and tested with the prescribed protocol. Along with four replicant arrays, it has been definitively demonstrated that batteries in parallel cannot share current evenly when uncontrolled current flow is implemented regardless of

the cell matching performed prior to installation. Additionally, this is the first reported data on the determination of state-of-health data for multiple cells in parallel, as well as the first development of a diagnostic capable of non-destructively determining battery core temperature.

Using the full-frequency data acquired during the periodic EIS sweeps of the batteries both in single-cell and multiple-cell formats, a model of the electrochemical system has been developed. The model was designed to account for four areas of the cell: physical aspects such as diagnostics and current conductors; solid electrolyte interface (SEI) layer; anode materials; and the cathode characteristics. The model successfully predicted that the anode material is the principal aging mechanism for cells discharged at high C-rates, the inverse of low C-rate cells with the SEI layer as the primary driver of aging. This assertion was validated with post-mortem analysis of select cells using photography of the jellyroll layers and computed tomography. Changes in the f_{SoH} are also correlated to damage observed in the analyzed battery.

The application that used the f_{SoH} diagnostic was a simulated array of batteries constructed in a manner that replicated the system performance of [71] and the power requirements similar to [72]. Performance of single-cell systems at high and low power was used to develop a baseline for comparison to the parallel testbed. The data collected successfully indicated a change in the electrochemical impedance response as a function of cycle and discharge rate at a single frequency, reducing system interrogation time. The full frequency sweep was used to generate a model of the experimental cells that correlated changes in f_{SoH} with physical damage to the anode substrate. The damage was validated with post-mortem analysis of select cells and computed tomography analysis.

The most direct application of this work is the development of an *in-situ* diagnostic that can be integrated into a battery management system (BMS) on a battery pack, providing active feedback to the operating system on the health of the battery. Due to the use of a single fundamental frequency, the electronics would be relatively simple to implement as an integral part of a BMS. The system can be programmed such that periodically a SoH scan is initiated, and with a history of the battery available to the microcontroller a decision can be made to alert the operator to place the battery out of service when an adverse impedance response is recorded. For logistics management, one can imagine additional programming that would track changes as a function of cycle and time and provide advance alerts as the pack is aging and needs to be replaced.

This research has produced several publications and a patent disclosure for the temperature diagnostic. Development of the battery system, with selection criteria and performance design was described in [31-35, 68, 69]. These papers were published in the IEEE Transactions on Plasma Science, the IEEE Transactions on Dielectric Sciences, the Proceedings of the 17th International Symposium on Electromagnetic Launch Technology, Proceedings of the IEEE Electric Ship Technologies Symposium, and the Proceedings of ASNE Day 2013. A detailed report [70] of the f_{SoH} diagnostic and key results was published in the Journal of the Electrochemical Society. A forthcoming analysis [1] of the battery post-mortem data using computed tomography will be published in *Advance Energy Letters*, which has shown for the first time in the literature that an electrode coupon can be analyzed with computed tomography without disassembly of the film. This ensure any damage measured by the diagnostic can be attributed to the battery and not the tool.

1.4 Dissertation Organization

Electrochemical storage devices are discussed in Chapter 2. This chapter reviews some of the typical battery systems (sealed lead-acid batteries, nickel-metal hydride, and lithium) available in the open market and their advantages and weaknesses as they relate to the objective of this work. Chapter 2 continues with aging mechanisms on lithium batteries and how they affect the anode, electrolyte, and cathode portions of a cell. The chapter concludes with a discussion on electrochemical impedance spectroscopy measurements and modeling.

The experimental setup is covered in Chapter 3, with initially a discussion of the battery selection criteria and how the final experimental cell set was generated. This is followed with how the state of charge measurements were conducted for the determination of both f_{SoH} and $f_{thermal}$. The instrumentation and cell holder design for the single-cell experiments is next, and the chapter is terminated with a detailed explanation of how the parallel-cell testbed was designed and manufactured.

Results and analysis of all of the experiments performed can be found in Chapter 4. The chapter opens with a discussion of how the f_{SoH} was calculated from the data obtained from the state of charge experiments, and is the foundation of the remainder of the chapter. A brief

discussion of the $f_{thermal}$ results is next, with caveats that were discovered. The single-cell lifetime data is next, with electrical and EIS analysis of the system performance at both 1C and 10C discharge levels. Parallel array data is in the subsequent section, with the added parallel EIS response and additional analysis, followed immediately by the replicant parallel arrays. Modeling of the different experiment groups is discussed in the penultimate section, tying the observed data to suspected physical aspects of the cells. Finally, the post mortem analysis of selected cells is used to validate the model with both photographic evidence of the battery films and computer tomography data.

Chapter 2

Electrochemical Energy Storage

An electrochemical storage device supplies electrical energy by the conversion of chemical energy stored in the device by means of an electrochemical oxidation-reduction reaction [51]. Electrons are transferred from the anode to the cathode through an external circuit, while the ions are transferred internally from the anode to the cathode. A proper definition of a single battery is a cell, where a collection of cells is called a battery. A battery can consist of any combination of cells in series, parallel, or (more typically) a combination of the two.

A cell consists of three major components: anode, cathode, and electrolyte. During the discharge process, the anode, or fuel electrode, supplies electrons to the external circuit and is oxidized during the electrochemical reaction. The cathode accepts electrons from the external circuit and is reduced during the reaction. The final component, the electrolyte, is an ionic conductor that provides the medium for the transfer of ions inside the cell between the anode and the cathode. The electrolyte is typically a liquid with dissolved salts, acids, or alkalis to impart ionic conductivity [51]. It is critically important that the electrolyte is ionically conductive but not electrically conductive, as this would cause an internal short in the cell.

There are two types of batteries, primary and secondary cells. A primary cell is a “one-shot” battery that can deliver energy to a load but cannot be recharged after it is exhausted. These cells will hold a charge for many years, but are limited in the amount of power they can source. An

example of this type of cell is an alkaline battery used for flashlights, toys, and digital cameras. These batteries are inexpensive, lightweight, and readily available.

A secondary cell is designed specifically for multiple uses, with distinct discharge and recharge characteristics. These cells typically have high power density, high discharge rates, and relatively flat discharge voltage characteristics. In contrast to the primary cells, these can be expensive and depending on the specific chemistry require complex management systems for both discharge and recharge. This work is focused on a specific secondary cell, a lithium-ion type using the $LiFePO_4$ cathode material.

2.1 Types and Characteristics of Secondary Cells

In the category of secondary cells, there are many types of batteries that can be used in applications requiring repetitive discharge and recharge cycles, each with a specific usage profile. As shown in Figure 2.1, there are many types of energy storage systems that fill a variety of specialized roles. The purely chemical, such as gasoline and methanol, tend towards mostly high specific energy and moderate power density. More advanced technologies such as flywheels and super capacitors tend towards very high power density, but low energy density. Lead-acid the first of the three most commonly used chemistries for power systems, and while it is on the low end of both power and energy density, it is very robust and is well understood. An increase in both key attributes can be seen with the nickel-metal and lithium batteries, with the lithium consistently outperforming the slightly older nickel-metal hydride technology in energy density.

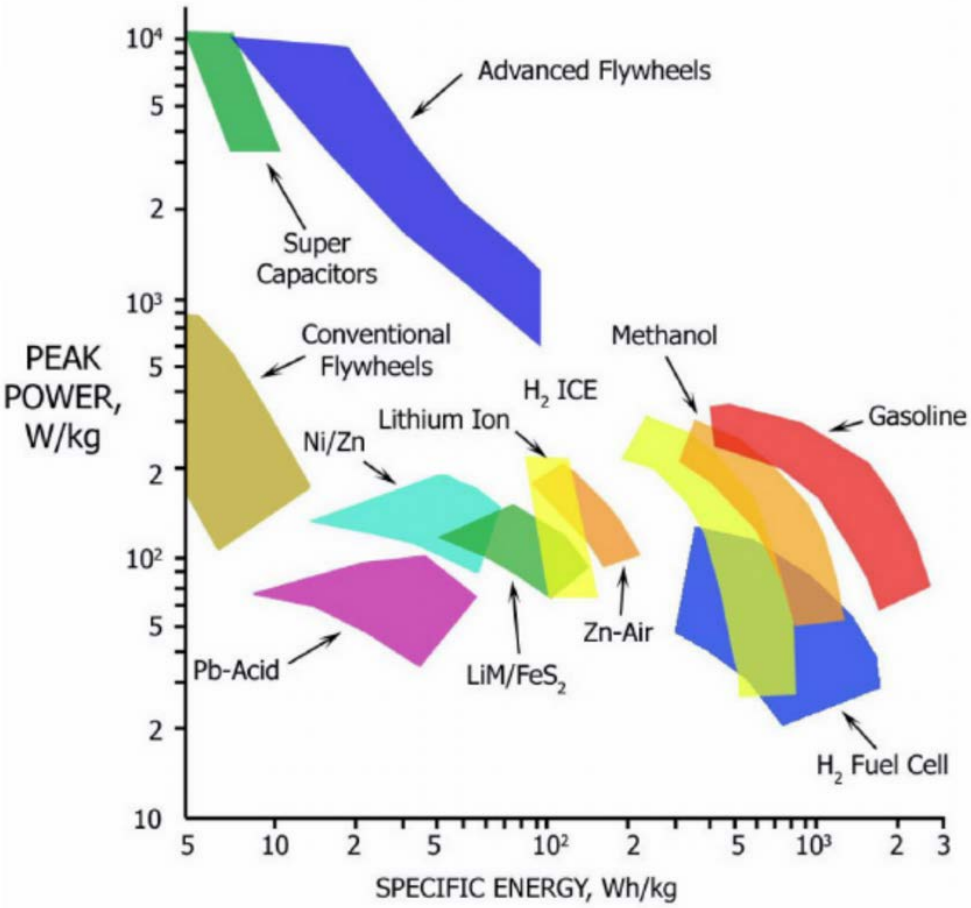

Figure 2.1: Ragone plot comparing the power density and energy density of various energy storage technologies [73]

Lead-acid batteries were first developed in 1859 by Planté, followed by the nickel-iron alkaline battery by Edison in 1908. Due to high cost, maintenance requirements, and low specific energy, the nickel-iron cell was eventually replaced by the pocket-plate nickel-cadmium battery first developed in 1909. This design used sintered plates that increased power capability and energy, and was further improved with the development of the sealed nickel-cadmium cell. In the last 20 years, the nickel-cadmium batteries have plateaued in specific energy and energy density, 35 Wh/kg and 100 Wh/L, respectively. Nickel-metal hydride, in contrast, has been improved to 70-100 Wh/kg and up to 430 Wh/L, largely supplanting most nickel-cadmium installations [51].

Lithium-ion cells were first commercialized in 1991 by Sony, and have largely replaced most other secondary cells in markets that require high energy density, high power density, and small form factor. The first lithium cells used $LiCoO_2$ as the positive electrode material, and remains in

use for a significant fraction of the secondary market. In the past 15 years several variants with different cathode materials have been introduced, such as LFP, LiMn2O2, Li(NiMnCo)O2, and Li(NiCoAl)O2. Each of these materials offers different advantages, from high-rate discharge capabilities, thermal stability, long cycle life, and/or low cost which often fill niche markets such as military applications or electric vehicles [51].

2.1.1 Lead-acid Batteries

The lead-acid battery is available in several configurations, which range from small sealed cells with a capacity of 1 Ah to large cells as high as 12 kAh, which makes it an attractive potential energy source for pulsed power systems. The largest market for these batteries is automotive, with nearly all car batteries of the lead-acid design. This type is often referred to as "sealed lead-acid battery," but the proper term is "valve-regulated lead-acid battery" (VRLA). While technically sealed to provide maintenance-free operation, a pressure valve exists to regulate the flow of gas to and from the battery. The valves are normally closed to prevent atmospheric oxygen from contaminating the cell during operation, but can open as needed to provide safety relief in case of overpressure. The introduction of plastics to the body of the battery allows for hydrogen permeability, which further increases the safety of the battery and reduces the risk of overpressure. As with other battery designs, VRLA designs can be either a cylindrical jelly-roll style in a cylindrical container, or in flat plates in a prismatic container. The jelly-roll design allows for pressures as high as 276 kPa while the prismatic is limited to a maximum of 14 kPa. [51].

Lead-acid batteries use a double-sulfate reaction as the fundamental electrochemical energy conversion. As shown in (2.1), during discharge a lead sulfate product is created with water as a byproduct. When reversing the process during recharge, these products are split into hydrogen sulfate and lead dioxide. When an overcharge condition occurs in flooded lead-acid batteries, the reactions generate excess hydrogen and oxygen gas, with a net loss of water. In VRLA designs, the sealed nature of the design forces most of the excess oxygen to recombine in the cell. The use of high quality lead and the avoidance of PbSb allows minimizes hydrogen production on overcharge and reduces the rate of self-discharge [51].

$$PbO_2 + Pb + 2H_2SO_4 \underset{\leftarrow charge}{\overset{discharge\rightarrow}{}} 2PbSO_4 + 2H_2O \qquad (2.1)\ [51]$$

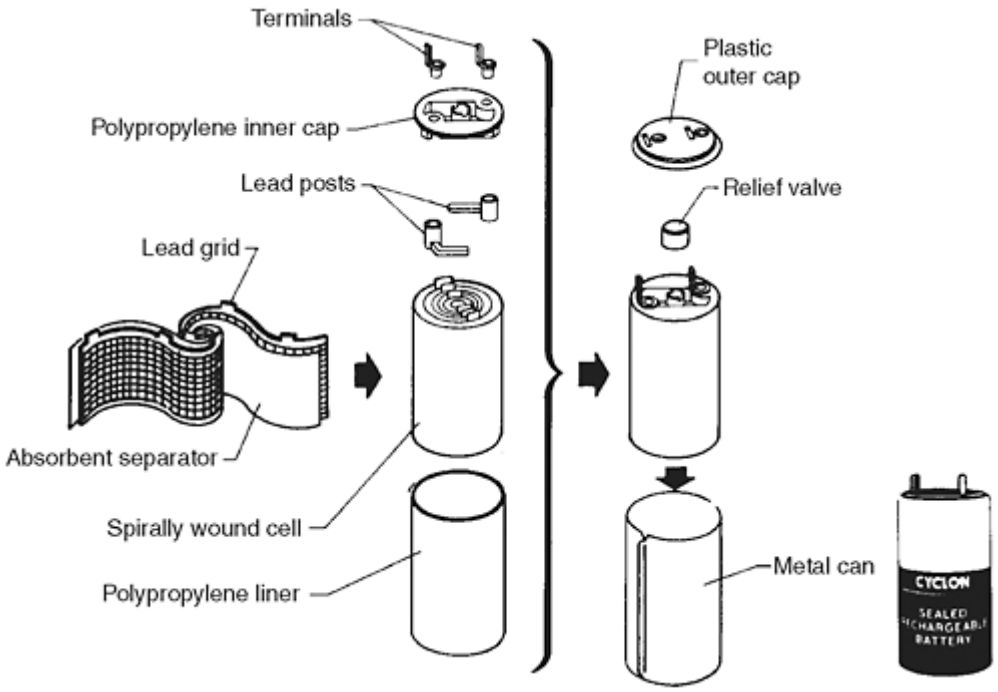

Figure 2.2: Components of a VRLA cylindrical cell [51]

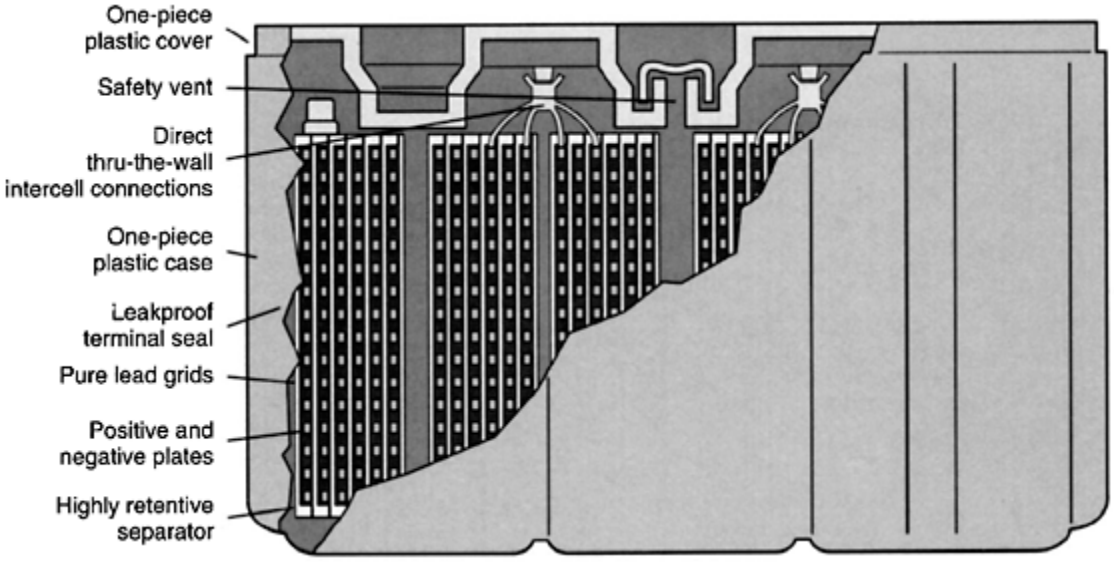

Figure 2.3: Components of a VRLA prismatic cell (typical of a car battery) [51]

High-power from VRLA batteries is achieved by either the increase in total voltage or by increasing the current. Increasing the voltage requires a volume increase, thereby reducing the total energy per unit volume. Increasing the current can be achieved with the use of thin electrodes

on metal substrates, but as the surface area increases between the current collectors and the active electrode materials the self-discharge rate also increases. This results in the inability to provide the required shelf life for many applications. Additionally, even after the improvements in power sourcing, the lithium-ion battery design offers high energy density, power density, and open-circuit voltages without the high rate of self-discharge. To further eliminate VRLA batteries from the prospect of performing as an energy source for pulsed power devices, VRLA batteries are sensitive to high temperature environments and cannot be stored in a discharged condition. Thermal runaway can occur with incorrect charging or poor thermal management techniques [51].

2.1.2 Nickel-metal Hydride-based Batteries

Nickel-metal hydride (NiMH) batteries were first studied in the 1960s as an environmentally friendly, lower cost, and higher energy density alternative to nickel-cadmium cells. NiMH was introduced commercially in 1989, and has since been the battery selected for nearly all electric vehicles and the small portable electronics market, with 10% of the total rechargeable battery market in 2008. This chemistry is the preferred choice for electric vehicles, as it has an excellent safety record, can tolerate substantial abuse, and has long cycle life. Additionally, NiMH cells can retain 85% of their charge for one year. Performance at low temperatures is an issue, however, and VRLA cells are still the optimum choice for automobile starter batteries. [51].

NiMH batteries available in several configurations: cyclindrical, button, and prismatic. A schematic of a typical cylindrical cell is shown in Figure 2.4. Highly porous electrodes are used to provide a large surface area for low internal resistance and high discharge rate capability. The positive electrode has nickel compounds pasted on the active material by electro-deposition, typically a foam-nickel substrate in modern NiMH cells. The negative electrode is also a highly porous structure using a perforated nickel foil or grid onto which the active hydrogen storage alloy is coated. The separator is a synthetic nonwoven material, which insulates the two electrodes and acts as a medium for absorbing the electrolyte. The electrolyte is typically a mixture of about 30% KH in water, with approximately 17 g/L of LiH to promote improved charging efficiency by suppressing oxygen generation [51].

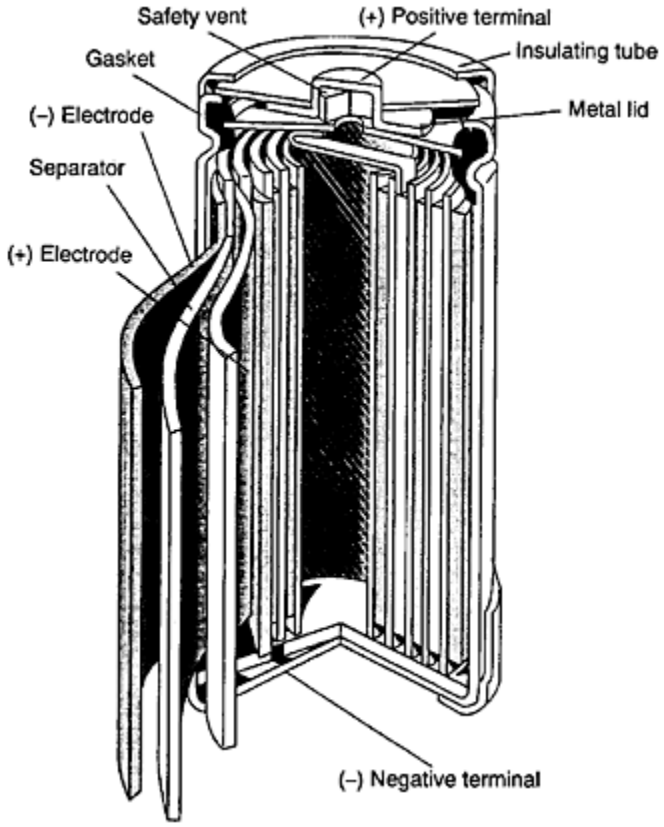

Figure 2.4: Schematic of a sealed, cylindrical NiMH battery [51]

During discharge, NiOOH is reduced to Ni(OH)2 as shown in (2.2), while the metal hydride (MH) is oxidized to the metal alloy (MA) in (2.3). During recharge, the process is reversed. NiMH cells are permanently sealed to contain the gases generated during the recharge process, as during the charge process the positive electrode begins to evolve oxygen. The oxygen gas diffuses through a separator to the negative electrode, where it reacts with the hydrogen electrode to produce water. With the generation of liquid water, the pressure in the cell is stabilized. The cell is designed so that the negative electrode never becomes fully charged, preventing the generation of hydrogen gas [51].

$$NiOOH + H_2O + e \rightarrow Ni(OH)_2 + OH^- \quad (2.2)\ [51]$$

$$MH + OH^- \rightarrow MA + H_2O + e \quad (2.3)\ [51]$$

In the design and application of NiMH batteries, there is an energy versus power trade-off that must occur. An NiMH cell can be designed for energy, power, or a combination of the two to meet a specific goal. For purely electric vehicle applications, a specific energy of 62-80 Wh/kg

and specific power of 200 W/kg are generally desired, as the battery is required for all transports modes of the automobile. In contrast, a hybrid electric vehicle, with an internal combustion engine as the prime mover, has a goal of greater than 1000 W/kg for the specific power. This results in the specific energy for a typical hybrid car to be in the 32-56 Wh/kg range [51]. While an NiMH battery may seem like an ideal choice for a system requiring power discharge, the nominal voltage of 1.25 V per cell is well below the nominal voltage of a typical Li-ion cell (3.3 V), requiring the use of three NiMH cells for every one Li-ion cell. Additionally, the equivalent series resistance (ESR) for an NiMH cell is typically 20 mΩ, which is twice the nominal ESR for a Li-ion power cell.

2.1.3 Lithium-based Batteries

Lithium-ion batteries utilize lithium storage compounds in the anode and cathode materials to exchange lithium ions between the positive and negative electrodes, as shown in Figure 2.5. This contrasts with conventional batteries that involve the formation and dissolution of covalent bonds and structural changes, such as found in the NiMH cells. There are many different types of Li-ion batteries, nearly all of which are distinguished by the specific materials used in the cathode. For these experiments, LFP was used, and the reactions described in the following sections will be tailored to that chemistry. The design of the experiment and specific selection of cell chemistry is discussed in Chapter 2.

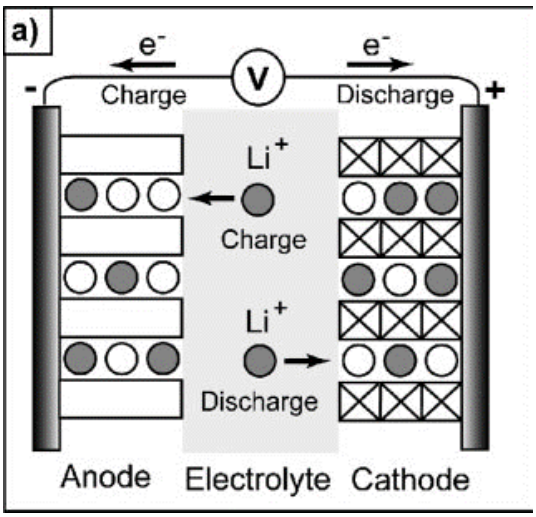

Figure 2.5: Schematic illustration of a Li-ion battery [74]

A section view of a cylindrical Li-ion battery cell is shown in Figure 2.6. Li-ion cells are sensitive to water and air, and are hermetically sealed. The case cover is typically designed as a pressure-relief valve that will allow any internal gasses generated in a thermal event to safely escape the cell. For this work, 26650 (26 x 65 mm) cylindrical cells were used, and are nickel-plated steel cans sealed by crimped gaskets. Current collectors are used to connect the active material to the electrical circuit. The anode uses a Cu foil, while an Al foil is used for the cathode. The surfaces of the foils are treated to promote adhesion to the active material, seen on microscopic analysis as a roughened surface [52]. The current collectors are connected to a number of tabs that are made of larger material to handle large currents and connect directly to either the positive or negative terminals. The tabs can be seen in Figure 2.7, with the positive terminal tabs in white and the negative terminal tabs shown as darker shapes. The difference in contrast is due to the attenuation of the material to x-rays, with the denser material blocking more x-rays, thus appearing brighter on the radiograph.

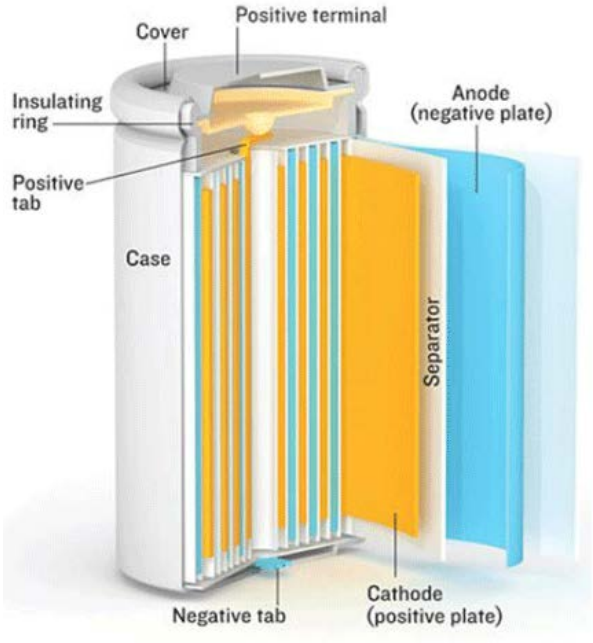

Figure 2.6: Section view of a cylindrical Li-ion battery cell [75]

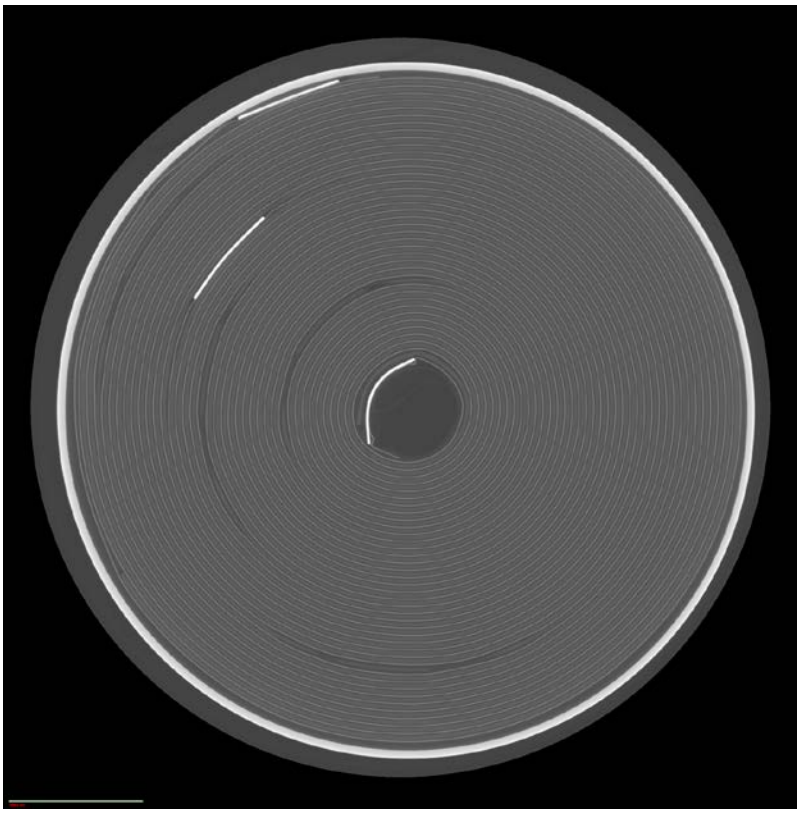

Figure 2.7: Computed tomography axial slice of Li-ion 26650 battery

Each electrode is comprised of an active material bonded to a metal current collector, as shown in Figure 2.8. The external circuit (load) is connected to the two terminals of the battery, and electrons flow through the circuit from the cathode into the anode. Ions flow between the electrodes internal to the cell, via a conductive medium called the electrolyte. The electrolyte is a solution of $LiPF_6$ with proprietary additives that provides a medium for the ions to travel between the electrodes. It is electronically insulated to prevent electron travel, which forces them to travel through the external circuit and prevents self-discharge. However, it is not a perfect insulator, and a small percentage of charge leaks over time. This is evidenced as self-discharge and can generally be predicted as a constant value for Li-ion cells. The electrolyte for Li-ion batteries is typically a non-aqueous inorganic compound such as $LiPF_6$, mixed with ethylene carbonate and ethyl methyl carbonate. The resulting electrolyte is about 100 times more resistive than what is used for VRLA batteries [52].

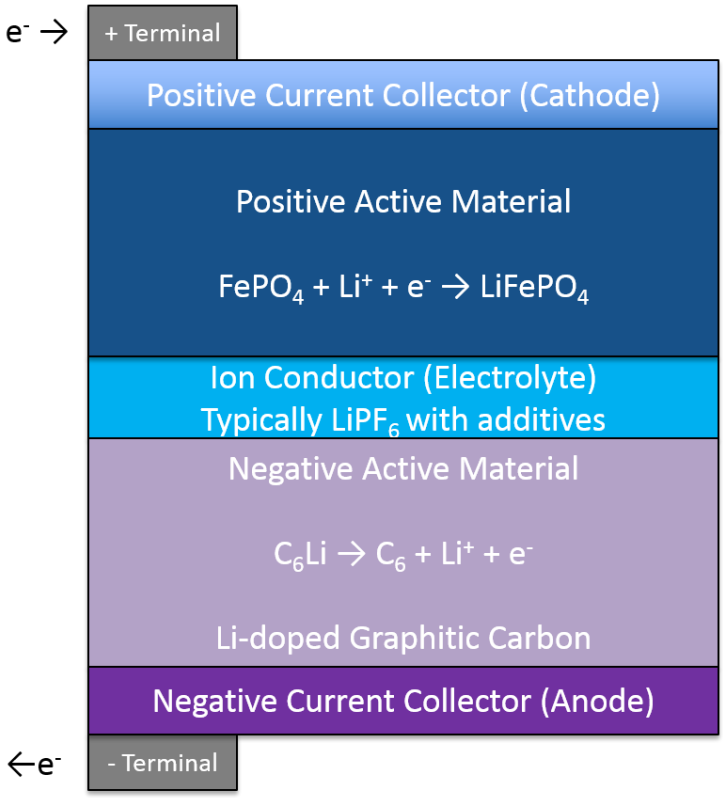

Figure 2.8: Diagram of Li-ion electrode configuration in discharge mode [52]

The non-aqueous electrolyte used in Li-ion batteries presents significant safety concerns. The $LiPF_6$ electrolyte mixed with the ethylene carbonate and ethyl methyl carbonate has a flash point of 25.5°C, and will produce significant heat if burned. Additionally, any incident that breaks the battery's hermetic seal could result in a fire when atmospheric moisture contacts the electrolyte [52]. An internal short would also drive a thermal event in the battery, but the extent of that event would be heavily dependent on the specific chemistries involved in the cathode. Detection of an adverse condition in the battery would significantly reduce the risk involved in the use of Li-ion cells, particularly in harsh environments.

A support material called a separator is used to physically isolate the anode and cathode materials. The separator is designed with specific values of porosity and tortuosity to allow the ion conductor to fill the pores of the separator, and have a finite thickness to engineer a specific path length to minimize interference in the flow of ions. Separators can be multi-layer, microporous structures tuned for specific electrolyte mixtures. Some separators are designed to prevent ionic transport at elevated temperatures to increase the safety of the cell [52].

The active material undergoes an electrochemical reaction at its interface, as shown in (2.4). The anode is reduced by electrons from the external circuit, and the cathode is oxidized, which releases electrons during the recharge process. In discharge, electron flow is reversed, allowing the recombination of the ions with the active material. The potential difference between the two sides is the cell voltage. If the cell voltage is allowed to drop below a specified point, 2.0 V in $LiFePO_4$, the copper current collector in the anode will become oxidized, and the resulting Cu^{2+} ions will diffuse to the cathode, where they are further reduced to Cu metal and form dendrites. The dendrites will continue to grow as more Cu is collected, and until the separator is penetrated and an internal short is formed [76].

$$Li^+ + e^- \leftrightarrow Li^0 \quad (2.4)\ [52]$$

The cathode is a positive active material, and is reduced by electrons from the external circuit, as shown in (2.5). The free Li^+ ions are captured in the $FePO_4$ matrix and removed from the electrochemical reaction. The cell is considered exhausted when the supply of free Li^+ ions has been consumed [52].

$$FePO_4 + Li^+ + e^- \leftrightarrow LiFePO_4 \quad (2.5)\ [52]$$

The negative active material, the anode, is comprised of a Li-doped graphitic carbon, typically graphene in modern Li-ion batteries. During a discharge, the material is decomposed as shown by (2.6). The Li-doped carbon releases a Li^+ ion and an electron, with the Li^+ ion moving into the electrolyte [52].

$$C_6Li \leftrightarrow C_6 + Li^+ + e^- \quad (2.6)\ [52]$$

Mass transport through the electrolyte is a major contributor to the limitation on power transfer inside a battery. A simple model for the current density as limited by the mass transfer physics is shown in (2.7), "where D_{eff} is the effective diffusion coefficient (m^2/s), c is the concentration of the lithium salt in the electrolyte or the solid-phase lithium sites (mol/m^3), and δ is the diffusion length (m) [52]."

$$i_d = \frac{FD_{eff}c}{\delta} \quad (2.7)\ [52]$$

In practice, diffusion limitations occur due to salt transport in the ionic phase that covers the entire cell and the lithium transport inside the active materials. In the electrolyte, practical design using non-aqueous electrolytes at useful rates forces the use of thin electrodes (<100 μm) and separators (<30 μm) [52]. This comes at the cost of energy density, which is why manufacturers have specific cell lines devoted to either high energy density or high power density. One cannot do both, as there are always trade-offs.

In the active materials, porous electrodes are used to achieve an effective increase in power without increasing the thickness of the materials. The fine particles used in a porous layer enable fast solid-phase transport by reducing the diffusion length, while the porosity enhances access to the solid via liquid-phase transport. As mentioned, trade-offs exist in the cell design. Thicker and more densely packed layers enhance energy density, while the opposite will increase power density [52]. To a limited degree, one could fine-tune the balance between the electrolyte, anode, and cathode thickness to obtain a cell with the desired balance of energy and power density for a particular application.

In general, Li-ion cells have a higher specific energy and energy density when compared to other competing technologies for weight or volume sensitive applications, especially VRLA. Additionally, they have a low self-discharge rate (2-8% per month, depending on chemistry), cycle life of greater than 1000 cycles, and a larger operational range than most other battery types (typically -45°C - 65°C) [52]. The single-cell voltage of at least 3 V is twice the level observed with competing technologies such as NiMH, cutting the total number of cells required for an application by a factor of three. Finally, Li-ion cells can natively support high discharge operations, with 30 times the normal discharge rate considered normal.

2.2 Lithium-Ion Electrochemical Aging Mechanisms

As with any product, it is highly desirable to extract as much useful life out of a component as possible to minimize the economic costs associated with purchased, operating, and maintaining a system. Goals set by organizations such as the United States Advanced Battery Council and the FreedomCAR Research Initiative require a calendar life of at least 15 years for hybrid electric vehicles and 10 years for purely electric vehicles, with cycle life of at least 1000 when discharging

the batteries to 80% of their starting capacity [77]. It is necessary to develop an understanding of how batteries age in order to both predict their expected lifetime and to potentially design a better battery that is capable of meeting the design goals.

Lithium-ion batteries are a fairly new technology, with the first commercialized cell available in 1991. Unlike other batteries, such as VRLA, there are many dozens of possible cathode chemistries that perform in very different manners. In general, however, they do behave approximately the same, and can be treated as such. The specific causes of aging are quite complex, but can be split into anode and cathode processes. As an additional complication, the electrolyte has a role in the aging process and must be considered as part of aging on both sets of electrodes [77].

Anodes in Li-ion batteries are made of carbon, most typically graphite and specifically as graphene. A diagram of the aging mechanism for the anode is shown in Figure 2.9, with the anode material on the left and the electrolyte on the right. Changes at the electrode-electrolyte interface, known as the Solid Electrolyte Interface (SEI) layer, is considered to be the major source of aging of the anode [78]. Lithium-ion battery anodes operate at voltage levels higher than the electrochemical stability window of the electrolyte, thus resulting in an irreversible consumption of lithium ions at the electrode-electrolyte interface when the anode is fully charged. This is coupled with decomposition of the electrolyte to build up a layer that covers the surface of the electrode. This process primarily begins at the start of cycling, but does continue at some level during the lifetime of the battery [77].

The SEI layer is a unique feature to Li-ion batteries, and function as a protective layer to the graphene surfaces. The SEI layer is permeable to lithium cations but generally impermeable to other electrolyte components and electrons. Preventing other compounds from interacting with the anode both protects the electrolyte from further breakdown due to the anode and minimizes corrosion on the electrode. During the SEI layer formation, there is a release of gaseous compounds as the electrolyte decomposes, which results in a small but finite loss of capacity. The capacity lost is a function of the surface area of the graphite [77].

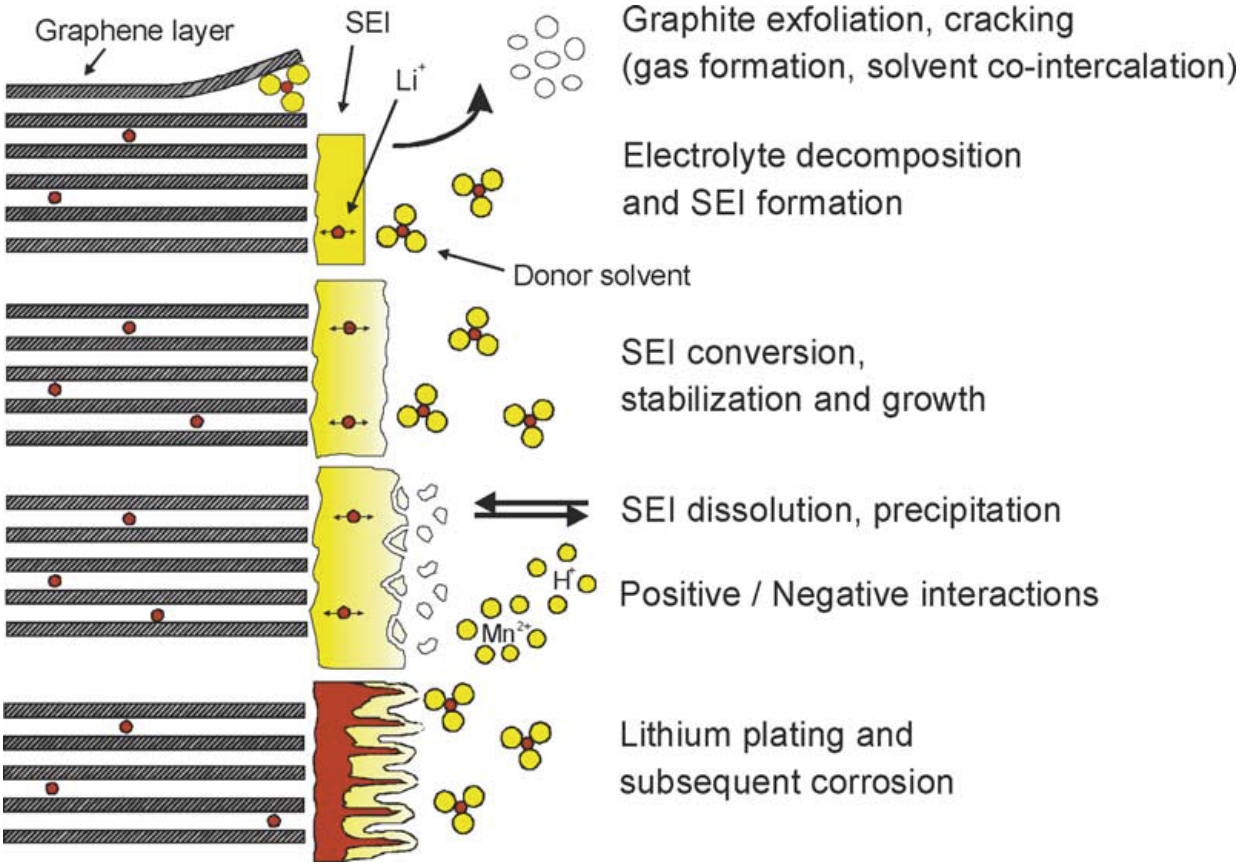

Figure 2.9: Anode aging mechanisms [77]

After an initial formulation series of cycles where the SEI layer is formed and stabilized, a significant portion of the battery life operates with a stable layer that grows relatively little in size. As the number of cycles increases, the cumulative effects of the small portion of charged (anions, electrons, solvated cations) and neutral (solvents and impurities) species that are not blocked by the SEI layer begin to take their toll. Corrosion of the graphite is observed as capacity fade, as portions of the active regions of the electrode are inaccessible to lithium ions. The electrolyte begins further decomposition, which results in a loss of electrolyte and SEI layer growth, and is observed as power fade, or decreased ion mobility [77]. The growth of the SEI layer is generally seen as an increase in the impedance of the cell, which can be measured externally.

Temperature can have a significant impact on the SEI layer performance. Elevated temperatures, especially above 60°C, changes the morphology and composition of the SEI layer. With sufficient thermal energy present, the cell could reach a thermal runaway condition with a subsequent fire and/or explosion. Studies have shown that increasing the cell temperature to 80°C

can result in exothermic reactions of the lithiated carbon resulting in self-heating. Other research has shown that the SEI layer may degrade completely in some areas of the electrode, exposing it to undecomposed electrolyte and redox reactions that lead to further capacity loss. Low temperature can also significantly affect cell performance. During recharge at low temperatures (0°C), with metallic lithium plating and lithium dendrite growth in the SEI layer. Subsequent reactions of the metallic lithium with the electrolyte accelerate the aging process and decrease the safety of the battery [77].

Towards the end of cell life, many of the effects of temperature are seen even when operated within thermal tolerance. The largest driver of a battery event is the nucleation of metallic lithium from the electrolyte into the SEI layer, forming dendrites. If these dendrites are allowed to continue to grow, enough lithium may become concentrated at a specific point to connect the anode to the cathode electrically inside the cell, resulting in a dead short. This can be prevented, however, by electrical measurements and other diagnostics during the cell life. The standard method of determining cell end of life (EOL) is when 80% of the original capacity has been reached. Below this point, the probability of a dendrite forming from the anode to the cathode increases significantly with each additional cycle.

The specific mechanisms of cathode aging are complex and appear to be an interdependent system of effects involving the aging of the active material, degradation of the electrode components (conducting agents, binder, corrosion of current collector), oxidation of the electrolyte components, and interaction of aging products with the negative anode, as shown in Figure 2.10. Degradation of the positive active material depends on the state of charge and cycling conditions, similar to the negative active material. The electrochemical reaction of the positive materials requires the repeated insertion and removal of lithium ions during each charge and discharge cycle, respectively, as shown by (2.8). Phase transitions can also occur, distorting the crystal lattice and adding additional mechanical stress [77].

$$LiFePO_4 \Leftrightarrow Li_xFePO_4 + (1-x)Li^+ + (1-x)e^- \qquad (2.8)\ [77]$$

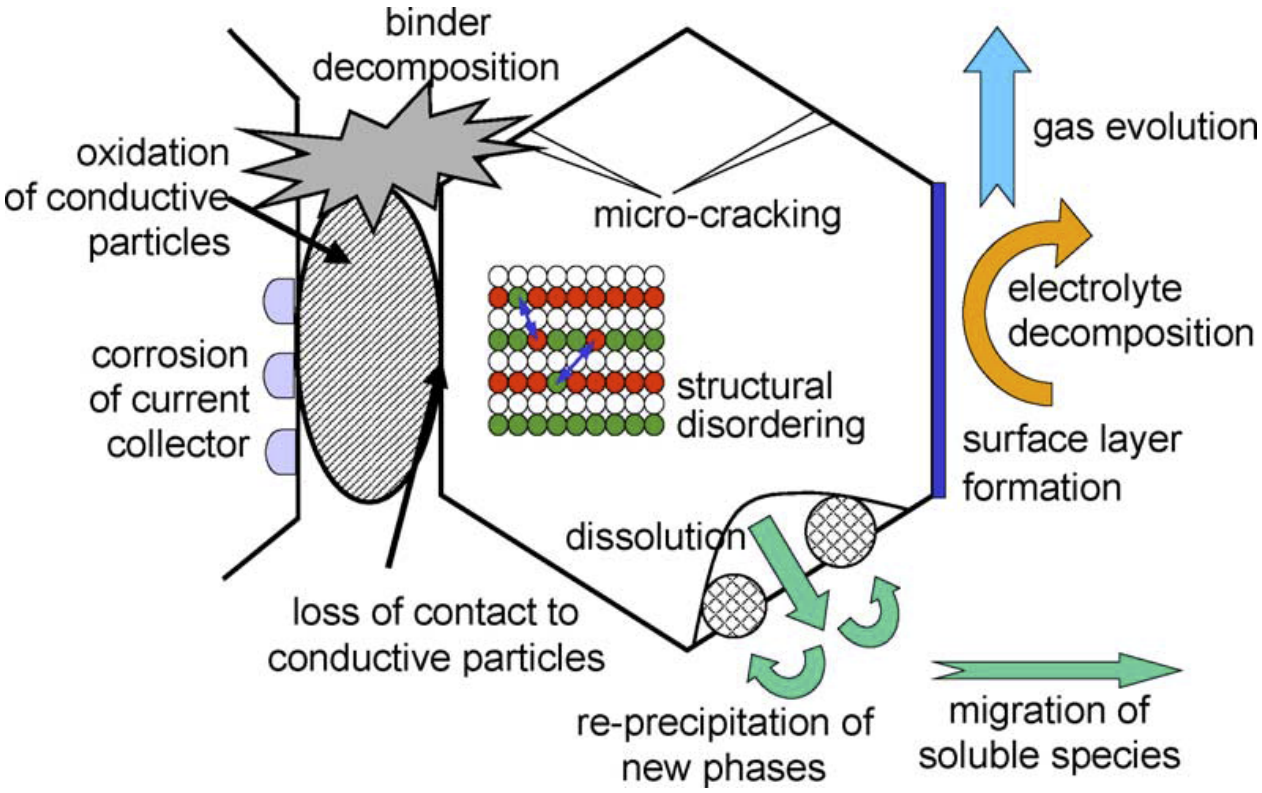

Figure 2.10: Cathode aging mechanisms [77]

2.3 Non-destructive, in-situ, Electrochemical Measurements

Due to the sealed nature of batteries, it is extremely difficult to quantify each of the respective mechanism's contribution to the progressive aging of a cell. The most conclusive analysis would involve a scanning electron microscope with specific portions of the interior films, but this would destroy the cell in the process, thereby rendering any additional testing impossible, and will likely change the physical characteristics of the cell in the process. An in-situ analysis is therefore critical to the continual analysis of a cell's behavior over the lifetime of the battery under test. These analyses range from relatively simple, such as the cell voltage and current, to more complex such as electrochemical impedance spectroscopy (EIS).

2.3.1 Voltage and Current Measurements

Using a meter to measure the voltage and current of a cell under test is a simple process that can be done with readily available equipment. The voltage measurement can be used to determine

how the potential drop changes as a function of discharge rate, depth of discharge, and cycle number. It is also used to ensure the cell remains in a safe operating area during discharge and recharge. The current can be used to also remain in a safe operating area, while functioning as a more advanced tool with computerized equipment.

Advanced measurements with a current probe can yield several useful metrics. First, combining the current with a clock enables the determination of the battery's capacity, typically measured in amp-hours (Ah). This leads to an important metric for battery research: the C rate. A 3 Ah battery discharged at 3 A will become exhausted after one hour, so it's 1C rate is defined as 3 A. Integration of the current as a function of time can yield coulombs, which can be used as a measure of how "full" a cell is by counting number of coulombs. This tends to be an imperfect method, as when the cell ages the maximum number of coulombs will change. A proper method of coulomb counting is to maintain a record of the last charge-discharge cycle values at the 1C rate as a comparison. The extracted charge is limited by the cell voltage, as the voltage will drop in the cell to maintain the current required by the external circuit. Allowing the cell to discharge below the minimum acceptable voltage will permanently damage the cell.

2.3.2 Electrochemical Impedance Spectroscopy (EIS)

While the current and voltage measurements can give a value for the internal resistance of a cell, it is only at one frequency (typically DC). Measuring at multiple frequencies, the larger the range the better, would provide an insight into the frequency response of the cell. Electrochemical impedance spectroscopy was originally conceived in the 1880s by Oliver Heaviside, but due to insufficiently advanced technologies it was of limited use until the mid-1990s. In the last 10 years EIS has increased in use dramatically with high-quality, solid-state electronics and high-powered computers. The measurements obtained by the EIS diagnostic can be correlated with chemical, physical, mechanical, and electrical variables. It allows the study of adsorption, charge- and mass-transport, and kinetics of coupled sequential and parallel reactions [79]. Due to its non-invasive techniques, it can be used for on-line analysis and diagnostics. For some experiments, the probes can be permanently installed in the system for long-term studies of the item under test. However, the ambiguity of the impedance data interpretation and its relationship to physical phenomenon

requires careful investigation and cross-correlation. It is the investigator's responsibility to convert the electrical data into useful parameters of interest.

The EIS spectra is calculated using a combination of Ohm's Law and Euler's relationship. Two types of EIS excitations can be used: galvanostatic or potentiostatic. Typically, potentiostatic is used single-cell analysis as the current response can be expected to be minimal due to the relatively high cell resistance (≈9 mΩ for LFP). Galvanostatic is reserved for groups of cells that collectively have a very low resistance (<1 mΩ) to limit the current handling requirement of the instrument. In a potentiostatic measurement, a sine wave with a precise excitation voltage is used at a specified frequency to excite a current response at the same frequency, but with a phase shift as shown in (2.9) and (2.10).

$$V(t) \rightarrow V_A * \sin(2\pi f t) = V_A * \sin(\omega t) \quad (2.9)\ [8]$$

$$I(t) \rightarrow I_A * \sin(\omega t + \phi) \quad (2.10)\ [8]$$

Using Ohm's Law, the impedance can be obtained, and Euler's relationship is used as shown in (2.11 to simply the impedance to either a complex number or split into real and imaginary parts. The complex number is used for the magnitude and phase plots, while the real (Re) and imaginary (Img) impedance values are used in the Nyquist plot. An example of a Nyquist plot is shown in Figure 2.11, and an example Bode plot is shown in Figure 2.12.

$$Z = \frac{V(t)}{I(t)} = Z_A(\cos\phi + jsin\phi) = \frac{V_m}{I_m}e^{-j\phi} = Re + jImg \quad (2.11)\ [8]$$

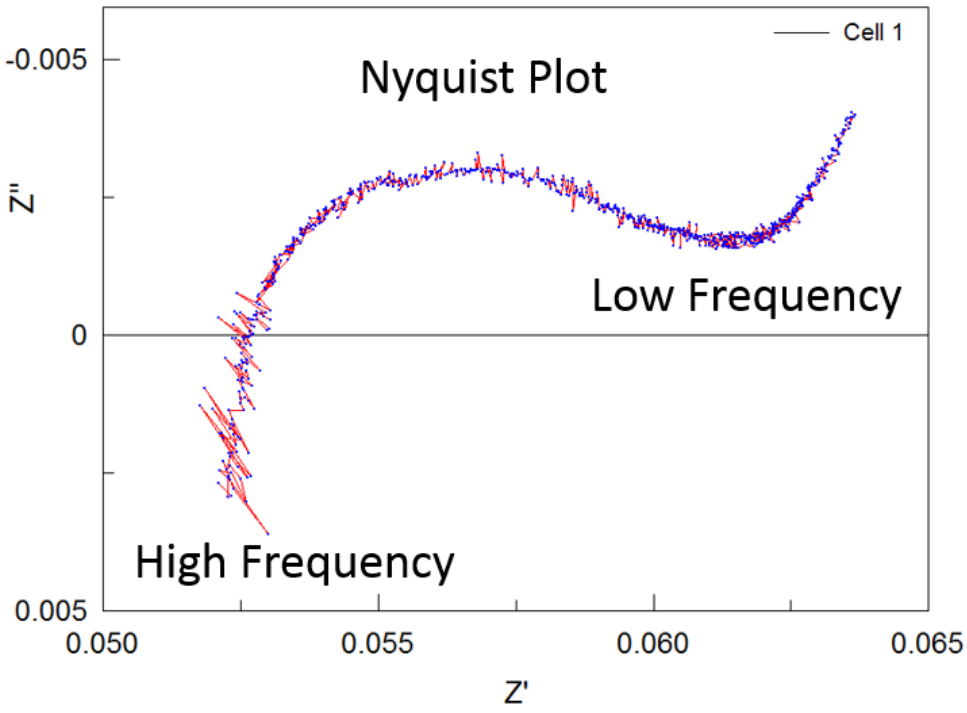

Figure 2.11: Example of a Nyquist plot for LFP cell

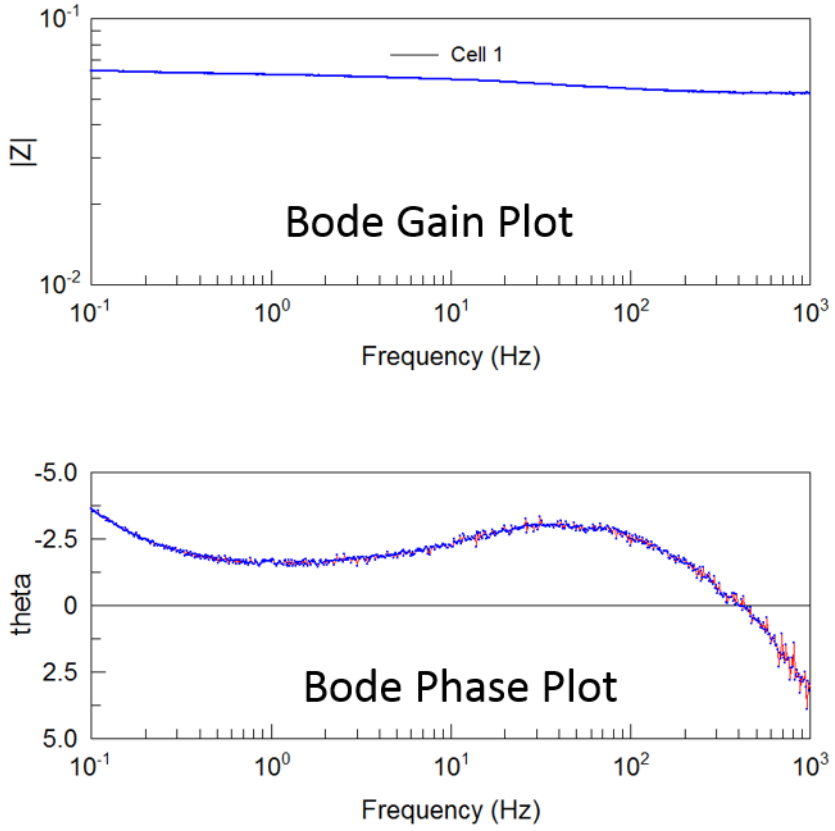

Figure 2.12: Example of Bode gain and phase plots for LFP cell

What makes the EIS diagnostic useful for battery research is that an electrochemical system acts like an RLC circuit, comprised of elements that act like resistors, inductors, and capacitors. A typical frequency sweep of a cell is from 20 kHz – DC, while other studies such as corrosion, biological analysis, and semiconductors can be in the MHz range. Extracting frequency information from the impedance values, and splitting the impedance into real and imaginary values, enables the modeling of a battery with a circuit diagram [79]. As shown in Figure 2.13, the regions of interest for this work begin when the EIS spectra first crosses the real axis, typically around 1 kHz. Data below the real axis is inductance due to cell windings.

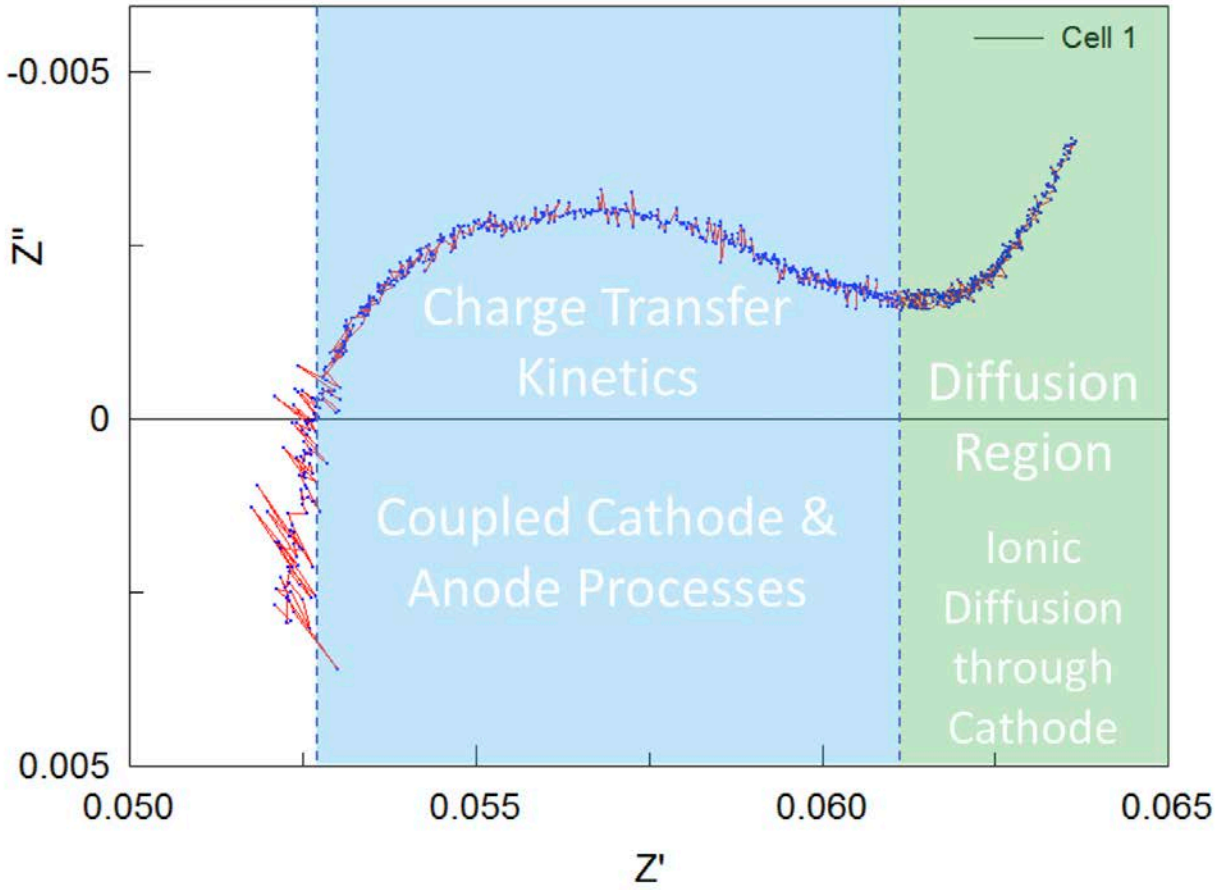

Figure 2.13: Nyquist plot of the EIS spectra from 10 kHz (left) to 0.1 Hz (right) and the approximate corresponding physical processes at 50% SoC [8]

For the LFP chemistry, a single semi-circle shape is observed for the region approximately 1 kHz – 10 Hz, and corresponds to anode processes. In general, the width of the semi-circle will stay the same, but the flatness of the semi-circle will change up or down depending on the state of

the chemistry. An aged cell will become depressed, as this is an indication of cell aging and the increase in impedance with the anode and the SEI layer. The remainder of the spectra, 10 Hz – 0.1 Hz, is associated with the cathode [8]. For this work, the cathode is of limited use as the frequency response is highly dependent on the state of charge of the cell, as shown in Figure 2.14. All of the testing in this work was performed at 50% state of charge to minimize the effects of the cathode response.

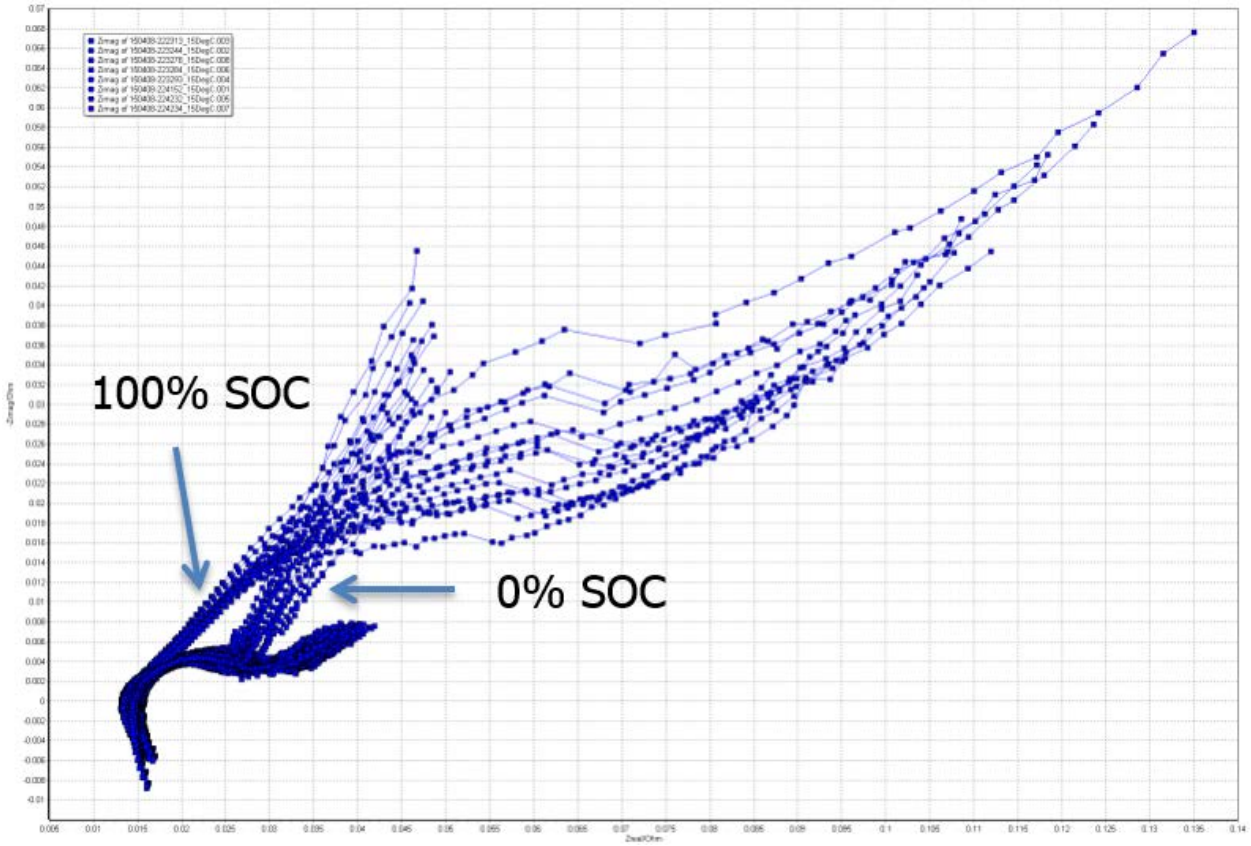

Figure 2.14: EIS spectra for an LFP cell as a function of state of charge (SOC) in 10% SOC increments

2.4 Electrochemical Impedance Spectroscopy Modeling

The EIS spectra can be modeled using an electrical circuit model to reproduce a similar frequency response. The model will consist of standard components, such as capacitors and resistors, but it will also include electrochemistry-specific circuits, such as constant-phase elements and Warburg impedances [8]. As previously mentioned, each section of the model is

designed to correspond to a physical component of the battery. There are six elements of the battery that are generally modeled; not all may have sufficient impact in every type of chemistry to warrant modeling in the frequency range of interest [80]. They can be sorted into three groups: resistance, capacitance, and impedance.

Resistances in the cell are not frequency-dependent. First-order resistances include probe contact resistance, casing resistance, internal current tabs, etc. Electrolyte resistance can be a factor in the impedance of a battery, but it typically does not have a uniform distribution across the entire electrolyte area. Typically, this is manually fit to the data, as it is virtually impossible to calculate based solely on the geometry and solution characteristics. This can be represented by a pure resistance value, and may be rolled into the same resistance as the probe contacts and other linear circuit connections. Polarization resistance is typically a corrosion reaction, where the current can flow through electrochemical reactions that occur at the electrode surface. The amount of current is controlled by the kinetics of the reactions and the diffusion of the reactants both towards and away from the electrode [80]. Charge transfer resistance is formed by a single, kinetically-controlled electrochemical reaction. In contrast to the polarization resistance, where a mixed potential may occur with the corrosion, in this case it is a single reaction at equilibrium. This reaction is heavily dependent on one externally controllable factor: temperature. If one assumes that the concentration of the reaction products is controlled due to the cell construction and state of charge, the charge-transfer resistance is directly proportional to the temperature [80]. For the experiments where the temperature was varied while maintaining a specific state of charge, it is imperative that this factor be taken into account and a separate resistance in the model created.

A double-layer capacitance exists in the interface between the electrode and the surrounding electrolyte. It is formed as ions from the solution absorb into the electrode surface, and is separated from the charged ions by an insulating space typically on the order of angstroms. Charges separated by a dielectric barrier will form a capacitor, and it can be affected by many variables such as electrode potential, temperature, ionic concentrations, electrode roughness, and impurity adsorption [80]. Since this feature behaves like a capacitor, it is sensitive to frequency. However, capacitors in EIS experiments rarely perform as true capacitors. Instead, they are represented as constant phase elements (CPE), forming a semi-circle on the Nyquist plot, as shown in Figure 2.15

At this point in time, the physical meaning of the CPE is poorly understood and can only be justified by the empirical fit to measured data [81, 82].

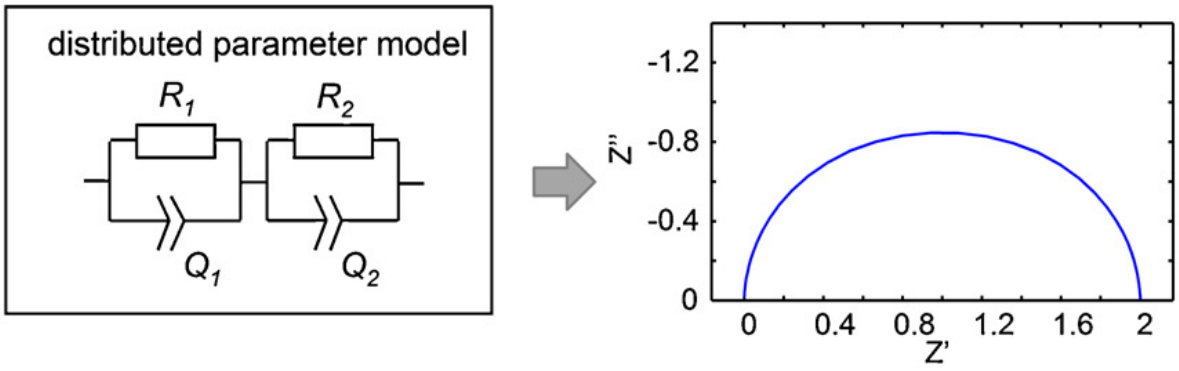

Figure 2.15: Nyquist plot of two series constant phase elements [8]

The impedance of a CPE can be written as shown in (2.12), where Q is the proportionality coefficient, ω is the angular frequency, and n is the arc depression factor. In general, Q will define the width of the curve and n determines the "flatness," or depression of the curve. A value of one for n changes the CPE into a real capacitor, and the lower bound is theoretically zero but in practice a real system will never have this response characteristic.

$$Z_{CPE} = Q^{-1}(j\omega)^{-n} \quad (2.12)\ [17]$$

Diffusion is the final process that can be modeled in this manner, and it is typically represented with a Warburg impedance calculated with (2.13), and an example of the Warburg Open Circuit model is shown in Figure 2.16.

$$Z_W = \frac{\mathrm{R}*\mathrm{ctnh}((j*T*\omega)^n)}{(j*T*\omega)^n} \quad (2.13)\ [83]$$

The Warburg model primarily uses a hyperbolic cotangent function to generate the characteristic shape seen in Figure 2.16. Similar to the CPE model, the Warburg uses T as a quality factor and n as a curve modifier, with ω for the angular frequency. At high frequencies, the Warburg impedance is small due to the small distances diffusing reactants need to travel. At low frequencies, the diffusion distance is much larger, and the impedance becomes larger. Previously recorded data show that the diffusion region (typically less than 100 Hz) that the state of charge of the cell has a significant impact on the impedance. At 0% state of charge, the real impedance is

relatively stable, while the imaginary impedance is growing with frequency. At 100% state of charge, the opposite occurs. This is likely due to the ion diffusion lengths increasing when all of the receptor sites are occupied due to the recharging process. To some degree this can be used to determine the state of charge, but as shown in Figure 2.14, it is limited to either a depleted cell or a fully charged cell.

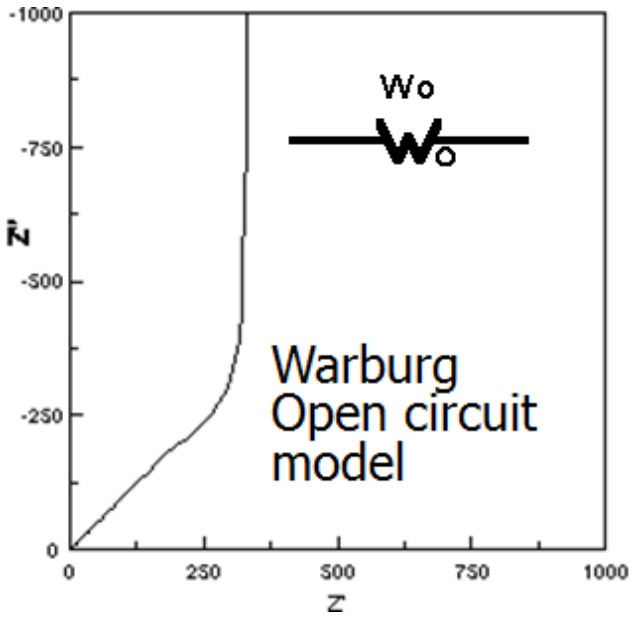

Figure 2.16: Example of the Warburg Open Circuit model used to model diffusion impedance

With the basic modeling blocks discussed, a model can be constructed that represents the LiFePO4 battery and evaluate changes in the model as a function of temperature, cycle rate, and calendar age. Using the model shown in Figure 2.17, a CPE in parallel with a resistor can be used to represent the interface between the anode and the electrolyte, which is driven primarily by the SEI interface. This is the region where changes are most likely to occur, as the SEI layer degrades over time. A lumped element model will be used to start, but will likely need to be split into multiple series elements to accommodate specific changes in the data. The interface between the electrolyte and the cathode can be modeled with a Warburg Open Circuit model. This interface is not as sensitive to the cycle-based aging, but it will change with calendar aging and state of charge [77]. Not included in the diagram, but essential to proper modeling, are the purely resistive elements of the battery. These will include contact and internal battery tab resistances, and will likely be lumped into a single resistor.

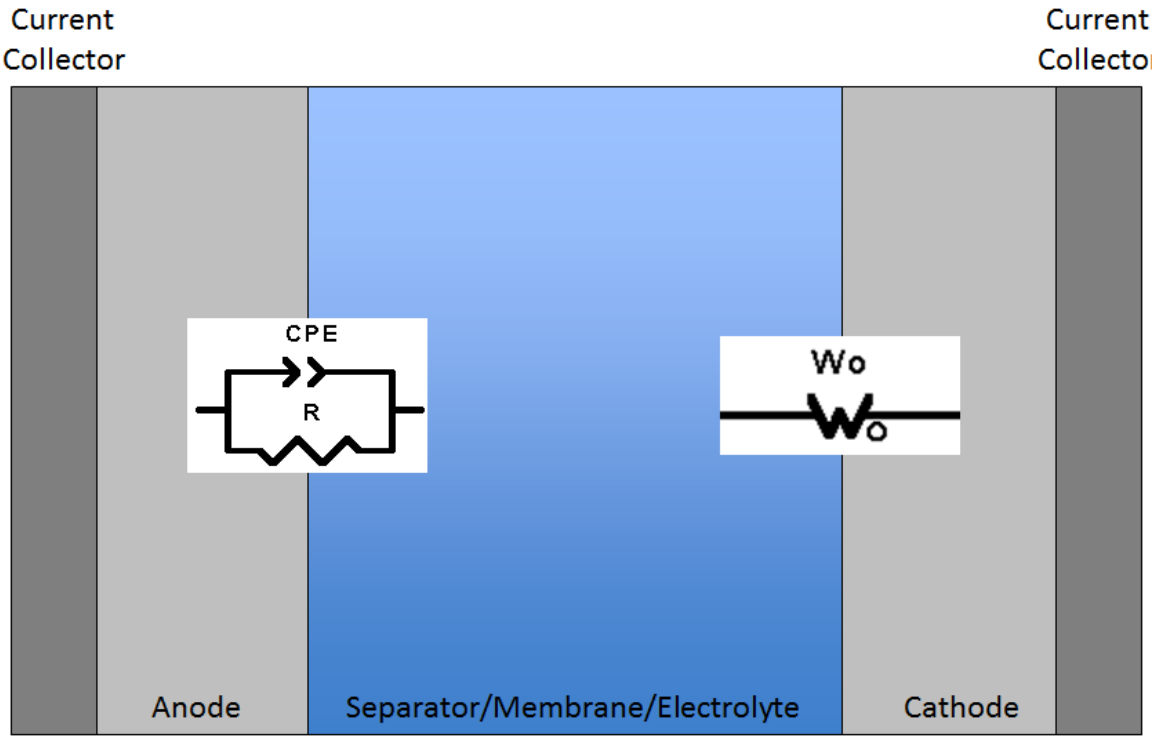

Figure 2.17: Representative model of battery cell with equivalent electrical circuit elements

Chapter 3

Experimental Setup

The experiment performed has two primary objectives: (i) evaluate current sharing and degradation within a parallel array of cells via the setup of a parallel cell testbed and (ii) characterize aging at different two different discharge rates by carrying out an individual cell lifetime study. The parallel cell array was being used to understand how a multi-parallel cell battery operates when it is populated with cells that have a known 1 kHz ESR measured on an EIS diagnostic from 10 kHz to 0.1 Hz, with a 10 mV perturbation amplitude. A programmable DC load was utilized to load the battery under representative profiles of interest. It should be noted that all of the experiments discussed here were performed within thermal chamber set to maintain the ambient air at 25°C. The temperature maintenance was periodically verified using the history function of the controller, in addition to each cell having an independently monitored thermocouple.

For each of the test series performed, at specified intervals each cell had an EIS sweep performed from 10 kHz to 0.1 Hz, with a 10 mV perturbation amplitude using a Solartron Analytical ModuLab XM system. The 1C population was set on a 200-cycle interval, as the depth of discharge was very shallow and many cycles were expected to be necessary to show any aging of the batteries. Conversely, the 10C population was on a 25-cycle interval to increase the

resolution of EIS scans due to the expected accelerated damage on the cells at the higher discharge rate. The parallel array was on a 50-cycle interval, as the 10C single-cell array was duplicating some of the aging data.

The batteries were cycled with a specific pulsed discharge profile, which was selected to describe the behavior of a large-scale experiment currently operating at the US Naval Research Laboratory (NRL). The NRL experiment uses 3,072 batteries to repetitively drive a pulsed power system into a load with an ultimate goal of 50, 1 MJ shots in five minutes [35]. Each individual shot is four seconds on, two seconds off, with a total of 50 shots before a recharge cycle is initiated. The understanding of how the batteries age and change performance as a function of cycle number and discharge rate is essential to moving this technology from the laboratory to the fleet.

3.1 Selection of Batteries for Testing

One of the factors identified in the paper study was that variations in the cell construction due to manufacturing defects and inherent physical differences (i.e. active anode material from Vender A versus Vendor B). Therefore, it was necessary to collect cells from a large population; in this case 200 cells were purchased new direct from the manufacturer. The population was cycled according to the procedure described in [84, 85], and detailed in Figure 3.2. To ensure proper solid electrolyte interface (SEI) layer formulation, it was desirable to choose cells that had a 1C (2.6A for these cells) charge/discharge capacity variation of no more than 0.2% for the second stage of the selection process.

An illustration of the need for a formulation series to stabilize the batteries is shown in Figure 3.1. The data shown is the measured ESR value when the cell is removed from the shipping box (Initial), and the measurement after the completed formulation series has been performed (Post-Stage II). While it may appear that a large number of cells measured below 9 mΩ when first removed from the box, the mean value was 9.237 mΩ with a standard deviation of 0.637, which is within the stated parameters of the manufacturer's specifications. After the formulation series, the cells stabilized at a slightly higher center, 9.457 mΩ with a larger standard deviation of 0.830 mΩ. According to the authors of [84, 85], the new statistics should be stabilized for selection of cell for experiments.

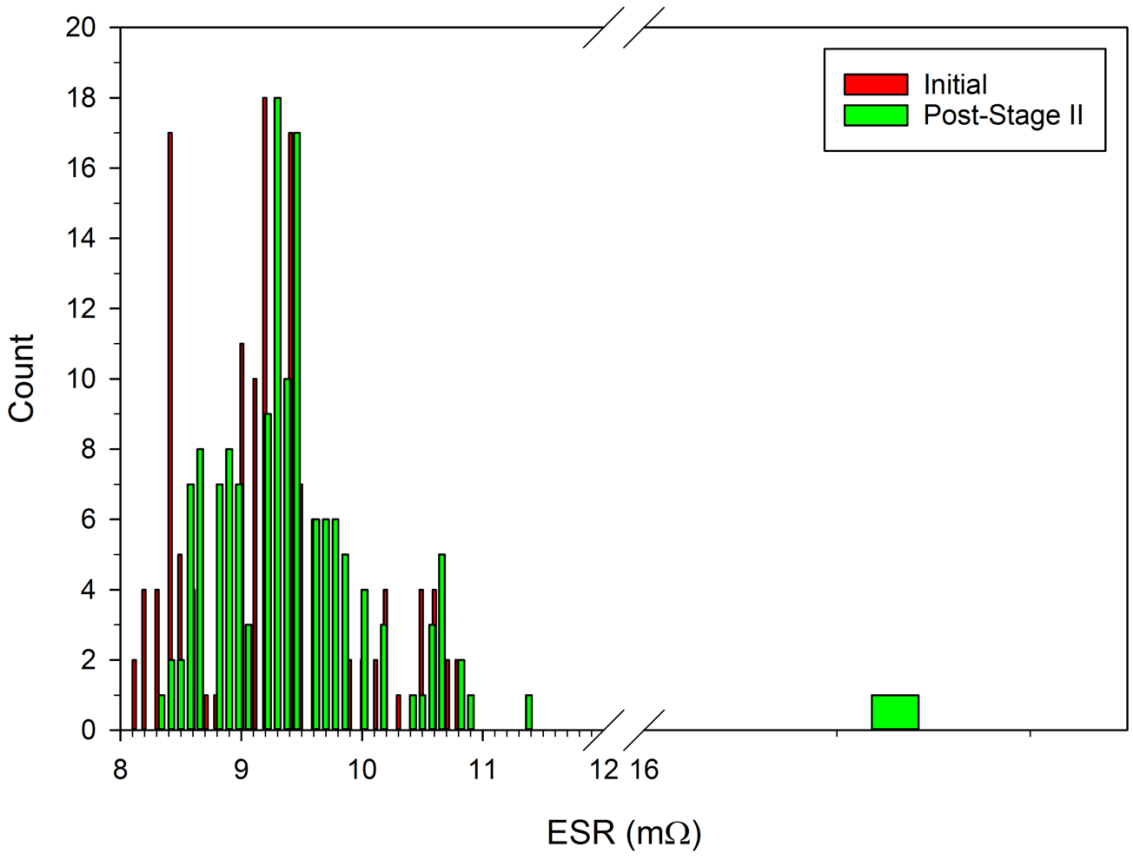

Figure 3.1: 1 kHz ESR measurement changes before and after formulation series for cells in experimental dataset

The “recommended CC-CV” charge profiled mentioned in Figure 3.2 was obtained from the manufacturer of the cells under test, and a graph of the profile is shown in Figure 3.3. Using the specific setpoints outlined in Table 3.1, the battery first starts at the lowest allowable point, 2.0 V. The current is held steady at 32.5 mA until the voltage increases to 3.0 V. This region is sensitive to current during recharge, due to the low potentials of the electrodes. The recombination of the lithiated carbon in the anode needs to be performed at a controlled rate until the voltage setpoint is reached. Once that occurs, the second stage of the CC recharge begins with the current held to a rate of 1C until the voltage reaches 3.5 V. If the 1C rate can be maintained, which is highly dependent on the internal resistance of the battery, this stage will take approximately one hour to complete. After the voltage setpoint is reached, the constant voltage (CV) phase will begin with the voltage held at 3.5 V until the current drops to 32.5 mA. This is followed immediately by

another constant current (CC) phase, and finally a CV stage that ends after either the cell current drops to 25 mA or one hour has elapsed.

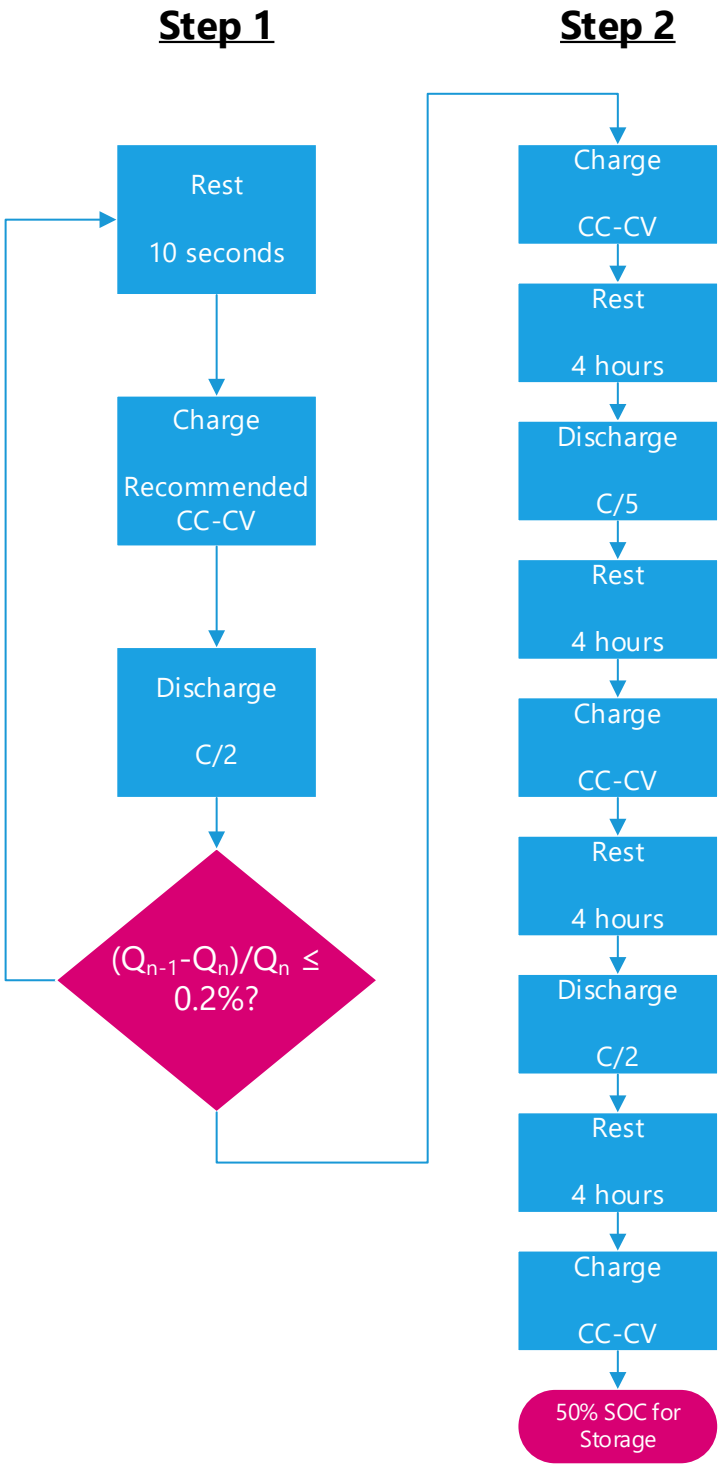

Figure 3.2: Flow chart for LFP formulation series [86]

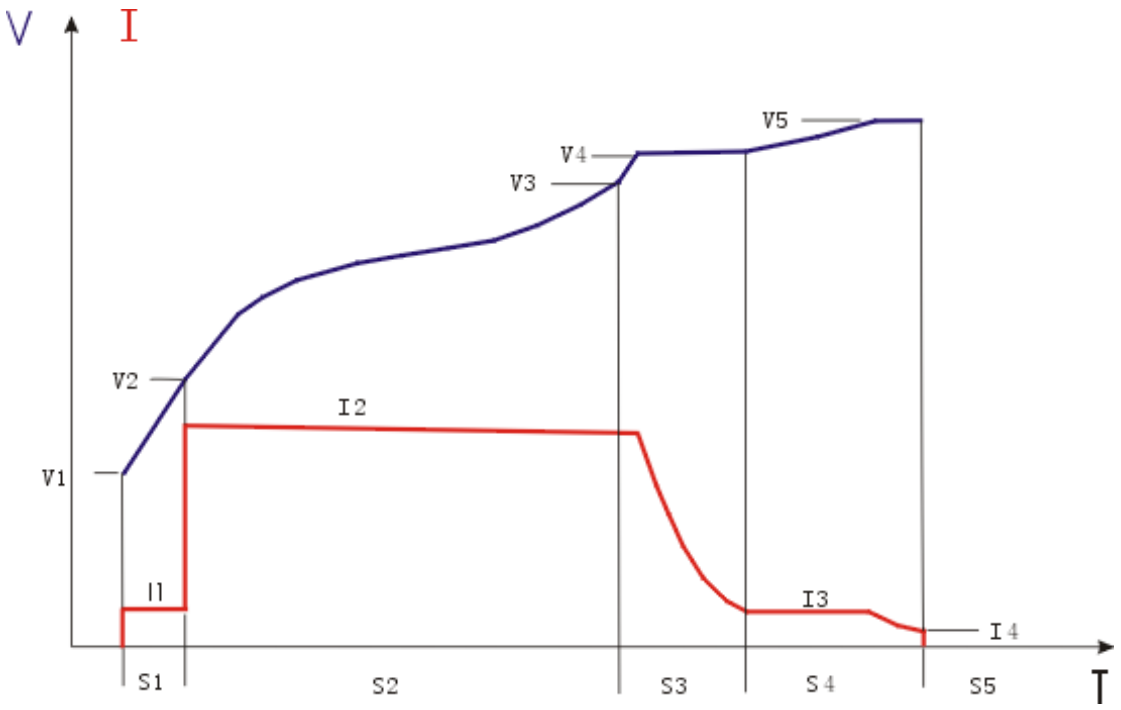

Figure 3.3: Constant Current (CC) - Constant Voltage (CV) recharge profile

TABLE 3.1: SETPOINTS FOR LFP 26650P CC-CV RECHARGE

Parameter	Voltage (V)	Current (A)	Time (hr)
V1	2.0		
V2	3.0		
V4	3.5		
V5	3.6		
I1 (C/80)		0.0325	
I2 (C/1)		2.6000	
I3 (C/80)		0.0325	
I4 (C/100)		0.0250	
S3 (max)			2.5
S4 (max)			1

For the subset of cells that passed the formulation series procedure, a second filter was applied using 1 kHz ESR as measured by a specialized battery milliohmmeter, commonly used by the battery industry. Cells were grouped into divisions of 0.1 mΩ at the 1 kHz frequency, and the largest group in a single division ±0.1 mΩ (equipment measurement variance) was selected for experimentation. Within this population of cells, the ESR was 9.3 mΩ. It is important to note that the cells selected from this smaller population for specific experiments were selected randomly,

and represent multiple lots from the manufacturer over several years. One can therefore state that the subsequent data recorded can reasonably represent a typical cell from this manufacturer.

The variability in the cells received from this manufacturer is shown in Figure 3.4, where 3327 cells were measured as they were removed from the battery conditioning equipment at NRL to be installed for another project, of which some lots were included in this work. While the majority of the cells were between 8 and 9 mΩ, there was a significant number of cells that had 1 kHz ESR values as high as 22.4 mΩ. This variability demonstrates the need to perform a significant amount of post-manufacturer filtering before installation in an operational system to obtain a statistical homogeneous cell sample, an experimental design requirement for testing the hypothesis stated in the introduction.

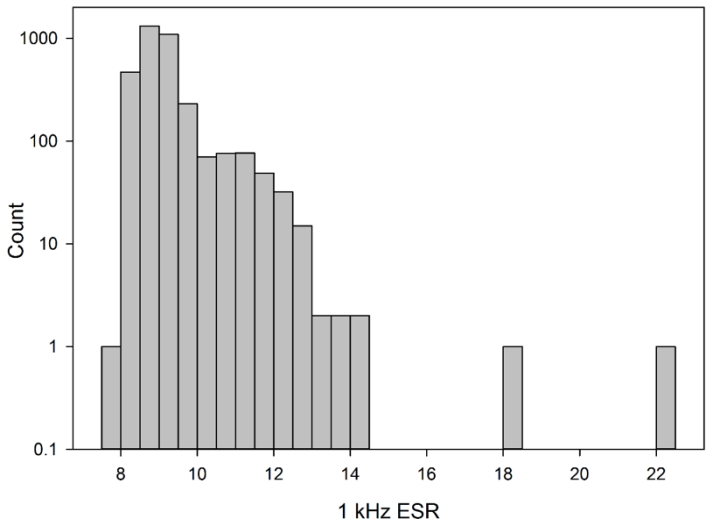

Figure 3.4: Frequency plot of the 1 kHz ESR values for 3,327 new cells from the battery manufacturer

3.2 State of Charge Measurements

As part of the effort to investigate a critical state of health frequency for the batteries in this experiment, 17 cells from the experimental group that were not selected for the other testing groups were cycled from 0% state of charge (SoC) to 100% SoC in 10% SoC increments. Each cell was discharged to 2.0V at a rate of 0.1C in multiple steps with rest periods to allow recovery before resuming discharge. Once the cell was electrically exhausted, two EIS sweeps separated by a five minute rest period were performed with the standard EIS parameters for each step beginning at

0% SoC. A rest period of 30 minutes was used after each 10% charge increment before the EIS cycles was started. The cell was charged at 0.1C to minimize internal heating during the recharge process. Each cell was measured individually, while the probes were not moved between experiments to maintain a consistent contact resistance. The entire cycle was automated by the ModuLab software.

The possibility of using the EIS diagnostic to estimate the battery core temperature in single-cell was described in [3] for a $LiCoO_2$ 18650 cell. This work looked at the feasibility of expanding that diagnostic to multiple cells in parallel, particularly after a discharge had been performed. Eight cells from the experimental population pool were selected to experience the same SoC measurements as the previous group, but an additional variable of temperature was added. The cells were placed in a thermal chamber that was computer-controlled via GPIB, and attached to a MACCOR 4300 series with a Frequency Response Analyzer for automated EIS sweeps. The cells were charged to 50% SoC, the chamber was set to the desired temperature, and allowed to rest for 24 hours to equilibrate the cell to the new ambient temperature. At this temperature, the cell was cycled through the various states of charge in 10% SoC increments. The cell was returned to 50% SoC, and the next temperature was programmed into the chamber.

3.3 Single-Cell Lifetime Testing

Three subsets of eight cells each were randomly selected from the experimental sample set described earlier. The first set was designed as a calendar-aging control set. The cells were left at the 50% SoC level from the Stage 2 formulation series, characterized with the EIS instrument, then placed in a storage box inside the thermal chamber. The cells were not used for any further discharge testing for the remainder of the experiment. The next set of batteries were used for pulsed discharge evaluation at a rate of 1C (2.6A), which would result in 0.144 Ah extracted from the cell, or 5.78% depth of discharge (DOD). The 1C discharge was performed to evaluate the manufacturer's data on the performance of the cell. The final set was discharged at 10C (26 A), with a DOD of 57.78% and a 1.44 Ah extracted from each cell. While data exists for the lifetime degradation of a similar cell at this rate, no lifetime data exists for a pulse discharge profile.

Therefore, these discharges appear to be relatively shallow, but they are intended to be representative of a real system under test.

A MACCOR Series 4000 computerized battery analyzer was used to cycle the cells under lifetime test. Each cell was assigned an independent channel for analysis and was continuously charged and discharged for a set number of cycles. Temperature, current, and voltage were logged to a file for later analysis if necessary. To eliminate individual channels as sources of error, the channels assigned to specific cells were rotated so that any error in the machine would be evenly distributed in the population.

A specialized cell holder was designed to permanently house the batteries during the entire test series. As shown in Figure 3.5, the batteries had Ni tabs welded to the cell and were soldered to Cu bus bars on the PCB. At the point of soldering, banana sockets were installed to facilitate the EIS probes. On the other side of the bus bar was a brass bolt that connected the MACCOR output cables to the battery under test. Each cell also had a 3D-printed end cap to standardize the welding and keep the cells isolated. It should be noted that the 1C discharge arrays were initially mounted using a commercial battery holder, which used gold-coated steel tabs and pressure to maintain electrical contact. The additional resistance in the circuit due to the steel tabs created significant errors in the EIS sweeps, and were replaced with the new design after 1600 cycles.

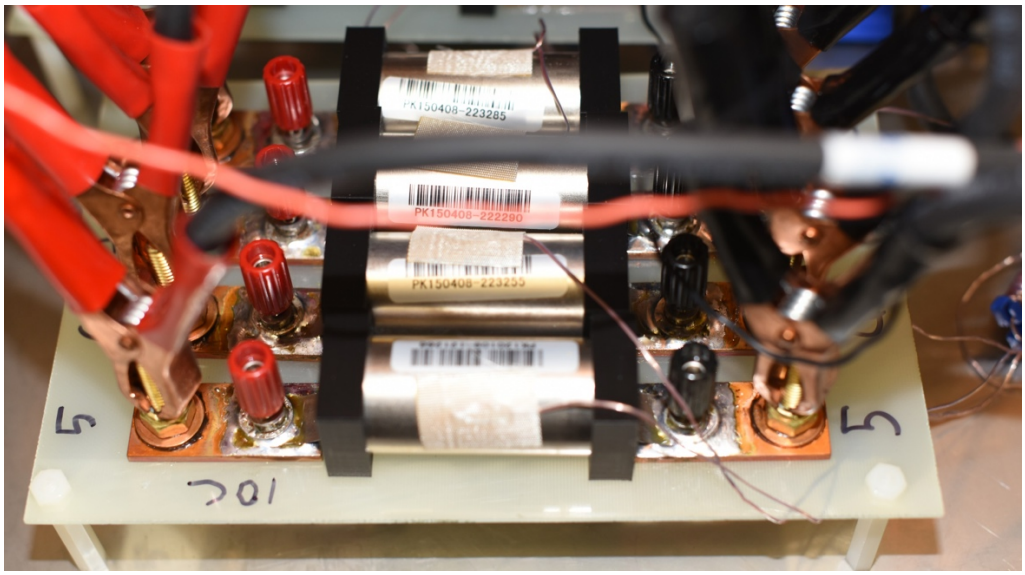

Figure 3.5: Custom cell holder for long-term cycling tests

3.4 Parallel Cell Testbed Design

A prototype discharge testbed was designed and built to collect the initial data from the 4P1S battery array, and is shown in Figure 3.6. Each cell was connected to a Cu-101 current collector plate via a 10-gage solid Cu wire, and was routed through the center of a Hall-effect current sensor (2 mA ± 18 μA) to measure the current on each cell. Each line was tuned with a milliohmmeter to be 0.4 ±0.02 mΩ. Each cell was connected to the discharge wire with welded Cu-110 0.0762 mm shim stock to provide a low-resistance connection to the circuit, a process that was developed for this work, and is described in [87]. For data acquisition, both the differential cell voltage probes and the current sensors were sampled at a rate of 20 kSa/sec/channel. A type T thermocouple was placed on each cell at the top (positive terminal), middle (body temperature), and base (negative terminal). The thermocouples were sampled at 0.5 Hz.

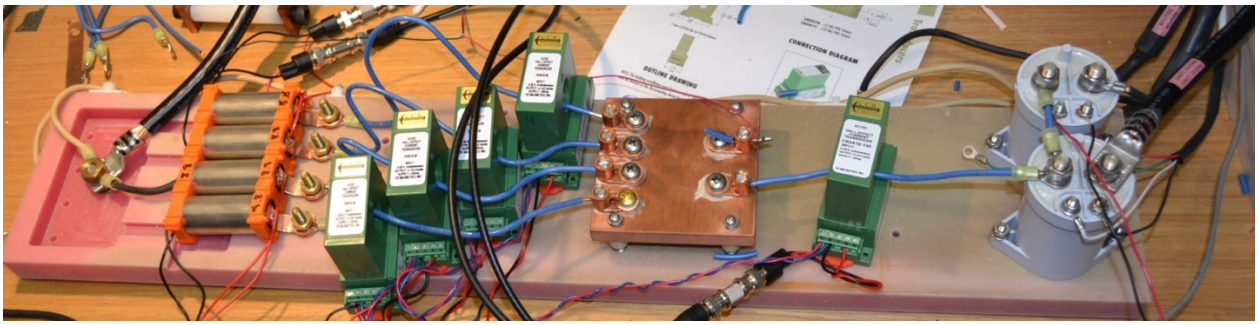

Figure 3.6: Initial parallel cell evaluation testbed

A limited test series of about ten discharges was performed at 10C with this configuration, and it was used for a significant portion of the development of the LabVIEW control and data acquisition system. The data obtained was used to develop a second-generation testbed, which incorporated several improvements in the quality of the experiment and the resulting data, a schematic of which is shown in Figure 3.7. A major driver for the design is the need for consistent data collection and a minimum load on the circuit so any changes are correlated to the batteries only.

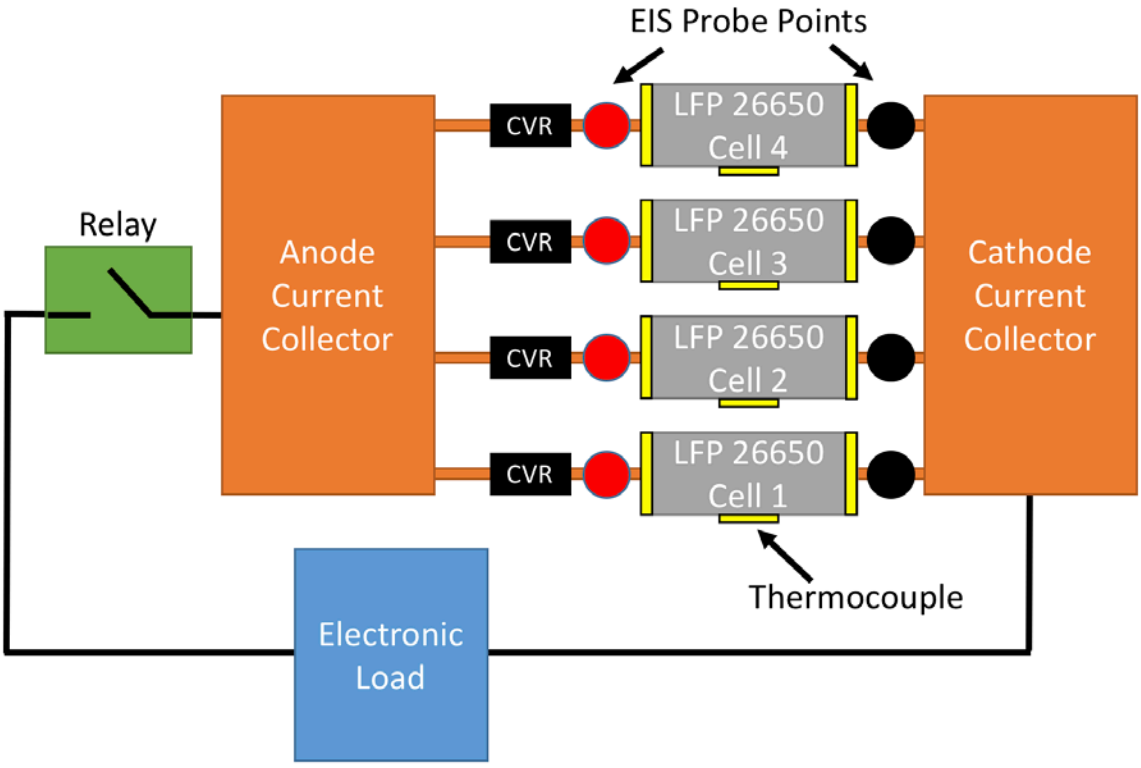

Figure 3.7: Schematic drawing of 4P1S battery array with connections to current sensors, electronic load and EIS probe points.

The most compact design is to integrate the 4P1S array onto a printed circuit board (PCB), which would enable the replacement of the 10-gage Cu wire with fixed traces on the PCB. Using the IPC-2221A design standards, calculations were performed to determine the size of the traces needed to handle at least 28.6 A (26 A + 10%) continuously, as shown in (3.1), where k is a constant for surface layer traces, ΔT is the temperature rise in °C, and A is the cross section in square mils.

$$I_{max} = k_{outer} * \Delta T^{0.44} * A^{0.725} \quad (3.1)\ [88]$$

Using (3.1), it was determined that a copper trace with a width of 6.35 mm and a thickness of 0.036 mm (1 oz. PCB standard) will support 28.6 A, but the temperature will rise by 130°C. As this is not a sustainable temperature for repeated testing, further analysis shows that increasing the trace width to 12.7 mm reduces the temperature rise to 42°C. More importantly, even with the increased size the power loss is 800 mW, which is still too high for sustained experiments that may last several months. Switching to a bus bar design that uses commercially pure copper (Cu-101),

a bar with a width of 12.7 mm and a height of 6.35 mm, assuming a length of 25.4 mm, under the same discharge conditions would have a power loss of 1.2 mW and a temperature rise of 0.052 K.

With the commitment to a PCB design, the current measurement can also be simplified. Instead of the very large, bulky hall effect sensors, Ohmite CS3 Kelvin current sensors were chosen to measure the current. The 1 mΩ (±1%) version was selected to minimize the impact on the current flow due to the instrument. Each unit is rated to 40 A continuous, and the Kelvin terminals ensure the instrument is isolated from the circuit. Assuming a maximum current of 30 A and a minimum current of 1 mA, the maximum power loss through the device was estimated to be 0.9 W, well below the device maximum of 3 W. Since this is a current viewing resistor (CVR), the voltage across the terminals is used to calculate the current. With the maximum current stated, 30 mV will be generated across the terminals. The minimum expected current of 1 mA would generate 1 µV.

With the original parallel testbed, the hall effect sensors generated a 0-5 V signal proportional to the maximum current of the sensor. The CVR sensors require amplification before the National Instruments data acquisition (DAQ) system can digitize the signal. A Dataforth SCM5B30-02D analog conditioning module was used for each CVR. This device will input ±50 mV and output ±10 V proportionally, which is a gain of 200. The maximum current expected, 26 A, would generate 5.2 V, while the minimum expected measurable current is at the 200 µV level. The minimum voltage to the DAQ is a concern, as at a certain point even if the device selected can technically digitize that value, it may be indistinguishable from noise that cannot be filtered with a reasonable effort. The NI 9221 C-series module was selected as the DAQ, as it features four channels with independent analog-to-digital converters for maximum digitization speed. With a full scale voltage of ±10 V and a 16-bit digitizer, the minimum step size is 8.6 µV when adjusted for quantum noise. In theory, this would enable the recording of current as low as 43 µA, which is well below the expected necessary minimum current measurement.

Other improvement included the installation of banana plug sockets for fast and repeatable insertion of the EIS probes, as they natively supported banana-style plugs. To isolate each cell during EIS data sweeps, a section of the Cu-101 bar tabs was designed to be removable. The screws were installed to a torque specification that was maintained throughout the test series. Both the anode and cathode current collectors were changed to be monolithic blocks of Cu-101,

rendering any difference in resistance between a particular cell and the unitary output to the load inconsequential. The batteries were connected to the testbed via Ni-201 tabs that were welded to each battery. The original Cu tabs were deemed too fragile for sustained testing, and the repeatability of the welding was an issue. While the Ni tabs are more resistive, the ability to guarantee a permanent weld was determined to be a higher priority. To ensure a consistent weld on each battery in the experiments, several parts were designed in SolidWorks and printed using a 3D printer. Three different parts were used in the assembly of the battery array. First, a Ni tab template was used to ensure the hole punched for the PCB mounting screw was in the same place for each tab, with a hole for the punch and guides to keep the tab in place. Next, the positive terminal cap was designed to only allow the welding to be performed on the exposed surface of the battery anode, and was printed in red plastic for easy visual identification. Finally, the negative terminal cap had a longer opening to allow welding to the entire bottom surface of the cell, and was printed in black plastic.

A final design consideration for the parallel cell testbed is the cables that carry the current from the array to the load. Assuming a maximum current of 26 A per cell, the total current expected through a cable is at least 104 A. With a design margin of 10%, the cables need to be capable of sustained 115 A during the entire experiment. An additional design consideration is the voltage of the cells, which may be as high as 3.5 V and as low as 2.0 V. Using manufacturer data sheets, the smallest acceptable size wire for power transmission is 1 gage. After testing and evaluation, 1/0 gage is required to prevent loading the cell and artificially lowering the voltage during discharge. The shortest possible lengths of wire were used to further reduce cable resistance.

In the first phase of testing, the battery array was discharged into a programmable electronic load manufactured by Kepco Inc. and recharged with an HP 6554A DC power supply. The second phase of testing added three-channel HP 6050A mainframe and three HP 60504B electronic load modules. The National Instrument (NI) LabVIEW programming language was used with the IEEE-488 protocol to program the load and the source devices during the experiment. The LabVIEW software was programmed initially for a single battery array, but was modified to enable four independent battery arrays to be run simultaneously. A flow chart diagram of the process is shown in Figure 3.8. The user will set up the experimental parameters after all of the devices have been initialized and verified to be communicating properly. Once initiated, the experiment will

discharge at the programmed rate, wait for a specified period of time, recharge, wait again, then go back to another discharge if so programmed. At the end of each charge-discharge cycle, the data is recorded to a National Instruments TDMS file and exported to a data management software suite for later processing.

The pulse discharge was initially achieved by programmed control of the output relay using the FPGA on the NI cRIO-9066 device. The resulting current data had spikes due to the in-rush current from the battery, as the source impedance is in the 9 mΩ range, and no damping was in the circuit. This was replaced with a programmed pulse discharge in the Kepco load, which has native damping circuitry. The resulting waveforms more appropriately replicated the expected load profile of the NRL experiment. When the HP 6050A was introduced as a load for the 4P1S replicants, the programmed pulse discharge was not a feature. Instead, the analog programming option was used to accept a scaled voltage waveform to module the input. A separate cRIO-9149 Ethernet expansion chassis was used to generate the analog waveforms. The control system would program the FPGA on that device prior to the experiment, and trigger the pulse discharge diagram when needed for the electronic load. The three channels in the HP 6050A could be independently operated in this fashion.

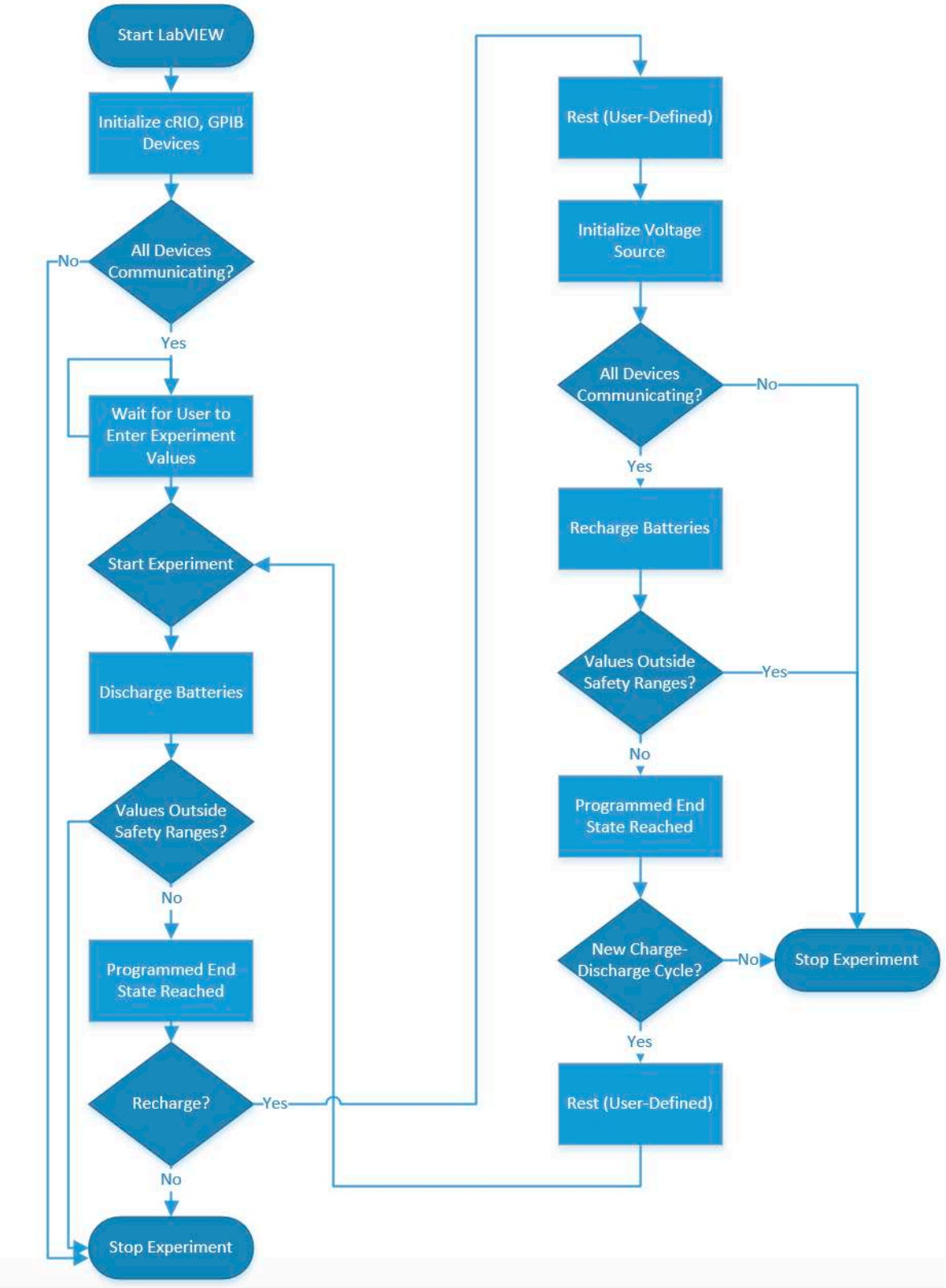

Figure 3.8: Flowchart diagram of LabVIEW control and data acquisition system

3.5 Battery Post-Mortem Analysis

An inspection of the battery internal components is essential to properly correlate electrical and impedance observation data to physical phenomena. To this end, a standardized procedure is necessary to ensure that the methods of opening, disassembly, and documentation avoid damage and contamination. Due to a number of hazards associated with the disassembly of lithium-based batteries, the process is not recommended by manufacturers. With the proper precautions and equipment, there exists the possibility of creating a short circuit which can cause thermal runaway in some chemistries, as well as contact burns during the extend of the short circuit. Additionally, inhalation hazards can exist if the room is not properly ventilated. Procedures have been established in the literature for several years [89, 90], and have been followed for this work. When the prescribed methodologies are followed, disassembly of lithium batteries can be safe and will provide reliable results concerning the composition of the materials.

Prior to disassembly, the cell is cycled to record the capacity, and then discharged to 0% SoC. This is done to reduce the possibility of a short circuit occurring during the disassembly process. While a deep discharge to 0 V would provide complete assurance of low energy in the cell, passing the 2 V mark on the $LiFePO_4$ chemistry may introduce material changes not associated with the specified experiment performed prior to disassembly. For this work, the cell was discharged at C/2 until the voltage limit was reached.

Once the cell has been cycled to 0% SoC, it is moved into a dry room where the dewpoint is maintained at approximately -30°C to eliminate as much moisture from the air as possible, however in practice the dewpoint is -10°C when the room is occupied. A Dremel tool is used as shown in Figure 3.9 to cut the cell casing open. The cell is taped to the bottom of a plastic tub to both fix the cell in position and contain any parts that may separate from the battery. Since the case is part of the electrical circuit, the plastic tub is used to isolated the cell from the table as well.

Figure 3.9: Dremel cutter is used to open the battery case to expose the cathode electrical connections

Multiple cuts with the Dremel are required, with constant rotation of the cell and limited time on the case to prevent excessive heating. It is critical that the cuts are performed as close to the edge as possible to prevent accidental damage to the jellyroll. Once a complete circle has been cut, the core can be removed from the case as shown in Figure 3.10. Partially dried electrolyte can be seen near the cut portion of the core. The extent the core can be removed varies from cell to cell, with the amount removed in Figure 3.10 on the high end. The anode connections usually limit the amount of core that can be removed. It is necessary to remove as much as possible to successfully perform the next step.

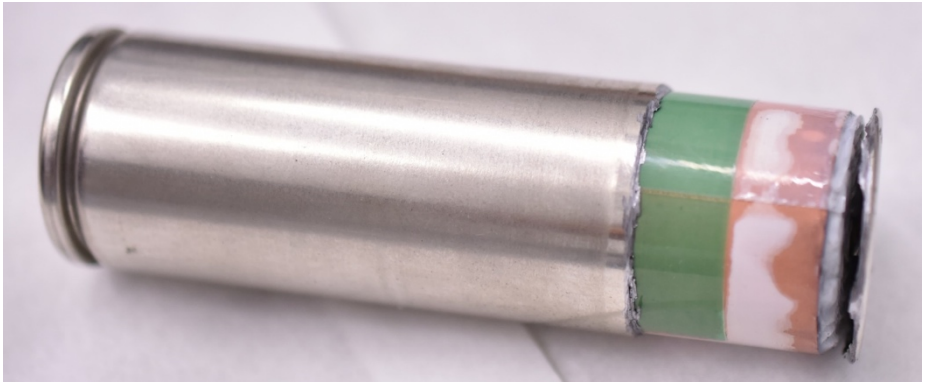

Figure 3.10: Battery core removed from cell case after cathode cutting completed

Similar to the cathode process, a Dremel tool is used to cut the battery case near the top of the cell. The cut is performed as close to the indent as possible to avoid damaging the core, as shown in Figure 3.11. Once the cut has been completed, the top can be removed as shown in Figure 3.12 using tweezers.

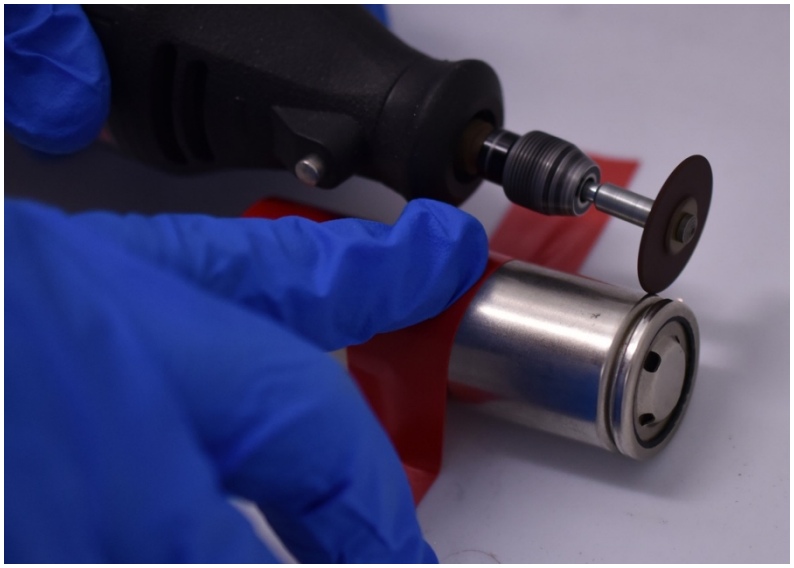

Figure 3.11: Dremel tool used to cut the anode section of the battery case

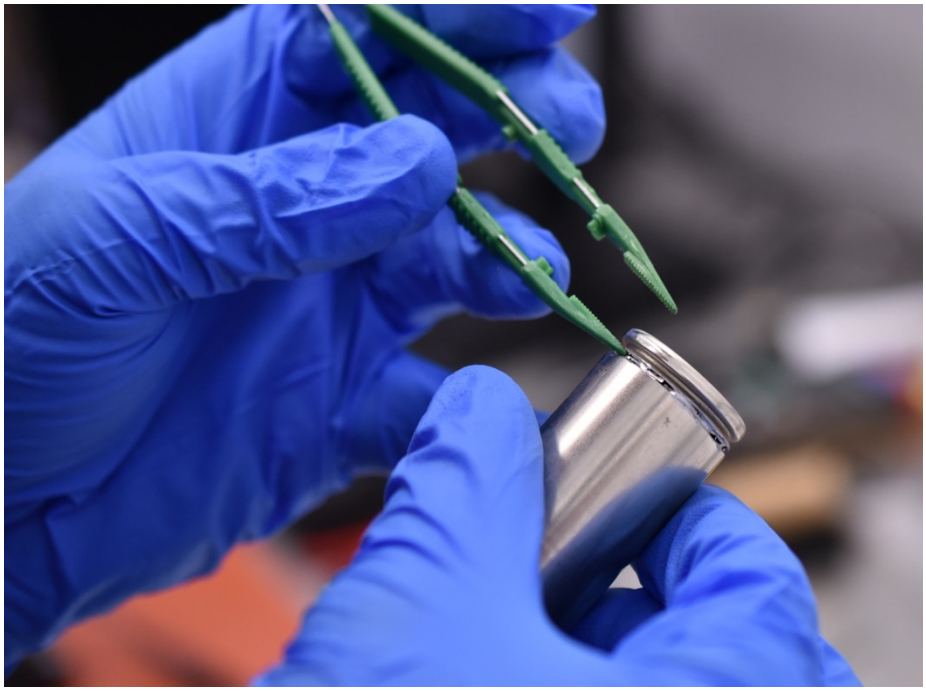

Figure 3.12: Removal of the top of the battery after completion of cutting the cell case

Once the top is removed, the tabs connecting the cell core to the anode can been seen, as shown in Figure 3.13. After photo documentation has been completed, the tabs are cut using pliers to separate the case top from the core. This is repeated for the bottom section.

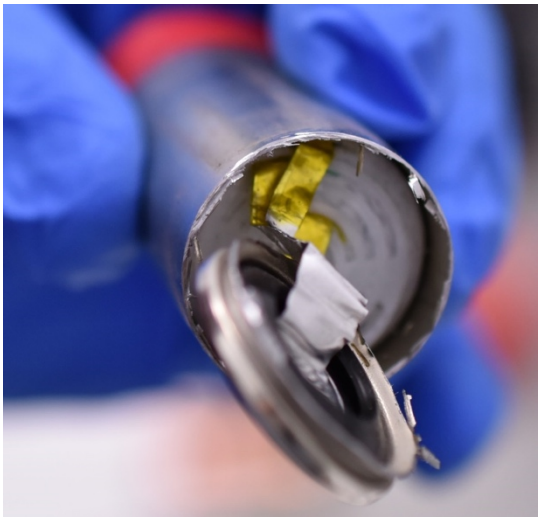

Figure 3.13: Anode electrical connections from the cell core to the top of the battery

A razer blade is used to cut the core binding and allow the unraveling of the electrodes. The jellyroll is slowly unwound to prevent mechanical stress damage and is laid out on a table, as shown in Figure 3.14. On the top is the separator (polypropylene), the anode, another separator, and on the bottom is the cathode. The break in the anode seen in Figure 3.14 is for one of the electrical connections to the top of the battery. These are also seen in the cathode, as shown in Figure 3.15.

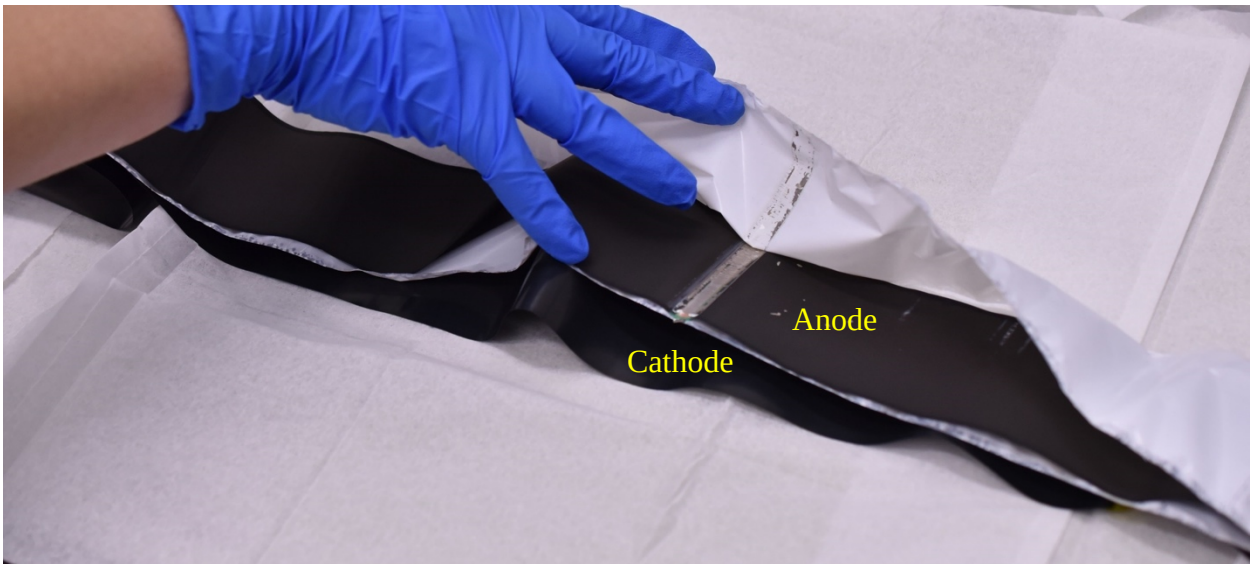

Figure 3.14: Exposed battery films with the anode (top) and the cathode (bottom)

Finally, the anode and cathode materials are photographed with a measuring tape to allow for reference to specific locations in the roll, which can be measured with techniques such as computed tomography (CT) performed prior to the disassembly of the battery. This allows for non-destructive analysis to identify key structures prior to changing the state of the battery when disassembly is performed. For this work, sections of the film were removed after identification by the CT scan for additional analysis.

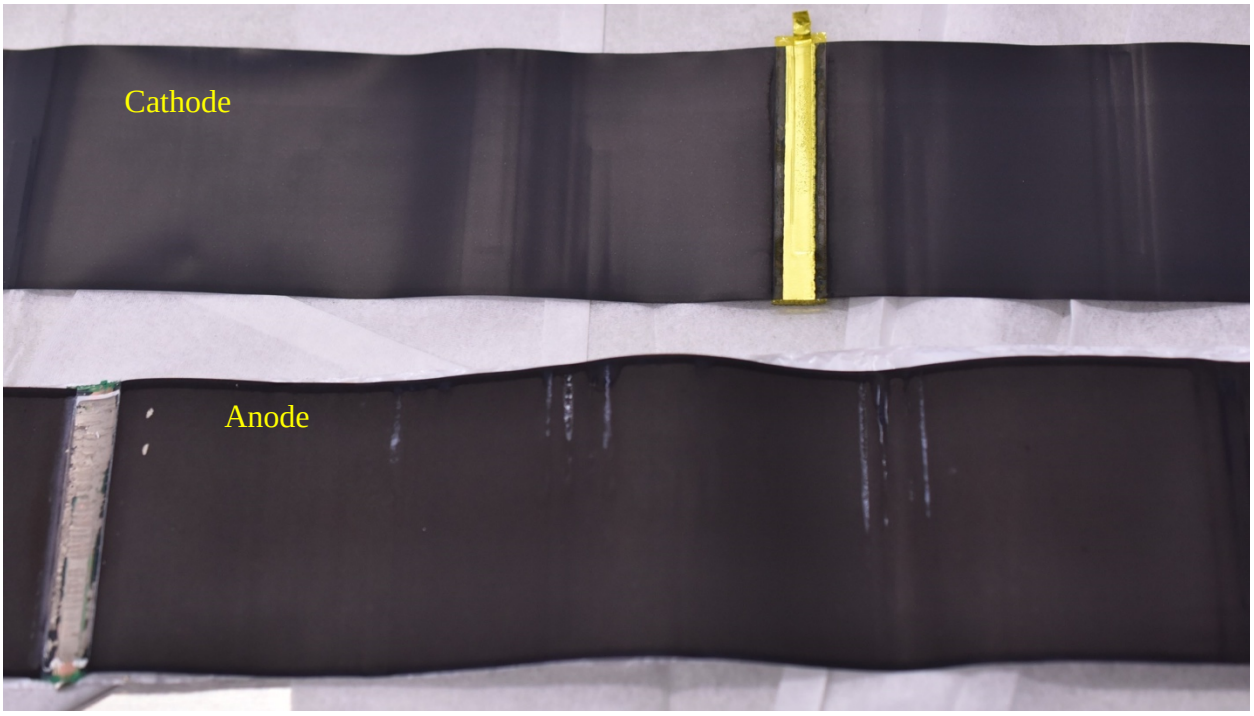

Figure 3.15: Typical film section with the cathode on top and the anode on the bottom.

The compact CT used for this work was the Zeiss Xradia 520 Versa, which features < 700 nm spacial resolution and is specifically designed for the study of materials, shown in Figure 3.16. An industrial CT scanner is similar to a medical-grade scanner, in that both use high-resolution radiographs to capture images of a subject at multiple angles to generate a 3-D image. Unlike a scanner found in a hospital, the non-biological test samples enable the use of higher x-ray energies and longer exposure times to maximize resolution and penetrate high-Z materials such as steel. Another major difference is that the part is rotated, not the detector. While a synchrotron generates a beam not unlike a laser, the x-ray profile for the CT is a cone. This can prove useful, as x-ray magnification on the detector can be used to increase the effective resolution of the scan. However, the shape of the source can also introduce artifacts on the image if not taken into account prior to a scan. The ability to capture internal images of a battery while leaving the sealed case intact is invaluable, as it would enable the possibility of studying the physical changes in a cell as a function of cycle. Other experiments can be performed such as evaluating the structure after extreme temperature, shock, vibration, and impact testing [91-96].

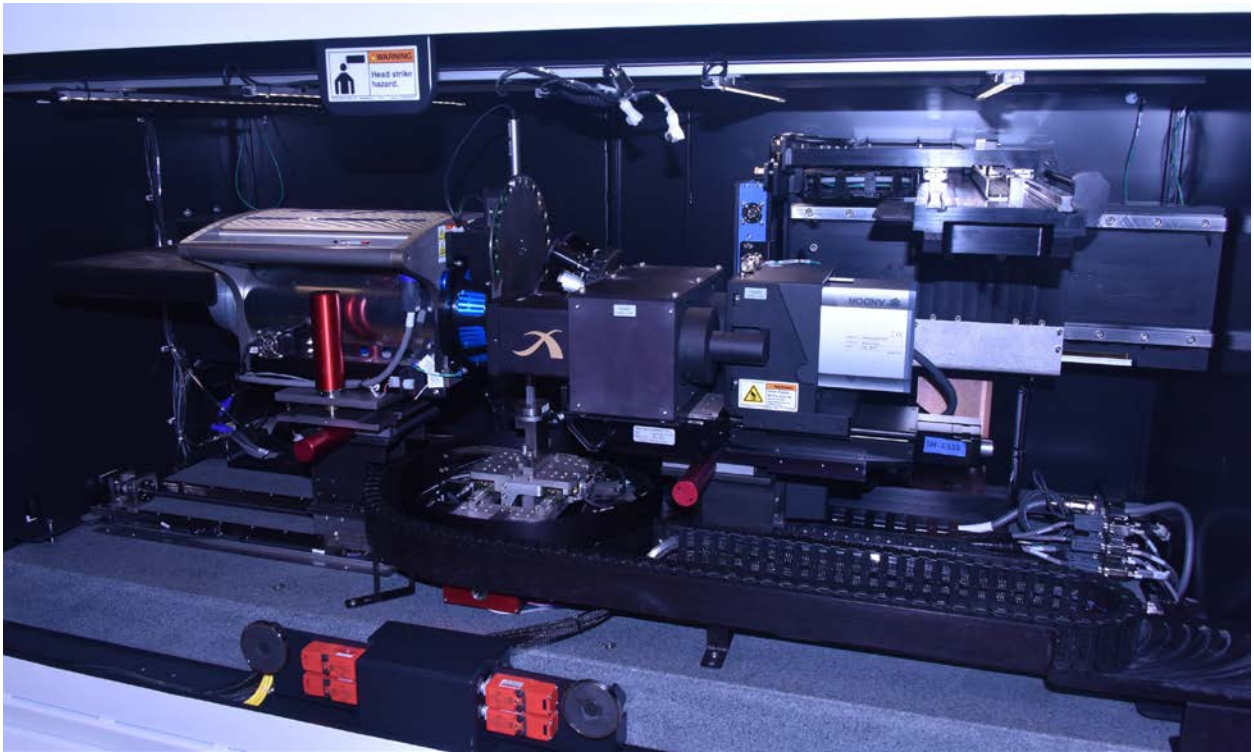

Figure 3.16: Interior of Zeiss Xradia 520 Versa with the X-ray source on the left, sample stage in the middle, and detector on the right

Chapter 4

Experimental Results and Analysis

An understanding of the baseline behavior of the parallel cell array is necessary before any valuable conclusions can be drawn. Data from the three sets of parallel experiments were collected and are discussed here. It is noteworthy to mention the importance for the collected single-cell data to be analyzed first before applying them to a parallel cell array, because the resulting data cannot be interpreted otherwise. Indeed, the lifetime data collected from a single cell with the specified discharge profile is essential to determine the expected drift in ESR as a function of C-rate and cycles, which will be used with the parallel cell array to simulate the aging process of the latter. In conjunction with the lifetime data is the expected SoH frequency, which will be the primary diagnostic when examining the SoH of a parallel array of cells.

4.1 Determination of SoH Frequency

Lithium-ion cells have a unique impedance response that changes with its state of charge (SoC). Seventeen cells from the lot discussed earlier, were baselined and placed on a test fixture to record their EIS as a function of SoC. This part of the experiment was meant to identify the singular frequency which has the least amount of deviation in both real and imaginary impedance. As previous studies have concluded, this frequency can be used as a reliable SOH metric even as

the cells lose reversible capacity over their lifetime [2-4, 97]. Example data collected from one of the seventeen cells is presented in Figure 4.1, with the error bars indicating one standard deviation from the median values of the data. It appears the first half of the semi-circle in the high frequency region has relatively low variations in the data, and after this point (approximately 100 Hz), the data begins to vary significantly. Standard deviation is an appropriate descriptive statistic for this application, as analysis of the data in the region of interest (100 – 1000 Hz) shows that the median deviates from the mean no more than 0.4 mΩ for both the real and imaginary data, indicating that for each frequency and SoC combination the distribution is nearly symmetric. Furthermore, it is found to be approximately normal for the specified frequency range.

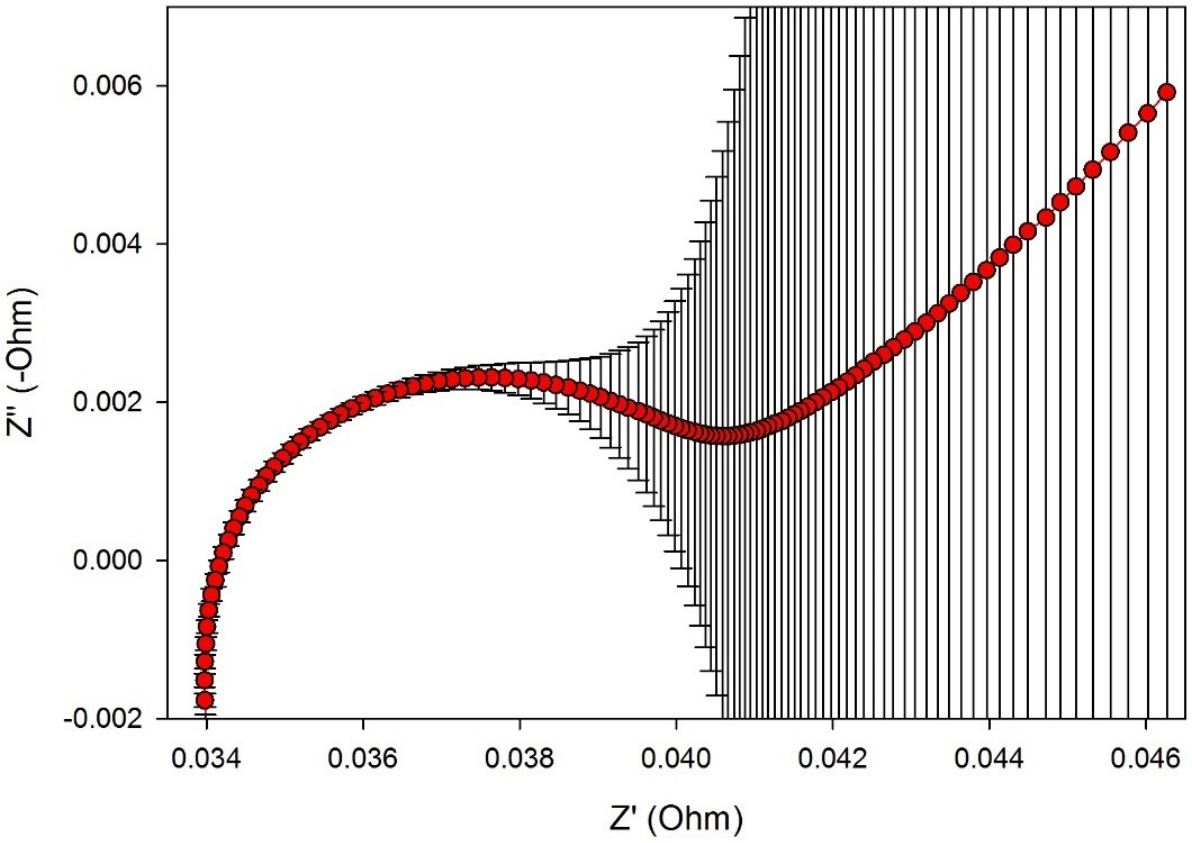

Figure 4.1: Nyquist plot with mean impedance response and standard deviation error bars of a single cell as the SoC is varied from 0% to 100%

The data collected from the seventeen cells can be compiled into a single graph to demonstrate the trends. As shown in Figure 4.2, the imaginary impedance median values along with the associated points situated at one standard deviation away from them are negative from

approximately 35 Hz to 600 Hz. Note that a positive value for the imaginary impedance suggests inductance effects, which are not of interest here. Furthermore, we notice that the standard deviations of the real impedance values barely change from 10 Hz through 10 kHz over all of the various SoC. However, for both the real and imaginary impedances, it is expected that their values will exhibit large variation as the frequency decreases because the processes associated with lower frequencies are more sensitive to the SoC of the cell.

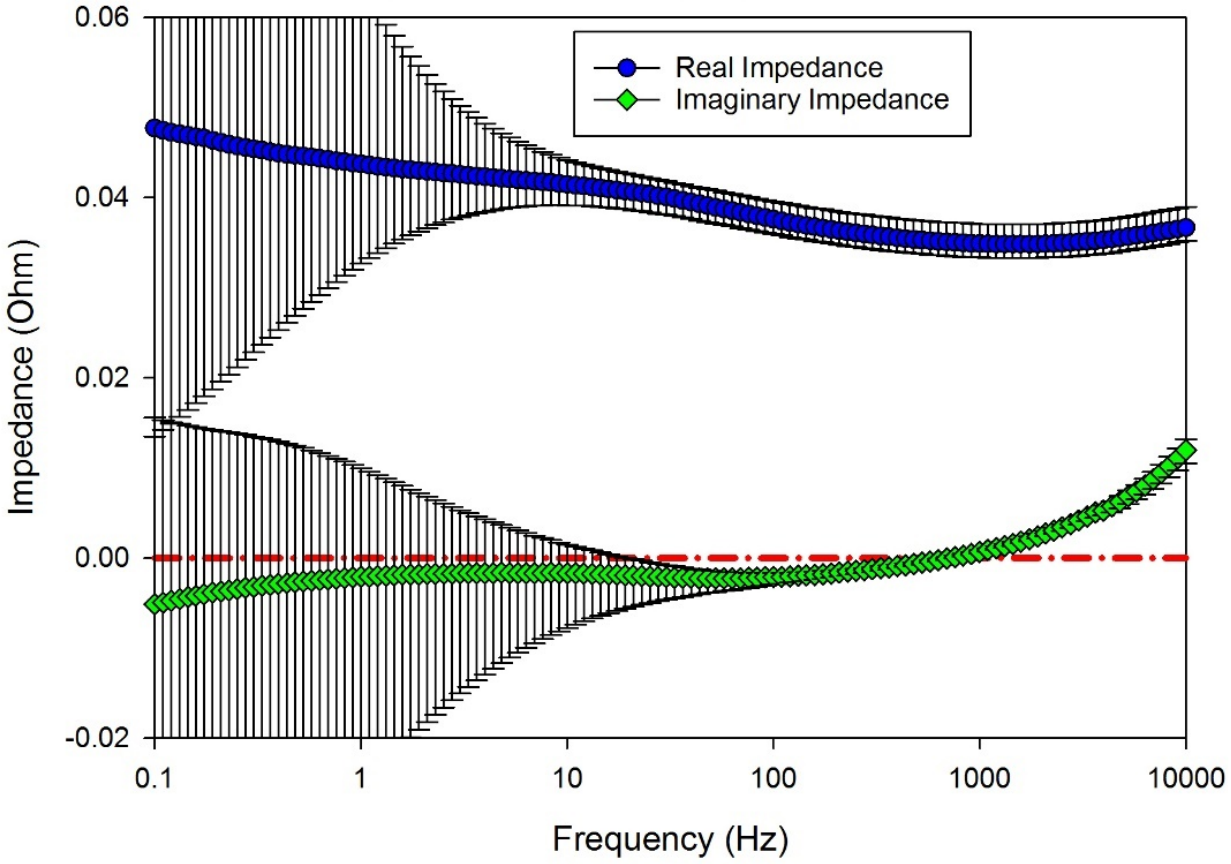

Figure 4.2: Median values of the real and imaginary impedance data along with the associated standard deviations shown by error bars.

Further examination of the plots displayed in Figure 5A, which are those of the median values of the standard deviations shown in Figure 4 versus the frequency, reveals that the standard deviation of the real impedance flattens out starting from 100 Hz, while the imaginary impedance continues to decrease. A zoom in of the standard deviation data is shown in Figure 5B, where the frequency range was limited to 100-250 Hz. As shown, the median values of the real impedance

along with their associated standard deviations of error are equal for two specific frequencies, namely 145 Hz and 158 Hz. We may expand the frequency range of interest to 174 and 191 Hz, but the one-standard-deviation error bars maintains a plateau only between 145 and 158 Hz, with a negative slope starting 209 Hz. In this same frequency band, the median value of the imaginary impedance's standard deviation is approximately 0.4 mΩ, which is a very small deviation from the median values on all seventeen cells for the entire 0-100% SoC regime. Because of the constant characteristic of the standard deviation of the real impedance values and the overall low standard deviation of the imaginary impedance values around 158 Hz, the latter frequency was selected as the frequency of interest for SoH determination, f_{SoH}. This means that only analyzing how the impedance varies at 158 Hz may be sufficient for revealing how the cell ages as a function of its cycle life.

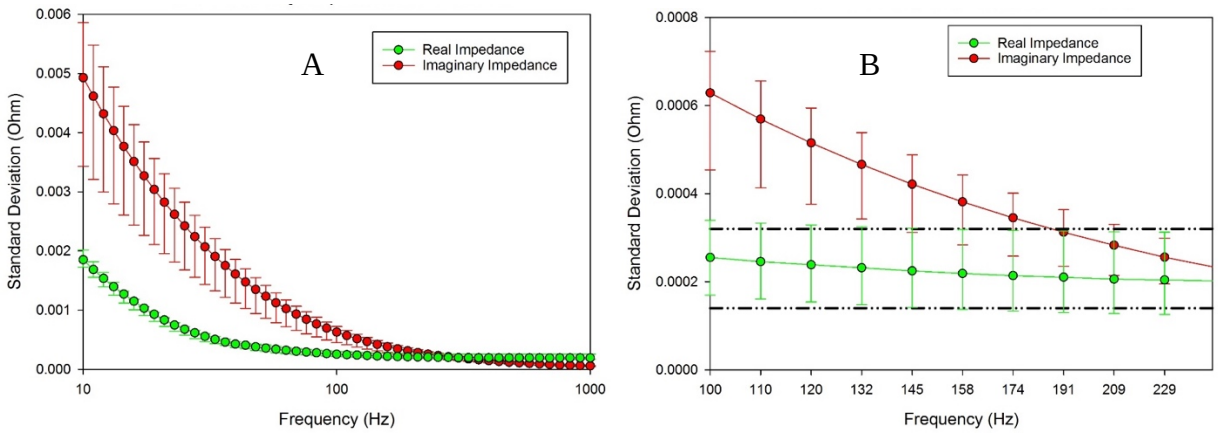

Figure 4.3: Distributions of real and imaginary impedance standard deviation median values as a function of frequency, where A) is from 10 – 1000 Hz and B) is from 100 – 240 Hz.

4.2 Expansion of SoH Frequency to Temperature

The determination of a critical frequency that is sensitive to temperature followed an analysis procedure similar to the state of health frequency. The objective of the following analysis is to find a critical frequency that is both independent of state of charge and highly sensitive to temperature. With this analysis, the data at all temperatures tested (-10 to 60°C) was included in the median values of the real and imaginary impedances in the EIS spectra range. The median values of impedance with one standard deviation error bars is shown in Figure 4.4.

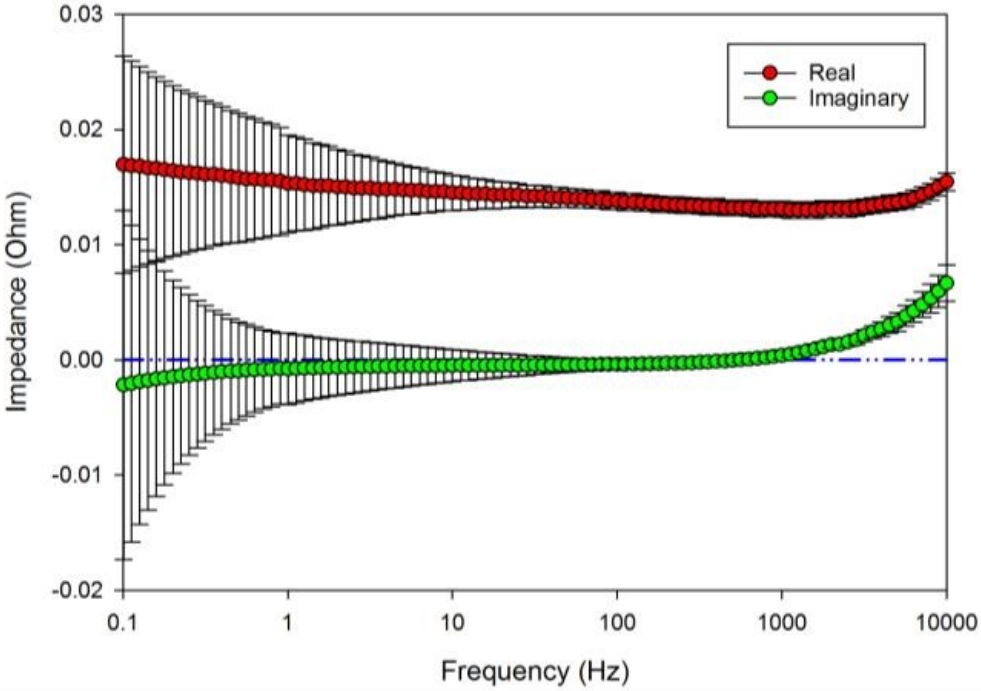

Figure 4.4: Median values of impedance for thermal critical temperature determination

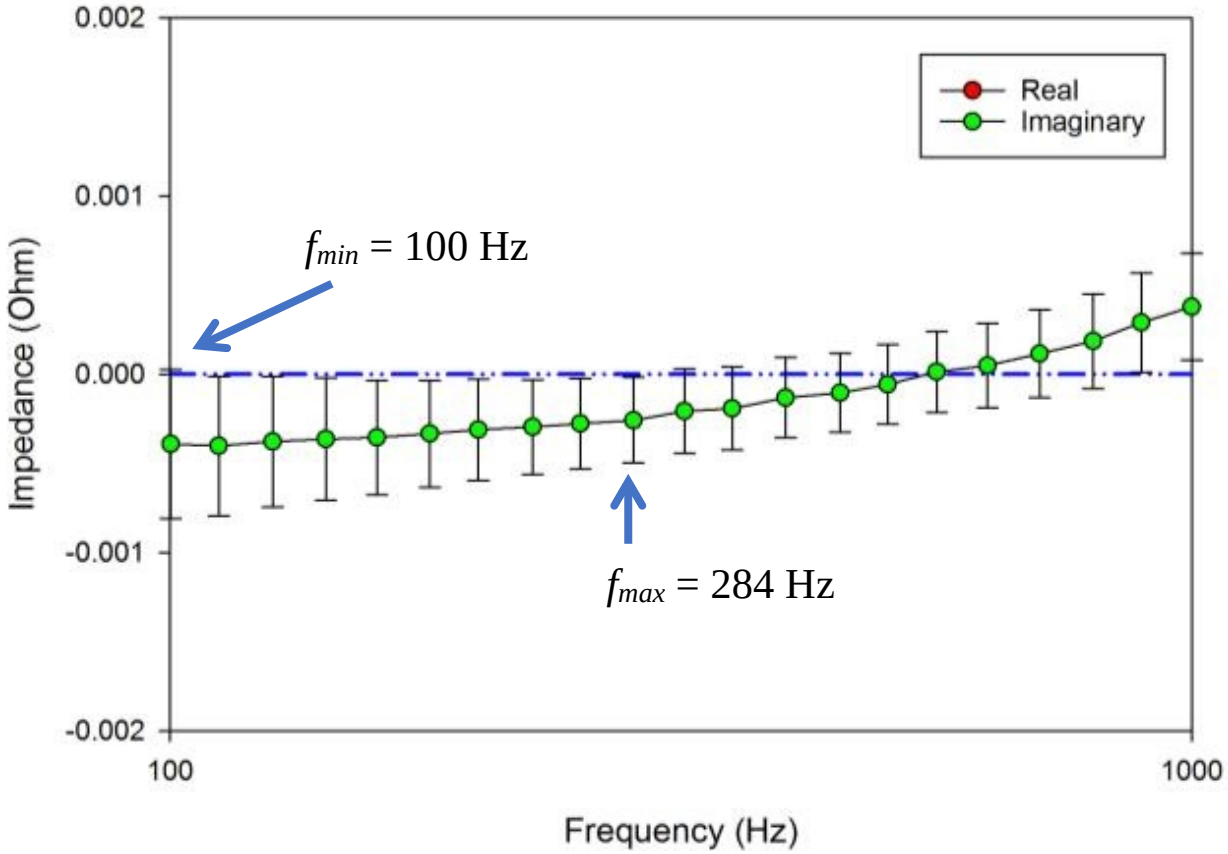

Figure 4.5: Detail view of median values for real and imaginary impedance from 100 to 1 kHz

The next step required the elimination of data to satisfy certain conditions. First, all frequencies below 50 Hz were truncated. As seen by the data in Figure 4.4, the standard deviations are too large. Additionally, the distribution is approximately normal only from 100 -10 kHz. Second, positive imaginary impedance values indicate inductive effects in the circuit. As shown in Figure 4.5, this limits the data to 100 – 284 Hz.

After the region of interest has been identified, a plot of the standard deviation for the real and imaginary impedances as a function of frequency was generated, and is shown in Figure 4.6 A. A clearer picture emerges when the frequency is limited as shown in Figure 4.6 B. Starting at 200 Hz and continuing through 226 Hz, a flat portion of the real impedance standard deviation is seen. Since those two frequencies are also in a region where the standard deviation of the imaginary impedance is also very low (< 0.3 mΩ), either of these two frequencies would be sufficient for a critical thermal frequency. 200 Hz was selected for this work.

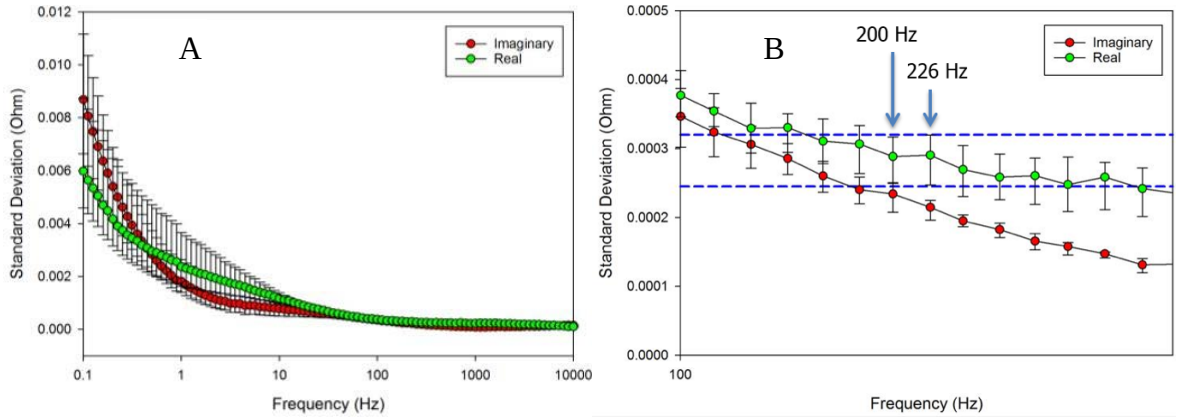

Figure 4.6: Standard deviations of the real and imaginary impedances with the full spectrum (A) and the detail view (B)

Once the critical thermal frequency was determined, the imaginary impedance for each of the temperatures tested was plotted and the data fitted to an equation, as shown in Figure 4.7. Similar to the work presented in [3], an exponential was required to match the data. Unlike in [3], the data in Figure 4.7 is for eight cells. Note how the exponential fit line is able to pass through the median line of nearly all of the temperature box plots.

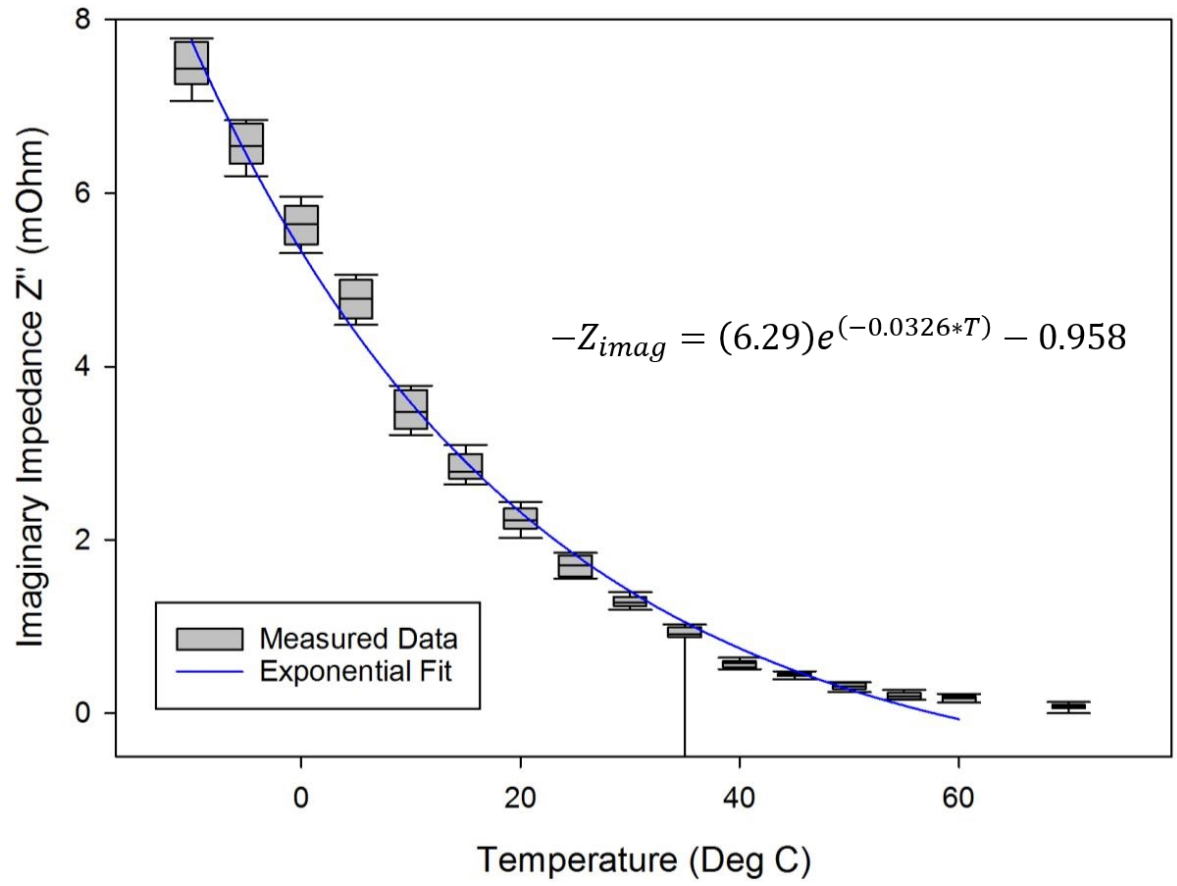

Figure 4.7: Single-cell temperature data with 200 Hz critical frequency

A comparison of the $LiCoO_2$ cell from [3] and the LFP cell is shown in Figure 4.8. While it may appear that the real impedance and the magnitude of the impedance response both have changes as a function of temperature, a closer examination shows that many of the box plots overlap, and particularly after 40°C the response is almost flat. Only the imaginary response shows a definitive difference between each temperature level. When comparing to the $LiCoO_2$, note the change in slope compared to the LFP. As mentioned in [3], the critical thermal frequency for the $LiCoO_2$ and the 18650 form factor is 300 Hz. This work shows that the critical frequency for LFP is 200 Hz in the 26650 form factor. While further research is necessary, one could provisionally conclude that the frequency may be a function of the form factor, while the slope of the exponential fit is dependent on the chemistry.

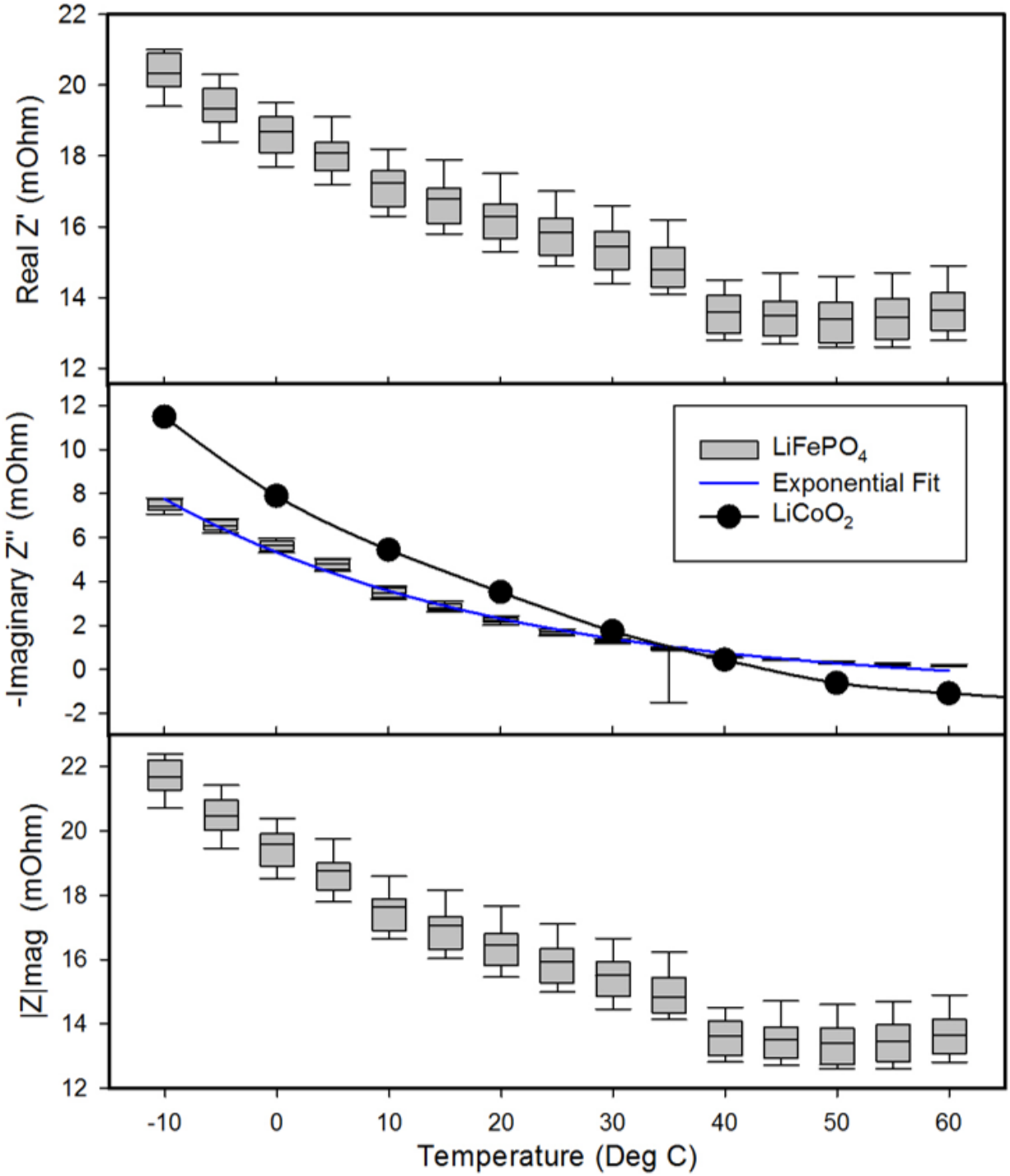

Figure 4.8: LFP 26650P temperature response with real impedance (top), imaginary impedance (middle), and magnitude (bottom). $LiCoO_2$ is included for reference to [3].

Using the critical thermal frequency of 200 Hz, an experiment was performed with a single EIS sweep of the 4P1S (ideal) array in situ. The EIS data was measured after two separate 50-

pulse discharges using the single-frequency technique on the Modulab XM unit. One major modification was found to be necessary, which was to have a long integration time (≈1 sec/point) to increase the stability of the response in the single-frequency mode. In this mode, the frequency is fixed but repeated as many times as possible in the defined integration time to calculate an average value with a small standard deviation. As shown in Figure 4.9, the start and end values of the test match the battery case thermocouple values. Immediately after discharge is completed, however, the thermocouple is measuring much higher than the EIS response would indicate given the derived exponential fit. After about 1200 seconds the EIS response and the thermocouples resume matching values.

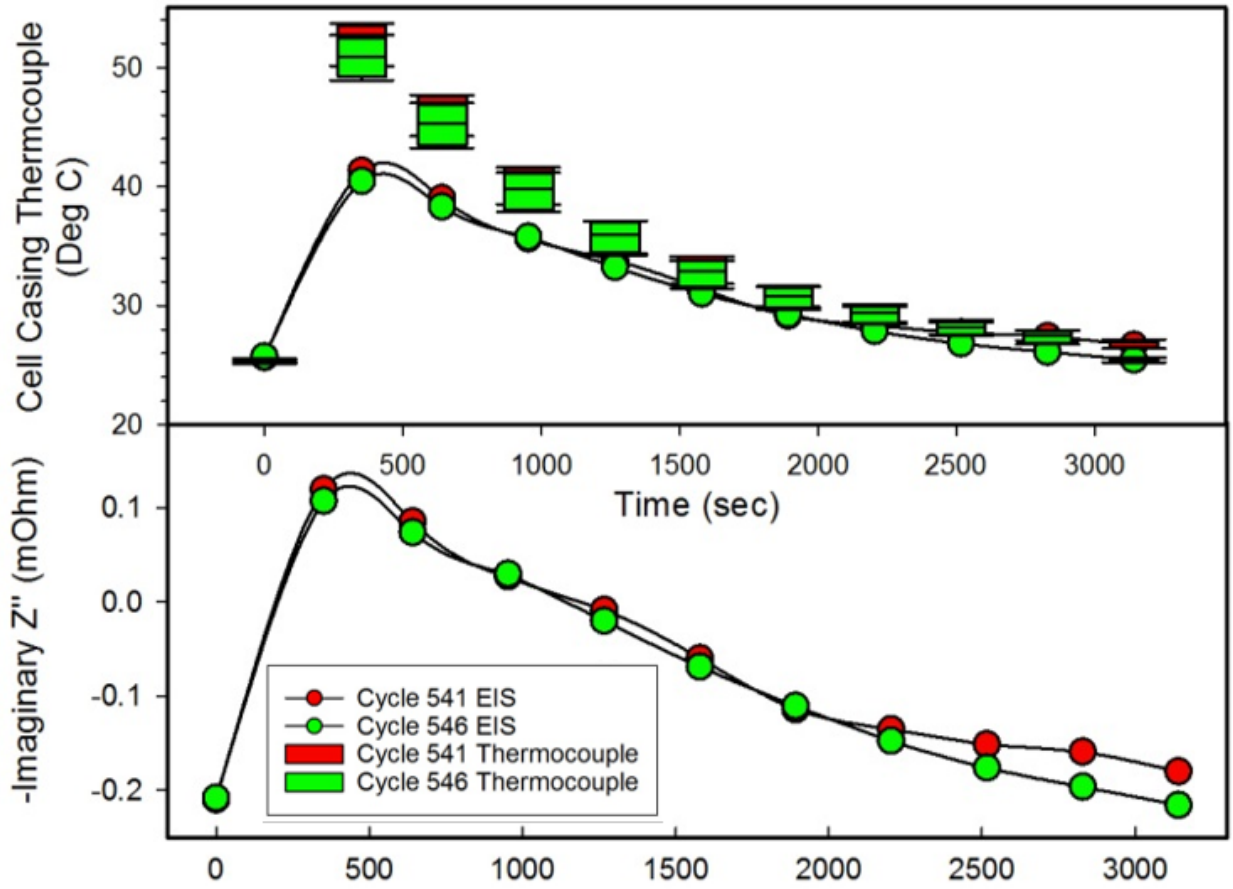

Figure 4.9: EIS response and calculated temperatures after a 10C pulse discharge

It is important to note that while the parallel EIS response as a function of temperature does not appear to calculate the correct temperature after a discharge, it does work for the steady-state conditions. This is extremely important in situations where a battery pack may be idle and has

been called into service. A diagnostic of this type could quickly interrogate the pack and determine if the current temperature is in a safe operating area, particularly in cold environments such as an airplane at high altitudes. Dendrite formation in temperatures approaching 0°C is a major cause of battery failure [98].

Clearly, the derived model does not function properly after a cell has been discharged at a high C rate. One would expect the core temperature, measured by the EIS machine, to be a higher value than the case, as the thermal transit time is measured in many tens of seconds. The most likely explanation is that the exponential fit only works for the case where the entire cell is at an equilibrium, such as in the thermal chamber during the baseline testing. After a high C discharge, a temperature gradient exists across the entire cell, perhaps an uneven gradient as different structures in the cell change the thermal conduction of that local region. Further investigation of this diagnostic was discontinued, as a substantially larger experiment is required. The best exploration of this technique is to employ embedded thermocouples in the cell and match that data to the EIS response. Only then can a model be derived that is consistent for all operational modes of the cell.

4.3 Single-Cell Lifetime Data

Cell performance as a function of cycle life when they were cycled using a pulsed discharge procedure at two different C-rates, namely 1C and 10C, will be presented next. The EIS spectra were recorded at regular intervals at 10C rate (25 cycles) and 1C rate (200 cycles), with the former used more frequently than the latter. A plot of the Nyquist data for a single cell at the 10C rate is displayed in Figure 4.10. Due to experimental equipment limitations, the probes were removed repeatedly during the experiment, which resulted in some variability of the real resistance. The median value of this cells real resistance amounts to 13.6 mΩ with a standard deviation of 1.12 mΩ. The baseline and 25-cycle sweeps were not given much weight since it is very likely that the electrochemistry was still settling over the time span of the experiment. Interestingly, it is observed from Figure 4.10 that the spectra for cycles 375-425 correspond to a move of the real impedance to the right; we do not have an explanation for that phenomenon, although it can be speculated that it is related to the aging of the cell. It is difficult to determine specifically the cause of any changes

in the real resistance in this experiment. A repeated experiment with permanently attached probes would be required to eliminate the probes as a source of error.

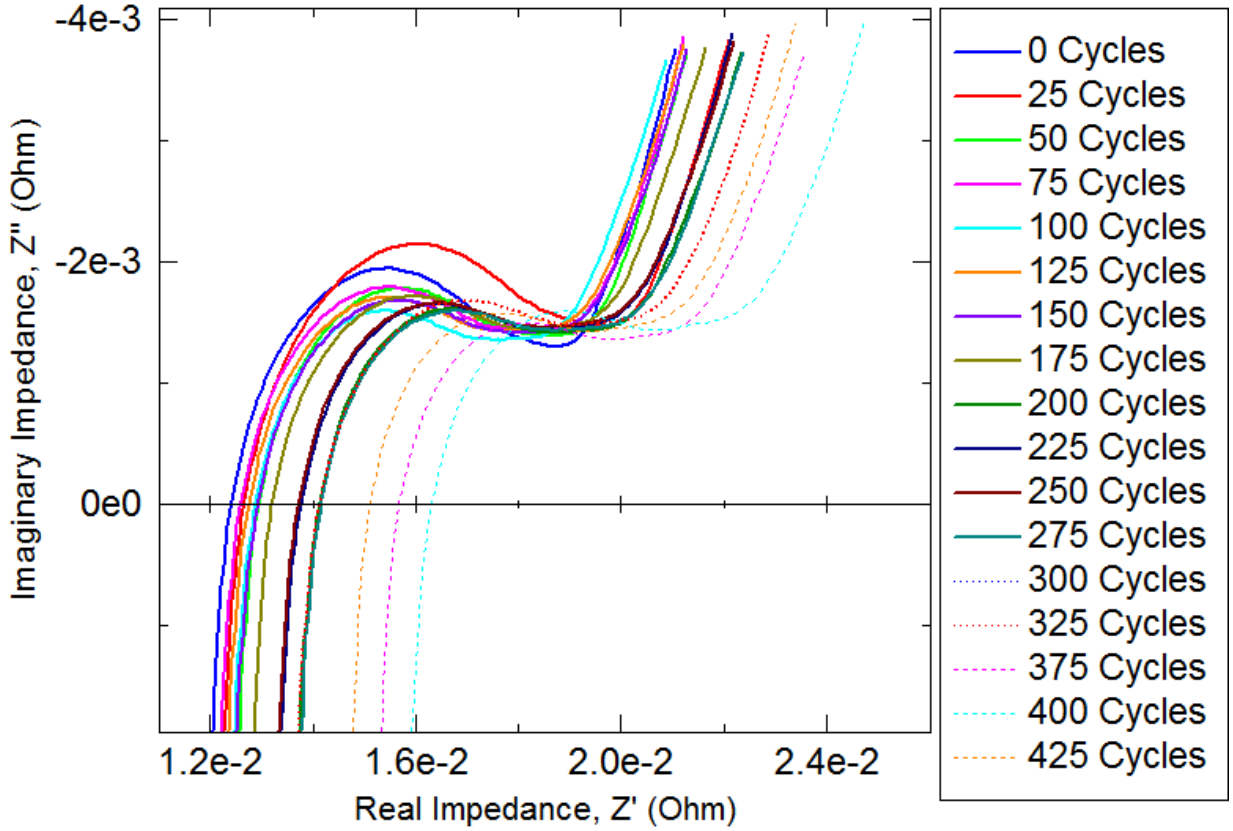

Figure 4.10. EIS spectra for single cell lifetime testing with pulsed load profile.

4.3.1 1C EIS Lifetime Data

The rate of capacity degradation is a significant indicator of battery health in a particular discharge scenario. As shown in Figure 4.11, the median capacity loss for all of the cells in the 1C discharge group is 6% over 6400 cycles. The specific capacity values have low variance until 4800 cycles, when the lower limit begins to increase. This sudden loss of capacity linked to a single cell that experienced an abnormal event at 4800 cycles. After examination of the data log, it appears the cell was over-discharged due to an error in the MACCOR cycler. The cell continued to recharge and discharge as before, but as evidenced by the data shown in Figure 4.11, a permanent capacity loss has occurred and appears to be accelerating with the number of cycles.

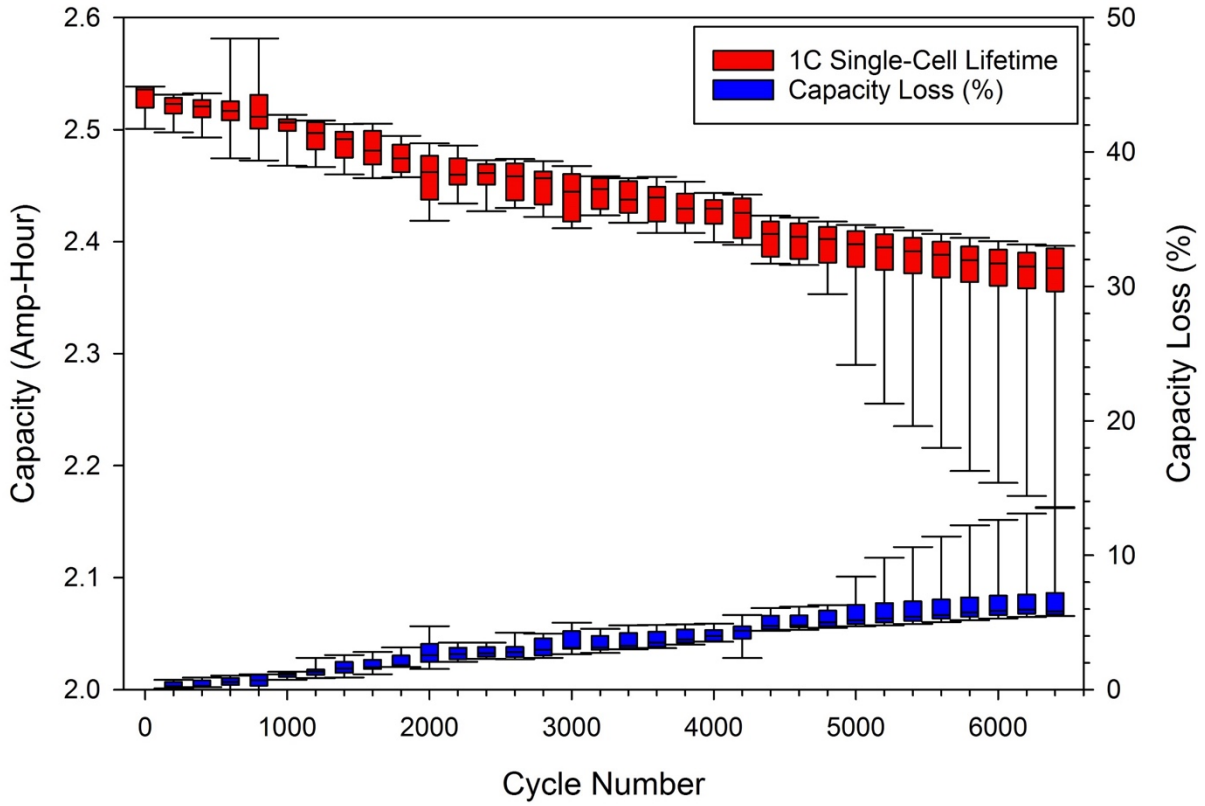

Figure 4.11: Capacity loss for the 1C single-cell lifetime testing group

Using the SOH frequency identified in the earlier section, a box plot of the imaginary impedance at 158 Hz as a function of cycle number was generated and displayed in Figure 4.12 for the 1C lifetime testing group. One significant feature observed in the data is that after 200 cycles the variability between the cycles is minimized. This may be of importance during the construction of a parallel cell pack, as it may take many more cycles than previously believed to settle the electrochemistry. Note the sudden change in the bottom outlier starting at Cycle 4800, which continues through to the end of the test series. This outlier is the EIS response associated with the same cell seen in Figure 4.11 that experienced an over-discharge event. Since the response is permanent, one can conclude based on this case that an over-discharge event causes permanent damage to a battery that can be detected through the EIS diagnostic at the critical SOH frequency.

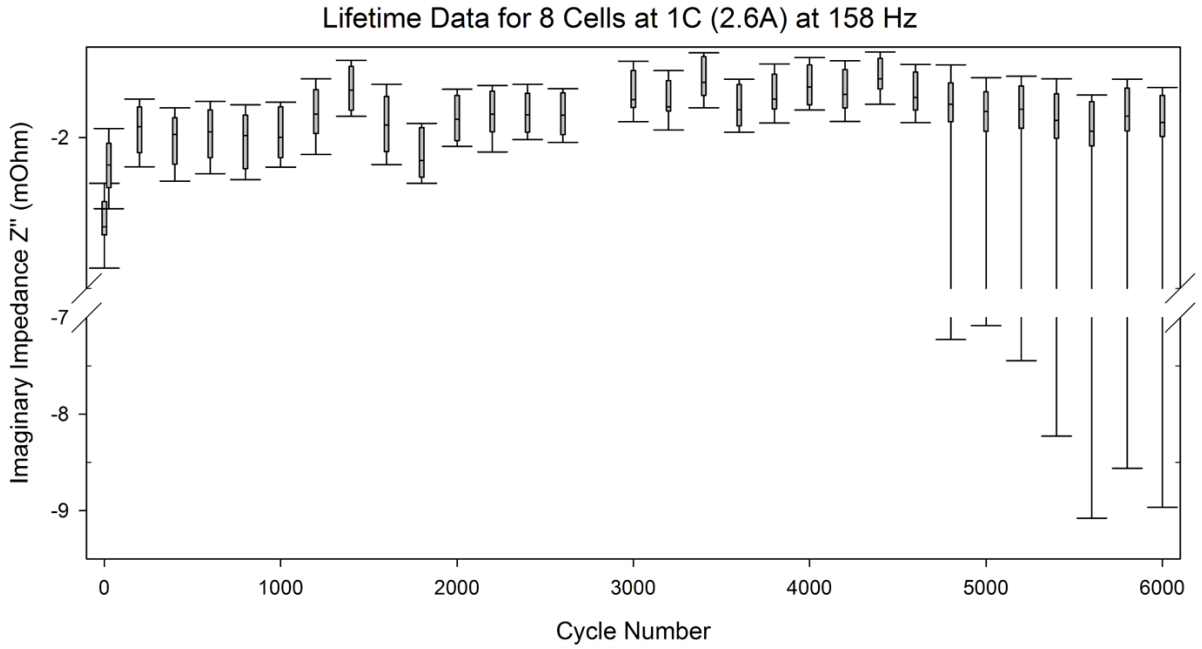

Figure 4.12: Imaginary impedance at 158 Hz as a function of cycle number for eight cells subject to lifetime testing at 1C.

The evolution of the 1 kHz real impedance is shown in Figure 4.13. Note that the values for cycles 0-1400 are significantly higher than the remainder of the data. This is due exclusively to the original battery cell holder design described in Chapter 3, with the gold-coated spring steel material. This data illustrates the importance of material selection when evaluating the performance of batteries with low source impedance, as the external circuit connections can modify the test results in unexpected ways. As would be expected, given the results shown in Figure 4.12, the real impedance has little variability until around 4800 cycles. As previously discussed, at 4800 cycles one cell had an over-discharge event. The change in the impedance can be observed in Figure 4.12, with the outlier impedance over twice the value of the median cell impedance. Given that the 1C pulse discharge testing exceeded 6000 cycles with a capacity loss of 6%, for the remainder of this work it will be assumed that the aging for cells discharged at this nominal rate is significantly longer than the 10C group, and does not require further analysis.

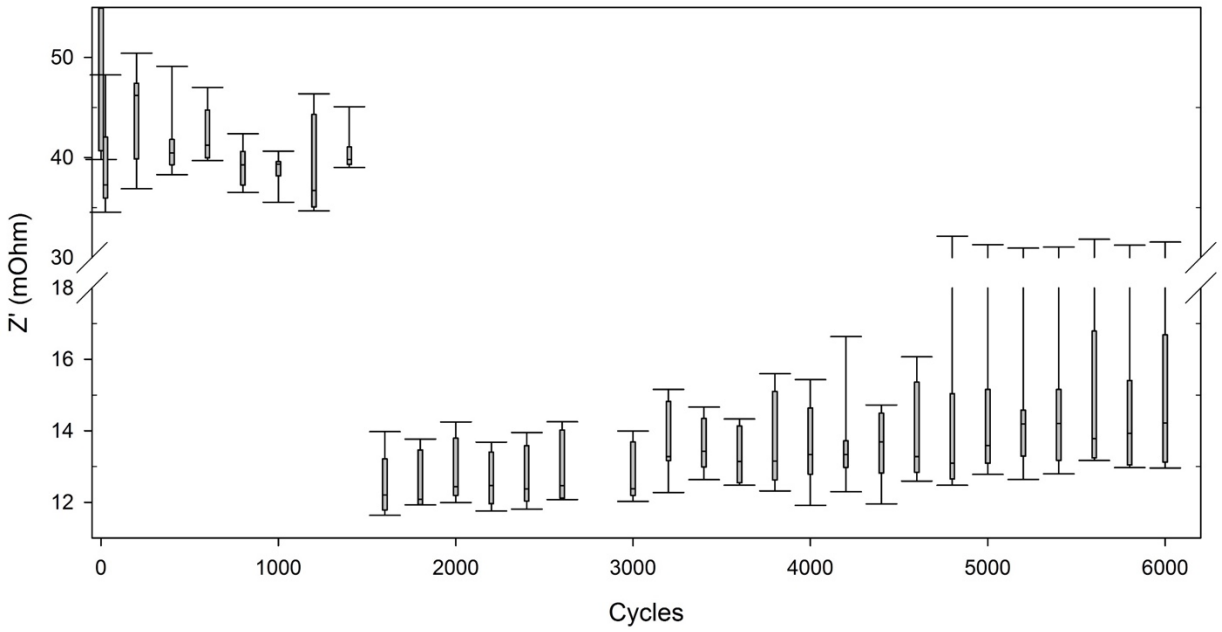

Figure 4.13: Box plot for 1C single-cell real impedance at 1 kHz

4.3.2 10C EIS Lifetime Data

The capacity loss as a function of cycle for the 10C single-cell cycling group is shown in Figure 4.14. Discharging the cells at 10C appears to greatly accelerate the capacity loss, as the median capacity loss reaches 20% after 1125 cycles. For the first 600 cycles, the interquartile range is approximately the same, and the outliers have a small but growing increase in variance. After 600 cycles, the interquartile ranges decrease in size, continuing throughout the end of the test series. This would appear to indicate a critical point is reached around 600 cycles, but based on purely electrical data it is unclear why that is occurring.

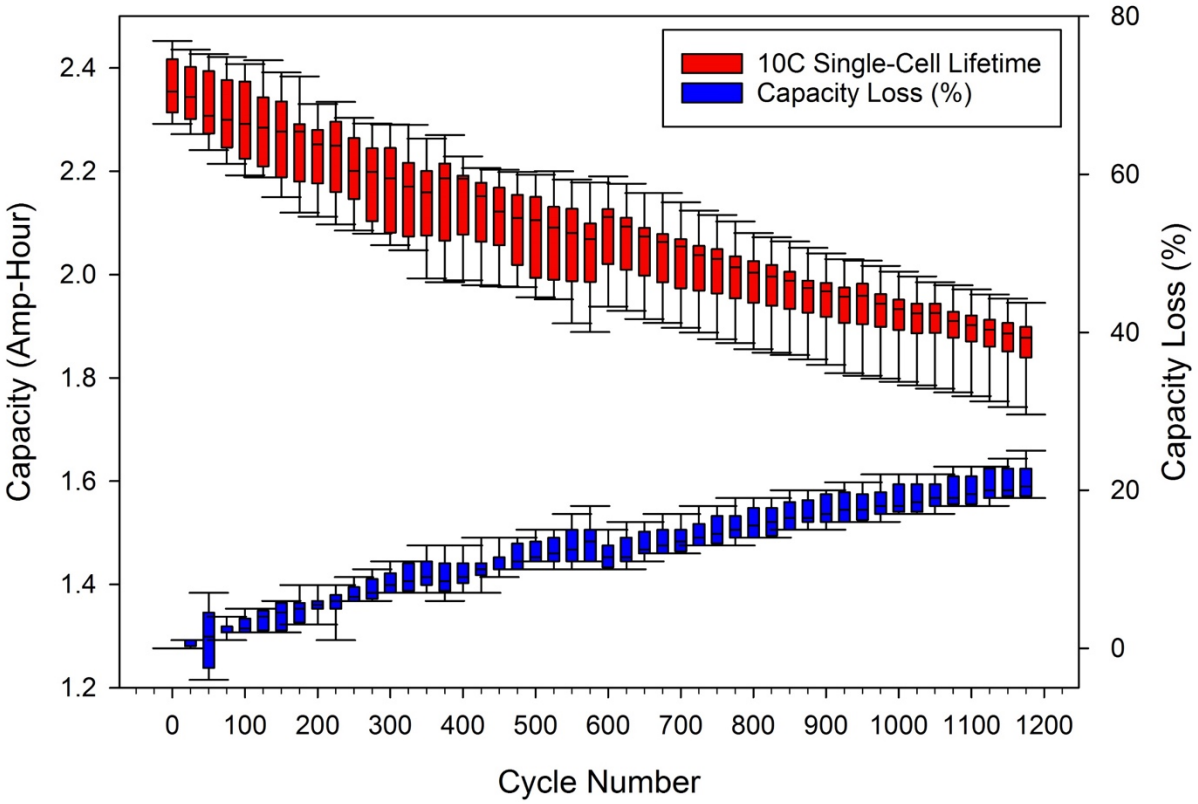

Figure 4.14: Capacity loss for the 10C single-cell lifetime testing group

Further examination of the electrical data from the 10C lifetime test series can prove useful. As shown in Figure 4.15, the energy delivered per cell remains constant throughout the test series, with some minor deviations at the end. The minimum cell voltage, however, declines throughout the series. This is expected, as the voltage must drop to maintain a specified current if the resistance is increasing with cycle number. One cell in the series reached terminal end of life at approximately 1100 cycles, as seen by the sudden decrease in energy delivered to the load. For that cell, the voltage reached 2.0 V and the channel was disconnected by the MACCOR cycler per the settings in the programming file.

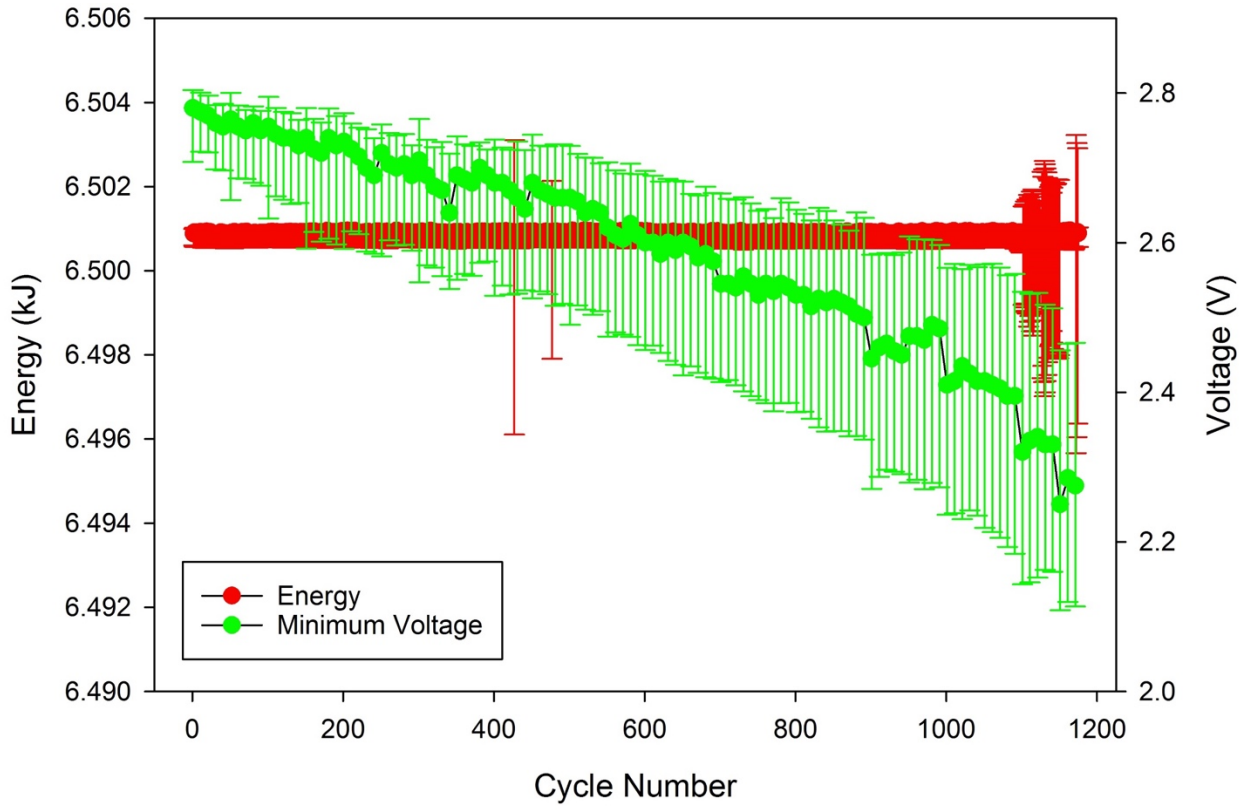

Figure 4.15: Energy delivered to load vs. minimum cell voltage for 10C single-cell testing, with median values and one standard deviation error bars.

When examining battery electrical behavior, the voltage and current measurements can be used to calculate the on-state resistance, as shown in (4.1), where Voc is the open circuit voltage. Von-state and Ion-state are the conducting state voltage and current values, respectively.

$$ESR = \frac{V_{oc} - V_{on-state}}{I_{on-state}} \tag{4.1}$$

The DC ESR shown in Figure 4.16 is the ESR value calculated from (4.1 during the first pulse of each discharge cycle. This was selected to indicate the status of the cell before a full cycle, as it will drop as energy is expended during the discharge process. The 1 kHz AC ESR values were measured after a discharge, but the time delay was sufficiently long to allow for cell recovery and measure the cell at approximately the same state of charge as the DC ESR. The error bars in the DC ESR measurement are significantly larger than those associated with the AC ESR

measurement, and for the purposes of comparing relative cycle to cycle changes in a cell, the AC ESR is a more reliable diagnostic.

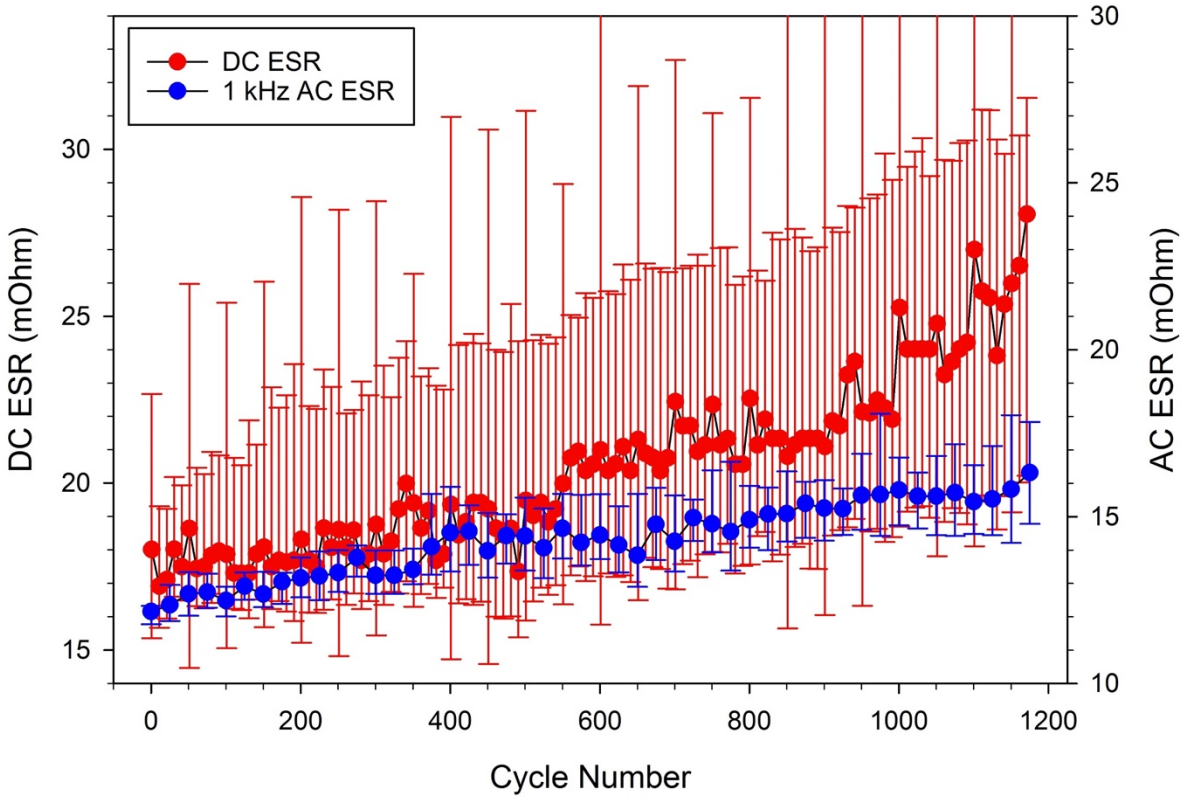

Figure 4.16: Calculated DC ESR and measured 1 kHz AC ESR comparison for 10C single-cell testing, with median values and one standard deviation error bars.

A final examination of the ESR data is shown in Figure 4.17, with a comparison of the AC ESR and minimum cell voltage. The ESR median values linearly increase as a function of cycle consistently for all of the cells in the test group, starting at 12 mΩ and ending at 16 mΩ. The minimum cell voltage, however, is only linear from cycles 0 – 900. After 900 cycles, the inflection changes and the median values are no longer linear with the preceding data. Given that the ESR response is constant at 1 kHz, and the cell minimum voltage has a sudden change not reflected in the ESR, leads to the conclusion that neither the DC ESR response nor the AC ESR response can be used as a reliable indicator of cell health or performance.

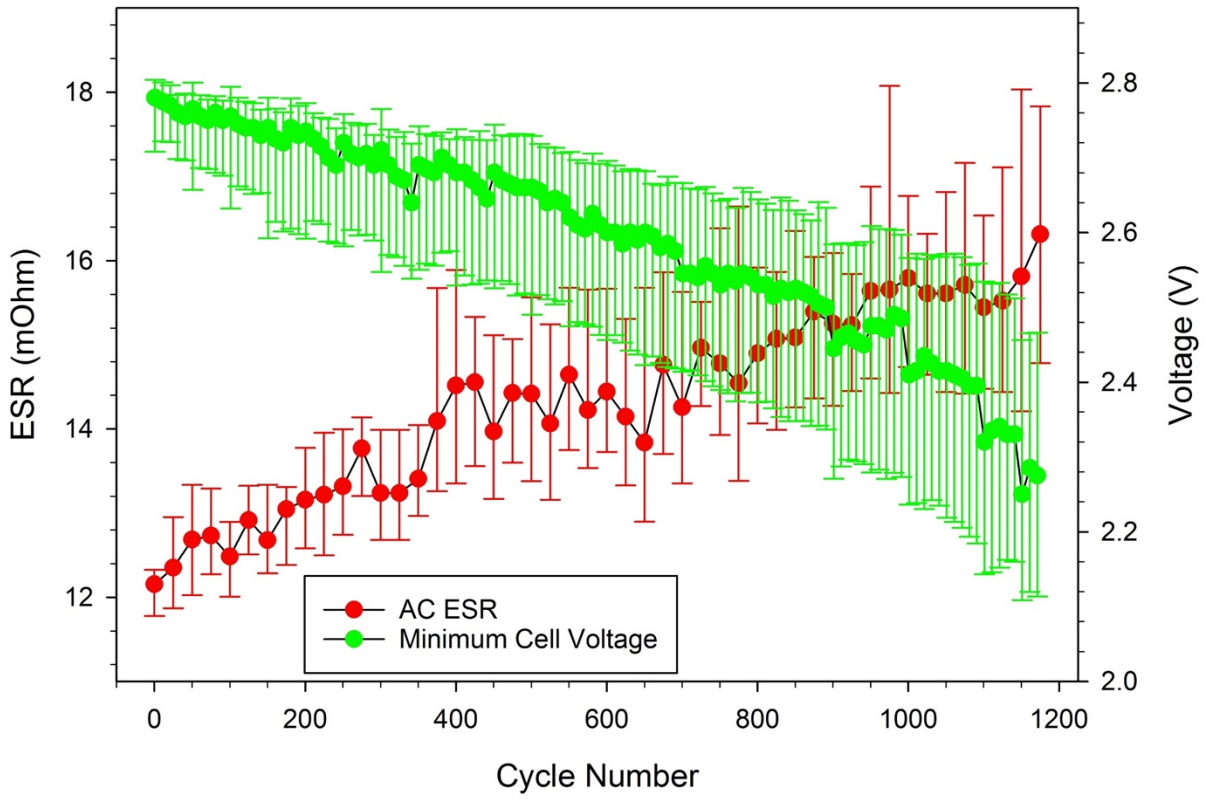

Figure 4.17: 1 kHz AC ESR vs. minimum cell voltage for 10C single-cell testing, with median values and one standard deviation error bars.

The analysis of the purely electrical data has not yielded any useful insight into cell behavior at the electrochemical level, and does not address the question first posed at the beginning of this section. The box plot of the imaginary impedance data at 158 Hz for the 10C lifetime group is shown in Figure 4.18. The general shape of the EIS response as a function of cycle is a semi-circle, with an apex around 600 cycles. As noted in Figure 4.14, a sudden change appears to occur at this point. However, further analysis will require a model of the system, which will be discussed later in this chapter.

As observed, at low cycle numbers, the interquartile ranges of the imaginary impedance values are rather large. However, as the cells are repeatedly cycled, they narrow down around a median value of 1.3 mΩ. The interquartile range begins to decrease from 50 cycles until about 200 cycles. It appears the cells reached a common equilibrium from approximately 375 – 800 cycles, where the median value is approximately the same and the distribution spread is relatively

small. The negative slope observed in the right half of the plot would be consistent with the hypothesis that the internal impedance of the battery is growing as the cell ages.

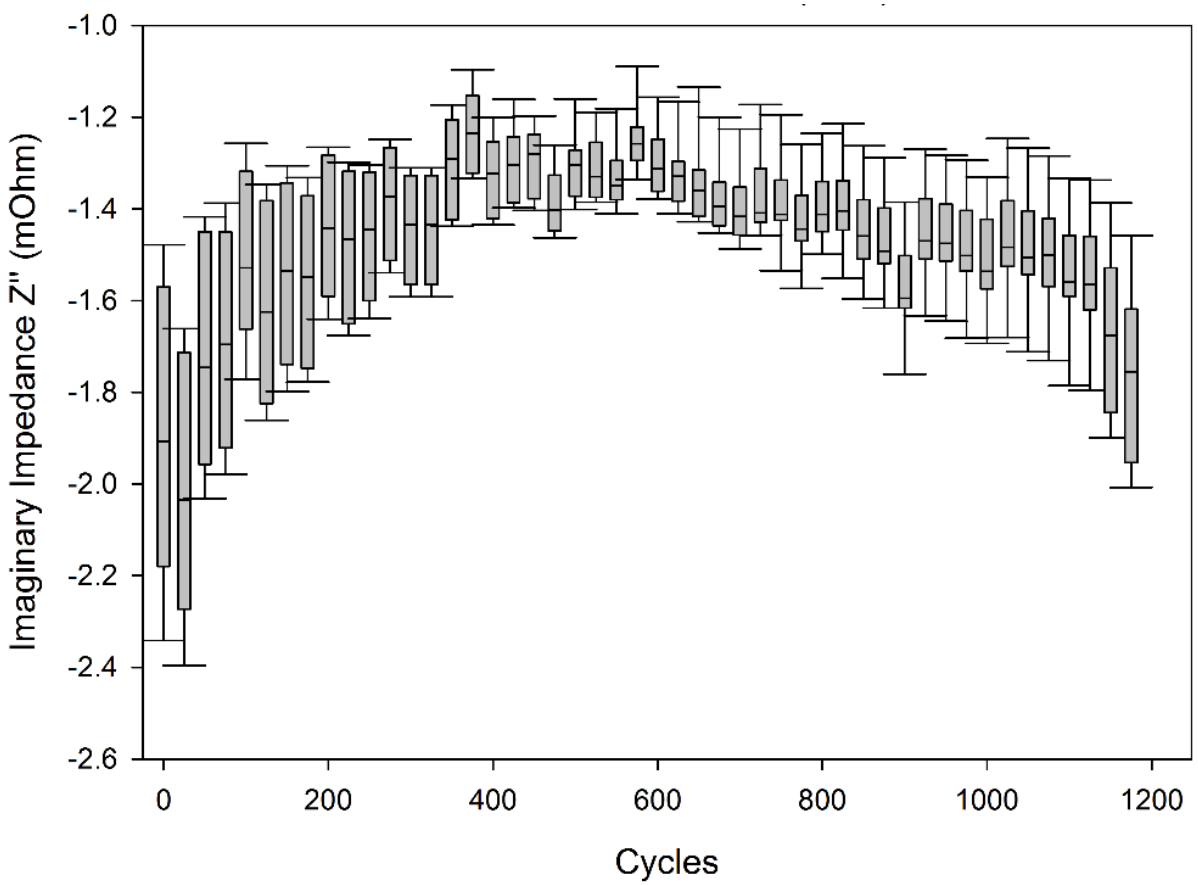

Figure 4.18: Imaginary impedance at 158 Hz as a function of cycle number for eight cells subject to lifetime testing at 10C. End of life reached at 1175 cycles.

The median value of the imaginary impedance is lower than the 1C cell group after the first 50 cycles, as the median value of the data shown in Figure 4.12 remains at approximately -2 mΩ for the first 6000 cycles. In the 10C group, it decreases quickly over the next 200 cycles to a low of -1.3 mΩ, then increases to a terminal median value of nearly -1.8 mΩ. This is most likely due to the high discharge rate causing structure changes in the cell, increasing the relative mobility of the ions in the cell, and thereby reducing the effective impedance of the battery. As the cell ages, however, the effect declines and the cell performance begins to return to the baseline characteristics of the 1C lifetime group.

As shown in Figure 4.19, the median ESR at 1 kHz is approximately 12 mΩ at the beginning of the cycling process. After 625 cycles, the median value increases to 14 mΩ with a 1 mΩ standard deviation. This data supports the hypothesis that the cells will age unevenly and presents a range of possible ESR values after 450 cycles of usage. One may speculate that a large portion of the variability between readings is due to resistive contacts with the EIS probes changing between data measurements. A follow-up study with permanently attached EIS probes and multiple data channels would allow for precision determination of the ESR growth as a function of cycle. However, it is believed that with a sufficiently large sample size such as in this work, the data recorded are sufficient to describe a typical cell response as a function of cycle and C rate.

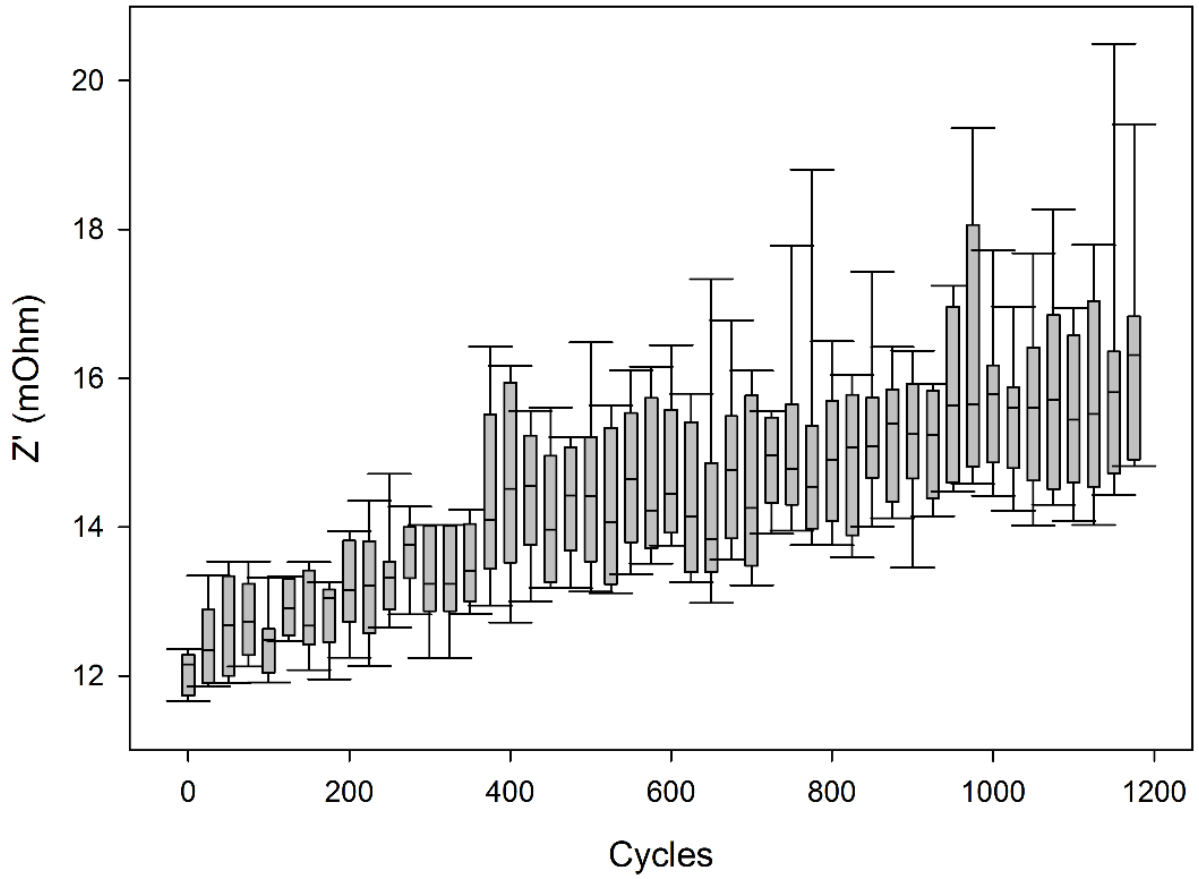

Figure 4.19: Real impedance as a function of cycle at 1 kHz for cells cycled at 10C. The data indicate a progression towards a higher real impedance with cycle aging.

The ESR variability shown in Figure 4.19 can be attributed to some extend with the contact resistances changing as the EIS probes are moved between cells, but as shown by the AC ESR

measurements the variability increases with the number of cycles. At the begin of the test series, the spread of the impedance values is at least 1 mΩ, increasing to a peak of over 5 mΩ near the end of the series. The imaginary data at 158 Hz shown in Figure 4.18 varies less than 1 mΩ for all cycles, with many less than 0.5 mΩ. This leads to the conclusion that the imaginary data at 158 Hz is relatively insensitive to real impedances such as contact resistance, and after the following brief examination of the DC ESR values, can be disregarded as part of the battery health analysis.

4.4 4P1S Parallel Array Testing

From the EIS spectra measured from the seventeen cells, data collected at 50% SoC was examined to identify four cells with nearly identical Nyquist plots. As shown in Figure 4.20, four cells were identified that met the selection criteria, with a real axis crossing median of 13.073 mΩ and a standard deviation of 41.42 μΩ. Each of the four cells was placed in a similar cell holder, and the EIS probes were semi-permanently attached. Each cell was discharged to 0% SoC and recharged in 10% increments with a programmed 30 minute pause prior to an EIS sweep to allow the electrochemistry to settle and equilibrate the internal cell temperature. After the cells were installed in the testbed, a high-precision 1-kHz milliohmmeter was used to determine the resistance from the battery anode to the collector plate for each cell. A median resistance of 3.288 mΩ with a standard deviation of 0.121 mΩ was recorded. This resistance value was determined to be sufficiently low for the cells, given their 9.3 mΩ 1 kHz source impedance with the ESR meter.

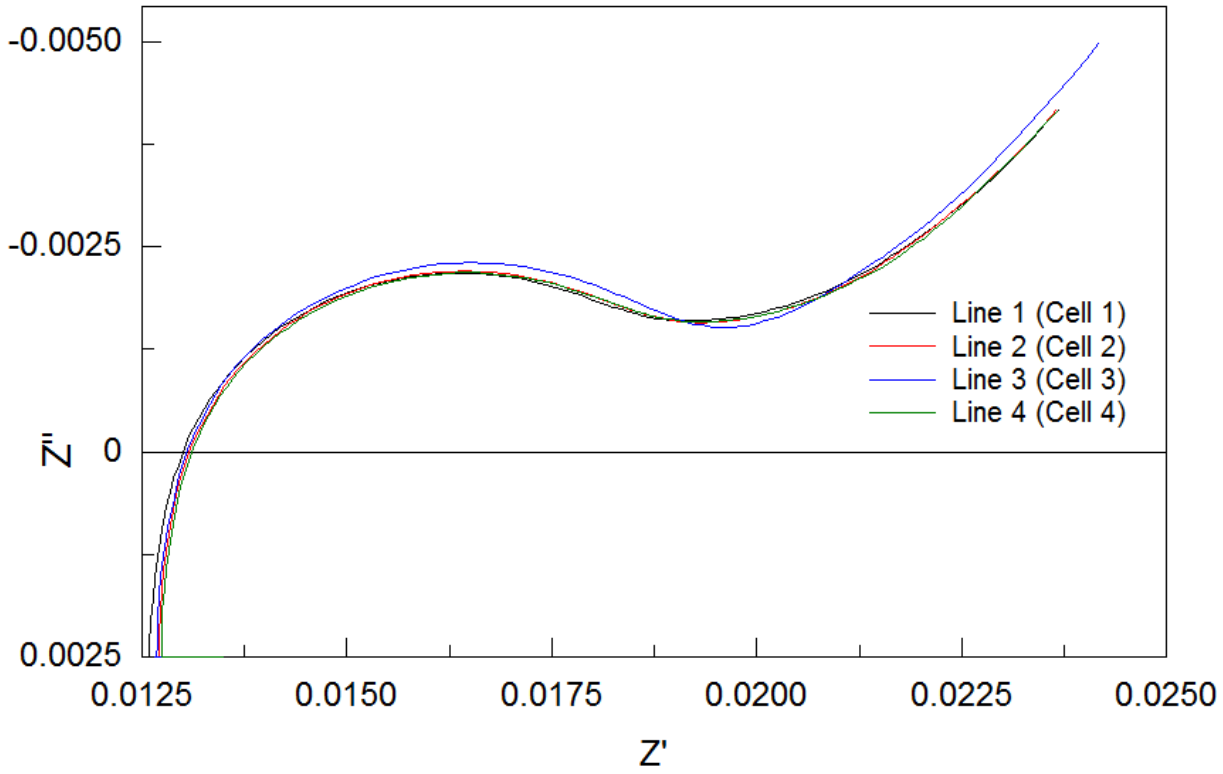

Figure 4.20. Cells selected for baseline analysis in parallel cell array. Data was recorded in situ for each cell (isolated from the group) at 50% SoC in the array.

4.4.1 Initial Testing on Baseline 4P1S Array

As previously stated, the hypothesis under test is that four cells that are as identical as possible (electrical and EIS spectra) will share current evenly when discharged as an array into a load, with ideally 26 A maximum per cell. This hypothesis was tested using the discharge profile described in Chapter 3, and the current data for each battery is shown in Figure 4.21 for one of the first ten discharge cycles. The data shown in Figure 4.21 would appear to support this hypothesis, with an observed 3% difference between the peak discharge current of 26.4 A on Cell 2 and the lowest current output from Cell 4 at 25.6 A. The low overall cell-to-cell variation tracks well with the effort to balance the discharge lines and force any changes to the battery cells. The current changes over the time of the pulsed discharge test can be explained by the SEI film development. Cell 2 appears to source current at a relatively steady rate, while Cell 4 is decreasing as Cell 3 increases. The slight decrease in Cell 1 appears to track with the slight increase in Cell 2. This phenomenon

has been clearly illustrated in these parallel experiments and should be researched further in future efforts to determine its effect on long-term degradation and power quality in a larger system.

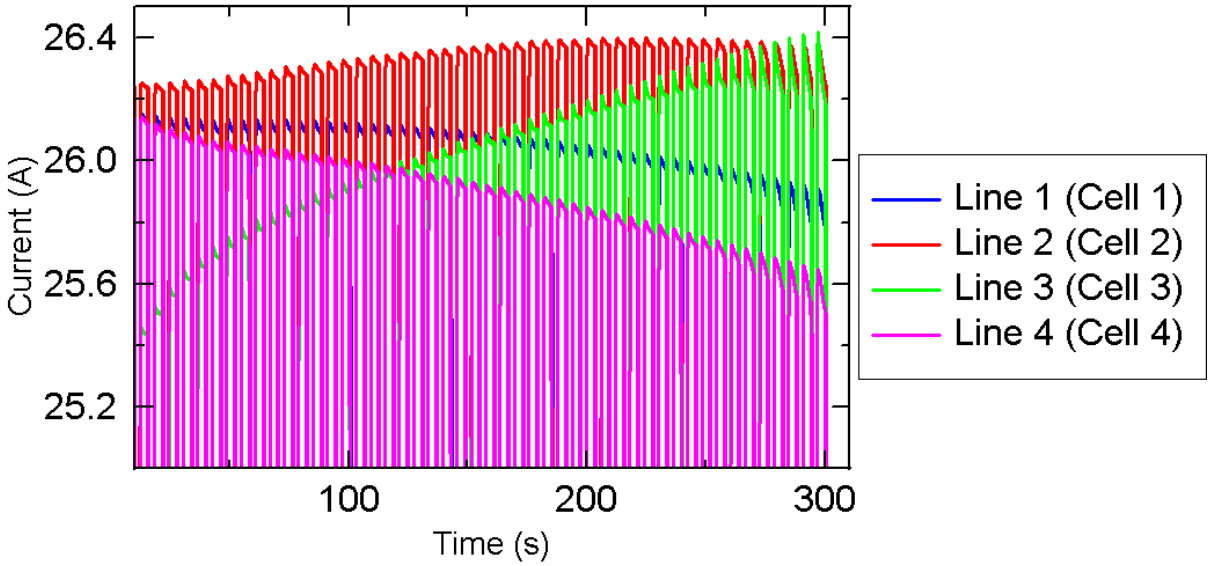

Figure 4.21. Current recorded from parallel array at 10C with pulsed discharge program on the EL for Cycle 10 in the test series.

The voltage recorded for each cell is displayed in Figure 4.22. Cell 1 has the lowest voltage, which indicates that it is under stress sourcing current. Cells 3 and 4 have overlapping voltages under load, and Cell 2 is between the two extremes. One can observe the load voltage increasing at approximately 50 seconds, which corresponds to the temperature data reaching 28°C. Given that the cells have an initial temperature of 25°C, a measurable temperature rise on the case of each cell indicates sufficient internal heat is being generated to reach the exterior case and cause the internal ESR of each cell to decrease.

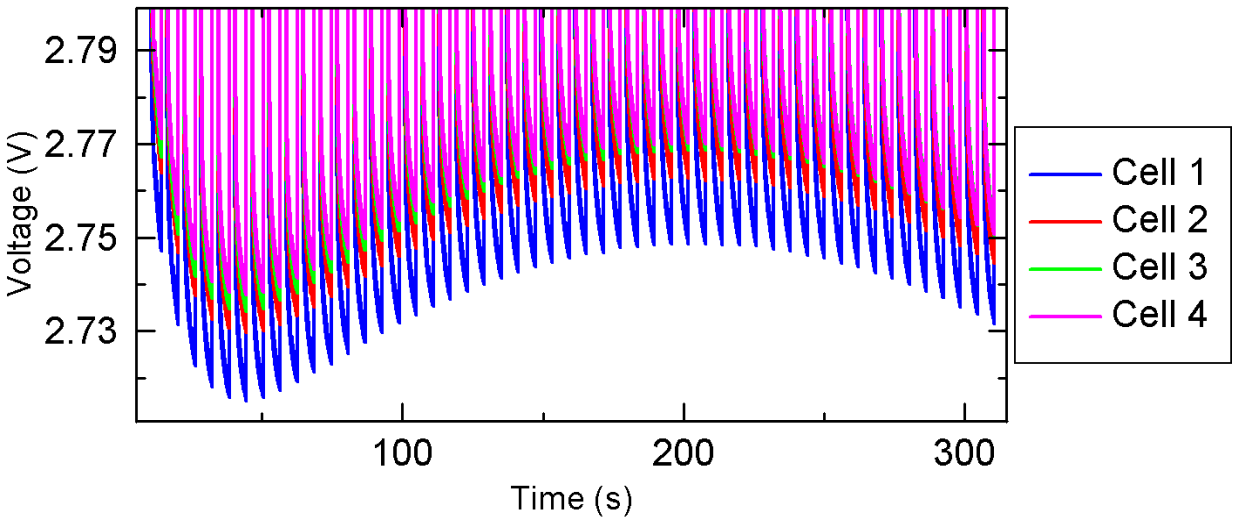

Figure 4.22. Voltage recorded from the parallel array at 10C with pulsed discharge program on the EL for Cycle 10 in the test series..

A plot of the cell case temperatures for the entire discharge cycle and recovery period is shown in Figure 4.23. Cell 4 has the lowest overall temperature, which is expected since it sources the least amount of current. Temperatures variation is a result of imbalance in the current delivered by each respective cell to the load, shown earlier in Figure 4.21.

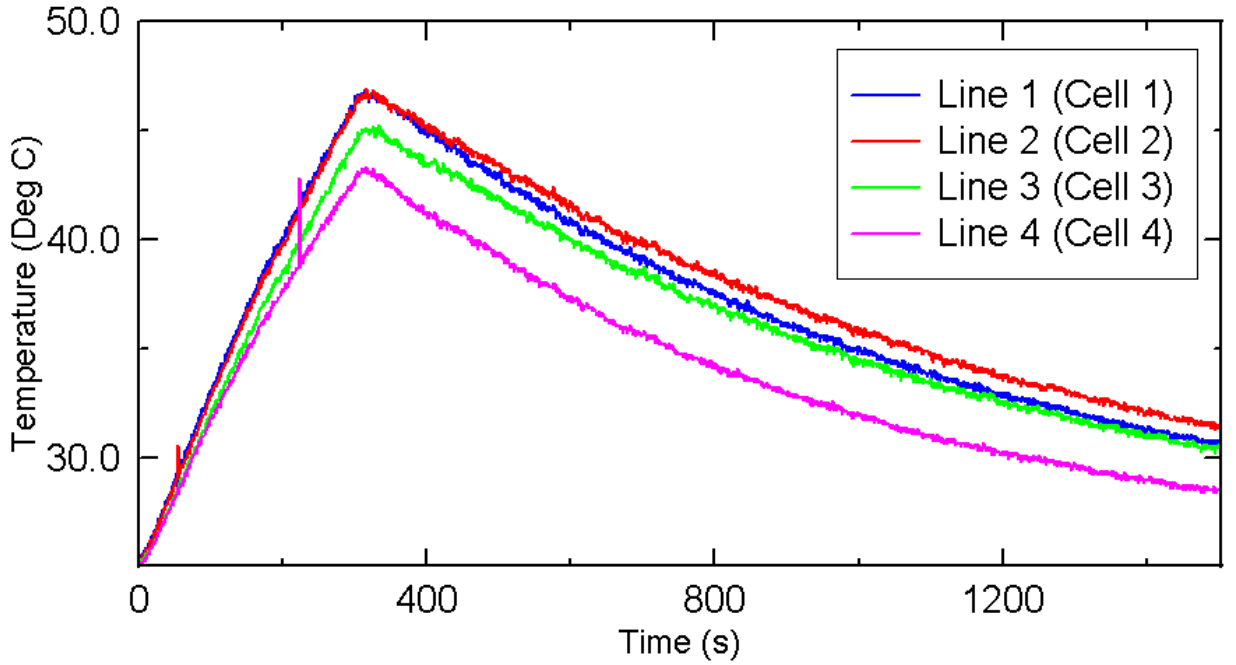

Figure 4.23. Cell case temperatures from the parallel array at 10C with pulsed discharge program on the EL for Cycle 10 in the test series..

4.4.2 Analysis of Electrical Data for Baseline 4P1S Array

The analysis of the baseline 4P1S array for the entire experiment is continued in this section, with a plot of the total energy delivered to the electronic load per cell as a function of cycle is shown in Figure 4.24. The data indicate that after approximately 150 cycles the hypothesis is disproved. For the first nearly 150 cycles, all of the cells appear to source approximately the same amount of energy, with some various cycle-to-cycle. In this period, Cell 2 appears to dominate a portion with the most energy sourced. After about 150 cycles, Cells 2 and 3 source the most energy with the other two cells at about the same.

At the 200 cycle mark, however, Cell 3 is suddenly sourcing ≈200 J more than Cell 2. This trend continues, with Cell 3 reaching a peak of 6% higher energy than the other three cells before a slow decline to 4% as the cells begin to age with the onset of power fade. Also shown in Figure 4.24 is a box plot of the minimum cell voltage for all four cells in the array. Throughout the entire experiment, none of the outliers dropped below 2.0 V, the minimally acceptable threshold. As would be expected, the voltage drops as a function of cycle, as the source impedance increases with aging of the batteries. The most interesting aspect, however, is that the voltage for each cell does not change with the amount of energy delivered to the load. Given the relative differences in energy performance of the cells in the array, Figure 4.24 is further evidence that an electrical analysis of the system is insufficient to determine the causes of the disparity in current measurements.

A plot of the capacity as a function of cycle for the entire array is shown in Figure 4.25. The entire array has an initial capacity of slightly above 10 AH, which is reasonable with an average 2.5 AH per cell. From Cycle 0 – 300 the capacity degradation is approximately linear, but from Cycle 300 – 500 there appears to be a plateau in the capacity change. The linear response resumes after Cycle 500, with the typical end of life limit of 20% capacity loss reached at Cycle 600. As shown in Figure 4.25, the capacity loss between cycles 600 – 700 is less than 5%, and likely can be safely operated to 700 cycles. An abrupt change is observed in the interval between 700 – 750 cycles, which matches the changes seen in Figure 4.24 in the same period.

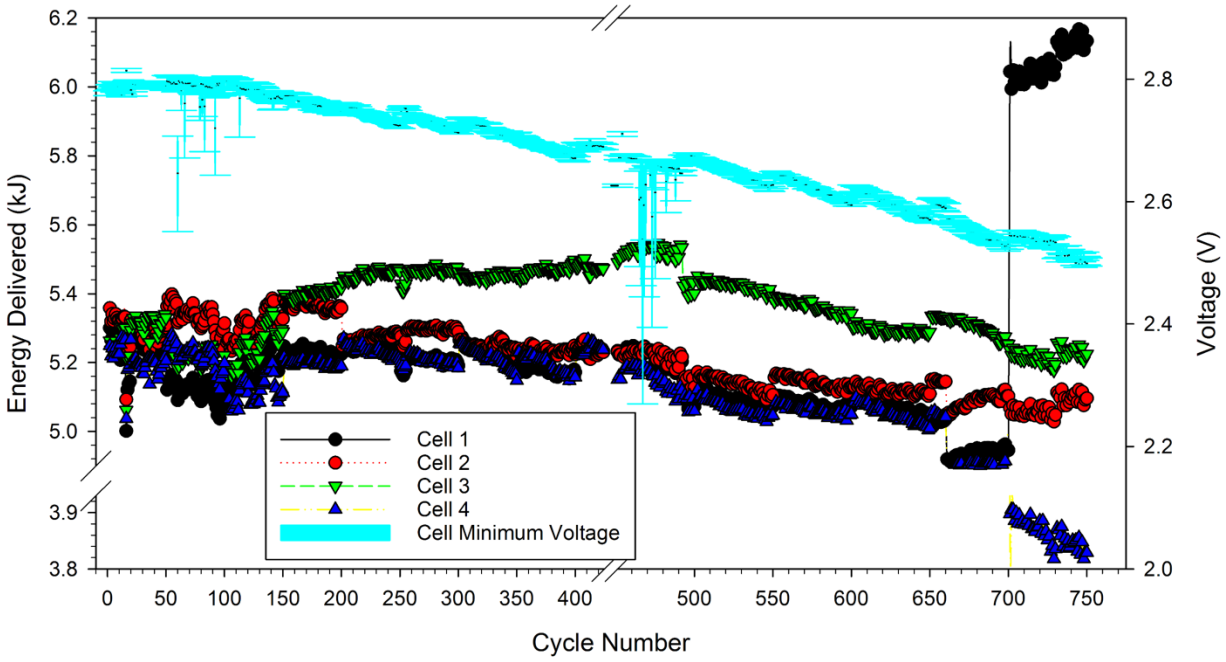

Figure 4.24. Energy delivered to the electronic load per cycle per cell with the minimum cell voltage in the baseline 4P1S array. End of life reached at 750 cycles.

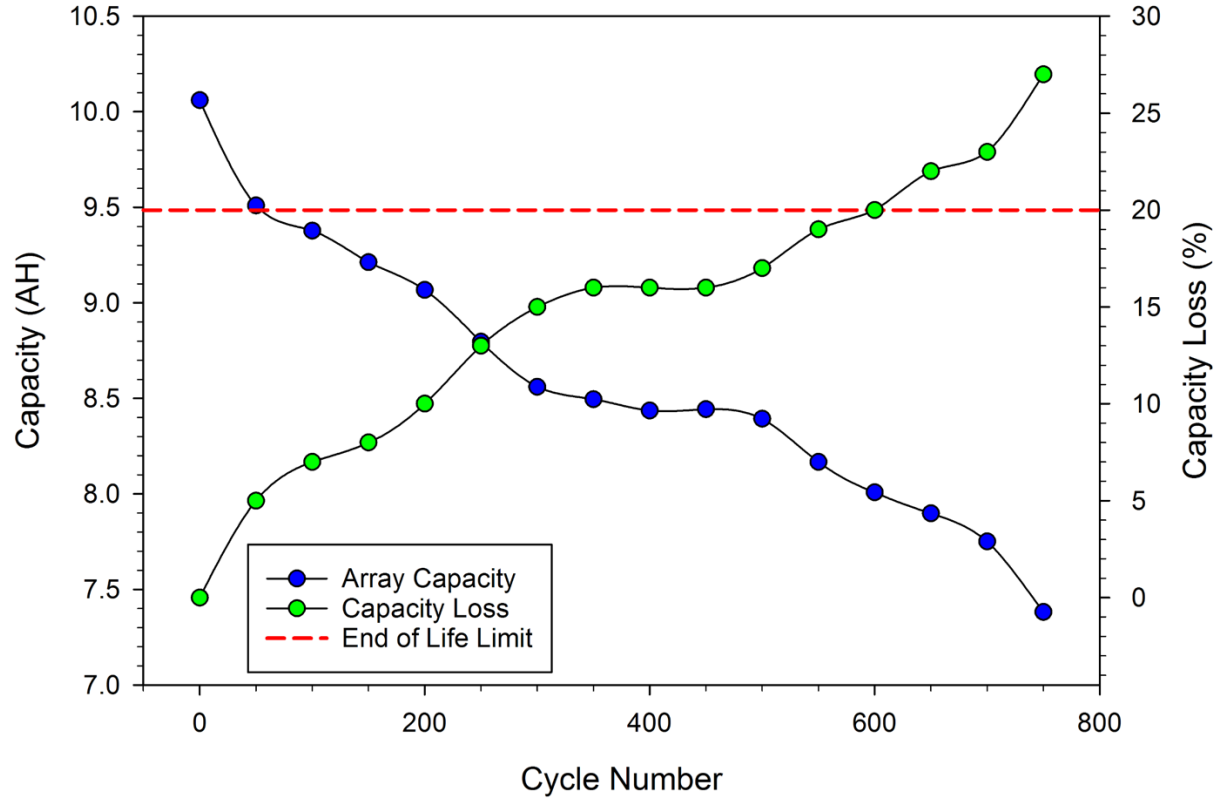

Figure 4.25: Capacity as function of cycle number with the loss in capacity as a percentage of the original measured capacity for the baseline 4P1S array

The temperature response of each cell in the array is shown in Figure 4.26, with each of the three thermocouple locations. From the data, both the thermocouple at the top of the cell and the one at the bottom of the cell show the lowest peak temperature for the entire experiment, and are approximately equal in value with the bottom thermocouple slightly lower overall. The bulk of the heating appears to be in the middle of the cell, which is consistent with knowledge of cell construction. The top and the bottom of the cell do not have the jellyroll structure. Instead, they are comprised of the current conductors for the anode and the cathode and do not have a thermally conductive path for large amounts of thermal energy transfer to the surface. All of the cells in the array have a less than 10°C rise for the entire experiment.

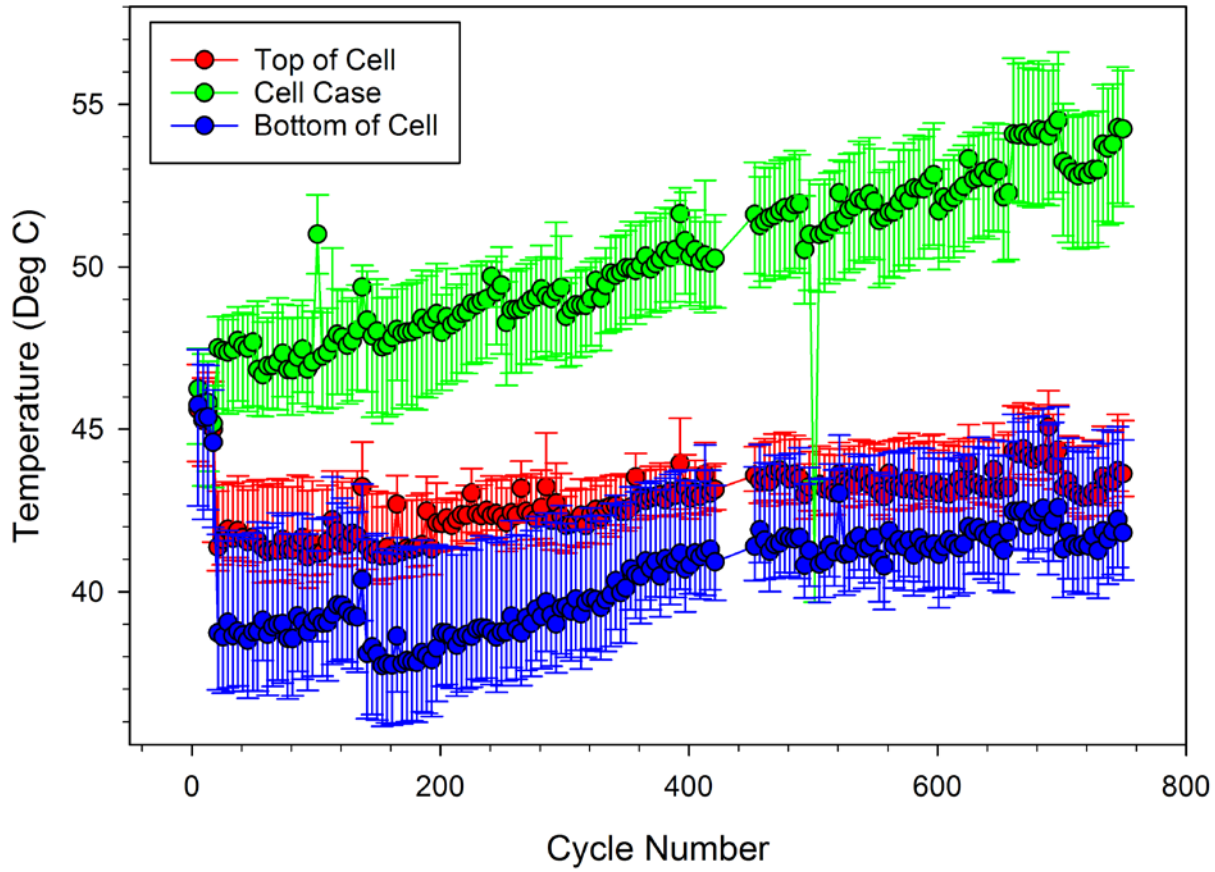

Figure 4.26: Maximum cell temperature as a function of cycle number for all three thermocouples in the baseline 4P1S array

4.4.3 EIS Data Analysis for Baseline 4P1S Array

As previously discussed, the four cells in the baseline parallel array were selected to have an overlapping EIS spectra from greater than 1 kHz (intersection with real axis) to 0.1 Hz. Figure 4.27 shows how as the array was cycled the EIS spectra diverged from the previously overlapping curves. At the end of 150 cycles, there is a shift on the real axis but it appears the general shape is consistent for all of the cells. This would be consistent with the data shown in Figure 4.24, as the energy delivered to the load per cell per cycle is approximately the same within an acceptable variance margin, and the hypothesis is upheld. A depression in the semi-circle shape as the cycle number increased would indicate a growth in frequency-dependent factors that have the effect of increasing the impedance of a cell.

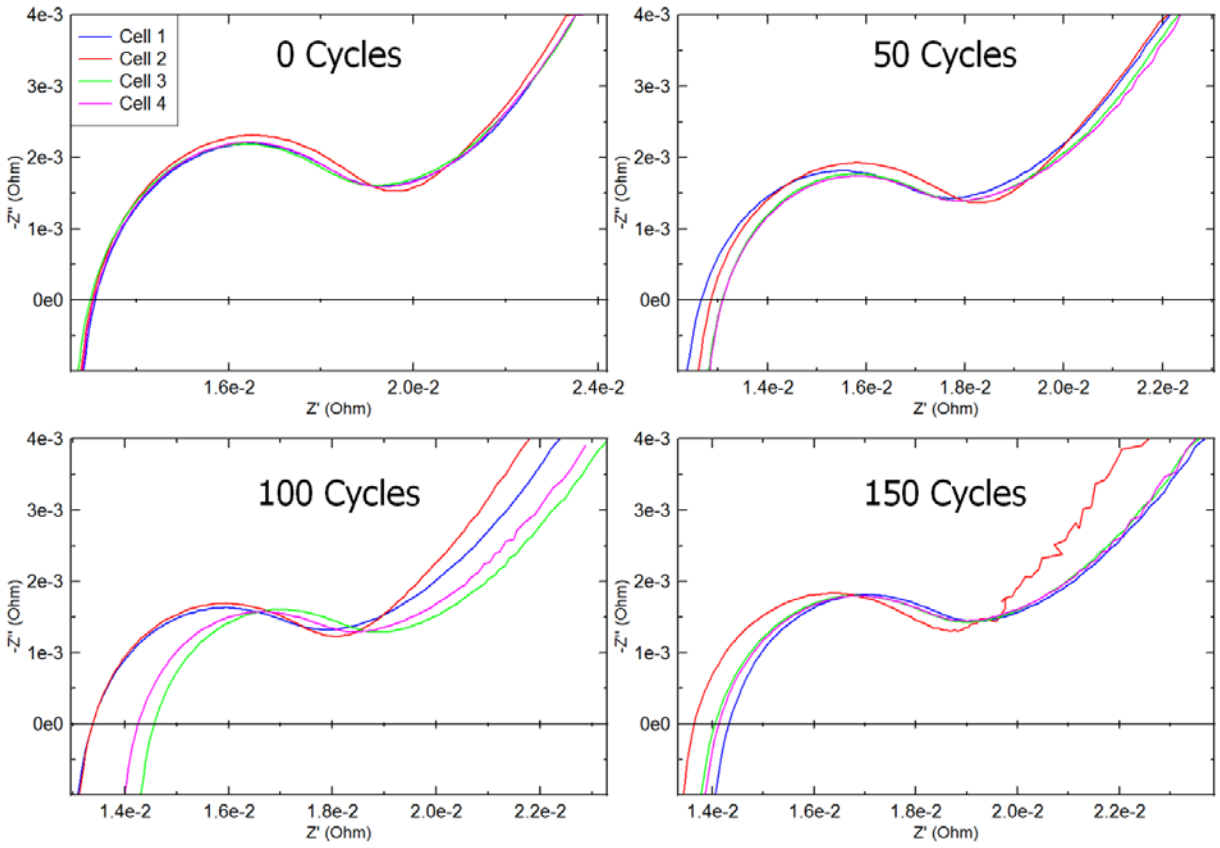

Figure 4.27. Individual EIS spectra for the four cells in the baseline parallel array as a function of cycle for the first 150 cycles at 50% SOC.

However, as shown in Figure 4.27, after 150 cycles the Nyquist plots have started to diverge and the cells no longer have identical impedance responses. In Figure 4.28 the EIS spectra is shown for every 200 cycles from 0 – 600 cycles, and the trend is observed to continue with the impedance response different for each cell. After 200 cycles, the diffusion region for all of the cells is nearly identical, with approximately the same slope. After 400 cycles, however, Cell 2 has a distinctly different slope in the diffusion region. This does not appear to affect discharge performance, and may just be a symptom of aging in the cell. The overall shape in the charge transfer kinetics region appears to be the same for all of the cells for the 600 cycles recorded.

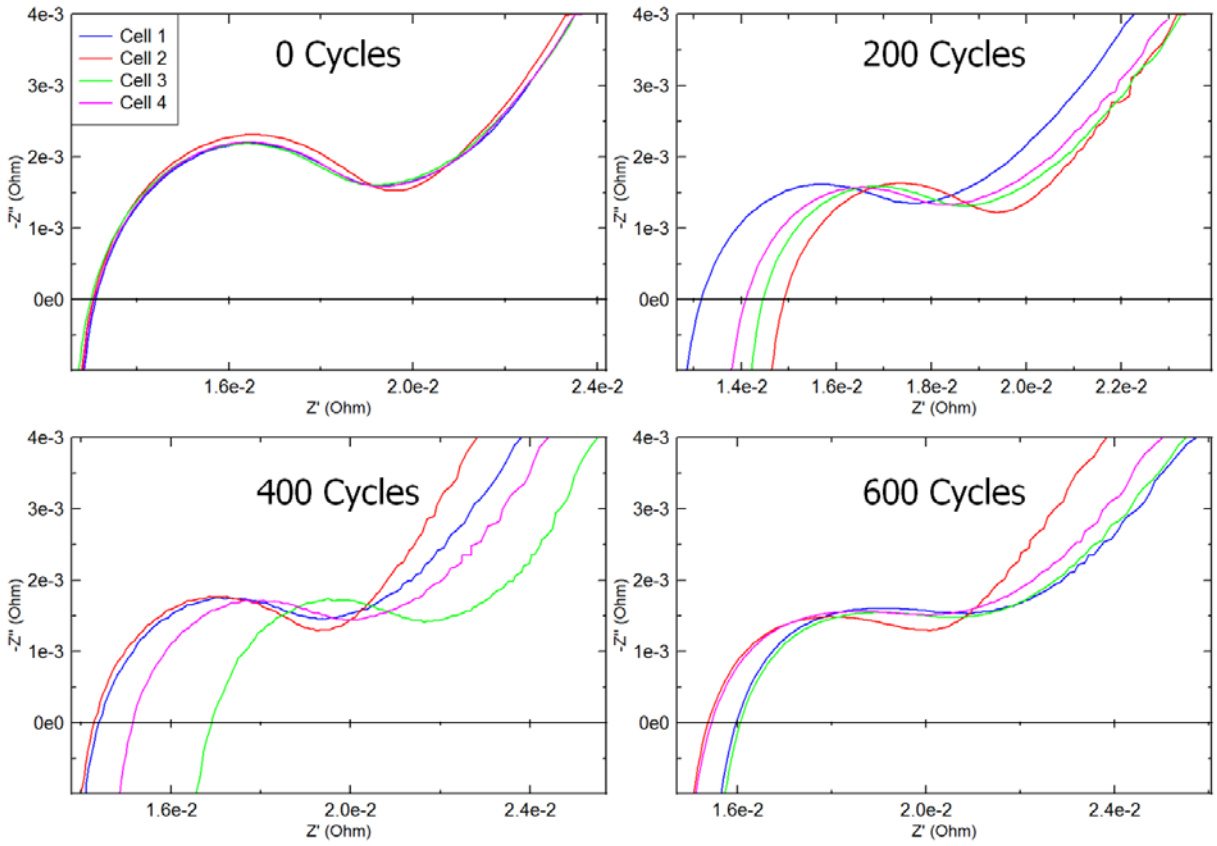

Figure 4.28. Individual EIS spectra for the four cells in the parallel array as a function of cycle at 50% SOC.

A plot of the aggregate EIS spectra is shown in Figure 4.29. This data is collected when all four cells were connected in parallel, and a galvanostatic EIS sweep performed. This data was normalized to zero for ease of comparison, as the real impedance changed significantly over time as the probes were repeatedly inserted and removed. In general, the diffusion region appears to be

relatively similar across all of the cycles sampled, with no deflections to the right or left of the main body of data. The charge transfer kinetic regions for the first 350 cycles also have approximately the same shape, indicating relatively healthy SEI layers for the cells. At the 400 cycle mark, a depression begins to appear in the semicircle region. It appears a change in the fundamental time constant for this region is occurring, with a progressive decrease in the peak value of the semicircle. It is likely the SEI layers are starting to show signs of aging. Near the end of the experiment, Cycles 700 and 750 show a sudden change from the typical shape, failing to follow the "trough" pattern established by all of the other spectra. This likely indicates a substantial change in the character of the electrochemistry of the cell, and a sign that further testing should be discontinued.

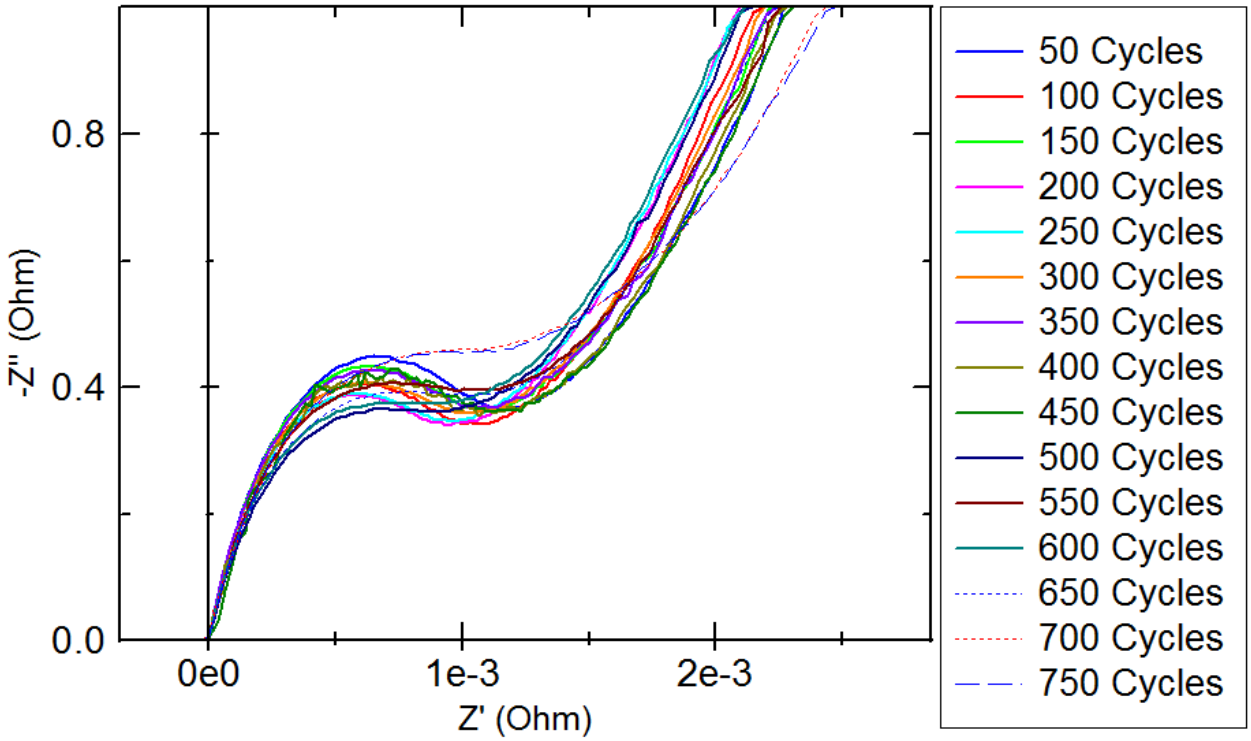

Figure 4.29. Normalized aggregate EIS spectra for the four cells in the parallel array as a function of cycle at 50% SOC.

Based on the single-cell data shown in Figure 4.30, it appears the aging of the SEI layer is being artificially accelerated by placing the cells in a parallel array. The imaginary impedance at 158 Hz follows the initial progression shown in Figure 4.18, with -1.9 mΩ (median) at 0 cycles

and -1.35 mΩ (median) at 100 cycles. The divergence occurs at 450 cycles on the parallel data, with an imaginary impedance of -1.35 mΩ. The drop to this value does not occur on the single cell data until at the earliest 775 cycles (single cell) and 900 cycles (median value). Since the controllable conditions are the same for both tests (pulse discharge rate, recharge rate, environment), one must conclude that the changes observed in the 158 Hz response must be related to changes in the SEI layer.

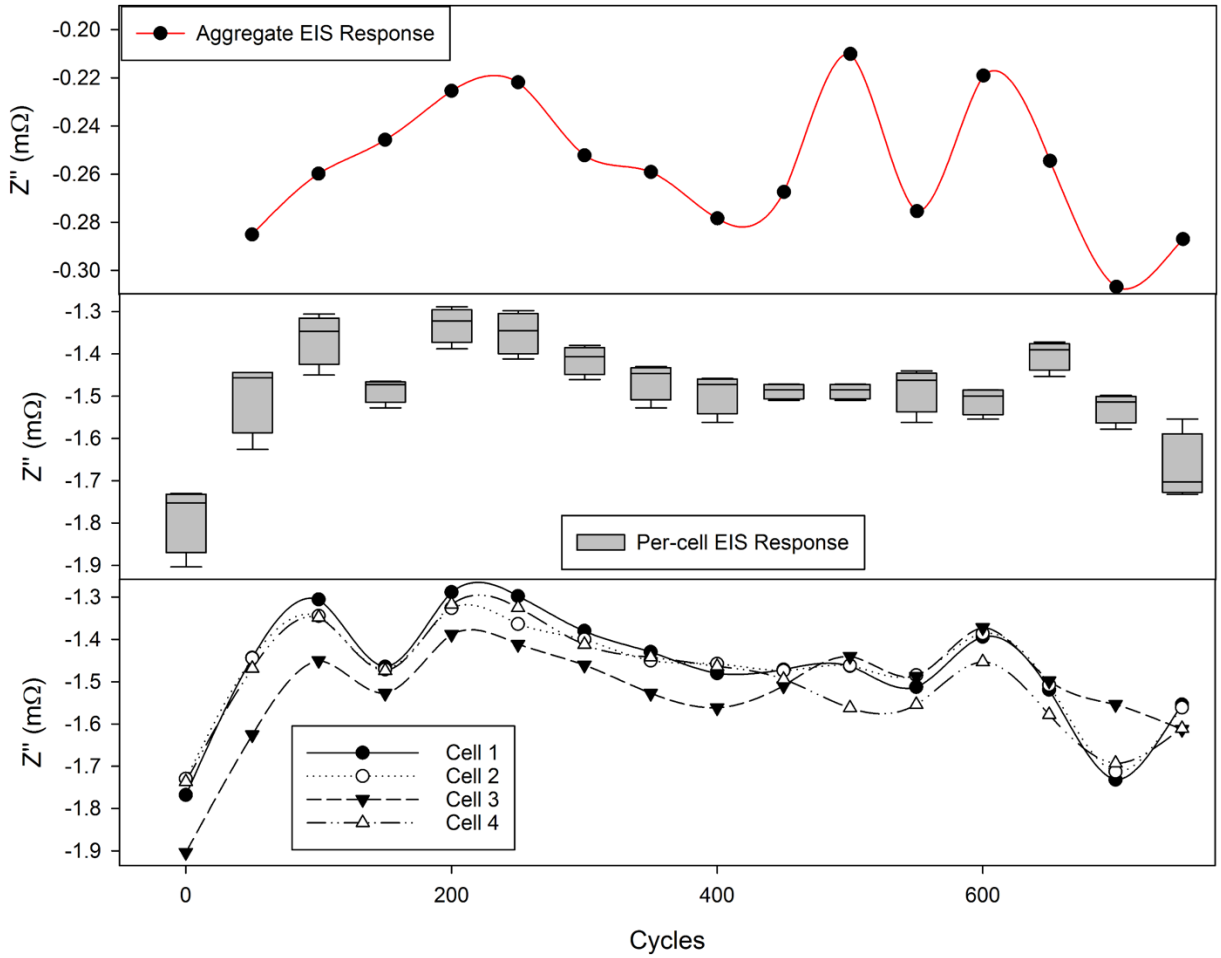

Figure 4.30. Imaginary impedance response at 158 Hz as a function of cycle for all four cells in the parallel discharge array, with aggregate response (top), and individual cell statistics (bottom).

The aggregate EIS data shown in Figure 4.30 follows the general trend of the single-cell data until Cycle 450, when the aggregate imaginary response for the array begins to oscillate. Under initial examination when compared to the flat response shown in the single-cell data for Cycles 450-600, it is unclear why the response with all of the cells in parallel has a sudden periodic quality

as a function of cycle. However, if one looks at Figure 4.24, there is a sudden drop in the energy delivered to the load for all of the cells at the 450 cycles mark. It is possible that the four cell impedances in parallel have lowered the effective impedance to a point such that other effects in the batteries may suddenly dominate the response. Temperature effects are believed to be negligible, as the array was discharged and interrogated in a thermal chamber held at 25°C, and the array was allowed to equilibrate to ambient for at least twelve hours prior to measuring the EIS spectra. Based upon this data, it appears the EIS single-frequency health diagnostic may be more sensitive to battery SOH in the parallel-cell mode than in the single-cell mode. In this case, it appears the power fade aging phenomenon was detected prior to the electrical data observations. Since this is only one data point, replication of the experiment is necessary.

The convergence of the imaginary and real impedance values in the paralleled cells can be explained by the stabilization of the SEI film in each one. Cells which have a higher impedance initially most likely have a more developed SEI film on the surface of the graphite anode. This means that less bare electrode is exposed to the electrolyte solution initially in these cells. Therefore, the impedance will also increase at a slower rate in these cells. On the other hand, the cell with a lower impedance have less developed films and a greater amount of bare electrode exposed. Thus, the potential for impedance increase is higher in these cells initially. As the electrodes in all the cells reach a stable state in SEI development, their impedances equalize and the cells begin to contribute an equal amount of current in the parallel configuration.

4.4.4 EIS Modeling

The creation of a model that can be used to correlate EIS data with physical features is highly desirable, as it may shed light on the performance of the batteries when other diagnostics such as voltage, current, and temperature have proven to be insufficient. To this end, an equivalent circuit model of the EIS spectra for the batteries used in the parallel array was created, and is shown in Figure 4.31. Each simulation had a Chi-squared value of less than 1E-5 to ensure a close fit. The model uses an inductor in parallel with a resistor to model high frequency effects, such as the inductance associated with probe cables and internal battery connections. A series resistor was included to model the contact resistance, and at this time is lumped with the series resistance associated with the electrolyte solution. Since the probes were continuously removed between

each sampling event, it is difficult to determine precisely the difference between changes in the electrolyte and the contact resistance of the EIS probes. Two series ZARC elements follow Rs, with the first one modeling the SEI layer and the second capturing anode effects. Finally, a Warburg open impedance model is used to match the cathode diffusion. A comparison between the measured spectra and the model fit is shown in Figure 4.32, and the initial simulation values are shown in Table 4.1.

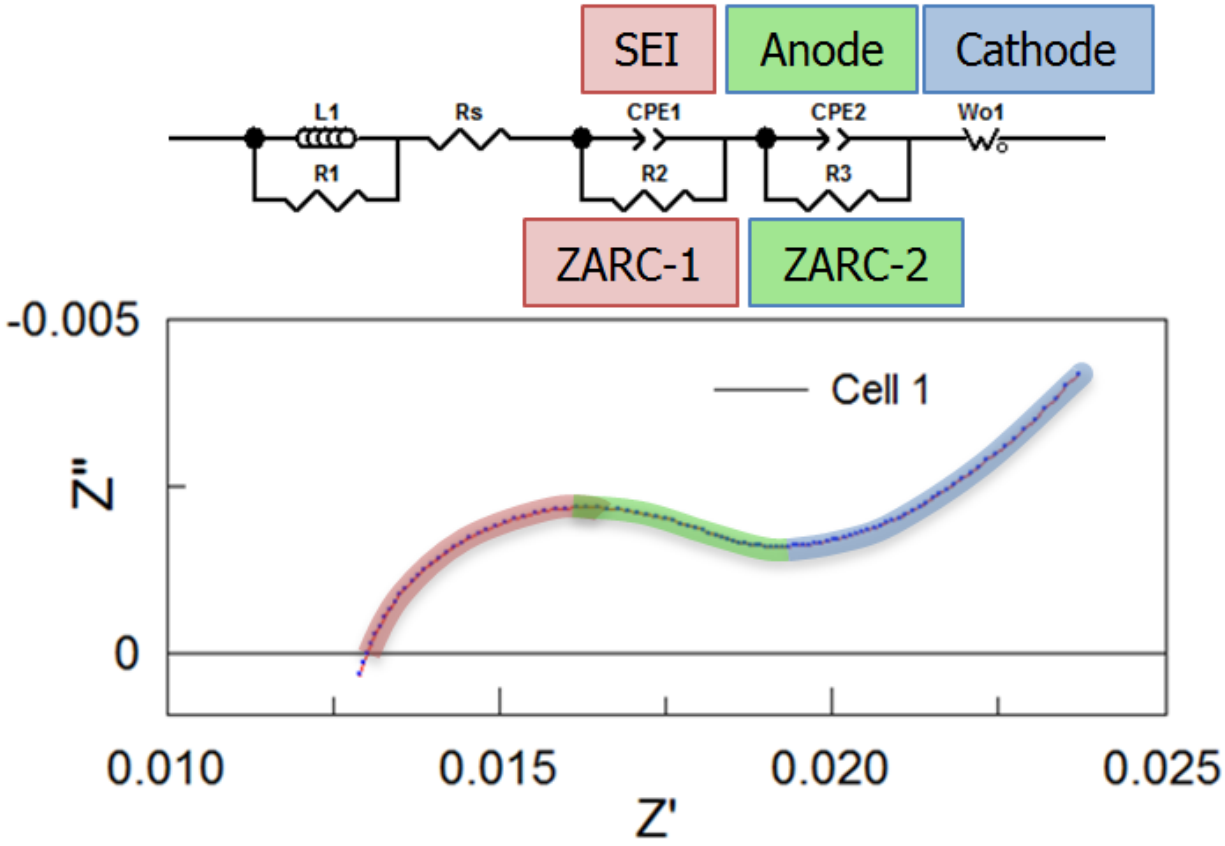

Figure 4.31: Electrical circuit model for EIS spectra

4.4.4.1 Baseline Parallel Array Model

The standard deviations for each of the model elements for each cell in the parallel array are shown in Table 4.2. The inductance element L1 appears to be relatively stable, with σ in the 10-7 range. The low change in L1 would indicate that the change in inductance from the probe cables is negligible, as they were moved frequently between data acquisitions, and the cell components

remained the same throughout the experiment. The resistor R1 had a higher σ than L1, and may be more sensitive to variations in the probe contacts. It is more likely there are high frequency effects outside the scope of this paper. The lumped series resistance Rs had a lower σ than expected, in the range of 10-4. Given that R1 varies substantially more than Rs, it indicates that Rs may represent the solution resistance more than initially believed. The Warburg model appears to change little, with standard deviations for the Wo1-R and Wo1-T variables in the 10-7 range, and Wo1-P in the 10-1 range. This is likely due to the cells always returning to 50% SOC before a spectra is recorded, and also indicates that the cathode is experiencing relatively minor damage from cycling and calendar aging.

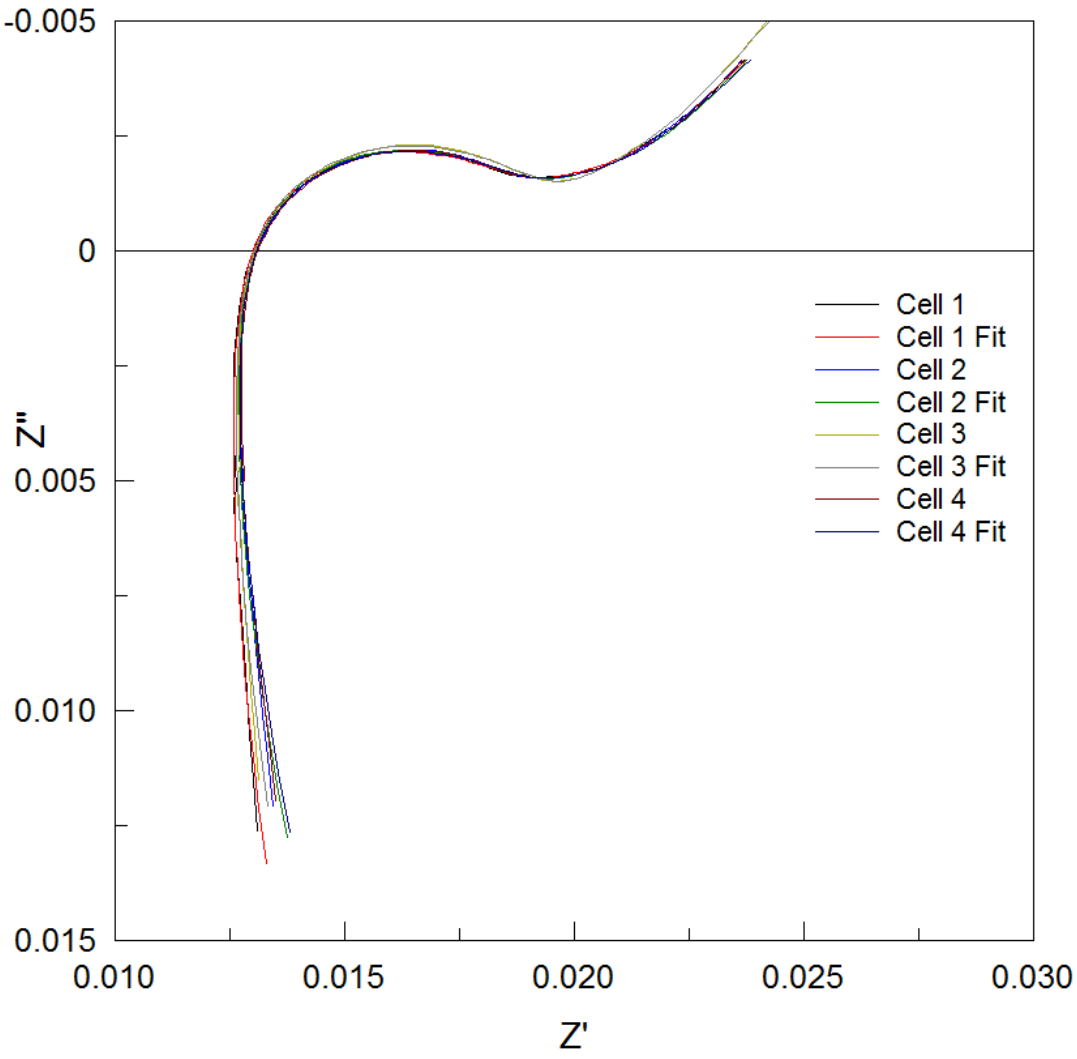

Figure 4.32: Measured EIS spectra for cells in parallel array with fitted data from EIS circuit model

TABLE 4.1: CYCLE 0 EIS SIMULATION VALUES

Parameter	Cell 1	Cell 2	Cell 3	Cell 4
L1 (H)	2.09E-07	2.01E-07	1.91E-07	2.08E-07
R1 (Ω)	2.51E-01	1.64E-01	2.20E-01	1.19E-01
Rs (Ω)	1.23E-02	1.24E-02	1.24E-02	1.23E-02
CPE1-T (s)	1.82E+00	1.75E+00	1.68E+00	2.27E+00
CPE1-P	7.21E-01	7.26E-01	7.18E-01	6.80E-01
R2 (Ω)	6.38E-03	6.39E-03	7.01E-03	6.95E-03
CPE2-T (s)	1.16E+02	1.15E+02	1.89E+02	1.98E+02
CPE2-P	6.51E-01	6.18E-01	6.27E-01	9.44E-01
R3 (Ω)	2.15E-03	2.62E-03	2.58E-03	6.13E-04
Wo1-R (Ω)	3.04E-07	1.11E-07	1.02E-07	3.37E-07
Wo1-T (s)	6.50E-08	5.46E-08	6.89E-08	5.47E-09
Wo1-P	2.85E-01	3.09E-01	3.20E-01	2.50E-01

TABLE 4.2: EIS SIMULATION VALUE STANDARD DEVIATIONS

Parameter	Cell 1	Cell 2	Cell 3	Cell 4
L1	1.62E-08	1.60E-08	1.22E-08	1.78E-08
R1	3.98E-01	1.53E-01	2.83E-01	1.04E-01
Rs	6.75E-04	9.99E-04	6.89E-04	8.31E-04
CPE1-T	7.37E-01	7.11E-01	5.83E-01	6.67E-01
CPE1-P	6.80E-02	5.63E-02	1.17E-01	5.18E-02
R2	1.32E-03	1.25E-03	2.22E-03	1.33E-03
CPE2-T	4.39E+01	4.71E+01	1.44E+02	6.91E+01
CPE2-P	1.45E-01	1.55E-01	1.23E-01	2.18E-01
R3	1.43E-03	7.17E-01	6.90E-01	6.12E-01
Wo1-R	2.34E-07	1.56E-07	3.86E-07	3.83E-07
Wo1-T	1.11E-07	4.89E-08	9.40E-08	5.80E-07
Wo1-P	2.59E-02	1.70E-01	2.69E-01	1.49E-01

The two ZARC elements had the largest changes in standard deviation, and are therefore the most likely elements to examine for correlation between the measured electrical data and cell electrochemical state. The first ZARC element corresponds to the frequencies from approximately 750 Hz to 30 Hz, and can describe the behavior of the SEI layer [14, 99]. As shown in Figure 4.33, the time constant for ZARC-1 changes significantly between Cycle 0 and Cycle 50, indicating the growth of the SEI layer as the battery is cycled. From Cycles 50 – 500, the time constant is approximately flat for all four cells. At 550 cycles, however, Cell 3 has a sudden drop in the time constant. When compared to the energy delivered per cell shown in Figure 4.24, this

corresponds directly to a minor increase in energy delivered from Cell 3 while the other cells remain relatively constant. At the same time, the arc depression factor (CPE-P) for Cell 3, shown in Figure 4.34, changes from approximately 0.6 for Cell 3 at Cycle 500 to nearly 0.9 at Cycle 550. Growth in the time constant starting at Cycle 650 corresponds to the sudden power fade observed in Figure 4.24, and is possible that the SEI layer is increasing in size and inhibiting the Li+ ion charge transfer process. A uniform decrease in the arc depression factor at Cycle 700 also correlates to measured changes in the energy delivered per cell.

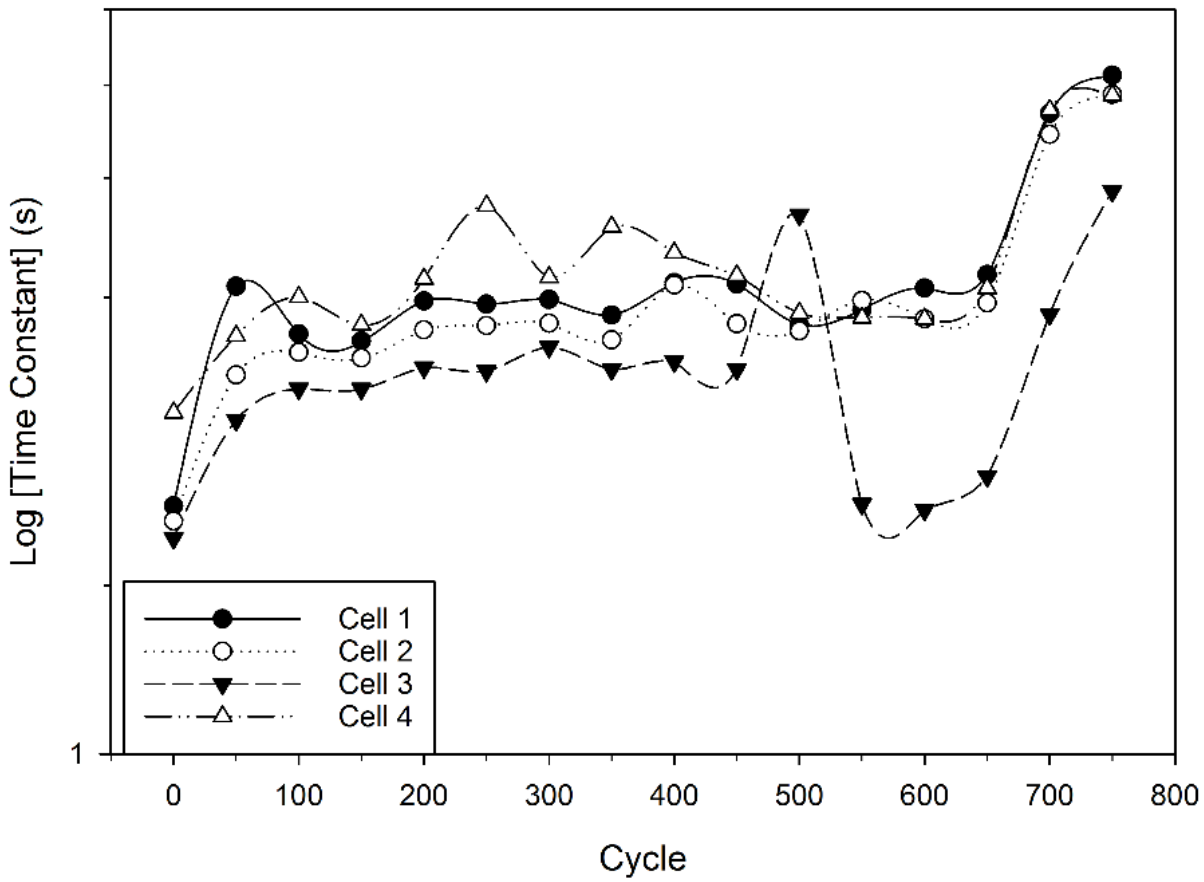

Figure 4.33: Time constant as a function of cycle for the ZARC-1 element in the equivalent circuit model.

The second element corresponds to anode-specific mechanisms. As shown in Figure 4.35, the time constant is relatively flat until Cycle 500, which is to be expected for a properly conditioned new cell. After Cycle 500, the time constant for Cells 1, 2, and 4 decrease while Cell 3 increases slightly. This corresponds to the data shown in Figure 4.24, where Cell 3 increases energy output

while the other three cells have lower total energy output. As the cycle number increases, the time constants continue to follow the trend shown in Figure 4.24, with a final value at end of life reflecting the observed collimation of the energy output from all four cells. The arc depression factor shown in Figure 4.36 oscillates between 0.6 and nearly 1.0 for all four cells until Cycle 500, where Cells 1, 2, and 4 are flat at approximately 0.5 until Cycle 650. Cycle 500 is the first cycle on Figure 4.24 where power fade is noticeable, and the energy slope of all four cells is decreasing as a function of cycle. This would indicate the observed power fade is affected by changes in the anode material.

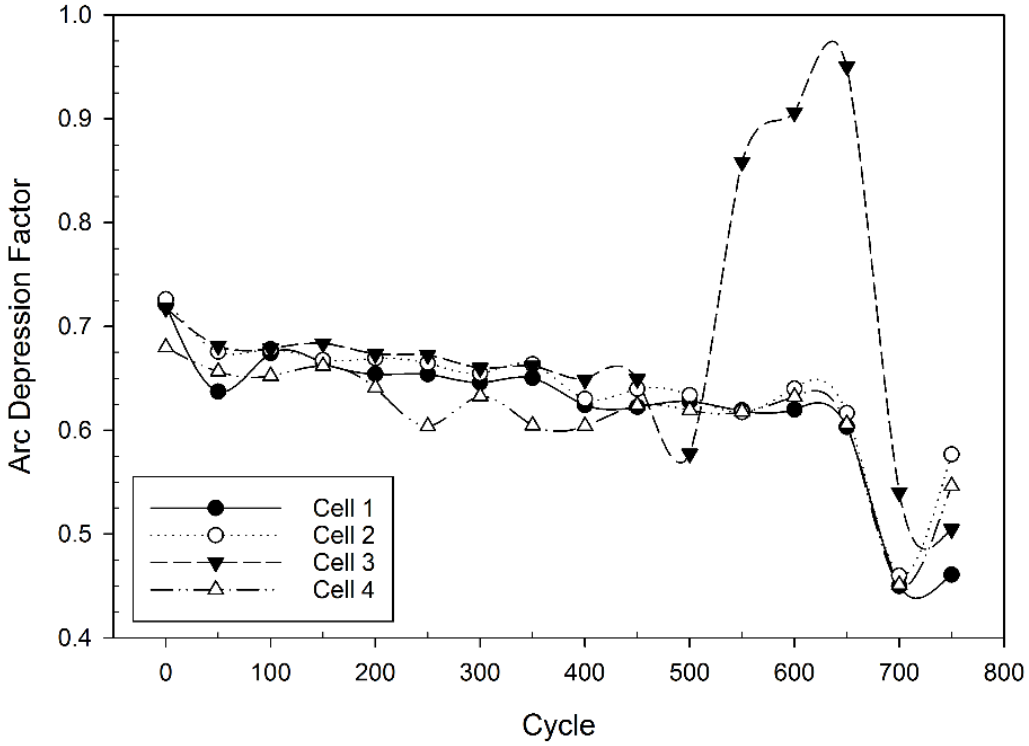

Figure 4.34: Arc depression factor as a function of cycle for the ZARC-1 element in the equivalent circuit model.

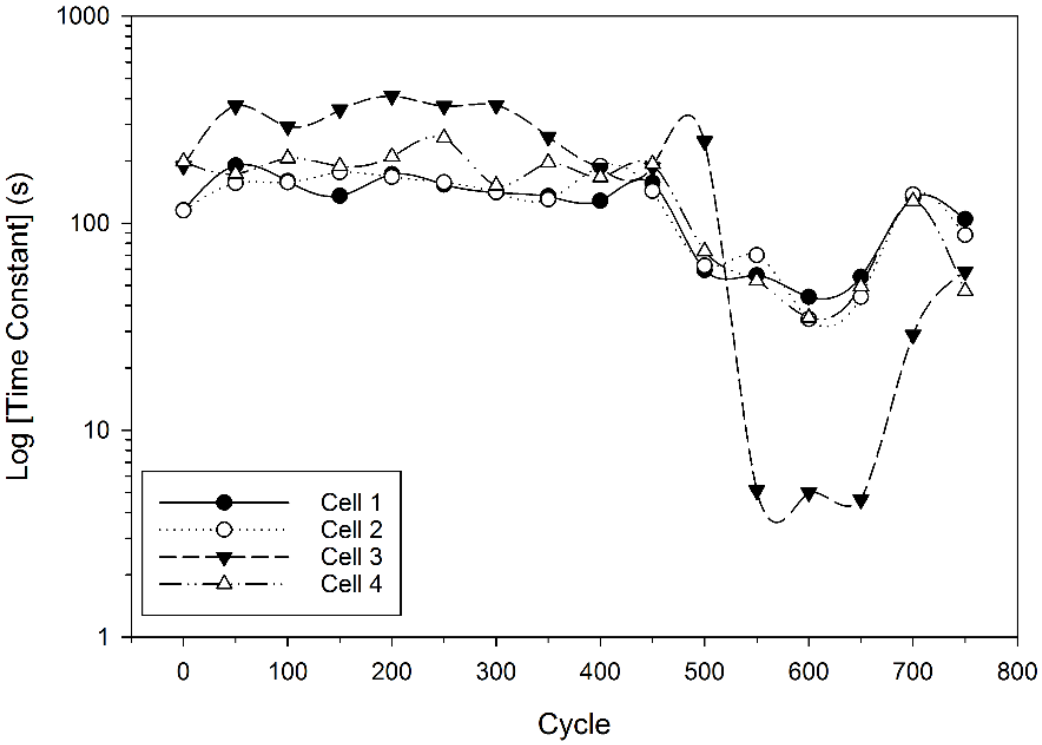

Figure 4.35: Time constant as a function of cycle for the ZARC-2 element in the equivalent circuit model.

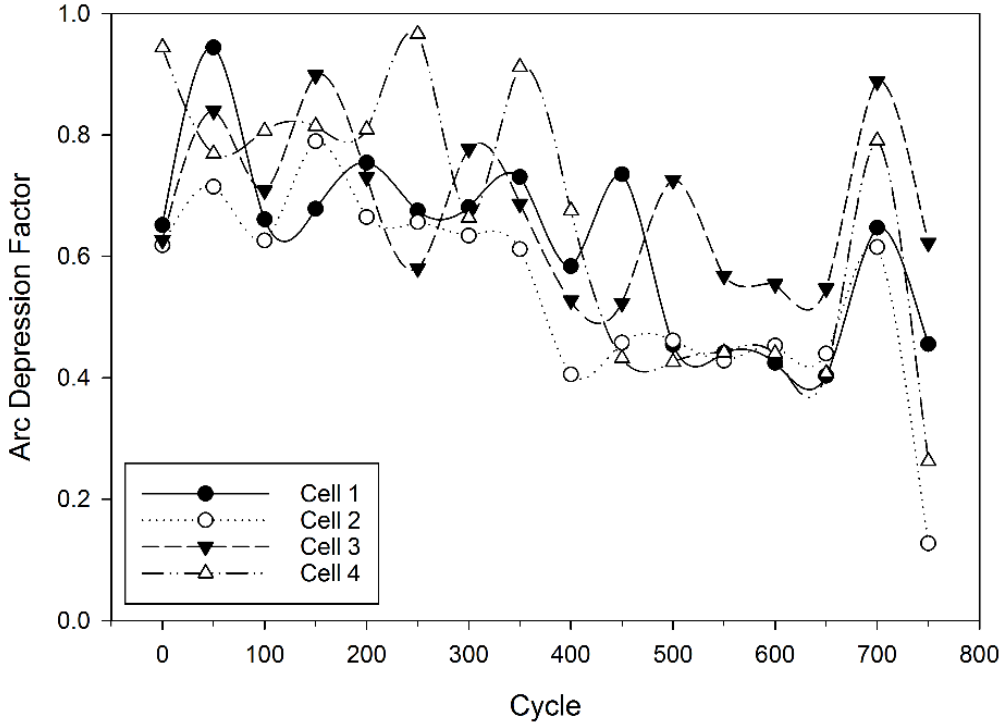

Figure 4.36: Arc depression factor as a function of cycle for the ZARC-2 element in the equivalent circuit model.

Finally, the impedance data suggests that Cell 3 is suspect while the energy data presented in Figure 4.24 appears to show that Cell 3 is actually performing well compared to the other cells in the array. However, examination of the data shown in Figure 4.37 shows that Cell 3 is, in fact, suffering from capacity fade after approximately 300 cycles. The data in Figure 4.37 is the measured current from each cell during the final rest period of the pulse discharge, when the electronic load is disabled. In an ideal battery array, there should be very little current moving between cells as they are all balanced and at the same potential. The data recorded for this array, however, indicate that a recharge event is occurring on Cell 3 from approximately Cycle 250 through the end of life. Cells 1 and 2 appear to source the current that is recharging Cell 3 until Cycle 300, when Cell 2 provides most of the energy to recharge Cell 3. An inflection point is observed at Cycle 300 for Cell 3, as the slope of the current as a function of cycle changes suddenly and the energy to recharge the cell during the rest period continues to increase. Until Cycle 650, Cell 4 remains at a constant level sourcing comparatively little current compared to Cell 1 and Cell 2. This suggests higher source impedance for Cell 4, which is supported by the time constant data for the SEI layer shown in Figure 4.33.

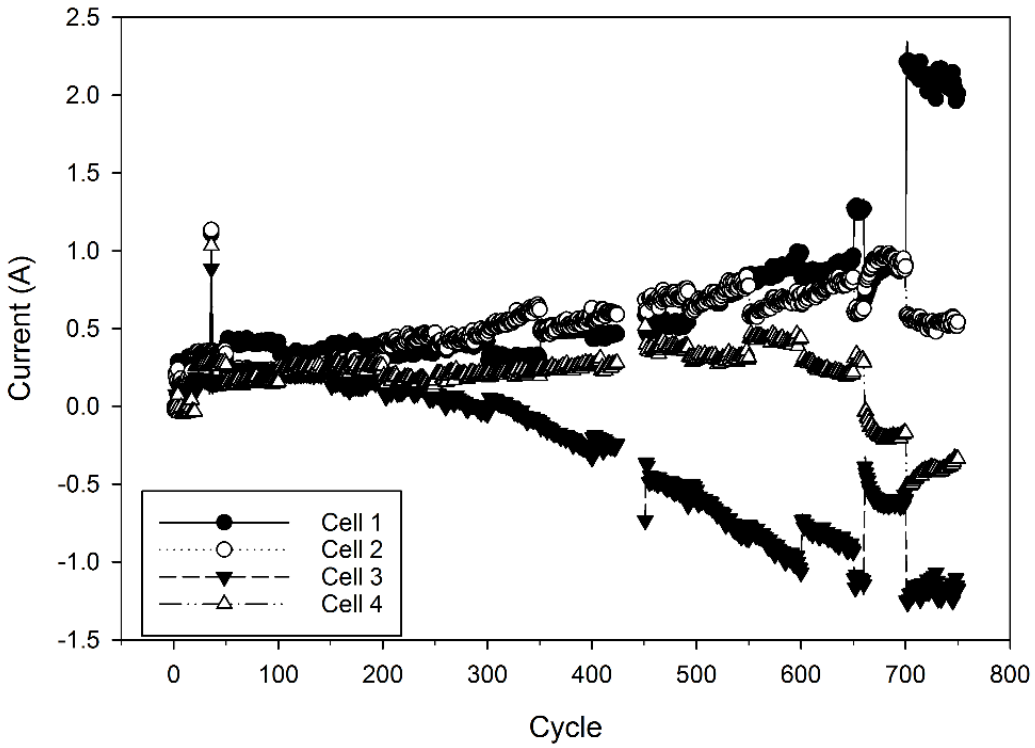

Figure 4.37: Current per cell as a function of cycle on final rest period in pulse discharge (296 s).

4.4.4.2 10C Single-Cell Lifetime Model

The model was applied to the 10C single-cell lifetime data to generate a profile of the electrochemistry under ideal conditions. The time constant for each of the cells as a function of cycle in the ZARC-1 element is shown in Figure 4.38. The time constant appears stable for the first 1025 cycles, with a slight decrease for all of the cells starting at 1050 cycles. This would be consistent with the literature stating the SEI layer is a primary driver of capacity fade. The large variance seen across the cells for the first 500 cycles is likely due to the differences in cell construction. In single-cell operation, this does not appear to affect performance of the cell.

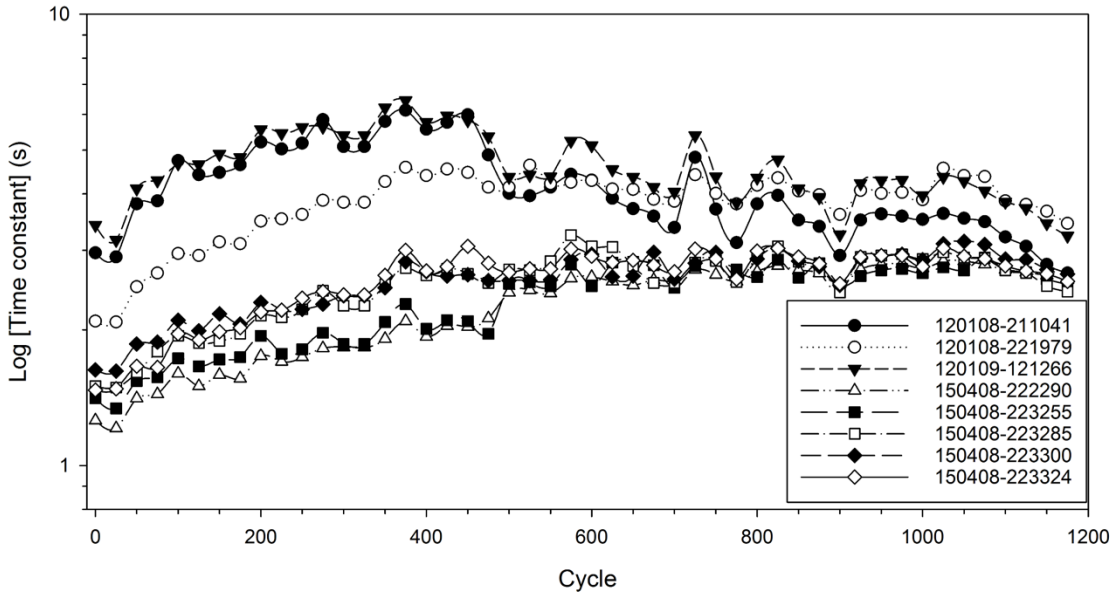

Figure 4.38: Time constant as a function of cycle for the ZARC-1 element for the 10C single-cell lifetime experiment

The ZARC-2 time constant is shown in Figure 4.39 for all of the cells in the experiment. Unlike the SEI layer model, the values for the anode material appear to be stable for the entire life of the cell. The deviant values are most likely due to errors in the measurement or numerical anomalies in the model, and do not reflect real changes in the electrochemistry.

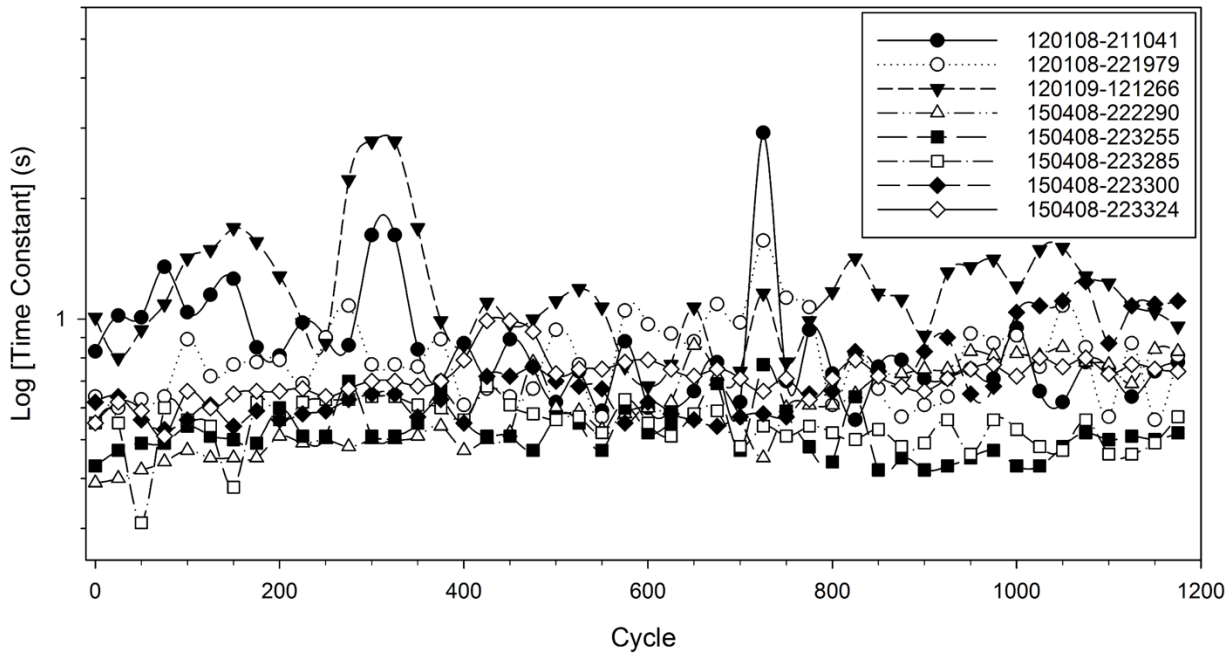

Figure 4.39: Time constant as a function of cycle for the ZARC-2 element for the 10C single-cell lifetime experiment

4.5 Parallel Array Replicants

Four replicant 4P1S arrays were constructed to evaluate the performance observed in the baseline 4P1S array discussed in the previous section. The major difference between the replicant arrays and the baseline array is the level of filtering performed prior to insertion into the arrays. With the baseline array, the intent was to build the best possible matched system and evaluate with a specified test protocol. In the replicants, the objective is to determine the impact of the EIS filtering process on the performance of the arrays. Thus, only the 1 kHz ESR and capacity filters were used to choose cells from the experimental data set. One additional modification was using only thermocouples attached to the body of each cell, as shown previously the top and the bottom temperatures are much lower than the bulk of the battery.

4.5.1 Analysis of Replicant 4P1S Array #1

The capacity loss data is shown in Table 4.3 for Replicant Array #1, which was recorded after 450 cycles on the array. With the standard cut-off limit of 20% capacity loss, it is clear that the array was operated beyond the typical end of life conditions, with nearly 30% capacity loss on Cell

4. Given the data in the table, it is likely the array reached end of life around 400 cycles, and potentially earlier.

TABLE 4.3: REPLICANT ARRAY #1 CAPACITY DATA

Cell Position	Cell Serial Number	Original Capacity	Capacity at 450 Cycles	Capacity Loss (%)
1	150408-224219	2.48	1.80	27.42
2	120108-211117	2.40	1.82	24.25
3	150408-224236	2.51	1.82	27.45
4	120108-210760	2.38	1.67	29.83

The energy delivered to the load per cycle for the first replicant array is shown in Figure 4.40. Unlike the data analyzed in Figure 4.24, the energy per cell had a large variance from the start of testing. It should be noted that the first 15 cycles of current data from this array were recorded improperly by the DAQ, but correct operation of the procedure was verified visually during testing.

First, the minimum voltage per cell per cycle never dropped below 2.5 V during the entire experiment. The negative slope on the approximately linear median voltage is expected and normal for cells that are gradually losing capacity as a function of cycle. In this data, it does not appear to be a correlation between the energy sourced per cell and minimum voltage value. When looking at the energy per cell, it appears that all of the cells have stabilized at an approximately flat level, with minor changes that increase with cycle number. In particular, Cell 2 appears to be limited on current sourcing for the entire experiment, with a negative slope. Cell 4 remains relatively flat, while the remaining two cells adjust their energy sourcing to accommodate the loss in Cell 2.

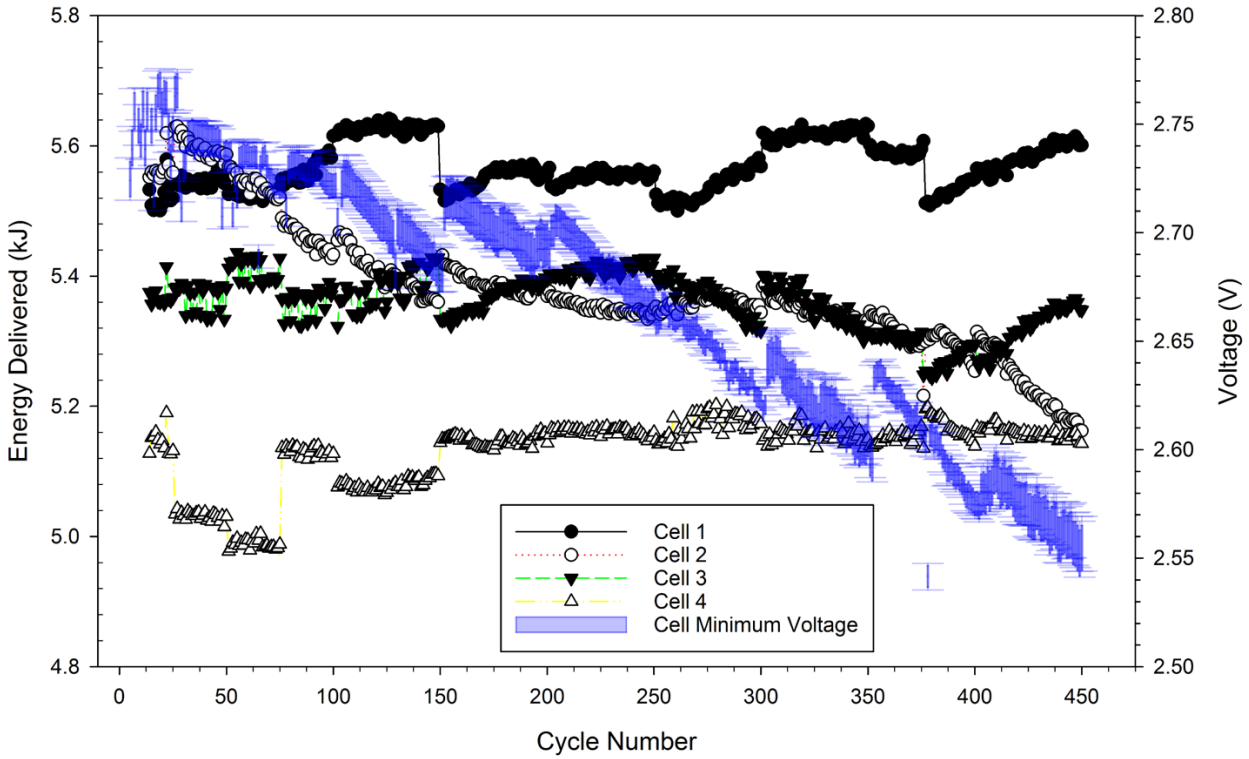

Figure 4.40: Energy delivered to the electronic load per cycle per cell for Replicant Array #1 and box plot of minimum cell voltage per cycle. End of life reached at 400 cycles.

The relationship between the energy sourced per cell per cycle and the terminal capacity measurements is not clear. The cell with the highest capacity loss, Cell 4, sources the least current. An examination of the real impedance at 1 kHz, as shown in Figure 4.41, indicates that the real impedance does not appear to play a factor in the amount of energy delivered to the load. If it did, the impedance for Cell 1 should be consistently lower than the rest of the cells for the entire experiment. Instead, it is approximately even with all of the cells. This is true for the other cells in the array and their observed performance. The real impedance for Cell 2 has a high variance, but given the rapid changes are not reflected in the energy data shown in Figure 4.40 these are likely due to the changes in contact resistance with the EIS probes moving between cell lines.

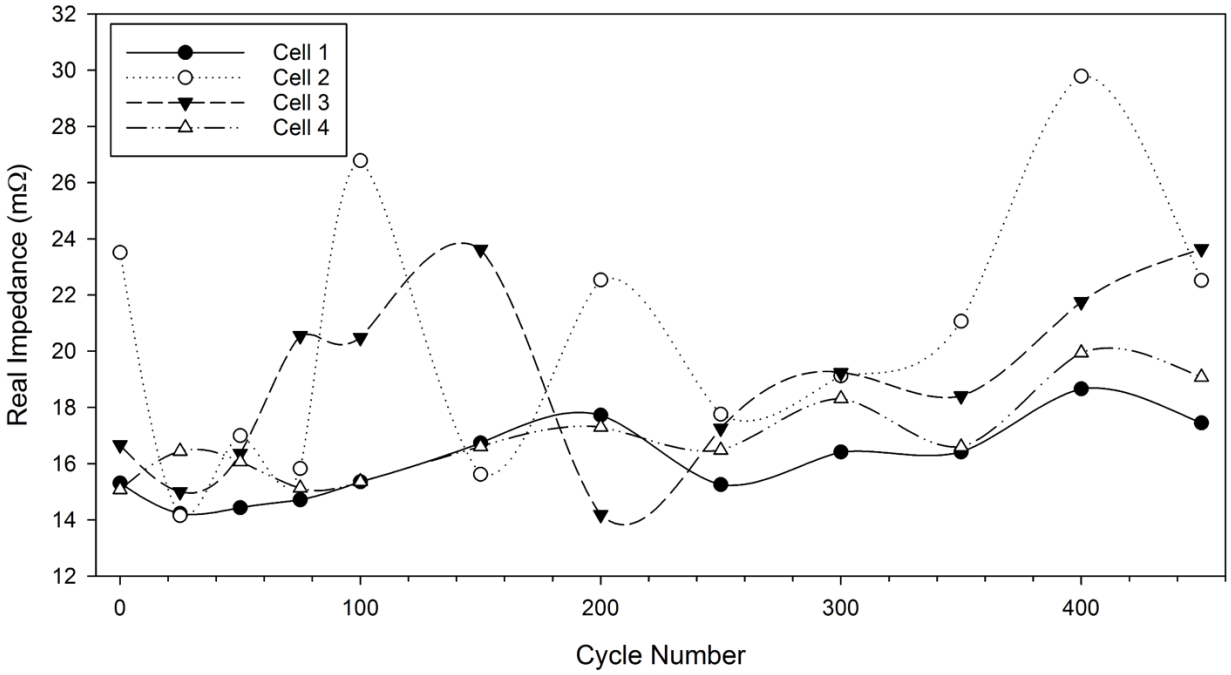

Figure 4.41: Impedance at 1 kHz as a function of cycle for Replicant Array #1

Since the 1 kHz real impedance from the EIS measurements does not offer any insights into the performance of the array, another potential metric to be considered are the thermocouple temperatures, as shown in Figure 4.42. With lithium-based batteries, joule heating (I2R losses) will dominate the thermal process for much of the discharge cycle, with some exothermic heating due to chemical reactions initially causing some heating. However, as long as the cell is operated within its operational limits, any exothermic reactions are limited. This work will assume any heating is joule unless the boundary conditions are exceeded. None of the cells in Figure 4.42 reached a peak temperature higher than the allowable maximum value of 60°C, or the minimum of 0°C.

The first feature to be noted is the sudden drop in thermocouple rise per cycle and the peak temperature at 150 cycles, which matches with the array sitting at rest in the thermal chamber over a weekend, with no activity for at least 50 hours. A second drop in the temperatures is at Cycle 375, where the array was in a resting state for an extended period due to a weekend. It appears if the array is allowed to rest for an extended period, the energy lost to thermal activity is minimized. In general, for the entire experiment the two extreme cells (1 and 4), matched their respective

energy data. The two remaining cells were in between, but not one consistently higher temperature than the other.

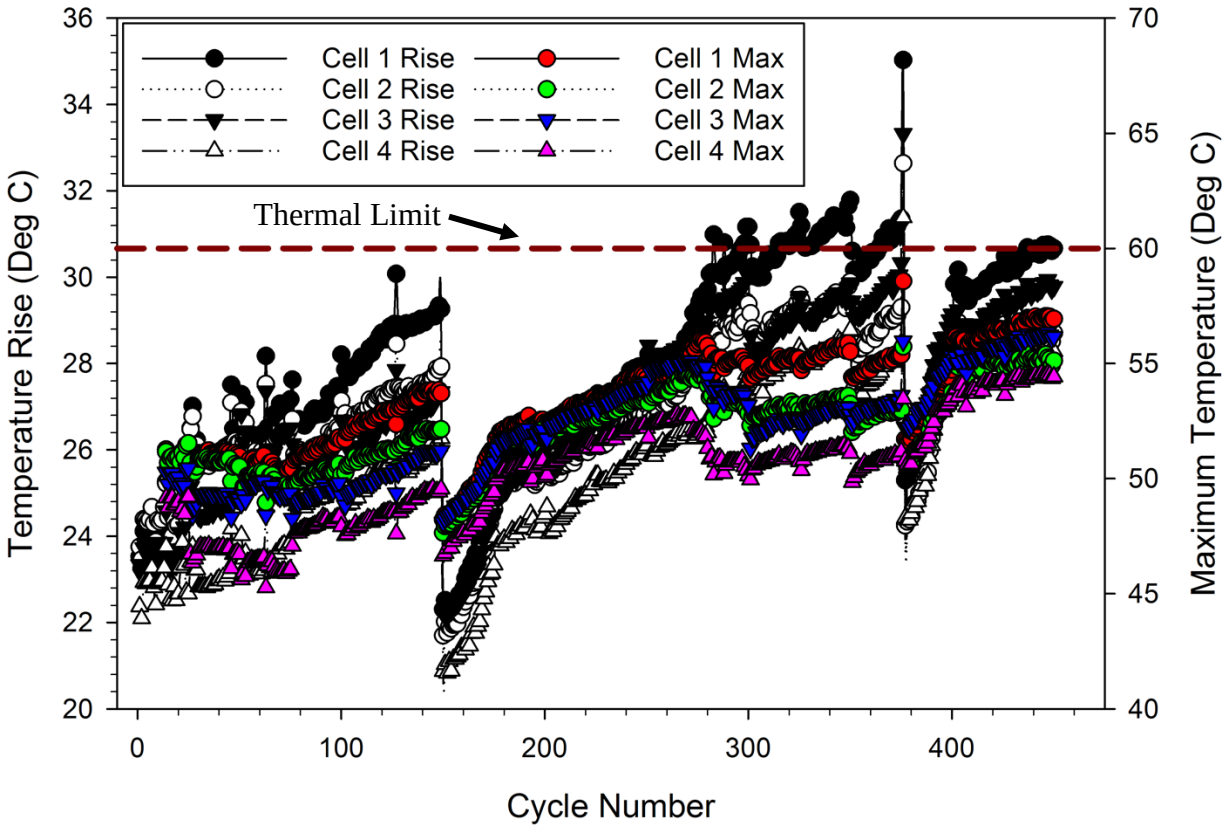

Figure 4.42: Temperature maximum and rise from ambient for Replicant 4P1S Array #1 as a function of cycle.

The EIS spectra for the four cells in this array before testing occurred is shown in Figure 4.43, with the as-measured data on the left, and normalized on the right. Cell 2 appears to have a significantly higher real impedance than the other three cells with an increase of 8.495 mΩ versus Cell 4. This cannot be attributed entirely to the contact resistance of the probes, and is likely attributable to cell construction. On the normalized graph, cells 2 and 3 have the lowest peak value of imaginary impedance on the arc, but this does not appear to have any correlation with performance of the cell as it relates to cycle number or change in capacity.

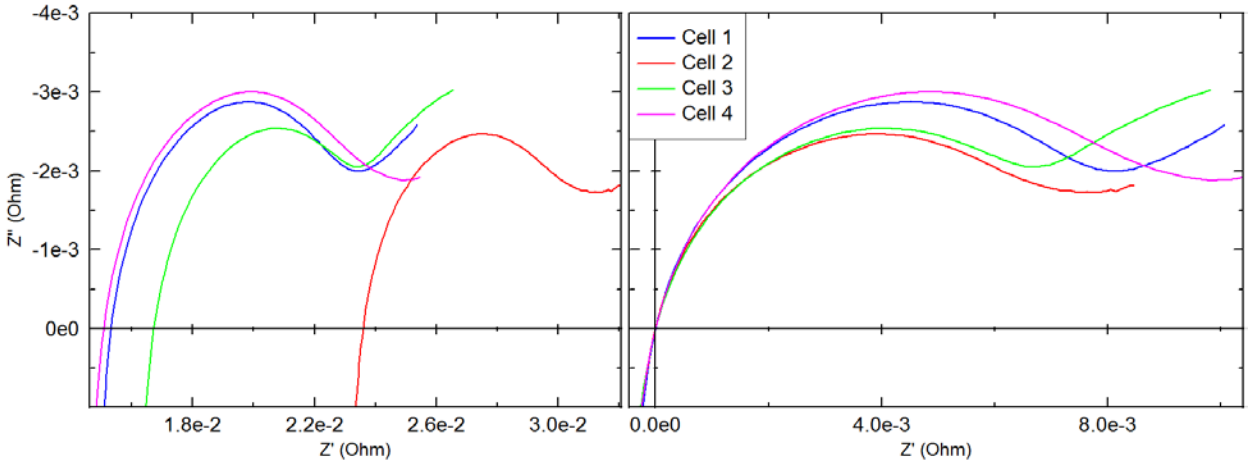

Figure 4.43: Baseline EIS spectra for Replicant Array #1, with as-measured data (left) and normalized real impedance (right)

A breakdown of the EIS response at 158 Hz for the first replicant array is shown in Figure 4.44, with the individual cell response on the bottom, the box plot of that data in the middle, and finally the aggregate EIS response for all of the cells in parallel on top. Unlike the preceding graphs, the individual EIS spectra for each cell matches closely with the end ranking of the capacity for each battery. Cell 2 is at the top of the graph, while Cell 4 is at the bottom. From this data, one could conclude that when comparing multiple cells, a lower imaginary impedance would imply a weaker electrochemical structure in that battery.

From previously discussed measured data, it is known that this battery array was substantially beyond end of life at 450 cycles, which means that it was likely very close to the 80% capacity limit at 400 cycles. Using Figure 4.18 as a reference, it would appear the ideal life cycle for this chemistry is to follow an inverse parabola shape, which can be seen for Cycles 0 – 400. The decrease in imaginary impedance, a crest, and then an increase in impedance seen in Figure 4.44 follows this trend. However, the sudden decrease in impedance after Cycle 400 should be interpreted as an adverse cell performance characteristic, because it falls outside the normal operation. Given the capacity measurements, this conclusion would appear to be correct and would have remove this array from service had it been installed in a deployed system.

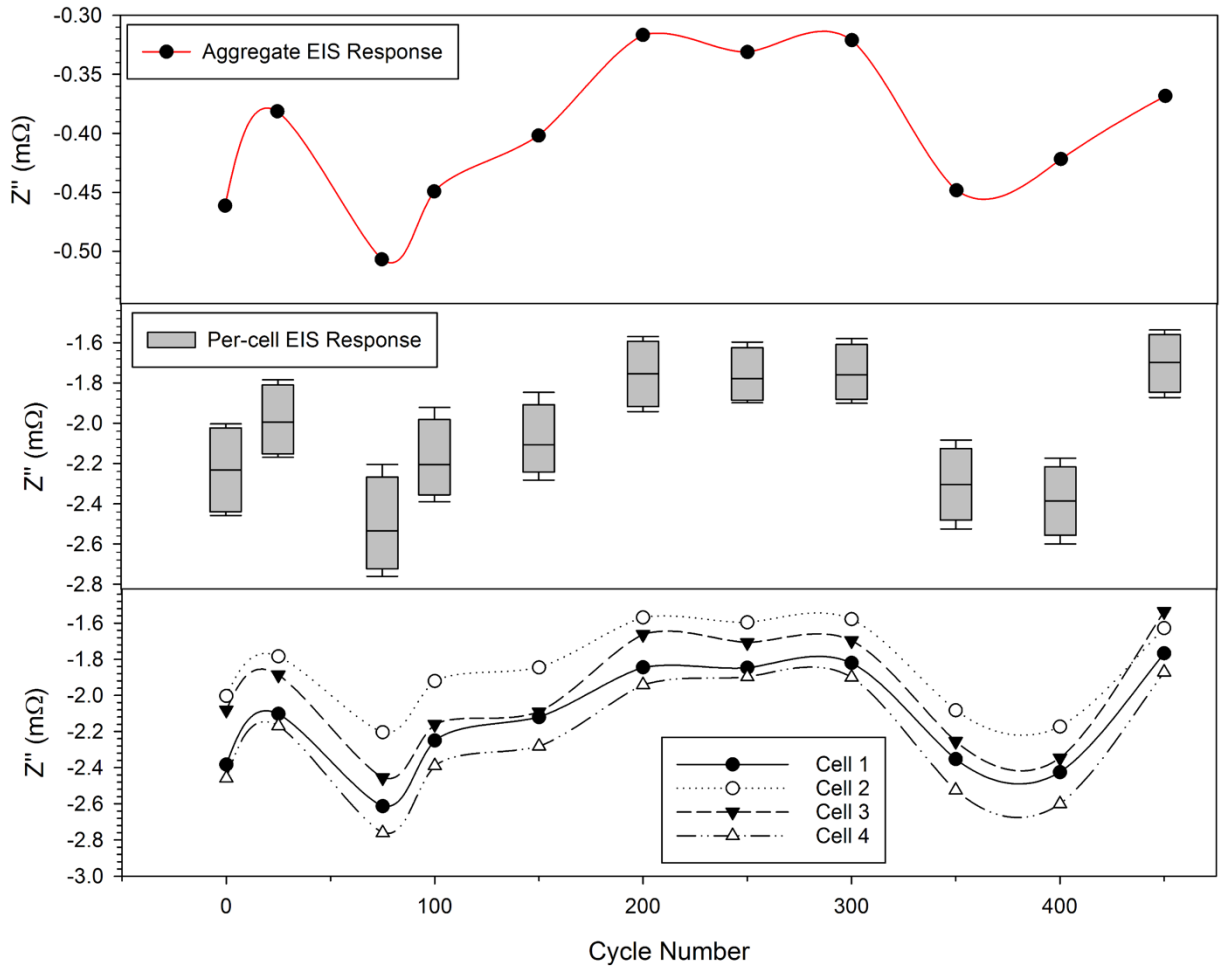

Figure 4.44: Replicant Array #1 single-cell and aggregate EIS data at 158 Hz as a function of cycle

Unlike the aggregate EIS data shown in Figure 4.30, the response of the array as a whole shown in Figure 4.44 reflects the shape seen in the individual cell data. The data in Figure 4.44 is vertically shifted more negative compared to the data in Figure 4.30, which is likely due to the mixed nature of the replicant array versus the tightly filtered data in Figure 4.30. The shift is -0.10 mΩ for the parallel aggregate data, and 1 mΩ for the individual cell EIS data. It can be speculated that the shift reflects an increase in the array impedance for the replicant. The individual cell response is likely marginally affect, however the parallel response is much lower and more sensitive. With the increased impedance on the parallel response, the effects observed with the baseline array are masked and the data reflects the individual EIS response more closely. The ability of the diagnostic to measure all of the cells simultaneously and in situ with a direct

correlation to the individual cell response is a very strong indication that the single-point diagnostic would work for a parallel array.

Using the electrochemical model described in Section 5 of this chapter, the time constants for the SEI layer and the anode for the cells in this array were calculated as a function of cycle. The changes to the SEI layer are shown in Figure 4.45. For this array, the SEI layer appears to be stable through Cycle 250 for all but Cell 2. At that point, the time constant permanently increases in value. The other three cells see this change after 350 cycles, and appears to correlate to changes in the energy delivered to the load. The anode model, shown in Figure 4.46, indicates that changes in the material also occur at the 250-cycle mark. All four cells change their values to some degree, with cells 1 and 2 showing the most change. At 400 cycles, the Cell 4 time constant increases from about 1 to 4 seconds. The decrease in time constant for cells 1 and 3 is reflected in Figure 4.40 with the sourcing of more current.

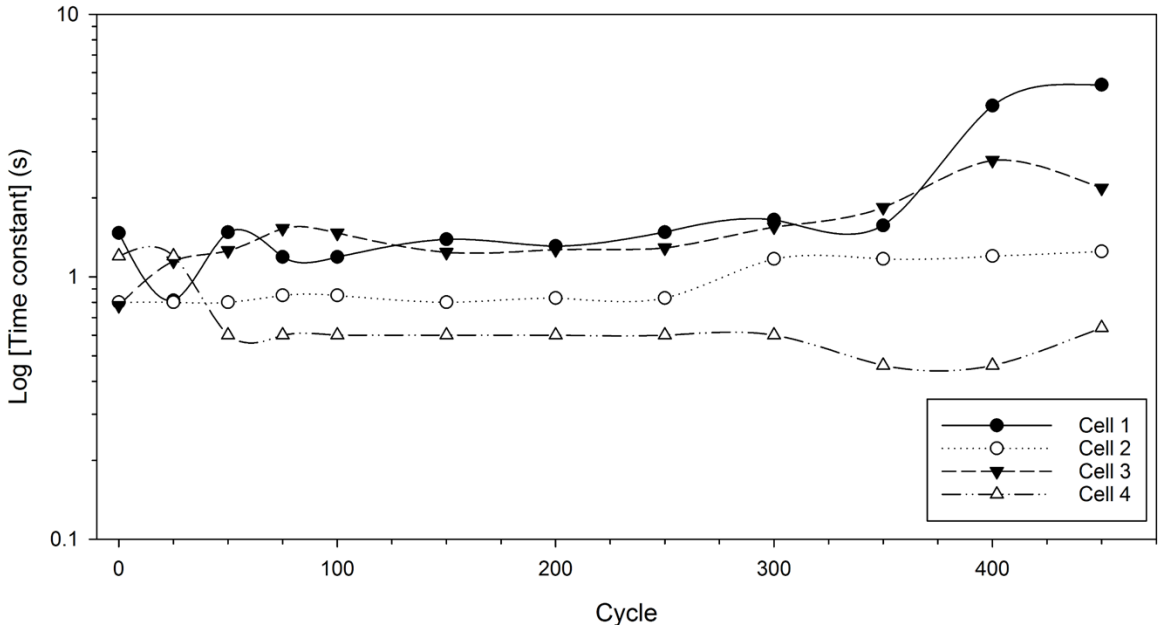

Figure 4.45: Time constant for the SEI layer model for Replicant Array #1

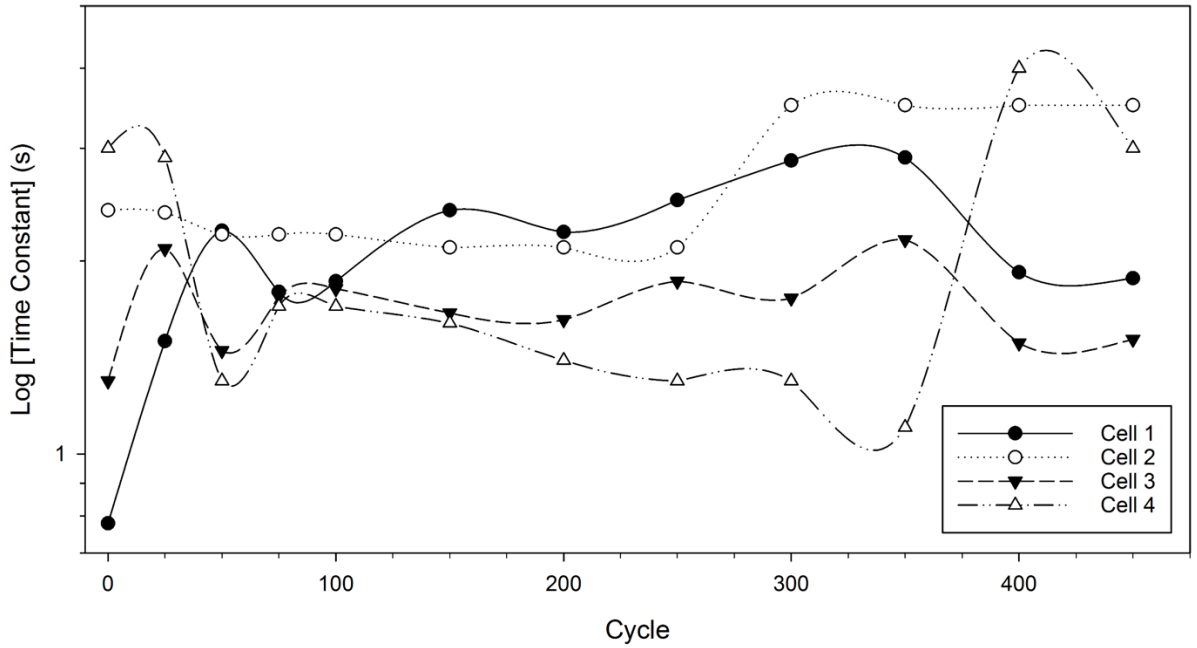

Figure 4.46: Time constant for the anode material model for Replicant Array #1

An examination of the available data allows for some conclusions to be made on this specific experiment. There appears to be a correlation between the EIS spectra of the cell with a baseline real-axis intercept with the highest value (Cell 2) sourcing the most current during the first cycle. When comparing the magnitudes of the imaginary impedance, the same cell has the lowest impedance value. However, this same cell loses energy delivered to the load each cycle. Cell 1 has the largest imaginary impedance value as well as the lowest real-axis intercept of the four cells. This cell consistently delivers the most energy to the load after the first discharge cycles.

4.5.2 Analysis of Replicant Array #2

The capacity measured at 450 cycles for Replicant Array #2 exceeded the 20% loss limit with an average loss of more than 30%, as shown in Table 4.4. The loss of over 36% of the original capacity by the first cell in the array is particularly concerning, as it is likely approaching an unstable electrochemical limit. It is likely given the data shown in Table 4.4 that this array reached end of life before 400 cycles.

TABLE 4.4: REPLICANT ARRAY #2 CAPACITY DATA

Cell Position	Cell Serial Number	Original Capacity (AH)	Capacity at 450 Cycles (AH)	Capacity Loss (%)
1	120108-222318	2.54	1.61	36.53
2	150408-224199	2.52	1.79	29.08
3	120108-210887	2.34	1.55	33.91
4	120108-210518	2.42	1.57	35.02

The energy delivered to the electronic load as a function of cycle is shown in Figure 4.47. As with the data analyzed for Replicant Array #1, the variance compared to the baseline array as quite large, however Cells 1, 3, and 4 had relatively low variance in that subset. Only Cell 2 appears to have sourced significantly more energy than the other cells in the array. As with the previous replicant array, the energy delivered per cell is relatively flat for the entire experimental period.

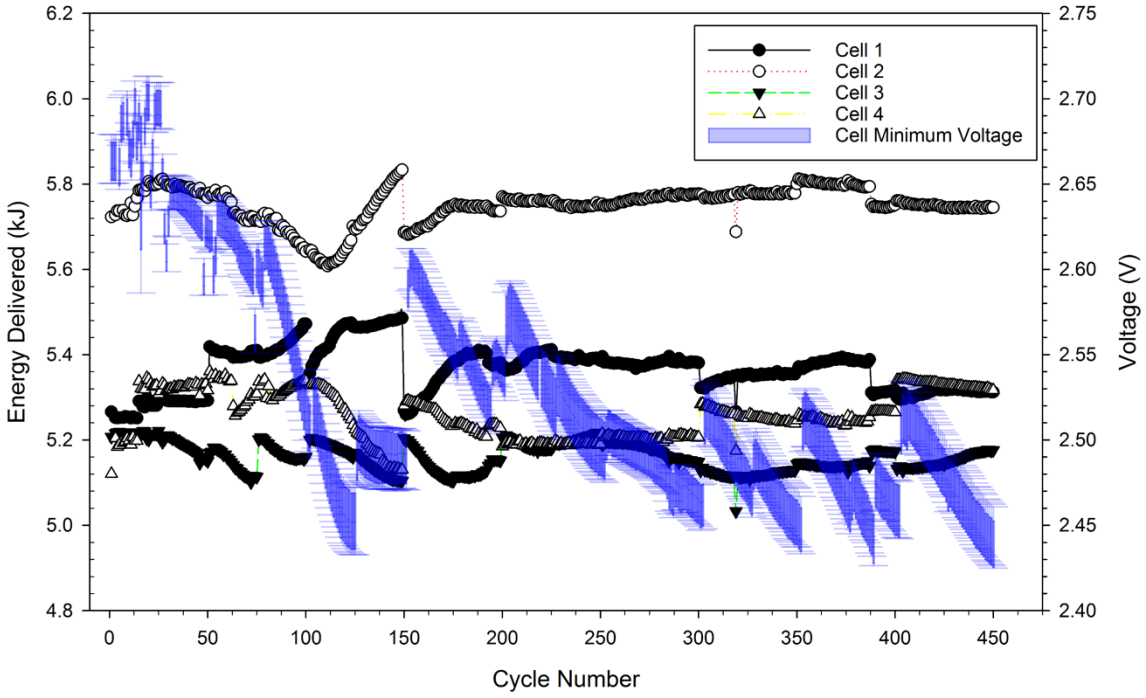

Figure 4.47: Energy delivered to the electronic load per cycle per cell for Replicant Array #2. End of life reached at 400 cycles.

The behavior of the cell voltages does not appear to have any direct correlation to the energy supplied by each cell, as the difference between the extremes in the box plot is in the 100 mV range, despite energy differences between cells in the 300-400 J range at times. The apparent sawtooth shape to voltage plot can be correlated to the test procedure, as it is in 25 or 50 cycle

periods. Due to memory limitations on LabVIEW, the experimental runs were broken into 25 cycle segments to avoid data errors seen on earlier cycles. Depending on when the 25-cycle run ended, it may have been several hours before the next cycle could be started. This introduced an artificial rest period into the data.

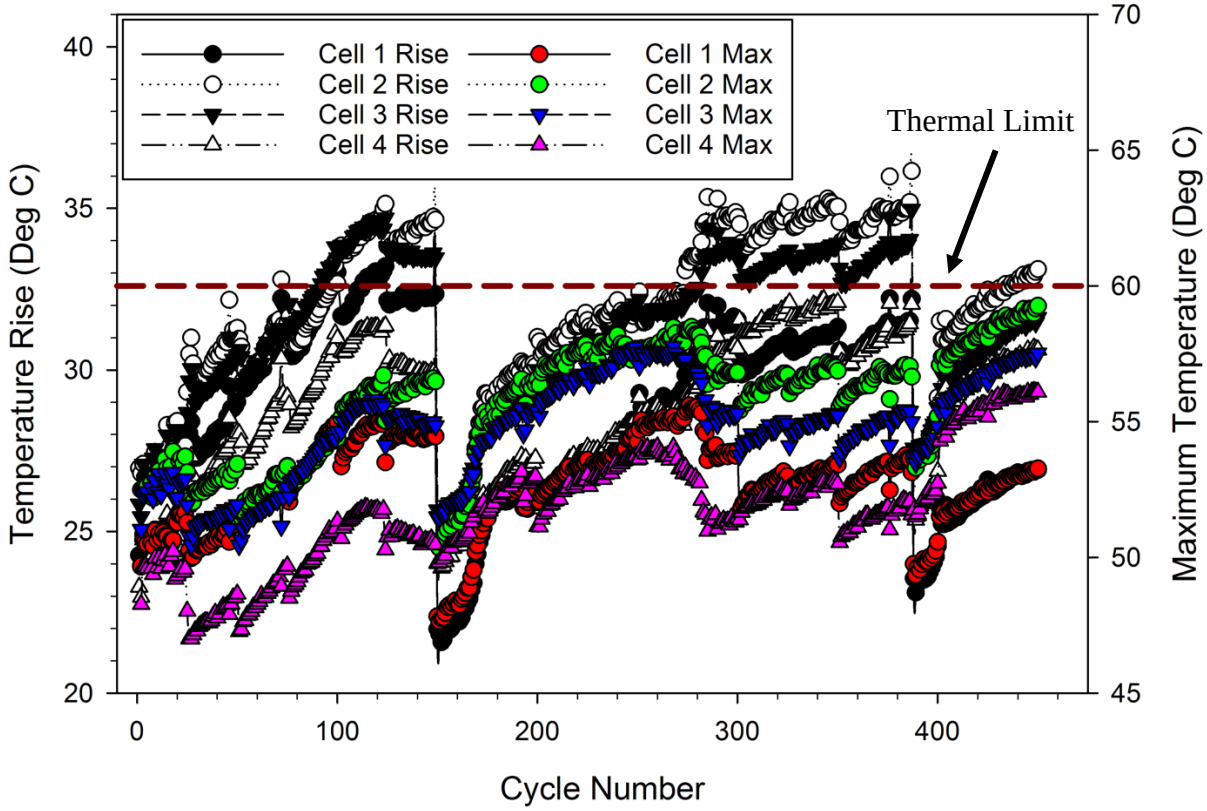

Figure 4.48: Temperature maximum and rise from ambient for Replicant 4P1S Array #2 as a function of cycle.

The thermocouple data shown in Figure 4.48 has the same general shape as shown in Figure 4.42, with the same breaks due to the same effects. However, the temperature rise is significantly higher for all of the cells. In the early cycles, the average temperature rise was approximately 25°C, 1°C higher than the other array. After 20 cycles, the temperature rise increased to 30°C, 4°C higher. The peak occurs at 120 cycles, with a 35°C temperature rise, while Replicant Array #1 did not exceed 30°C. A "reset" occurred at 150 cycles, as previously discussed, and the temperatures began to climb once more with a peak of 36°C reached at 275 cycles. Cells 2 and 3 were the consistently highest temperature cells, both in temperature rise per cycle and maximum temperature. Recall Figure 4.47, where these two cells are the maximum and minimum energy

sources. It is likely Cell 3, sourcing the least energy, was highly resistive and thus lost most of its energy as joule heating. Cell 2, on the other hand, was likely very low impedance compared to the rest of the array and was simultaneously capable of sourcing high energy and generating excess joule heating.

The EIS spectra for the cells in this array before testing occurred is shown in Figure 4.49, with the as-measured data on the left and the normalized on the right. For the as-measured data, cells 2 and 4 share a common real-axis crossing point, but diverge after approximately 175 Hz. The other two cells have a higher real impedance point, with a 2.966 mΩ increase from cell 2 to cell 3. In the normalized data, all of the cells appear to have similar high frequency responses, but diverge after 200 Hz. Cell 1 has the lowest peak value on the arc, but this does not seem to play a role in the amount of current sourced, temperature, or lifetime.

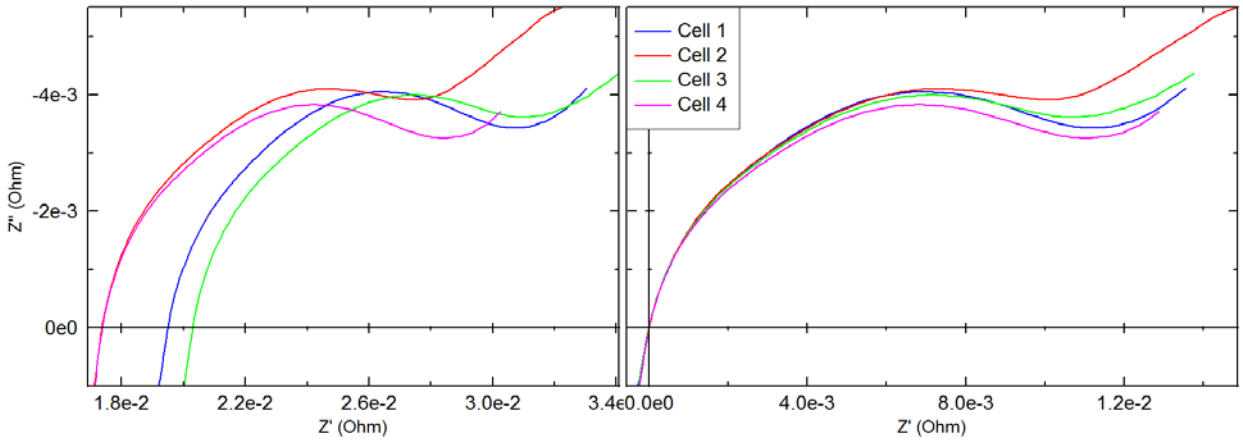

Figure 4.49: Baseline EIS spectra for Replicant Array #2, with as-measured data (left) and normalized real impedance (right)

The measured impedance response at 158 Hz as a function of cycle for Replicant Array #2 is shown in Figure 4.50, with the individual cell response on the bottom, the box plot of that data in the middle, and finally the aggregate EIS response for all of the cells in parallel on top. The single-cell EIS response at each cycle interval had low variance for nearly the entire experiment, which does not reflect the energy data shown in Figure 4.47 except for Cell 3. Cell 3 is the lowest for the entire experiment, which means it has the highest electrochemical impedance in the charge transfer region of the Nyquist diagram. The response of all the cells following the same pattern would indicate that despite the difference in energy output, the cells are aging at approximately

the same rate. The data also indicate that the 158 Hz response does not correspond to performance, only health.

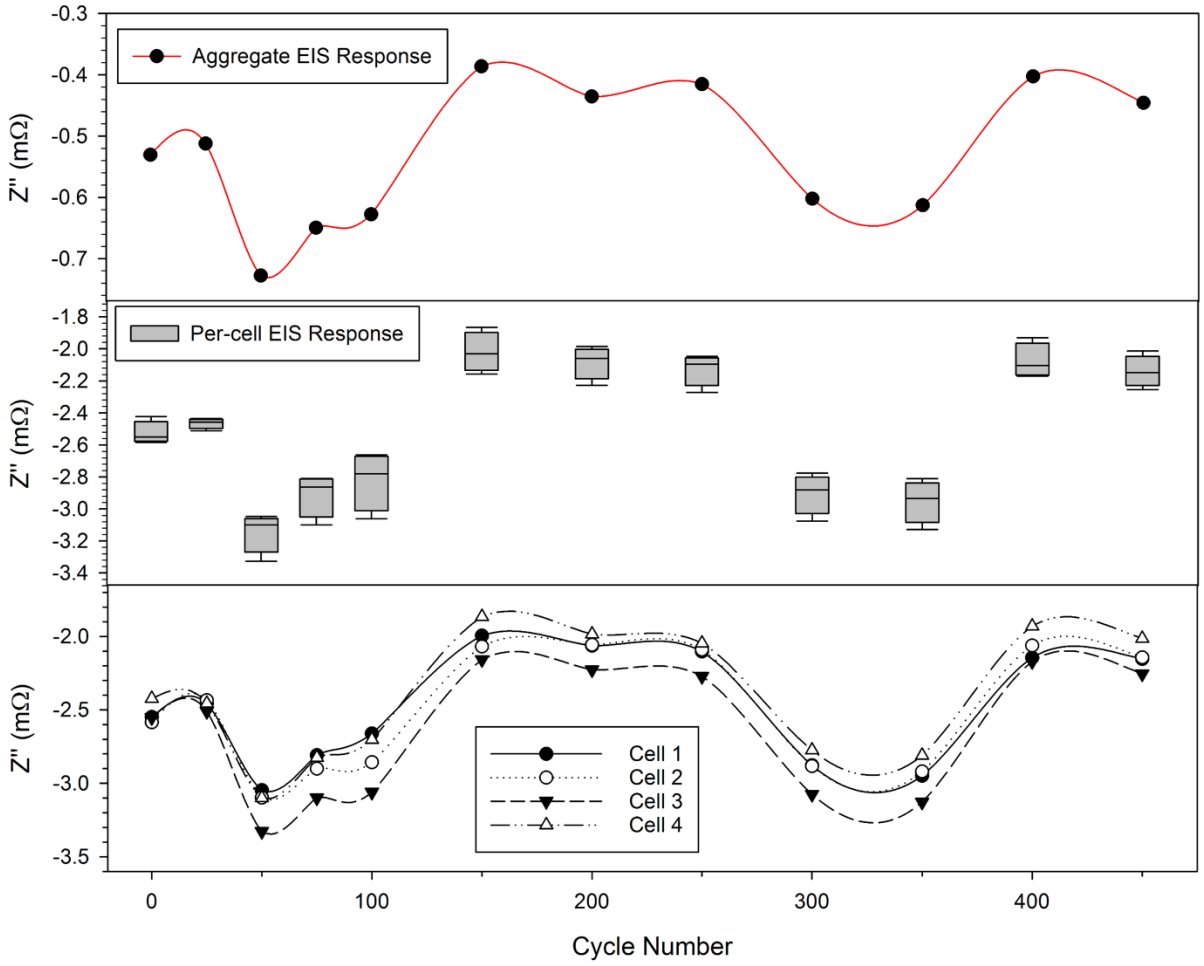

Figure 4.50: Replicant Array #2 single-cell and aggregate EIS data at 158 Hz as a function of cycle

Recall that this array had an unusually high capacity loss at 450 cycles. The aggregate data for this array appears to show the same waveshape seen in Figure 4.30, where the data near the end of cycling hits a trough, rises, and falls again. This waveshape is seen in the single-cell data as well, which does not occur in the baseline array, and is likely due to the vertical shift downwards in imaginary impedance as previously discussed. Given that the EIS response follows the expected trend of a rise, a plateau, and a fall to a trough, it is likely this array reached end of life at 350 cycles. This conclusion is supported by the excessive capacity loss at 450 cycles. The hypothesis

that a single aggregate EIS analysis for the entire array is also supported, with the features seen in the single-cell data reflected in the aggregate data.

The model data for the SEI layer shown in Figure 4.51 indicates that cell 4 experienced a permanent change at the 150 cycle mark, with an increase of two logs in the time constant value. When examining the data plotted in Figure 4.47, there does not seem to be any significant effect on the performance of the cell. The jump in energy delivered to the load at 150 cycles has already been attributed to an extended rest period over a weekend. It is most likely this increase was manifested as accelerated capacity fade and power fade, as the cell lost 34% of the original capacity after 450 cycles. The power fade may have only played a role if the depth of discharge was larger, but was masked by the relatively shallow discharge for this test series. The anode material data shown in Figure 4.52 has relatively low variance across all of the cycles. The dip at 350 cycles coincides with a drop seen with the 158 Hz data in Figure 4.50, followed by a slight rise in values. This is a likely indicator of health, with the anode material reaching a critical point.

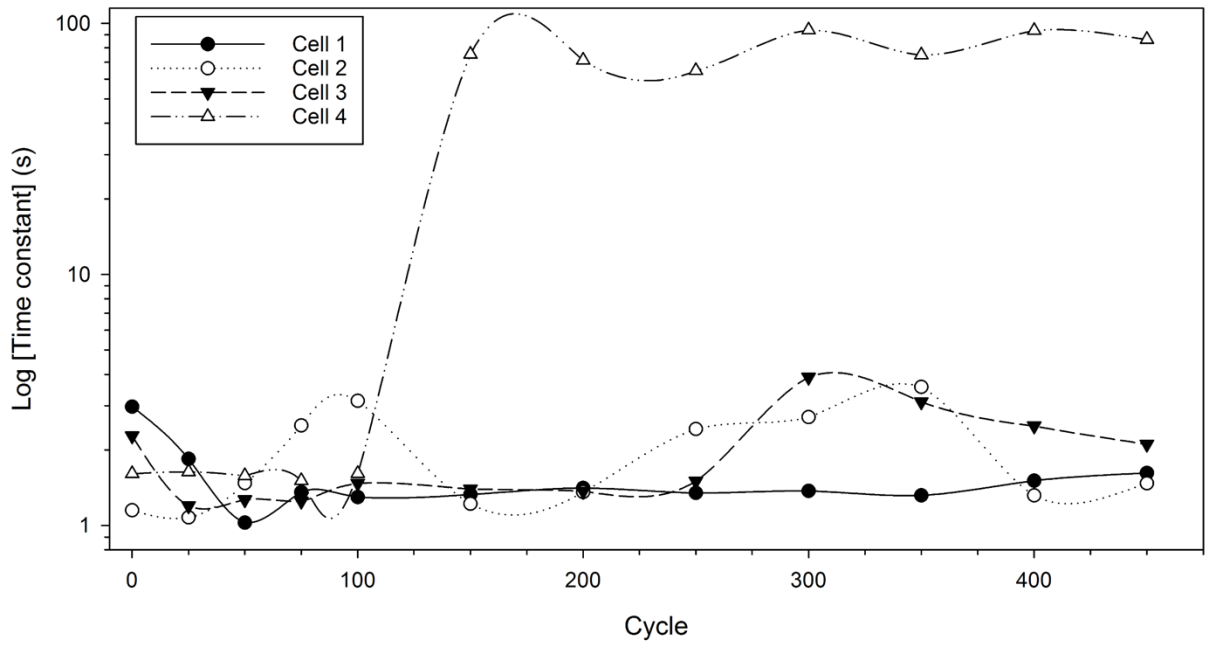

Figure 4.51: Time constant for the SEI layer model for Replicant Array #2

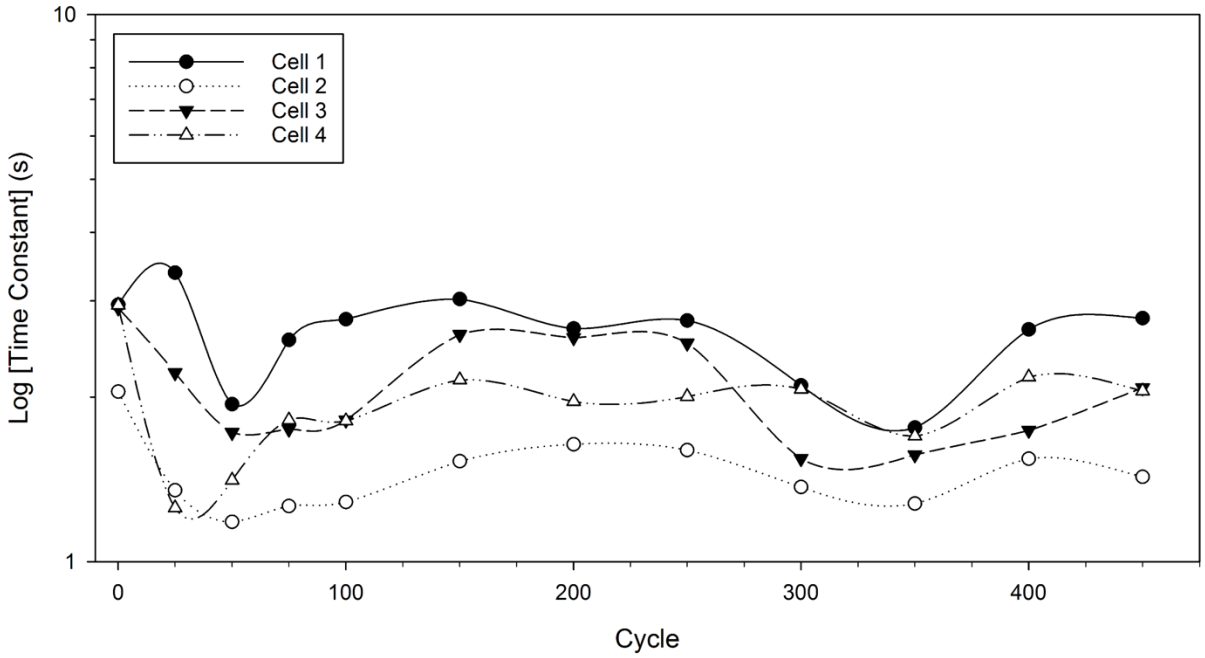

Figure 4.52: Time constant for the anode material model for Replicant Array #2

4.5.3 Analysis of Replicant Array #3

The third replicant array was also operated beyond the typical end of life conditions, with a minimum capacity loss of 28.45% and a maximum of 34.72%, as shown in Table 4.5. Unlike the other three replicants, this array was unable to recharge after 438 cycles. It is highly likely that the array reached end of life before 400 cycles.

TABLE 4.5: REPLICANT ARRAY #3 CAPACITY DATA

Cell Position	Cell Serial Number	Original Capacity (AH)	Capacity at 438 Cycles (AH)	Capacity Loss (%)
1	120108-222092	2.40	1.72	28.45
2	150408-223542	2.49	1.65	33.89
3	150408-223288	2.50	1.71	31.62
4	150408-223711	2.45	1.60	34.72

The energy delivered to the load per cycle per cell for this array is shown in Figure 4.53. The first 20 cycles were distributed oddly compared to the rest of the data due to the delayed start-up routines when setting up the DAQ for unsupervised operation. Once the automated software was operational, it appears this array had cells alternating the amount of energy sourced in increments of EIS intervals, either 25 or 50 cycles in length. It is possible this array recharged faster than

others and rested longer between EIS sweeps. The longer rest periods may have enabled different recovery rates for each cell.

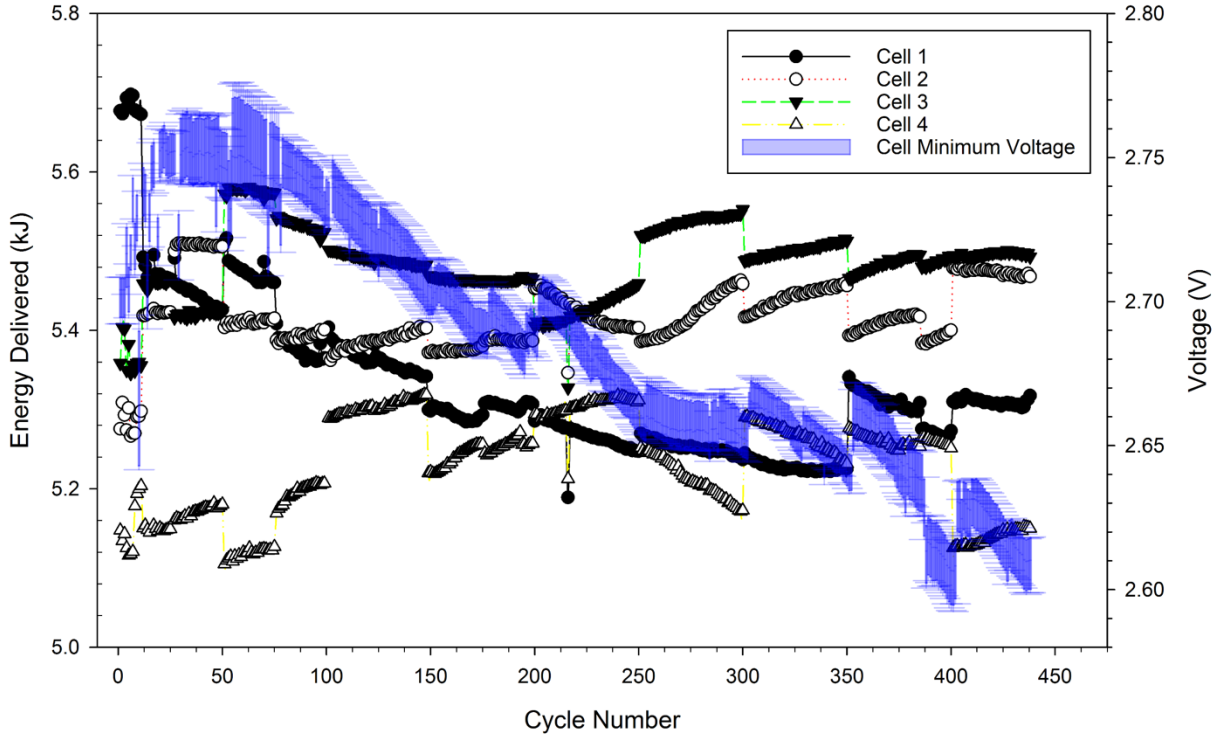

Figure 4.53: Energy delivered to the electronic load per cycle per cell for Replicant Array #3. End of life reached at 400 cycles.

It can be clearly seen in Figure 4.53 that the voltage per cell never dropped below 2.5 V, and the different between the maximum and minimum values was less than 0.05 V. The energy distribution, however, varied as much as 500 J at different points. As with the previous replicant array, this would indicate that the cell voltage is not related to the energy sourced by the cell and delivered to the load. Cell 3 appears to deliver the most energy to the load, and as shown in Figure 4.54 also has the highest temperature rise. Unlike one of the other replicant arrays, however, the maximum temperature for any of the four cells in this array did not exceed 55°C, and the maximum temperature rise per cycle was less than 30°C. It is interesting to note that while the electrical data showed multiple extended rest periods that affected the energy performance, the temperature data only show two periods with significant changes. At the 150 and 375 cycle mark there was a period of at least 48 hours of complete rest before discharge resumed. This was long enough for the cell to thermally reset.

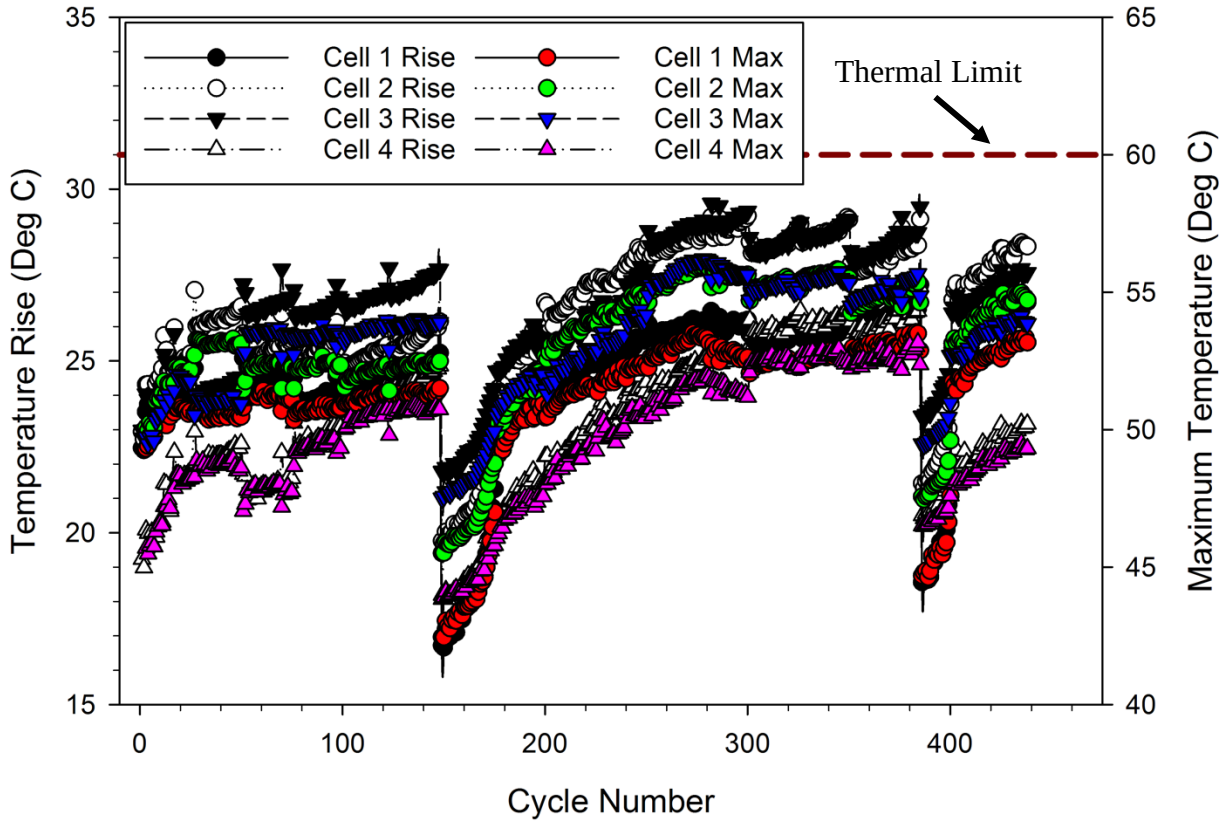

Figure 4.54: Temperature maximum and rise from ambient for Replicant 4P1S Array #3 as a function of cycle.

The EIS spectra for the four cells in this array before testing is shown in Figure 4.55, with the as-measured data on the left, and normalized on the right. Cell 2 has moderately higher real impedance than the other three cells with an increase of 2.42 mΩ, parts of which can be attributed to contact resistance of the probes. The normalized graph has the same spectra until about 500 Hz, where it starts to diverge. Cells 1 and 4 have the lowest imaginary impedance values at the peak of the arc, which appears to correlate to the low energy delivered to the load by those cells. Cell 4 had the lowest energy sourced to the load, and as shown in the normalized data has a slightly different curve. The diffusion region starts about 10 Hz sooner than the other cells. It is unclear from this data what implications that may have on the cell.

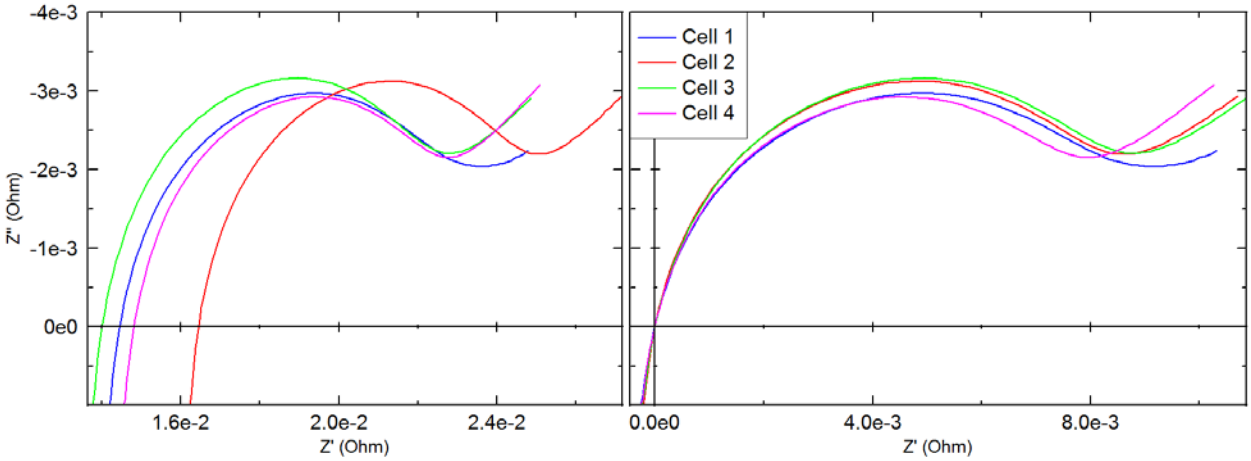

Figure 4.55: Baseline EIS spectra for Replicant Array #3, with as-measured data (left) and normalized real impedance (right)

The EIS response at 158 Hz for the third replicant array is shown in Figure 4.56 with the individual cell response on the bottom, the box plot of that data in the middle, and the aggregate EIS response for all of the cells in parallel on top. In the individual cell data, cell 1 consistently has the lowest value of imaginary impedance, while the other three cells were slightly higher. A peak is reached at 250 cycles, and after a drop at 300 cycles remains flat until 450 cycles. This change is somewhat noticeable in the aggregate data, with a peak at 200 cycles and a low at 350 cycles before rising again. The rise in response between 350 and 400 cycles is consistent with the measured capacity loss, as the 20% limit was likely reached in this interval. A state of health system that indicated a failure at 400 cycles would have been correct in this case. As with the previous two arrays, EIS data does not appear to correlate with energy performance but does match with health data.

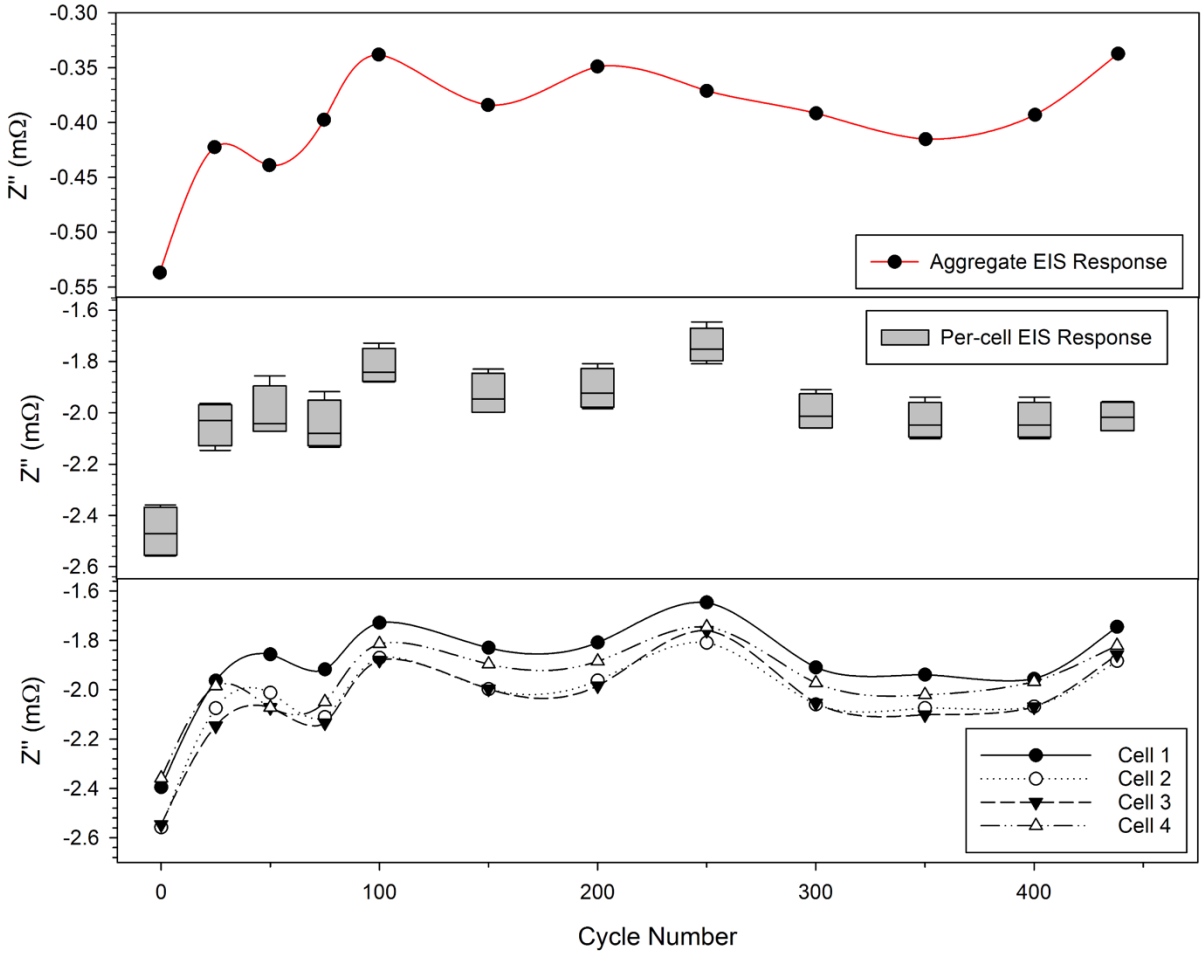

Figure 4.56: Replicant Array #3 single-cell and aggregate EIS data at 158 Hz as a function of cycle

A model for the SEI layer for the cells in this array is shown in Figure 4.57, with the time constant for each cycle interval. Cell 3 has the lowest time constant, and that cell sourced the most energy to the load. This cell also had the highest temperature rise per cycle. A low impedance SEI layer would enable more energy to be delivered from the cell, despite losses due to ohmic heating measured by the thermocouples. The drop observed at 350 cycles likely indicates further discharge on that cell would have resulting in electrochemical damage. The other three cells have relatively flat time constant values, indicating a stable SEI layer. The anode model, shown in Figure 4.58, is stable for all of the cells until after 250 cycles. While the other three cells remain stable, cell 1 experiences a 2 log increase in the time constant value. There does not appear to be a corresponding electrical change in the cell. However, based on data from the baseline cells it is likely the anode material was damaged, and this is further supported by behavior observed during

the recharge process. This array was prematurely taking offline due to excessive time required to recharge the array. After 24 hours on the power supply, the cell voltage was still at 3.3 V, and the current was not dropping as expected. Discharge behavior of the array did not change, but it appears an increase in the value for this array did modify the recharge behavior.

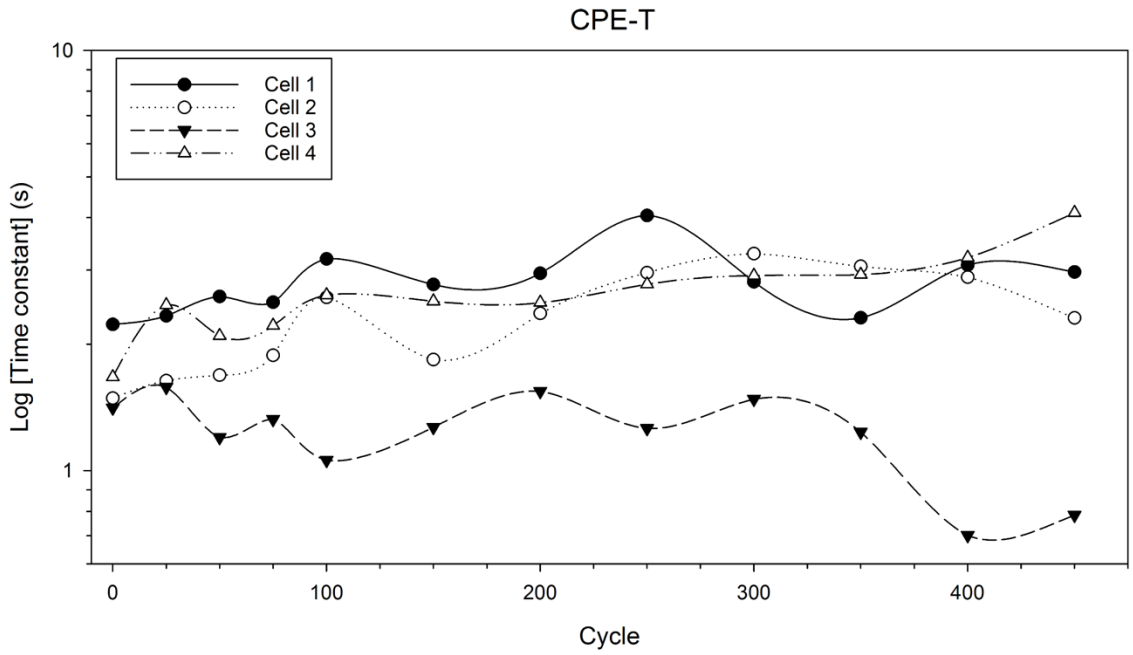

Figure 4.57: Time constant for the SEI layer model for Replicant Array #3

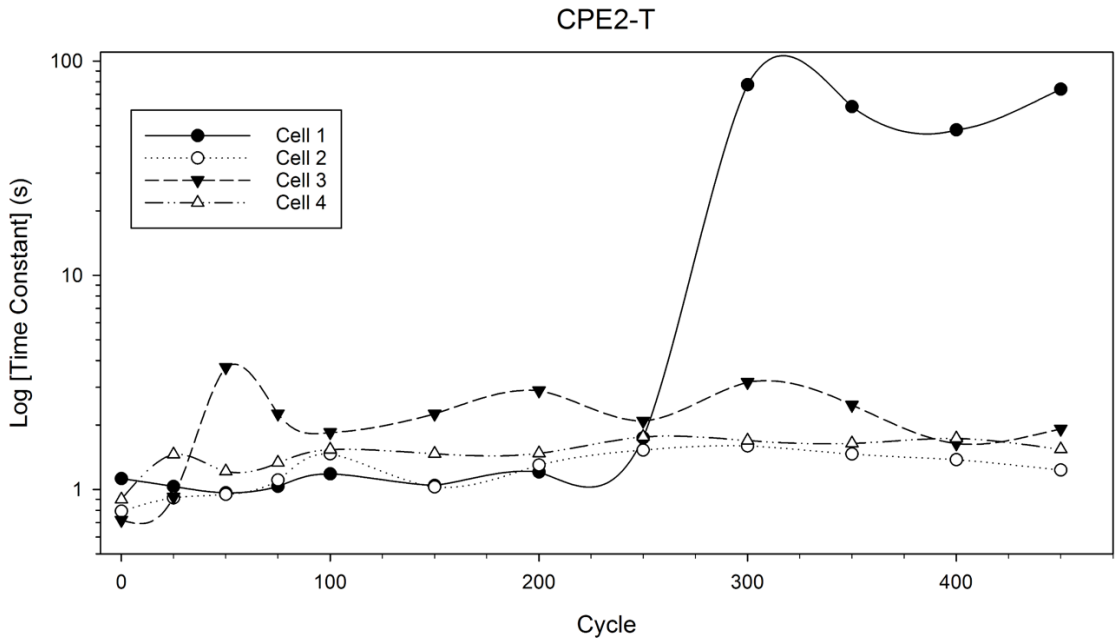

Figure 4.58: Time constant for the anode material model for Replicant Array #3

4.5.4 Analysis of Replicant Array #4

The capacity loss data for the final replicant array is shown in Table 4.6, which was recorded after 450 charge-discharge cycles. This array had moderate capacity loss at 450 cycles, with about 30% for each cell. Unlike other replicants, this array appears to have aged at an even rate.

TABLE 4.6: REPLICANT ARRAY #4 CAPACITY DATA

Cell Position	Cell Serial Number	Original Capacity (AH)	Capacity at 450 Cycles (AH)	Capacity Loss (%)
1	150408-223299	2.51	1.78	29.08
2	150408-223331	2.53	1.74	31.42
3	150408-224218	2.55	1.79	29.65
4	150408-224208	2.50	1.72	31.40

The energy delivered to the load per cell per cycle is shown in Figure 4.59, and like the previous replicants there was a large variance between the cells from the beginning of the experiment. The minimum cell voltage per cycle was the highest of the replicants, with a minimum of 2.67 V at the end of testing at 450 cycles. The drop in voltage does not appear to affect the energy delivered to the load, which is to be expected when the batteries are discharging inside their operational envelope.

The apparent discontinuities in the energy data can be explained with prolonged rest periods as the array was resting while other arrays in the test series were completing their cycles. As shown in Figure 4.60, only two periods had sufficient duration to impact the temperature of the cells. The two periods, 150 cycles and 375 cycles, match the other replicants and are directly correlated to a weekend period where the electrochemistry could relax. The per-cycle temperature rise and maximum values for the cells followed the amount of energy sourced, with Cell 3 the highest on both. However, the cell with the lowest maximum temperature, Cell 1, also had the highest temperature rise. It is possible the thermocouple was improperly calibrated for absolute temperature, but it is likely the temperature rise is correct. Cell 1 also sourced the second highest energy to the load, and would be expected to generate a significant amount of thermal energy.

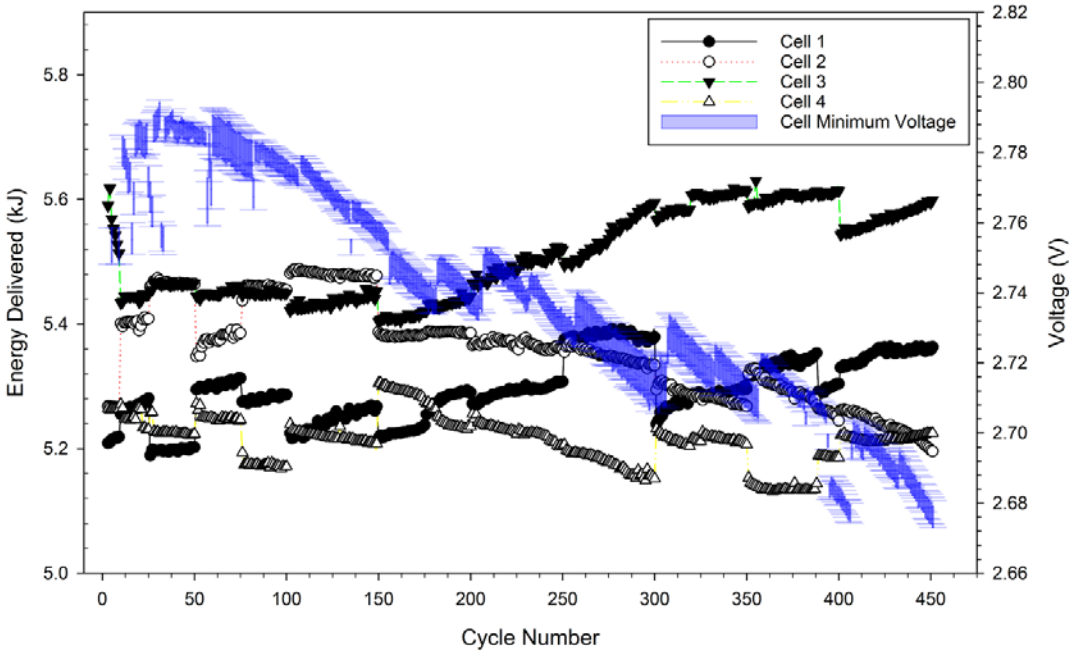

Figure 4.59: Energy delivered to the electronic load per cycle per cell for Replicant Array #4. End of life reached at 400 cycles.

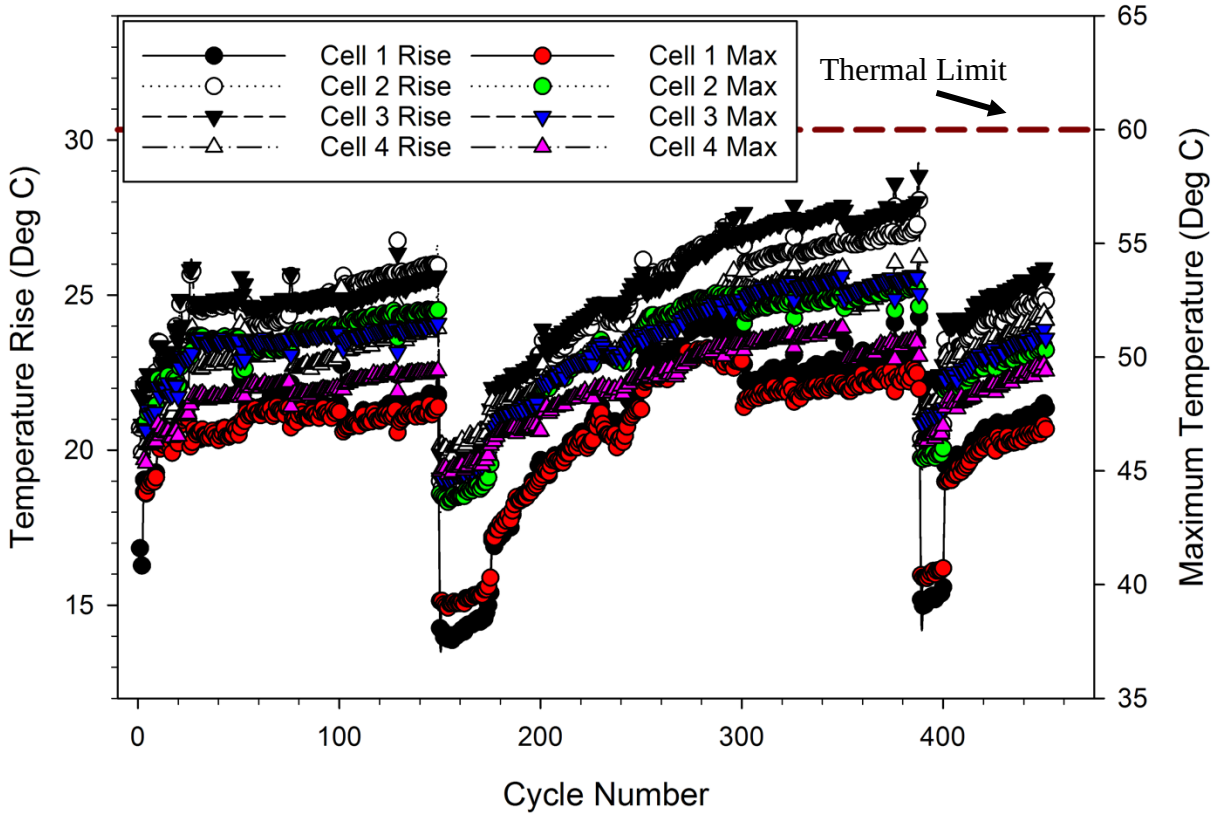

Figure 4.60: Temperature maximum and rise from ambient for Replicant 4P1S Array #4 as a function of cycle.

The EIS spectra for the four cells in this array before testing is shown in Figure 4.61, with the as-measured data on the left, and normalized on the right. Both cells 1 and 4 have higher real impedance than the other two cells, with an increase of 7.71 mΩ from Cell 2 to Cell 1, and this cannot be entirely attributed to probe contact resistance. In a marked departure from the other replicant arrays, the normalized spectra diverge after the real-axis crossing at approximately 1 kHz. While cells 1 and 3 have similar structure and arc height magnitude, Cell 4 has very low arc height magnitude and the change to diffusion physics is at a lower real impedance. Cell 2 has a slightly higher arc magnitude and diffusion impedance. Cell 3 sourced the most energy to the load, indicating that a combination of low real-axis impedance crossing and a higher real impedance in the diffusion region can identify the most likely cell to dominate the array.

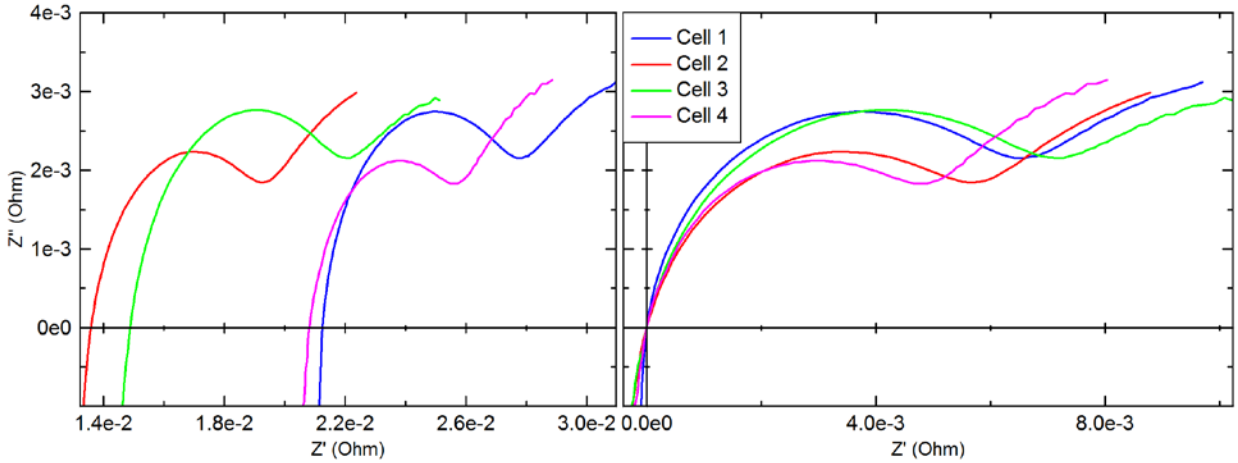

Figure 4.61: Baseline EIS spectra for Replicant Array #4, with as-measured data (left) and normalized real impedance (right)

The EIS response at 158 Hz for this array is shown in Figure 4.62, with individual cell response on the bottom, the box plot of that data in the middle, and finally the aggregate EIS response for all of the cells in parallel on top. The individual responses for the cells is more flat than seen in the other replicant arrays, however a decrease in values between 250 and 300 cycles can be observed. The slight increase between 350 and 400 cycles is a likely indication of end of life, evidenced by the high level of capacity loss measured at 450 cycles. The aggregate EIS response also shows a drop at 300 cycles, but without the other information it would be difficult to determine state of health on this array as there is also a drop at 150 cycles. The large disparity in real-axis crossing values for the cells in this array likely interfered with the diagnostic. The other three replicant

arrays had only one cell with a significantly higher real-axis crossing impedance, and it did not seem to impact the data significantly. The two cells with the highest arc height, 1 and 3, were also the cells that had the highest imaginary impedance at 158 Hz.

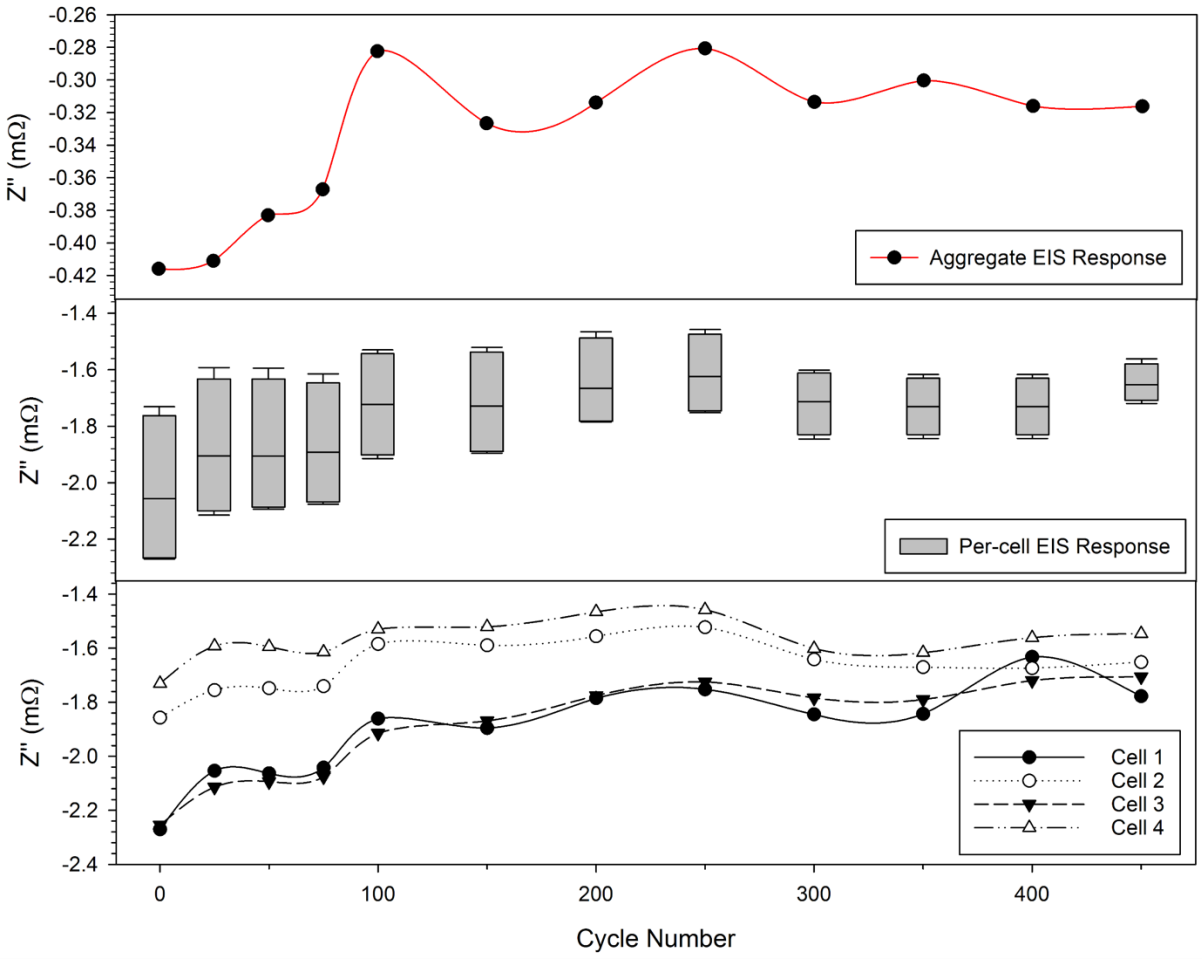

Figure 4.62: Replicant Array #4 single-cell and aggregate EIS data at 158 Hz as a function of cycle

The model for the SEI layer for this array is shown in Figure 4.63, and implies that after 200 cycles the SEI layer is experiencing growth. This coincides with a change in the electrical performance, where Cell 3 begins to dominate with a consistent increase in the energy delivered to the load per cycle until the end of testing, and the other three cells are consistently lower energy per cycle. Since this behavior is not observed for all of the cells simultaneously in any of the other replicants, it is possible the change in the SEI time constant may interfere with the state of health diagnostic. The anode model shown in Figure 4.64 indicates that Cell 2 might have a material

problem starting at 100 cycles, however there appears to be some degree of recovery at 250 cycles. This may be a model artifact due to errors in the specta acquisition, as it does not seem to have significantly impacted either the electrical data or the capacity loss. Unlike the baseline array model, the change is less than one log. This would imply minimal material changes in the cell.

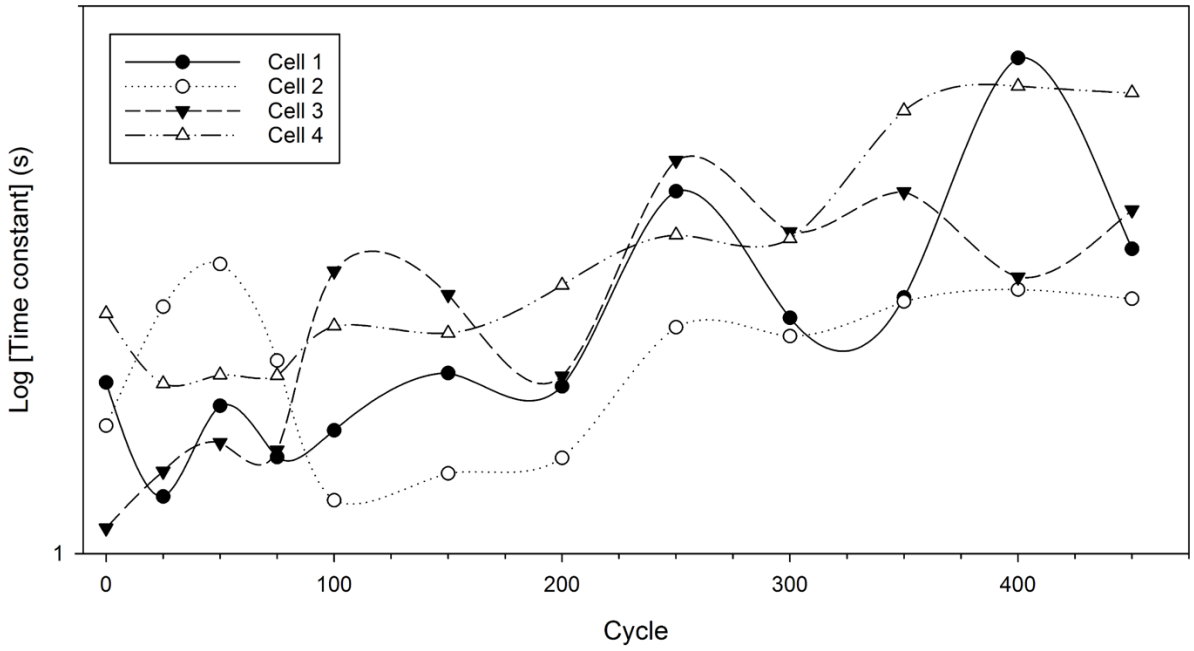

Figure 4.63: Time constant for the SEI layer model for Replicant Array #4

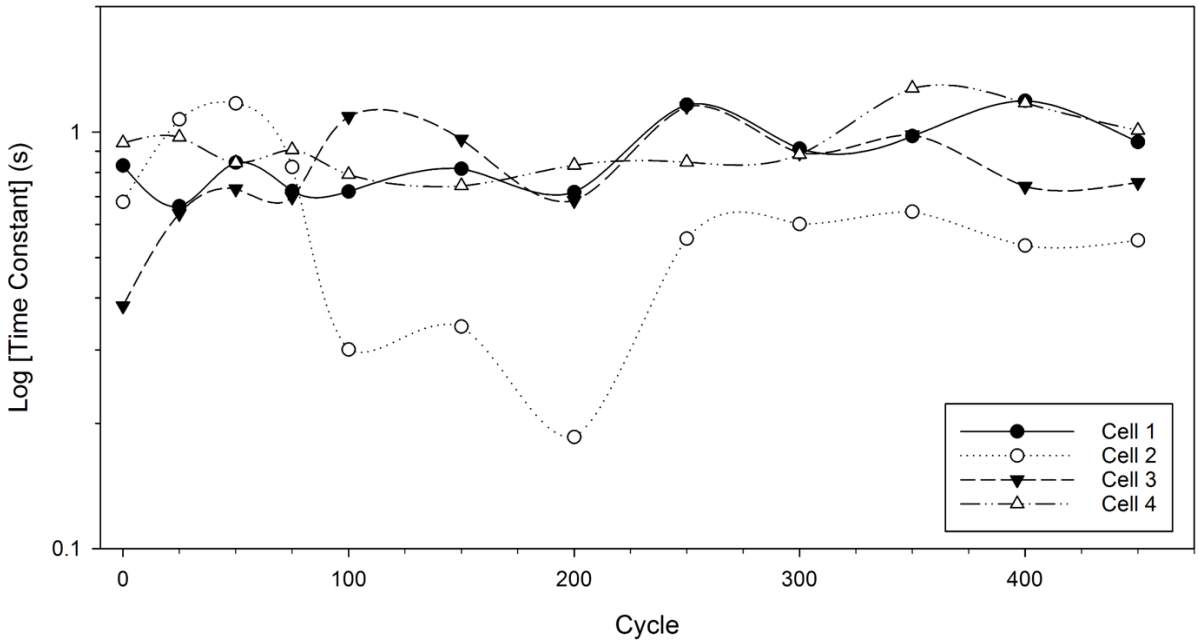

Figure 4.64: Time constant for the anode material model for Replicant Array #4

4.6 Replicant 4P1S Array Comparative Analysis

While the individual analysis of each replicant array is informative to study specific array behavior, the comparison of all of the arrays to derive trends can yield more useful results. While a comparison to the baseline array is essential to understanding the difference the filtering based in EIS spectra has influenced the lifetime of 4P1S arrays, comparing the data obtained for each array individually may also provide insights into the performance of a battery pack constructed with the methods available to a manufacturer, with an emphasis on minimal waste and cost efficiency. As previously mentioned, the replicant arrays were intentionally limited to filtering based only on the 1-kHz ESR values and the maximum capacity after the completion of the formulation series. The capacity specification was enlarged slightly to increase the available population and further replicate industrial conditions, with a maximum deviation of 150 mAH from the average capacity of 2.48 AH. Each of the arrays was constructed with random selections of the available cells in the decimated population to ensure minimal experimental bias. The cells used were comprised of two populations, with one in the 2012 manufacturing cycle and the other in the 2015 cycle. Verification of cell construction standardization was confirmed with the manufacturer, thereby eliminating material vendor changes as a potential source of error. End of life for these arrays was determined by a full 1C charge and 1C discharge to measure the capacity with computerized battery analyzers (CBA). Unfortunately, due to limits on funding and experimental equipment usage, the CBAs were not available until near the end of the replicant testing period. The baseline parallel array was able to use a MACCOR for calculation of capacity, which was unavailable for the replicant arrays.

4.6.1 Replicant Array Electrical Analysis

Prior to analysis, it is essential to verify all of the arrays operated inside the appropriate performance envelope. Two parameters are essential for safety during the operation of the replicant arrays. The first is shown in Figure 4.65, the minimum cell voltage during discharge. As shown, none of the cells were operated below 2.0 V, the absolute minimally acceptable voltage. Generally, the higher the voltage during discharge, the more capacity a cell will have. Therefore, the drop in voltage seen in Figure 4.65 for Array 2 would indicate a substantial loss in capacity for

the array after approximately 50 cycles, with a drop of 0.21 V over a period of 75 cycles. It recovers marginally at 150 cycles, but continues to remain at least 0.1 V less than the other three arrays.

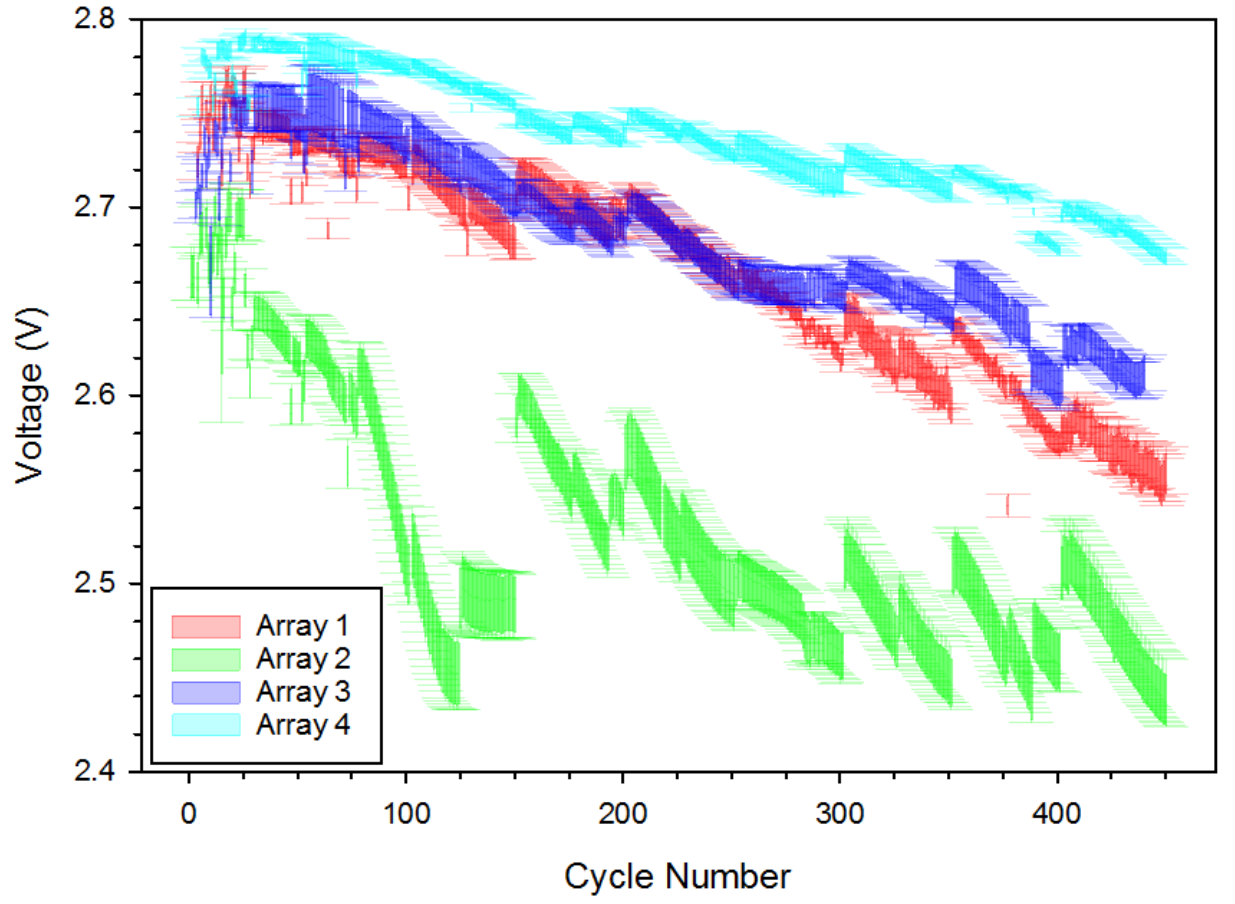

Figure 4.65: Box plots of the minimum cell voltage as a function of cycle for the four replicant 4P1S arrays

The second parameter is temperature, and the median value for each array as a function of cycle with maximum and minimum error bars is shown in Figure 4.66. The highest allowable temperature is 60°C, and only Replicant Array #2 had a cell that came close to that limit. In general, Replicant Array #2 had a higher median temperature than the other three arrays, and Array #4 had the lowest median temperature. The drops in median temperature at 150 and 375 cycles can be directly attributed to allowing the array to rest over a weekend, where the electrochemistry relaxed and the cells equilibrated to the thermal chamber.

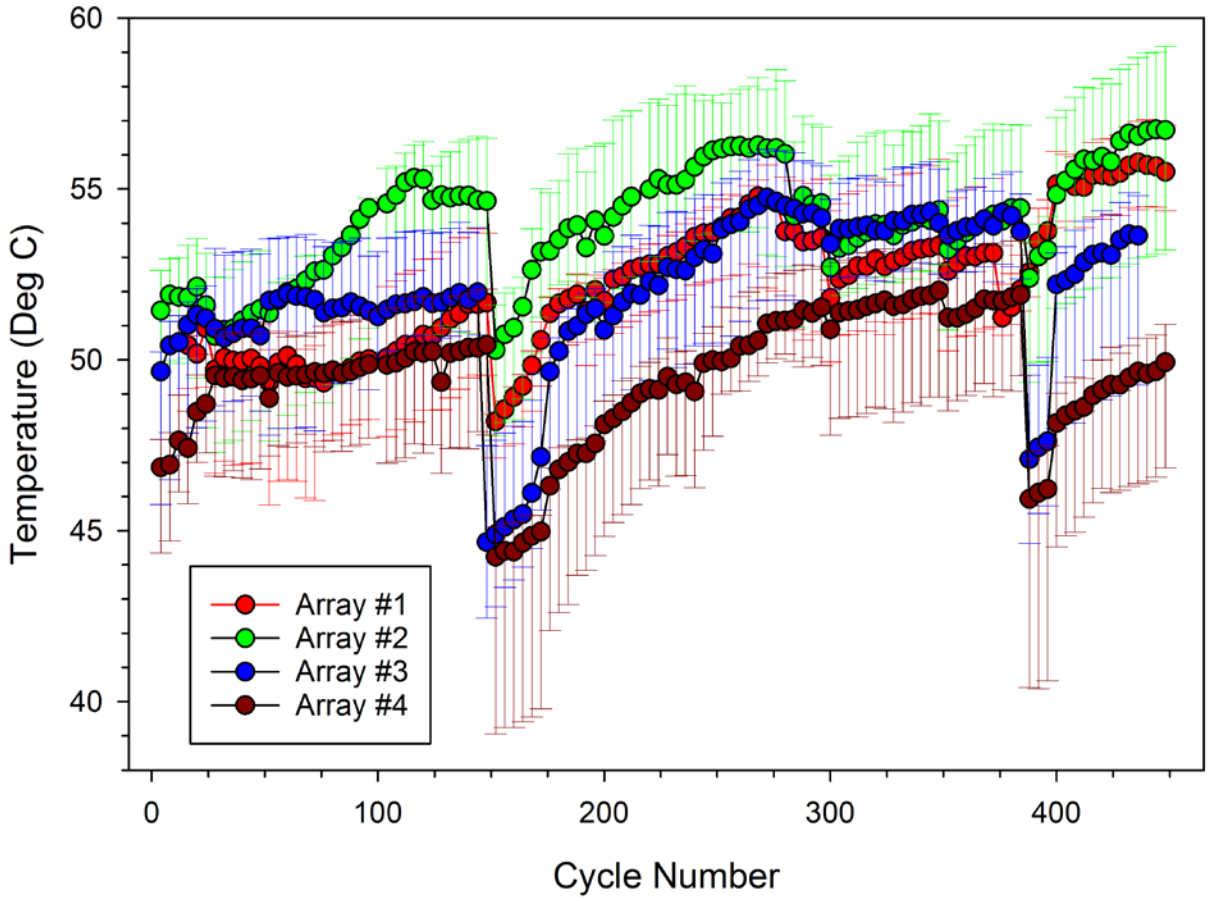

Figure 4.66: Median temperature as a function of cycle for all of the replicant arrays with maximum and minimum value error bars

As shown in Figure 4.67, the median values of the energy delivered to the load per cell per cycle for all of the replicants was higher than the baseline array, with occasional exceptions seen in Replicant Array #2. Since none of the replicant arrays were viable past 450 cycles, the data was truncated for the baseline array in Figure 4.67. A tabulated comparison of basic performance metrics is shown in Table 4.7, with the median, maximum, and minimum energy for the entire experiment length.

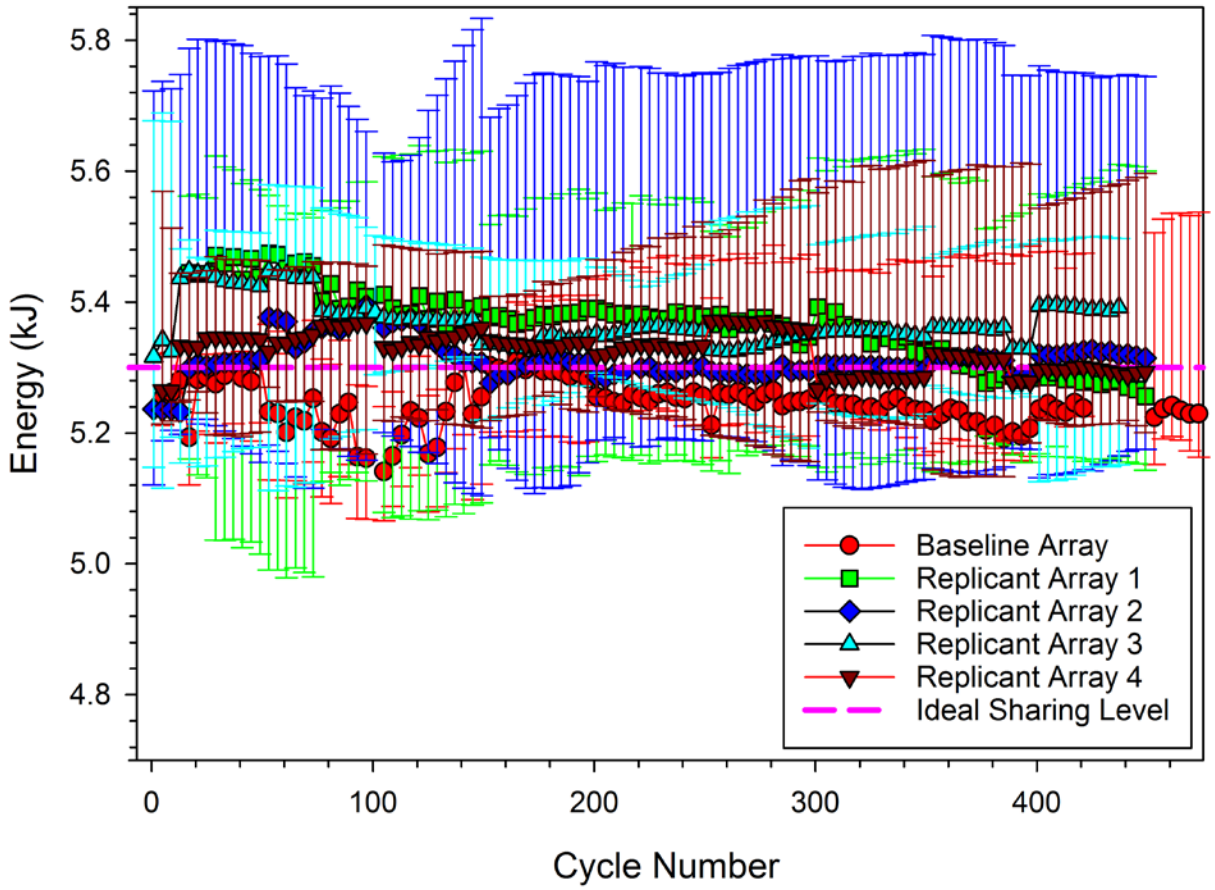

Figure 4.67: Median, maximum, and minimum energy for each of the parallel arrays as a function of cycle for the first 450 cycles

In this data, a lower median energy per cycle implies that the array is more balanced, with an estimated "ideal" sharing level around 5300 J/cycle. Recall that as discussed in Section 4 the baseline array had low variance for the first 150 cycles, then a divergence occurred where one cell source more current than the other three. As shown in Figure 4.67, the max-min error lines indicate that the data spread was confined to less than 331 J at the point of highest divergence (in the first 450 cycles). In contrast, the minimum variance per cycle for the replicant arrays was 48% higher than the baseline array (Replicant Array #4), and the maximum variance per cycle was 120% higher than baseline (Replicant Array #2). Additionally, the median value of all of the cycles for the replicant arrays was a minimum of 87 J (Replicant Array #2) and a maximum of 156 J (Replicant Array #1). One conclusion than can be drawn from this data is that even though the baseline array appeared to have an unbalanced condition after 150 cycles, the overall performance

of the array was within acceptable range, evidenced by the observed 43% increase in lifetime for the parallel array versus the replicant arrays.

TABLE 4.7: COMPARISON OF 4P1S ARRAY PERFORMANCE FOR CYCLES 0 - 450

Experiment	Median (J)	Maximum (J)	Minimum (J)	ΔJ_{max} Single Cycle (J)
Baseline	5220	5487	5001	331
Replicant Array 1	5376	5642	4977	594
Replicant Array2	5307	5834	5033	729
Replicant Array 3	5360	5698	5105	581
Replicant Array 4	5332	5630	5132	489

TABLE 4.8: REPLICANT ARRAY CAPACITY DATA

Array	Cell Position	Cell Serial Number	Original Capacity (AH)	Capacity at 450 Cycles (AH)	Capacity Loss (%)
1	1	150408-224219	2.48	1.80	27.42
	2	120108-211117	2.40	1.82	24.25
	3	150408-224236	2.51	1.82	27.45
	4	120108-210760	2.38	1.67	29.83
2	1	120108-222318	2.54	1.61	36.53
	2	150408-224199	2.52	1.79	29.08
	3	120108-210887	2.34	1.55	33.91
	4	120108-210518	2.42	1.57	35.02
3	1	120108-222092	2.40	1.72	28.45
	2	150408-223542	2.49	1.65	33.89
	3	150408-223288	2.50	1.71	31.62
	4	150408-223711	2.45	1.60	34.72
4	1	150408-223299	2.51	1.78	29.08
	2	150408-223331	2.53	1.74	31.42
	3	150408-224218	2.55	1.79	29.65
	4	150408-224208	2.50	1.72	31.40

The capacity loss for each array is detailed in Table 4.8. The original capacity for the entire cell population at the start of testing had a median value of 2.495 AH with a standard deviation of 0.062 AH. The capacity after 450 cycles had a median loss of 30.62%, or 0.78 AH. There was a standard deviation of 3.22% on the capacity loss. Using the median capacity values, the useful life limit of 80% of the original capacity would be reached after 1.996 AH. Assuming the degradation in capacity per cycle is approximately linear, the median cycle number where the cells

would be expected to reach end of life is 290 cycles. This represents a median loss of 75.32% of life compared to the single-cell testing, and 58.57% life loss compared to the baseline parallel array. This data definitively shows that operating these cells in parallel at high C-rates will result in a substantial loss of cell life.

4.6.2 Replicant EIS Analysis

The initial EIS spectra for each cell in a parallel array appears to play a significant role in the stability of the array. As shown in Figure 4.68, the baseline 4P1S array had overlapping EIS spectra with a real-axis intercept of approximately 13 mΩ. The replicant array real-axis intercept values, due to the lack of filtering, were spread from 13 mΩ to 24 mΩ, and is larger than can be expected from contact resistance alone. Note how the maximum value for the arc on the baseline array is lower than the replicant cells. The different in imaginary impedance between the highest point on the baseline spectra and the lowest point in all of the replicant spectra is 0.58 mΩ. Additionally, the shape of the EIS spectra for the replicants at lower frequencies is different than the baseline. This would imply that the anode material (and potentially some cathode effects) would increase the effective impedance in the cell and change the performance characteristics.

The examination of the baseline EIS spectra for each of the arrays has yielded a potential metric for determination of the cell most likely to be the primary energy source to the load in an array. For each of the arrays, the cell that consistently sourced the most energy had the lowest real-axis crossing impedance (where imaginary impedance is zero) and the largest real impedance change between the real-axis crossing and the “trough” that marks the beginning of the diffusion region, as shown in Figure 4.69. It is relatively easy to correlate low real impedance to high current from the cell, as that is pure resistance and can be modeled as a simple electrical circuit. In two of the four arrays (Array 2 and Array 4), the cell with the lowest real impedance did not source the most current. Therefore, other factors must be considered. The difference in real impedance between the zero-crossing and the “trough” appears to be another critical value. The cells that sourced high current had both low zero-crossing values and a large change between the trough and the zero-crossing. Additionally, it appears the frequency of the trough ($f_{diffusion}$) needs to be 4 Hz or higher to meet the criteria.

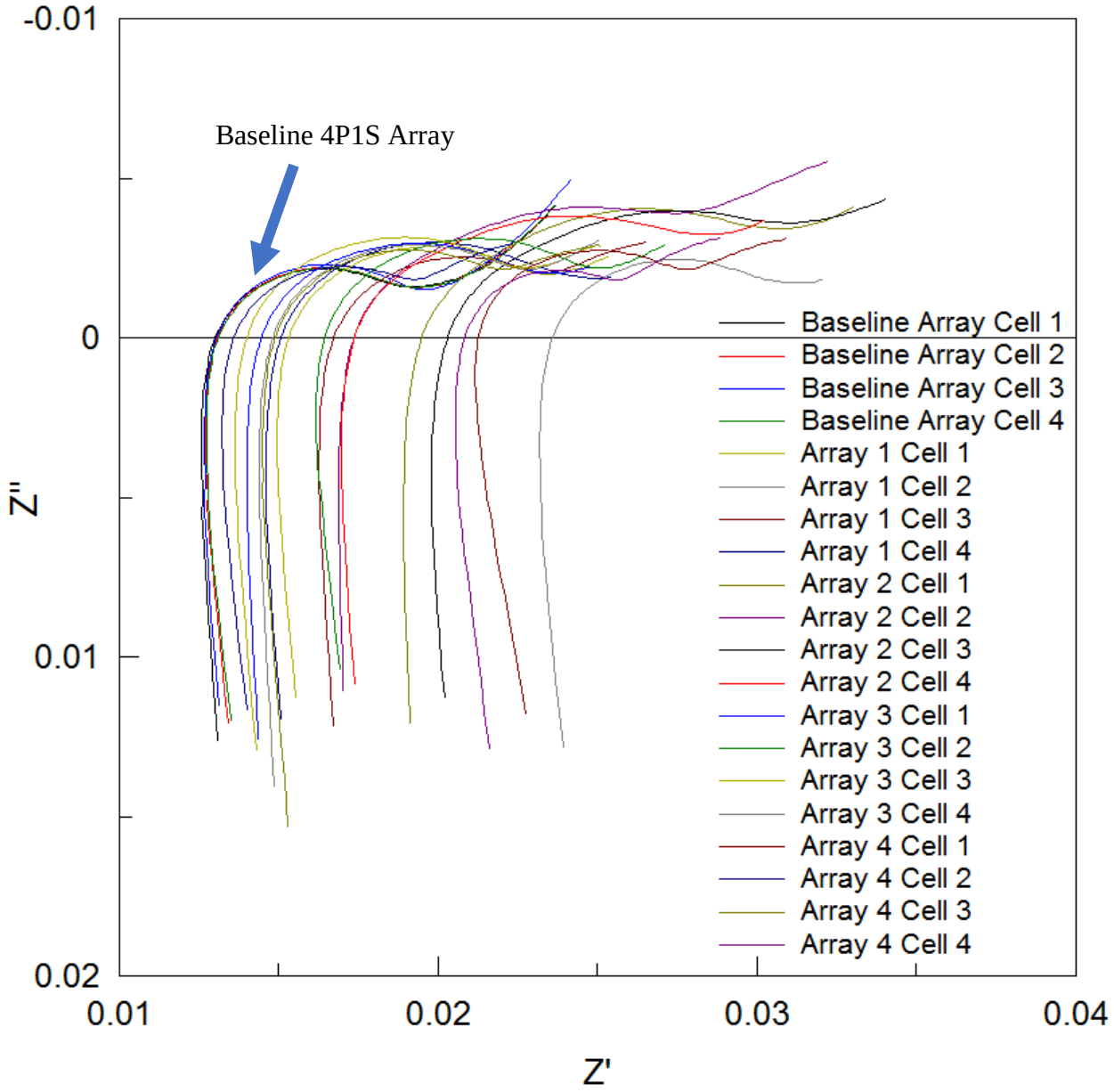

Figure 4.68: Comparison of baseline EIS spectra for all cells in the baseline and replicant parallel arrays

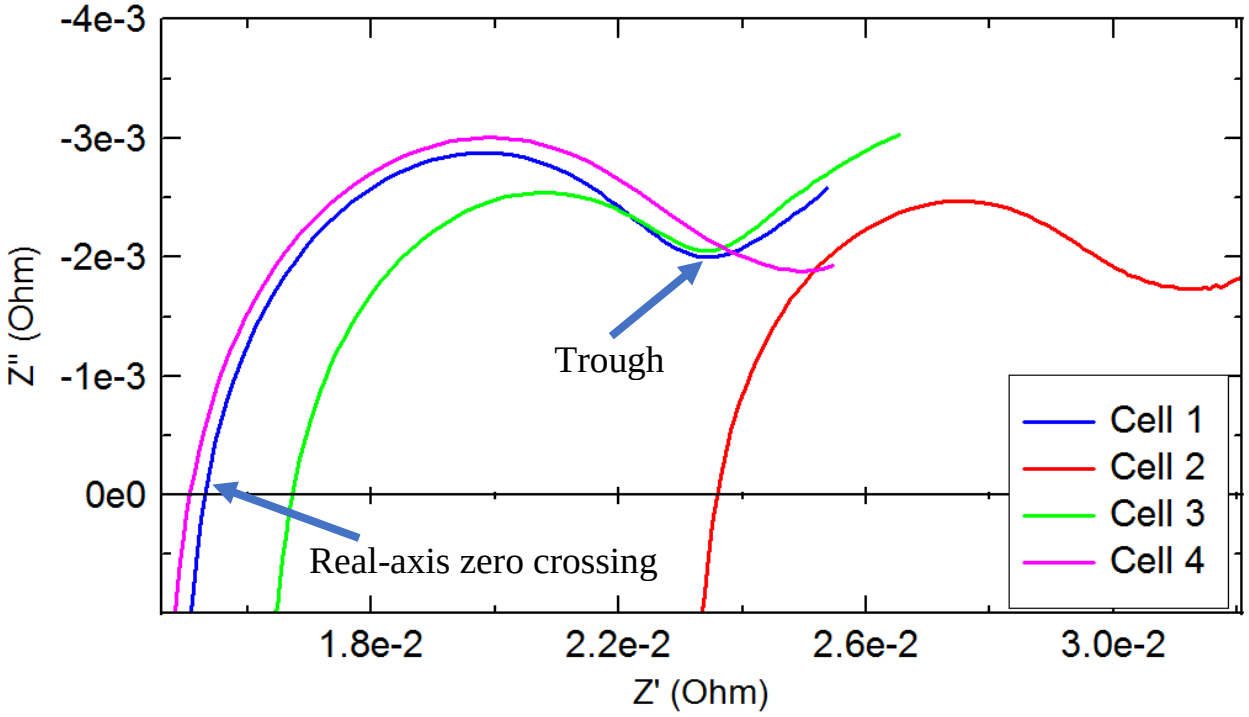

Figure 4.69: Diagram of locations for determination of dominate cell in parallel array

The baseline EIS data extracted from each array is shown in Table 4.9, with columns for the zero-crossing real impedance, the real impedance at $f_{diffusion}$, and the difference between the two values. The value for $f_{diffusion}$ is also tabulated. When applying the algorithm described, the first filter is the frequency. For Array 1, only Cells 1 and 3 have the critical frequency above 4 Hz. Next, the zero-crossing value is compared to find the lowest resistance. This corresponds to Cell 1, with 15.3 mΩ. If there were more cells close in value the difference would be compared between the two resistance values. Cell 1 has the highest resistant, 8.2 mΩ, and is in fact the cell that sources the most energy to the load. When this test is repeated for the remaining three replicants, the cell that passes all three tests is the cell that sourced the most current for that array.

A comparison between the baseline and replicants EIS data at 158 Hz is shown in Figure 4.70, with the aggregate data on the top and the single-cell responses on the bottom. It can be clearly noted that the imaginary impedance is shifted for the baseline versus the replicant arrays. Recall the 0.58 mΩ difference between the two groups of data. Looking at the baseline array at 0 cycles, the median value is approximately -1.8 mΩ. For the replicant data, the median value at the same cycle count is approximately -2.3 mΩ, a difference of 0.5 mΩ. This clearly demonstrates that the

baseline impedance spectra will influence the response at 158 Hz, near the top of the mid-frequency arc.

TABLE 4.9: REPLICANT ARRAY BASELINE EIS DATA

Array	Cell Serial Number	Zero-Crossing (Ω)	Diffusion Trough (Ω)	ΔReal Resistance (Ω)	$f_{diffusion}$ (Hz)
1	150408-224219	0.0153	0.0235	0.0082	4.70
	120108-211117	0.0236	0.0314	0.0078	2.00
	150408-224236	0.0167	0.0235	0.0068	7.51
	120108-210760	0.0151	0.0250	0.0099	1.59
2	120108-222318	0.0195	0.0310	0.0115	3.14
	150408-224199	0.0174	0.0277	0.0103	6.00
	120108-210887	0.0203	0.0311	0.0108	4.35
	120108-210518	0.0174	0.0287	0.0113	2.61
3	120108-222092	0.0145	0.0238	0.0093	2.42
	150408-223542	0.0164	0.0252	0.0087	4.54
	150408-223288	0.0140	0.0229	0.0089	4.33
	150408-223711	0.0148	0.0229	0.0081	4.99
4	150408-223299	0.0213	0.0280	0.0067	7.06
	150408-223331	0.0136	0.0194	0.0058	8.57
	150408-224218	0.0149	0.0222	0.0073	6.62
	150408-224208	0.0208	0.0267	0.0059	3.49

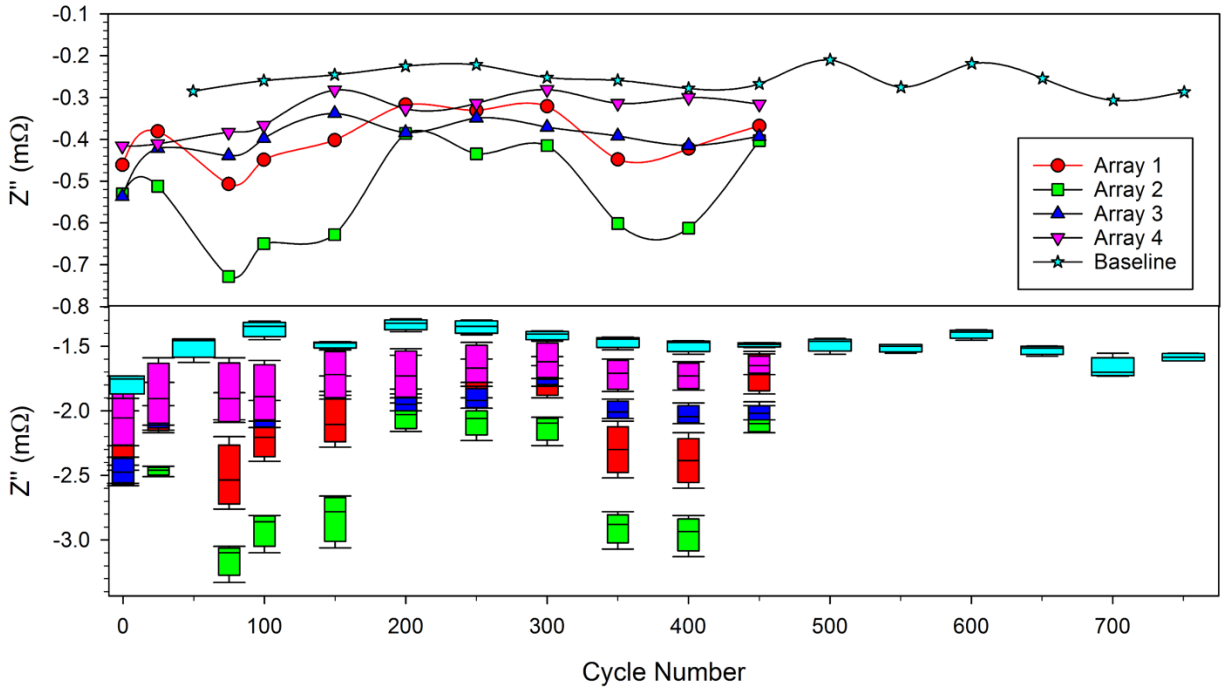

Figure 4.70: Aggregate and per-cell EIS response for each array in the replicant test series

For the aggregate response, the starting value for the baseline array is approximately -0.3 mΩ, and the average for the replicants is approximately -0.45 mΩ. The difference of 0.15 mΩ is 25.86% of the 0.58 mΩ value discussed previously, which using these close approximations indicates that the aggregate magnitude value for the cells can be expected to be the values seen in the single-cell spectra divided by the number of cells in parallel. Given how these impedance values can decrease significantly as the number of cells in parallel increases, it is highly likely that this diagnostic will cease to function after a certain number of parallel cells has been reached.

4.7 Battery Post-Mortem Analysis

Non-destructive state-of-health monitoring techniques such as the impedance modeling described in this paper, derivative capacity, and acoustic response modeling require complex analysis specific to cell chemistry and configuration which can be time-consuming and lack physical confirmation of the model assertions. The use of techniques traditionally used for medical diagnostics such as X-ray imaging can support not only post-mortem analysis but manufacturer quality control checks. This has been successfully used extensively in the fuel cell, energy storage, and energy conversion industries. Some battery researchers have also used the technique for studying lithiation/delithiation behavior and electrode fabrication, as well as diagnosing thermal runaway [1]. None of these studies, however, were devoted to diagnosing cell failure after an experiment designed specifically to evaluate cell life with a high C-rate pulse discharge profile. The following section was performed as a collaborative effort with the NRL Chemistry Division and was published as [1].

4.7.1 Non-destructive X-ray CT

Three batteries from the experimental sets were selected for post-mortem analysis: calendar aging control, single-cell cycled at 10C, and baseline parallel. Three different length scales were used to examine the cells on the compact CT. First, a “battery scale” was used to perform a non-destructive, 3 hour scan at 140 keV that rendered the entire interior of the battery with a pixel size of 9.77 μm, and is shown in Figure 4.71. This data was used to identify potential key areas of the cell for later investigation when the cell was opened, both visually and for coupons to use on more

detailed scans. The coupons were ≈0.5 x 1.0 cm sections of the electrode film, and were scanned at 80 keV for approximately three hours to obtain volume renderings of 4 x 4 mm with a pixel size of 2.37 µm, and is shown in Figure 4.72. A final scan used the Zeiss software to identify regions of interest on the coupon, and a long scan at 80 keV of > 20 hours was used to obtain data in an ≈0.2 x 0.2 mm region with a pixel size of 0.218 nm, and is shown in Figure 4.73.

Macro-scale defects can be seen using the tomographic images of the center section of the battery, and observations about the manufacturing of the cell. The current collectors and active materials can be easily seen, as well as the positive and negative tabs. Using the imaging software, since the precise scale is known, measurements on the lengths of the electrode rolls can be performed. Dense materials such as copper and steel absorb more x-rays than softer materials such as graphite, and are lighter in color. During the calibration process, care is taken to ensure sufficient absorption occurs to avoid saturation of the detector. An x-ray source with energy too high for the subject will render analysis useless, and in some circumstances could damage the detector. A pure white pixel means the material has completely absorbed the x-ray energy.

Using the rendering software, this battery has 38 concentric rings without a mandrel, or coil-initiating, central material. The core of the jellyroll is hollow and is subject to potential collapse if the battery material is stressed. The jellyroll itself is comprised of a polymer separator, copper current collector that is coated on both sides with anode material (graphite with intercalated lithium ions), another polymer separator, and an aluminum current collector that is coated with cathode material ($LiFePO_4$) on both sides. The negative electrode is copper coated with anode material, and is composed of 4 roll lengths welded together end-to-end to form a single monolithic film. At each weld a negative tab is mounted, for a total of three negative tabs which can be seen in the bottom right of Figure 4.71. The positive electrode consists of five rolls with four tabs, which are most likely aluminum and can be seen as dark semi-circles in the cross section of Figure 4.74.

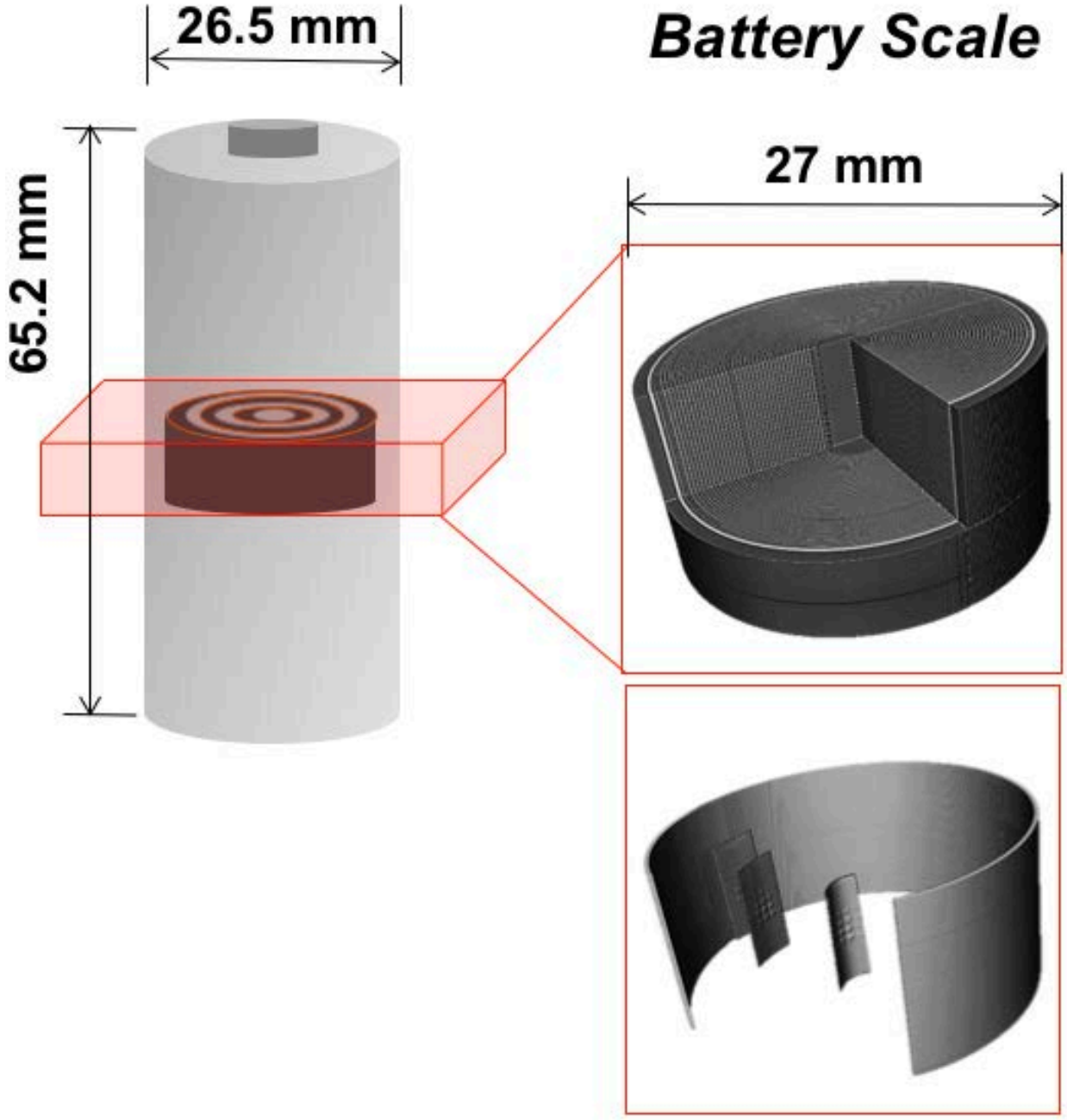

Figure 4.71: Example section of a CT image from a battery scale scan [1]

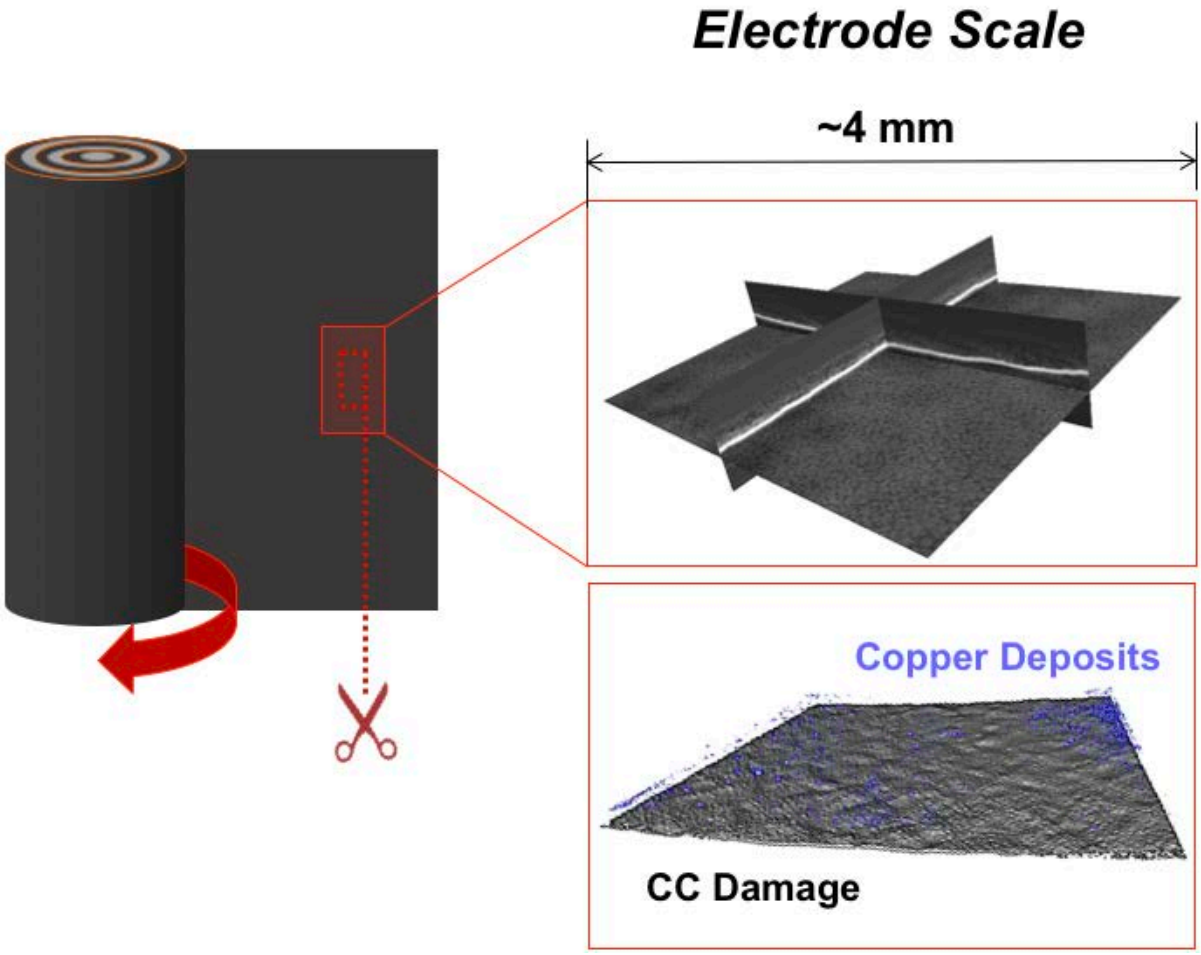

Figure 4.72: Electrode scale after opening the cell and extracting a coupon from the battery film [1]

A comparative investigation of the three different cells selected for analysis yielded little variation. Slight folds in the metal current collectors were observed, but the occurrence rate was not enhanced for any cell type versus another. Therefore, it can be concluded that macro-scale defects or features do not play a role in the capacity fade of the single-cell and parallel-cell samples. The battery rendered for Figure 4.74 was the 10C parallel cell, which reached end of life at 700 cycles, and can be considered near-pristine condition.

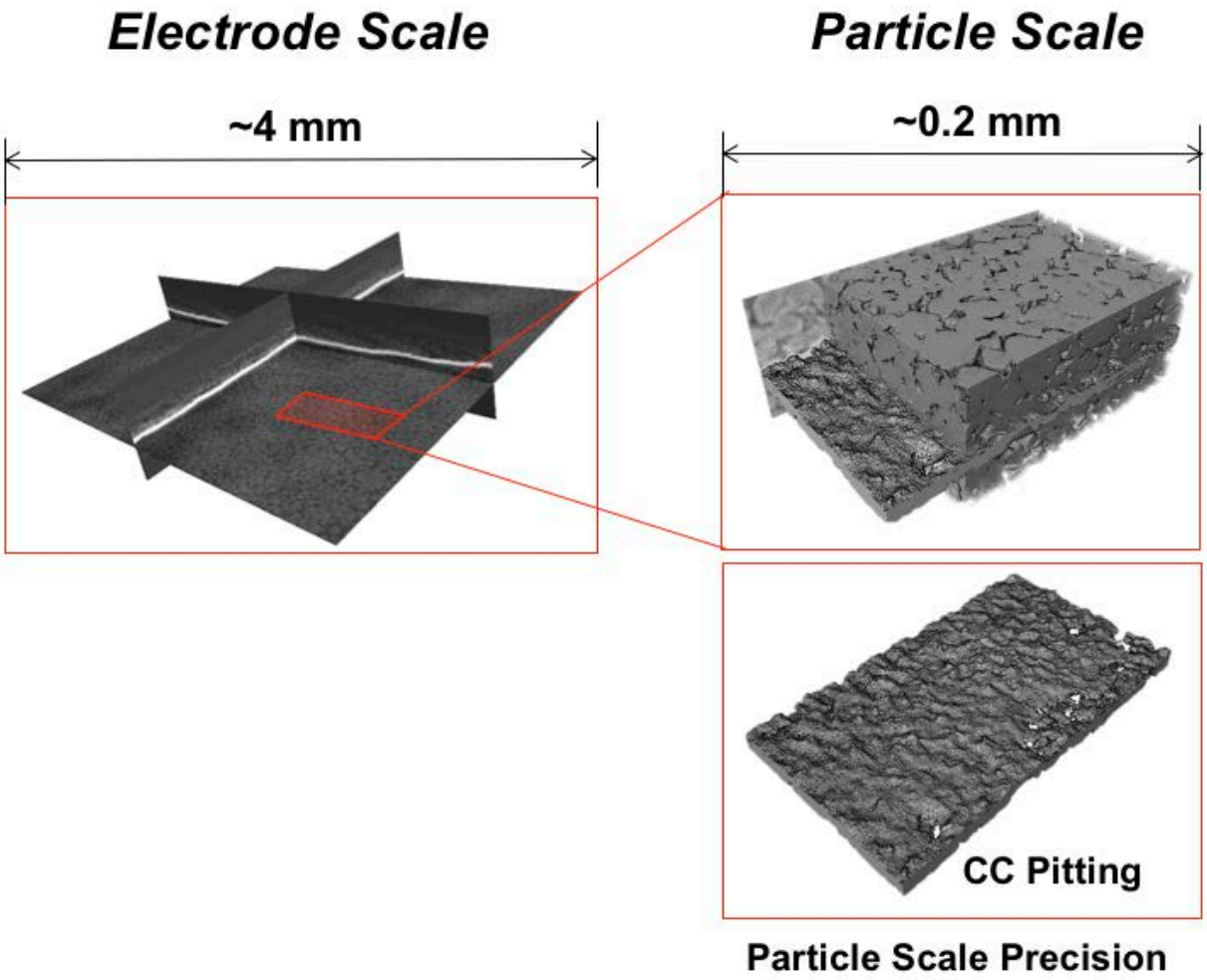

Figure 4.73: Extreme analysis of coupon after identification of areas of interest to identify particle types [1]

The intensity of the grey scale perpendicular to the rings, as shown in the lineout diagram of Figure 4.74, allows the verification of the battery jellyroll and estimation of the thickness of the stack and relative thickness of the component entities. Copper has the highest greyscale value (≈180) is observed as narrow peaks of thickness approximately the same width as the material. A valley with the lowest greyscale value (≈110) is indicative of the graphitic composite material. A low-intensity peak (≈125) can be correlated to the cathode composite, $LiFePO_4$, polymer binder, and conductive carbon. Finally, a narrow valley (≈121) indicates the aluminum current collector. The double-sided coating of the current collectors is confirmed by the bimodal nature of the lineout, and the similar thickness of the current collector and electrode materials with distinct material radiographic impedances ensures accuracy in distinguishing the layers.

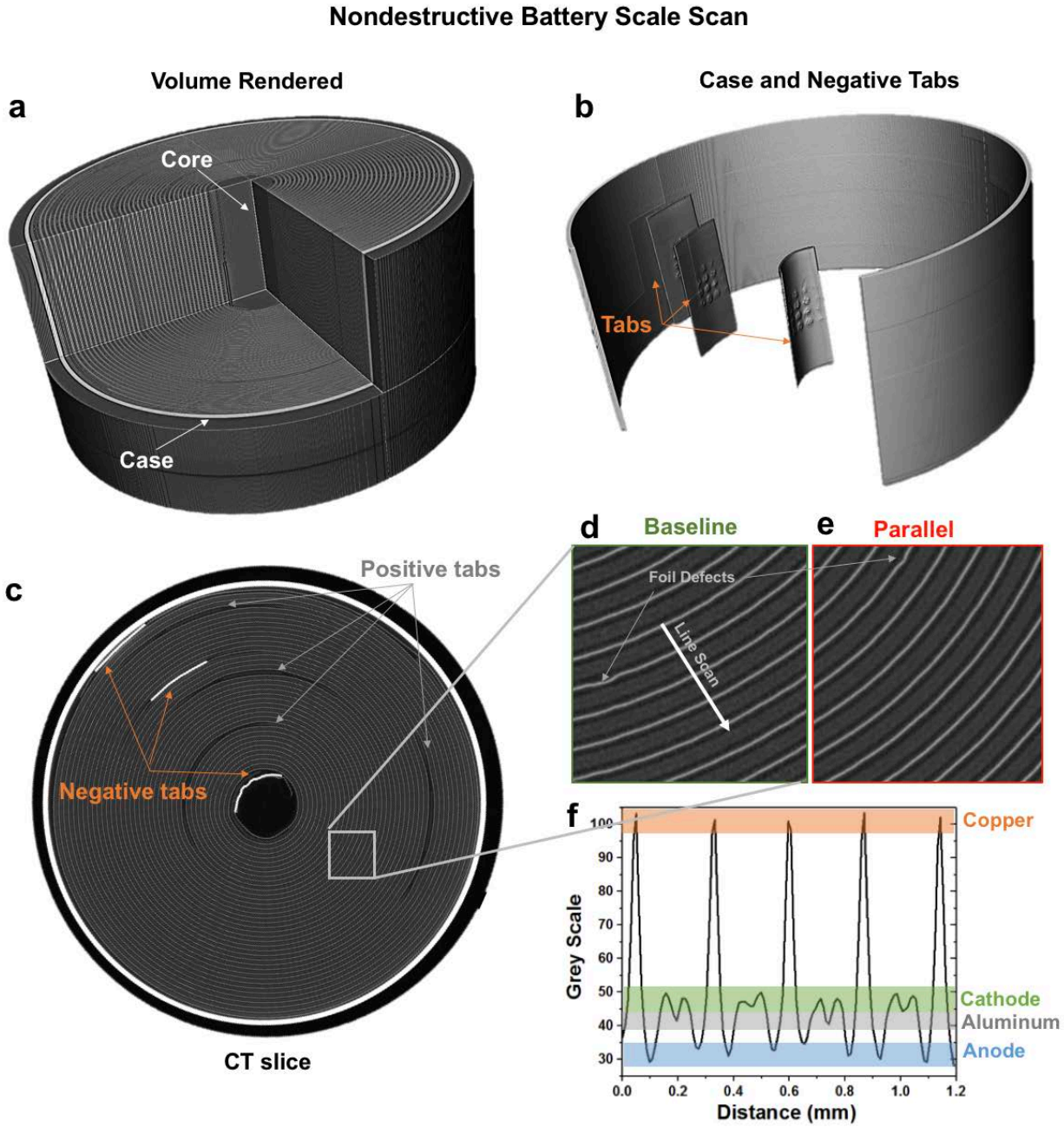

Figure 4.74: Non-destructive (a) volume-rendered X-ray CT of a cell cycled until end of life (EOL) in 4P1S array, (b) rendering of negative tabs and cell casing, (c) central slice of CT, (d,e) detail view of jellyroll for baseline and parallel cells, and (f) 8-bit greyscale lineout for jellyroll composition analysis [1]

4.7.2 Electrochemical Testing

The electrochemical response for each cycled battery needs to be examined to fully understand the implications of the physical phenomena observed in the post-mortem. The first and last five pulses for the single-cell cycling and parallel-cycled cells is shown in Figure 4.75, as well as the final cell discharge comparison for both batteries. The electrical behavior between the two cells is a sharp contrast, with the individually cycled cell exhibiting stable discharge current at the prescribed 10C rate and the parallel cell ≈0.7 A lower than the 26 A rate before shifting to ≈0.5 A higher at the end of the cycle. This deviation from the expected shared current is indicative of uneven current sharing between the four parallel cells.

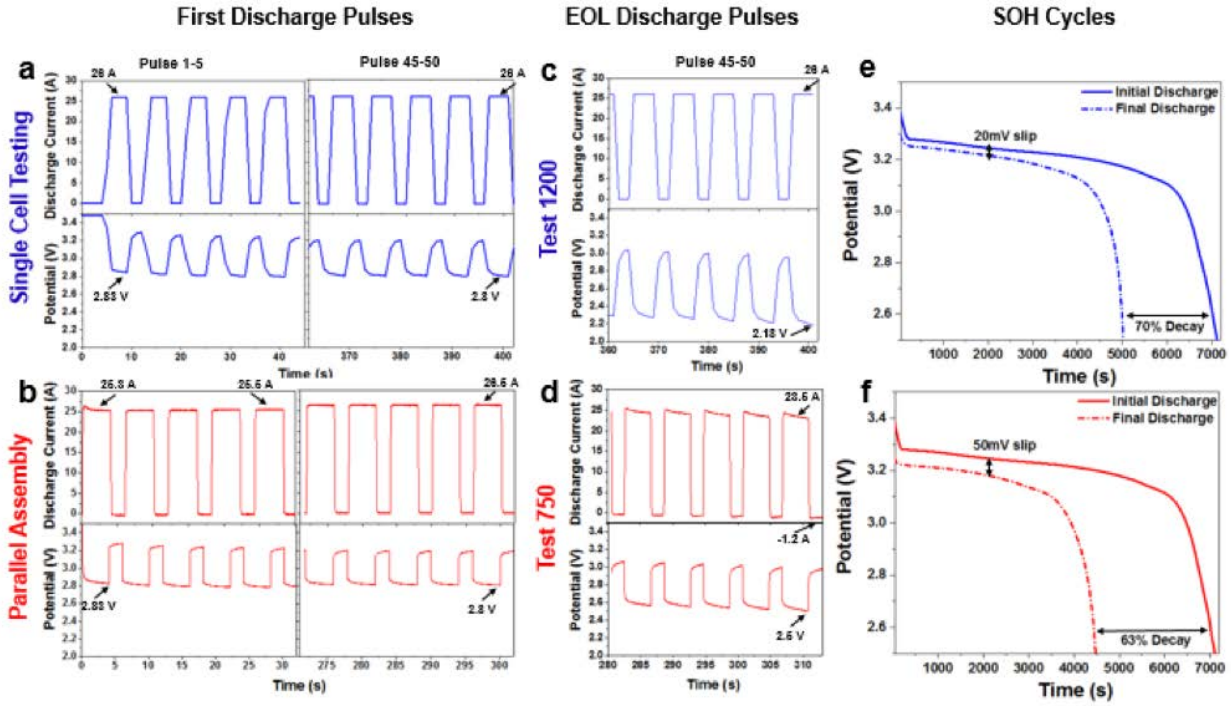

Figure 4.75: Current and voltage response from the first and last five pulses from the (a) single-cell cycling and (b) parallel cycled cell during the first cycle, (c-d) for the last cycle in the experiment for each cell, respectively, and the initial full discharge compared to final cell discharge before post-mortem for the (e) single-cell and (f) parallel cell. [1]

The voltage response of the single-cell battery drops from a fully charged state of 3.4 V to 2.83 V during the first pulse, and recovers by 0.46 V to 3.29 V before the second pulse. Near the end of the discharge cycle on the 50th pulse, the voltage drops to 2.8 V and recovers by 0.43 V to 2.32

V. At the completion of the 50-pulse cycle, the pulse potential and the voltage recovery in the open-circuit state had dropped by only 30 mV, preventing a low state of charge in the cell during the test. The parallel cell had similar voltage response in the first five pulses with an initial pulse potential of 2.83 V and a recovery of 0.45 V. By the 50^{th} pulse, the potential was 2.8 V during the discharge state and a recovery of 0.42 V.

The final pulses applied to the cells at the end of life are also shown in Figure 4.75. The final pulse on the single-cell cycled battery has a pulse potential of 2.18 V while maintaining the 26 A discharge current to the load after a deep voltage recovery of 0.75 V. In contrast, the parallel-cycled cell had a pulse potential of 2.5 V with a 0.5 V recovery, similar to the initial pulses on that array but at a reduced current of 23.5 A. Unlike the single-cell configuration, the parallel cell has current flowing in the load open-circuit state, dropping below 0 A by over an amp at the end of the cycle. This is a strong indication of internal balancing by the batteries in the array, with cells that have a higher resting potential charging the other cells to equilibrate the charge across the array.

Further examination of the pulse discharge behavior for the single-cell battery reveals that as the cell ages the potential drops closer to the lower bounds of the operational envelope. This indicates that the cell is experiencing a deep discharge and a low SoC at the end of the pulse cycle in order to maintain the 26 A discharge current. The degradation mechanism is typical of a combination of active material isolation, delamination, and SEI layer growth. In contrast, the parallel-cycled cell shows significantly less voltage drop but experiences fluctuating current magnitudes in discharge mode and inverse current flow during the open circuit periods. These current fluctuations are a result of cell pack current sharing with attempted voltage matching, and are the most likely cause of cell failure. This would lead to the conclusion that the post-mortem condition of the parallel cell will be less conventional than the single-cell battery.

On the far right of Figure 4.75 is a comparison between the two cells with the first and last cycle voltage performance curves. The parallel-cycled cell has an ≈7% greater capacity fade in addition to a 30 mV deeper voltage slip. Gradual voltage slip is to be expected, particularly with high C-rate discharges where the over-potential is enhanced. The slip is due to a shift in the reaction potential between the anode and the cathode, caused by degradation of both battery components. The slip in the parallel-cycled cell, ≈5.5% of the operating voltage range, could have allowed copper dissolution and deposition. If the operating voltage range is kept constant, the

discharge curve can slip down and charge up. This can cause copper oxidation, which should normally occur outside charge bounds of the cell (≈3.9 V) can now occur inside the voltage bounds with the change in relative potentials. In a subsequent discharge the copper would reduce the cathode inside the voltage bounds at ≈3.3 V.

4.7.3 Battery Deconstruction

While non-destructive testing is the ideal diagnostic to study a battery without disturbing the components, the steel case and the cylindrical nature of the jellyroll impede further study. However, the destructive post-mortem enables confirmation of the speculations in the previous section. The cell was breeched as described in Chapter 3, with a Dremel tool on the negative terminal. When the bottom section of the cell was cut off, three tabs were observed to connect the jellyroll to the bottom terminal, which matched the CT images. At the opposite end, four tabs were observed to connect to the positive terminal of the battery. The roll was removed from the casing and carefully unfurled in the dry room. A detailed view of the procedure, as well as the polymer separator, anode, and cathode can be seen in Figure 4.76.

The cathode material for all three cells were visually pristine and free of defects, and are indicative of high-quality manufacturing. The anode material presented the most noteworthy features. Slight damage on the anode where the active material was aligned with the positive tabs was observed on all three cells. The individually cycled cell had anode delamination at the edges of the cell, which may have been responsible for gradual capacity fade. An orange tinge on the surface of the anode, particularly through the center of the material, indicates some level of Stage I lithiation. It is possible the coloration is a result of lithiated material rendered inactive over the cycling period, which would manifest electrically as capacity fade with the removal of charge carriers from the cell. Other than the edge delamination and the partial lithiation, the individually-cycled cell resembled the control anode. The parallel-cycled cell, however, had copper deposits across the surface of the anode and the adjacent polymer separator. These are further indications of the suspected cell voltage slipping previously discussed.

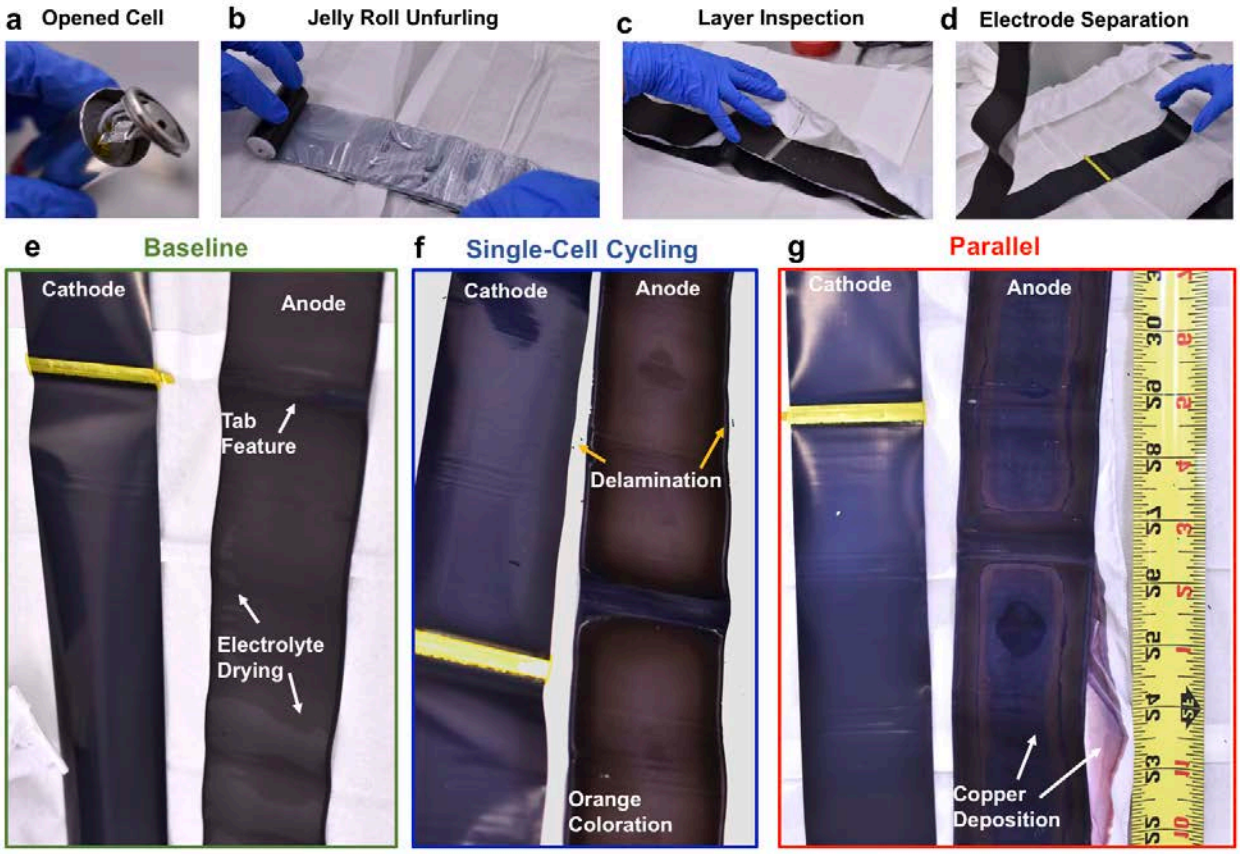

Figure 4.76: Post-mortem photographs of a cell after opening with (a-d) typical procedure for exposing the layers, electrode surfaces for the (e) uncycled baseline, (f) individual-cycled, (g) parallel-cycled cells. [1]

4.7.4 Cathode Characterization

While the visual inspection of the positive electrode in all three cells revealed high film quality and little degradation with increased cycling rates, a further study was desired. Coupons from each electrode were collected and assessed at the electrode scale for investigation. The typical particle size of $LiFePO_4$ is ≈300 nm in diameter, so the resolution at this scale can only resolve larger features but not the individual particles. Analysis of scans from all three samples yielded little variation, confirming visual inspection and perception of the high quality of the material.

The CT scans were rendered as volume slices, and the composite coating on each side of the aluminum current collector can be seen in Figure 4.77. The composite appears to be quite uniform at this scale, as well as compact and possesses minimum void space. These are features known to be conducive for effective high-power performance, as the effective surface area is increased to

maximize the charge transfer rate. Some bright regions are observed, which may be indicative of delithiated iron phosphate, which would appear radiographically dense. If a threshold analysis is performed, where the brightest areas are filtered out, the volume of these delithiated is estimated to be at ≈3%, excluding edge effects. The relatively low volume percentage is confirmation that the delithiated iron phosphate will minimally impact performance, despite being electrochemically inactive.

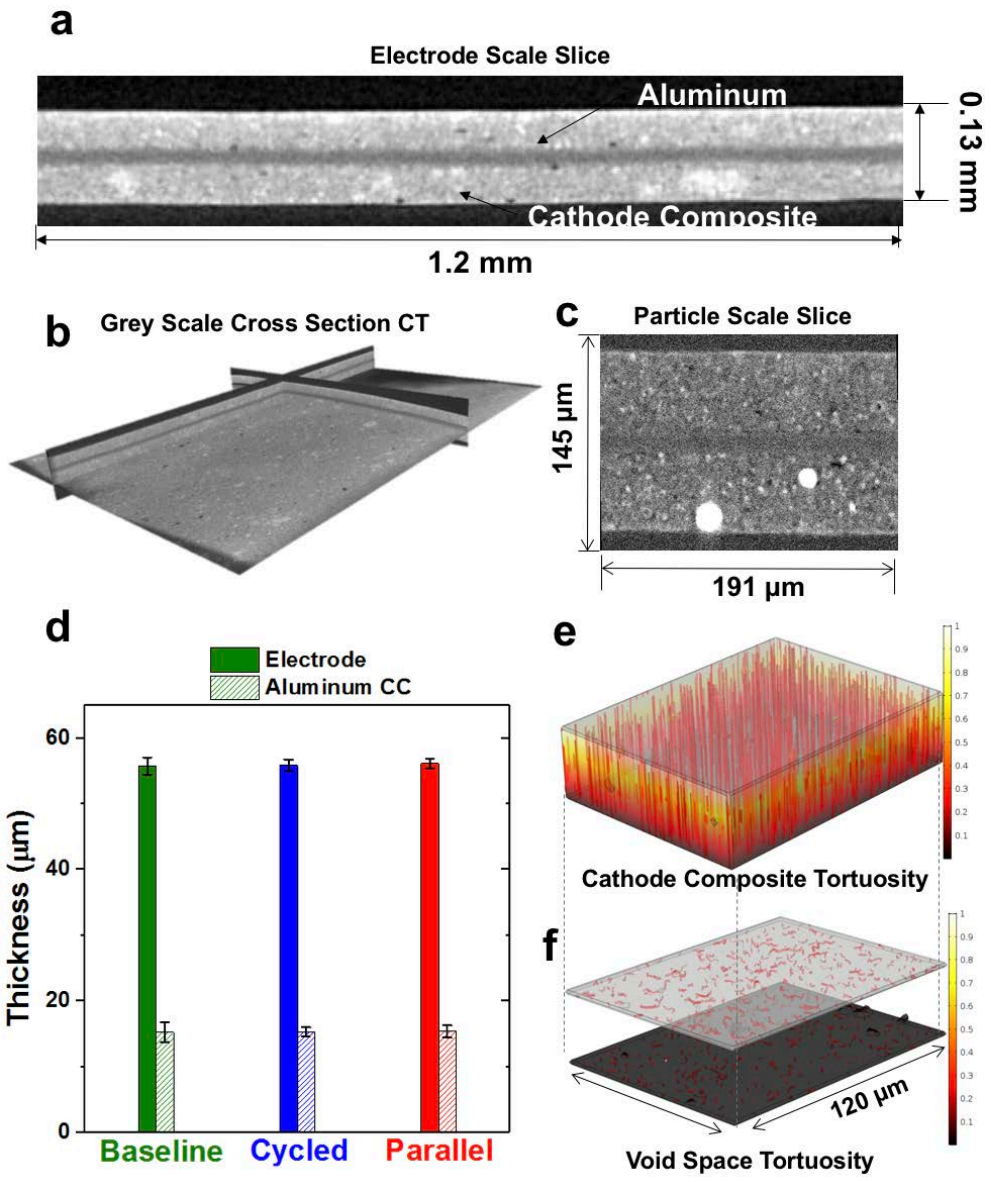

Figure 4.77: Cross-sectional CT slices (a,b) of the baseline cell cathode, with a particle scale slice (c), calculated electrode and current collector thickness averaged over 10 regions for each cell type (d), and tortuosity through the active material (e) and void space (f). [1]

The software package imageJ, a specialized open-source multidimensional image processor, was used to estimate the current collector and electrode thickness across 10 unique areas of the scan by analyzing the contrast thresholds of the radiographic data. The resulting calculations show minimal change to the electrode thickness and current collector, which eliminate any concerns for electrode swelling, delamination of the active material, or current collector damage. A plug-in for imageJ, BoneJ, was used to produce 3D meshes based on the thresholded rendering of the electrode material [100]. The resulting meshes were imported in to COMSOL for computation of tortuosity through the active material and void space, and are seen in Figure 4.77. The tortuosity for the composite material was calculated to be 1.02, which is due to the compact uniform nature of the composite material and can be considered extremely low. In contrast, the tortuosity for the void space approaches infinity with an estimated value of 6E27. Based on the micro-scale inspection, thickness study, and tortuosity calculations from the electrode-scale scans of the positive electrodes, the $LiFePO_4$ cathode is not responsible for cell degradation.

4.7.5 Anode Characterization

A cross-sectional comparison of the baseline electrode to the parallel-cycled electrode is shown in Figure 4.78, and appears to indicate the same electrode structure on both cells, but with some additional features on the parallel-cycled cell. Graphite particles for both cells are approximately the same size, assembled with similar composite porosity, and appear to coat the copper current collector to about the same thickness. The polymer separator presence is apparent on the parallel-cycled cell, as the copper deposit caused the separator to adhere tightly to the electrode surface. In contrast, the baseline and individually-cycled cells do not show any signs of bonding to the separator. To ensure integrity of the sample, the coupons were analyzed in the CT machine with the separator intact on both sides to prevent damage introduced by removing the material. In the parallel-cycled cell renderings, copper deposits of various sizes can be observed on the separator material.

The graphite active particles at the 2.37 µm/pixel scale can be resolved as small as 6 µm in diameter, unlike the scale used for the cathode material. This enables for the first time in the literature a study of a graphite anode without removal of the copper foil using X-ray tomography. The relatively high difference in radiographic impedance between the copper and graphite

materials made 3-D reconstruction difficult, but both materials were effectively rendered with adjustments to the exposure times. In particular, more radiographs in the cross-sectional view were required than in the axial view. Once the data was acquired, the marked difference in grayscale values for the different materials allowed for the isolation thresholding of the copper and graphite.

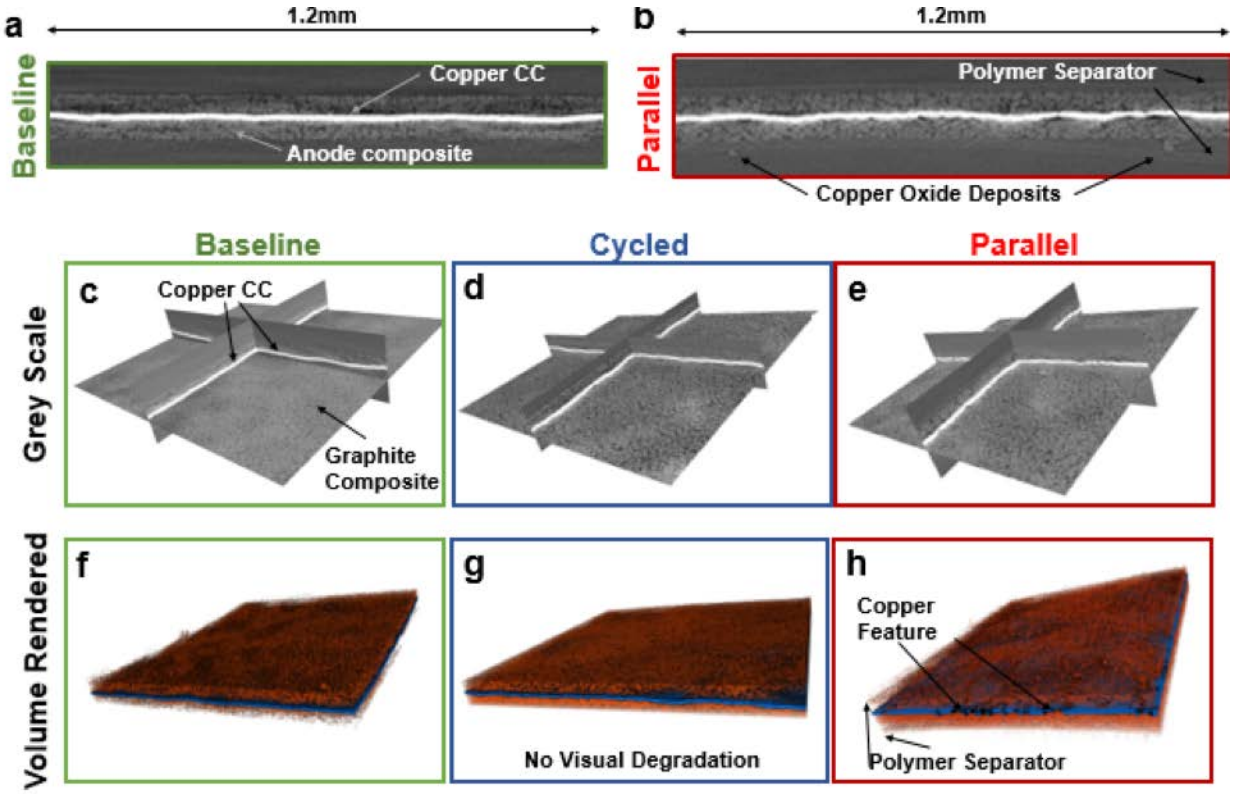

Figure 4.78: Cross sectional CT slices of baseline (a) and parallel-cycled (b) cells, 3D cross sections of (c) baseline, (d) individual-cycled, and (e) parallel-cycled cells, and volume renders highlighting graphite cells orange and copper current collector blue, respectively (f-h) [1]

The graphite is orange and the copper blue on each volume rendered for the three cell samples, as shown in Figure 4.78. Very little difference is observed between the baseline and individually-cycled cells. It is important to note that these samples were taken from the center of the electrode and do not reflect the delamination observed at the edges. Another feature observed from the physical examination was partial delithiation on the electrode surface, manifested as an orange color. If the capacity fade in the individually-cycled cell was due entirely to deactivated, partially-lithiated graphite, the anode would only exhibit an overall volume change of ≈1%, as it would

originate from a 5% fully lithiated volume expansion in 20% of the graphite. The low volume change would not be observable from this technique with sufficient accuracy to derive a definitive conclusive statement on partial delithiation as a cause of capacity fade. The most likely cause of cell failure in the individually-cycled cell is a combined effect of edge delamination and gradual deactivation of some anode and cathode material, resulting in routine battery failure of the $LiFePO_4$ cell.

The parallel-cycled cell, however, did suffer a non-standard battery failure, with new features observed throughout the copper current collector, as shown in Figure 4.79. Pits and scratch-like features are observed throughout the copper, in addition to copper deposits throughout the separator material. The damage to the copper current collector suggests the deposited material originated at the adjacent current collector before migrating towards the cathode surface. Despite the electrical data to the contrary, the data suggest the cell was operated in an over-discharge condition, evidenced by the copper dissolution and deposition and the current understanding of this phenomenon [76, 101].

The copper current collector was rendered as grey with purple deposits in Figure 4.79a. The copper damage appears to resemble pitting and correlates spatially to regions of dense particle deposition. The damage is macro-scale, and can be observed on a 2-D radiograph as seen in Figure 4.79b. The distinct copper morphology can be analyzed with the need to perform elaborate preparation of the cell coupons, a unique ability that enables better correlation between observed morphological changes, electrical data, and non-destructive techniques such as EIS.

Deeper analysis of the electrodes was performed to identify a root cause of the failure. Various calculations were performed on each electrode coupon sample to determine if the porosity, tortuosity, or particle size played a role in the copper damage, and the results are tabulated in Table 4.10. The copper thickness was calculated using the same method as the aluminum in the cathode, revealing an average thinning of ≈0.4 μm (3%) in the parallel-cycled cell, attributable to copper dissolution. The graphite particle size was analyzed, but yielded no appreciable variation between each coupon. This result was not unexpected, as the intercalation of graphite only delivers an ≈5% volume change, and the cells were fully discharged prior to being opened. The tortuosity of the active material and the void were analyzed last. The tortuosity through the active material was

reduced by 4% for the two cycled cells, which is expected when during the lithiation process the composite material “opens” slightly to enable optimal performance.

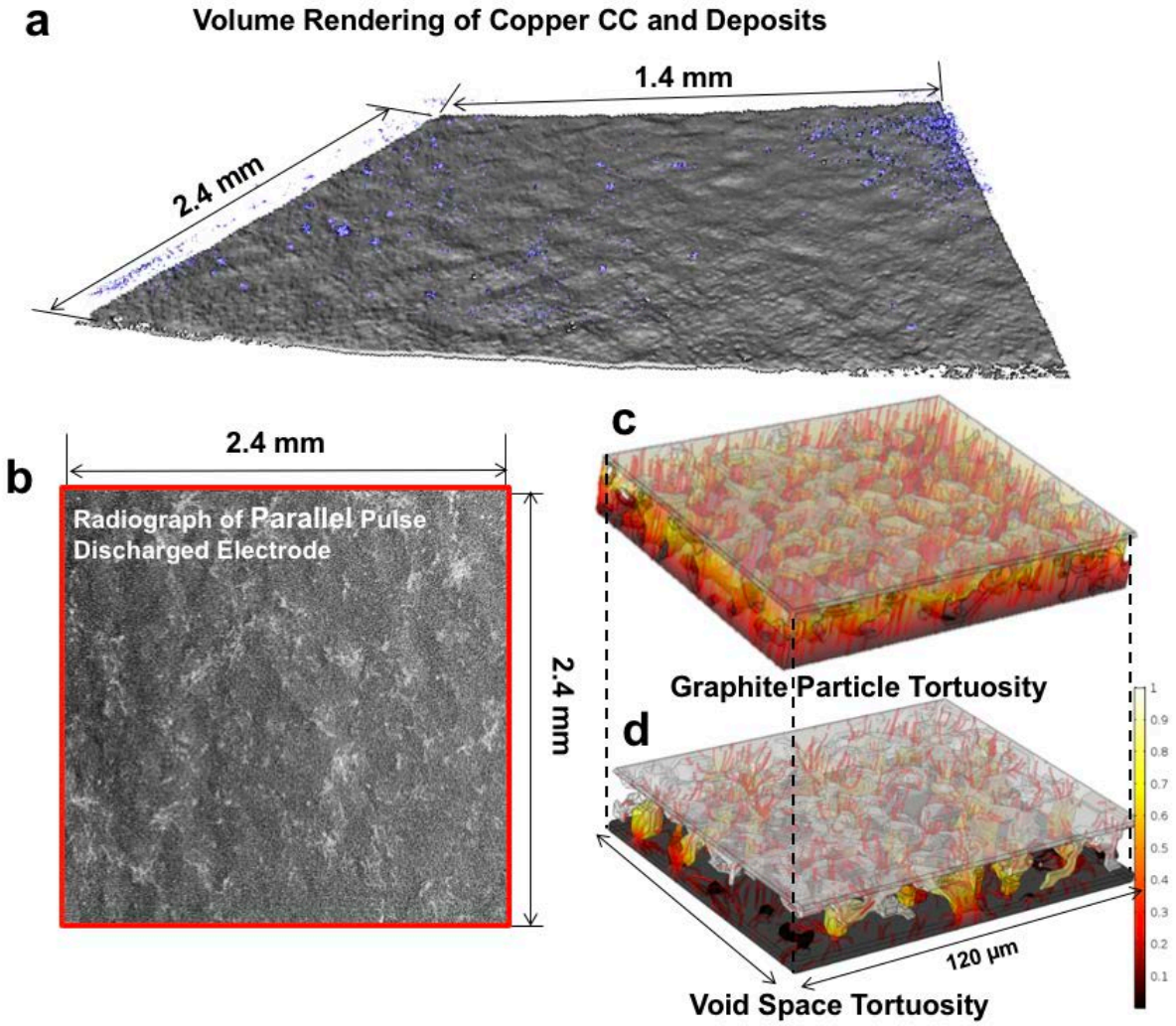

Figure 4.79: Electrode-scale analysis of copper damage, with (a) volume rendering of the copper current collector (grey) and copper deposits (purple), (b) radiograph of electrode revealing damage without rendering, and tortuosity through (c) graphic particles and (d) void space. [1]

TABLE 4.10: CALCULATED VALUES FOR EACH CELL SAMPLE [1]

	Copper CC Thickness		Graphite Particle		Active Material Tortuosity		Void Space Tortuosity	
Sample	nm	σ	nm	σ	a.u.	σ	a.u.	σ
Baseline	14.01	0.44	5.55	1.09	1.23	0.14	5.40	1.27
Individual-Cycle	14.18	0.55	5.47	1.06	1.18	0.02	5.7	0.77
Parallel-Cycle	13.58	0.29	5.54	1.19	1.18	0.06	5.10	0.69

Particle-scale scans of the baseline and parallel-cycled cells were acquired to further investigate differences between the two batteries at a much smaller scale. The samples were volume rendered, and are shown in Figure 4.80. The baseline anode, Figure 4.80a, shows a uniform distribution of graphite and a pristine copper current collector. This assertion is further reinforced with a transverse CT slice through the current collector in Figure 4.80c, as well as the volume rendering shown in Figure 4.80d. Some of the graphite features are observable at each surface of the copper, most likely due to the metal's high degree of malleability and the ultra-thin (≈14 μm) thickness.

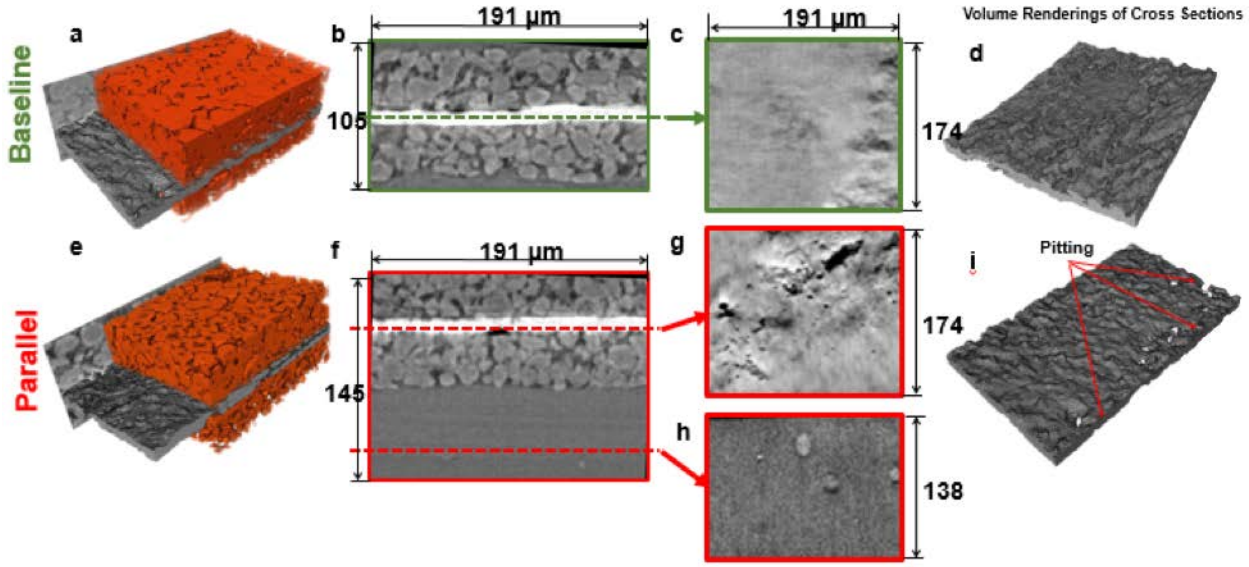

Figure 4.80: Particle-scale rendering comparison of a baseline cell and parallel-cycled cell (a, e) with the graphite in orange, cross section slice of the electrode (b, f), transverse slice through the copper layer (c, g), trilayer separator with copper deposits (h), and volume renders of the cross sections (d, i). [1]

The parallel-cycled cell CT render reveals pitting damage visible in the full-electrode render seen in Figure 4.80e. Slices through the copper seen in Figure 4.80g reveal significant pitting. The tri-layer polymer separator seen in Figure 4.80h has a range of deposit sizes and morphologies. The detailed rendering of this small volume exposes the extent of the copper damage, as the pitting completely penetrates the copper in several locations. This has several implications on battery safety, as current collector damage will reduce the surface area and create enhancement points, further increasing the damage to the cell. Additionally, field lines may be altered resulting in additional accelerated damage to the cell.

Clearly, operating cells in a parallel array at high discharge rates causes physical damage to the cell structure as well as reducing the expected lifetime of the array when compared to operating the same battery in a single-cell array. This work has developed a tool that is capable of diagnosing the dissolution of copper in the anode electrode, and will shed light on the risk associated with operating cells in parallel without additional safety mitigation. The spacial understand of the dissolution phenomenon and combined visualization of the interior copper damage will support research to develop better batteries design for high-power operation.

Chapter 5

Conclusions and Future Work

A series of experiments were performed to evaluate the performance of a 4P1S battery array using electrochemical impedance spectroscopy to identify key frequencies that may describe battery state of health at any state of charge. Using a large sample number of cells, the state of health frequency, f_{SoH}, for these $LiFePO_4$ 26650 cells is found to be 158 Hz. Four experiments were performed to evaluate the lifetime in different configurations: single-cell at 1C (2.6A), single-cell at 10C (26A), four cells in parallel at 10C (ideal match), and four cells in parallel (manufacturer match). The lifetime for each experiment set degraded substantially, with the final parallel series reaching end of life at 400 cycles, a 75.32% reduction in life compared to operating solo. Analysis of the f_{SoH} data for these cells revealed a change in imaginary impedance at the critical frequency that corresponded to changes in the capacity and current data, supporting the development of a single-frequency diagnostic tool. An electrochemical model of the battery was generated, and it indicated the anode material was aging faster than the SEI layer, the opposite of normal cell degradation. A post-mortem analysis of cells from three configurations (baseline, single-cell, and parallel-cell) supported the modeling, as physical damage to the copper current collector in the anode was visible in the parallel-connected cell.

Two hypotheses were proposed at the beginning of this work. First, it was hypothesized that a single-point impedance value can be correlated to cell aging when 26650 $LiFePO_4$ cells were

cycled in a standard, non-abusive pulsed discharge profile. This hypothesis was proven to be true in general. When the f_{SoH} is applied to the eight cells operated at 10C in the solo configuration, a profile was generated that described the typical impedance response that can be expected for any 26650 $LiFePO_4$ cell. The response will have an increasing slope, a plateau, and a decreasing slope. The point where the slope levels into a valley is where the cell has reached electrochemical end of life, and is typically very close to the 20% capacity loss limit for removing a cell from service. When this diagnostic is used on cells connect in parallel, a similar profile was generated, albeit with different cycle number endpoints. However, the diagnostic was proven to correctly predict battery end of life in nearly all of the experimental arrays. The diagnostic has been shown to function when analyzing all four cells in parallel, however the reduced impedance may reach a point where too many cells are connected for the instrument to successfully extract useful impedance information.

The second hypothesis was that four cells connected in parallel that were electrochemically identical using ESR, capacity, and EIS as filter mechanisms would share current evenly in an array with a high discharge rate. This was disproven, as the baseline parallel array was shown to create a disparity in energy sourced per cell per cycle after approximately 150 charge-discharge cycles. The corollary hypothesis was proven to be partially true, however. The replicant parallel arrays all demonstrated unbalanced operation with the first discharge cycle, and this continued throughout the experiment. The imbalance of the array accelerated capacity loss and resulted in a 75.32% reduction in lifetime compared to the single-cell experiment, and a 43% reduction in life compared to the baseline parallel array. The ESR imbalance hypothesis was not proven, as the X-ray computed tomography demonstrated that the dissolution of the copper electrode was the primary driver of aging and capacity loss.

X-ray computed tomography was used with this work to diagnosis the failure mode in two identical cells operated with the same pulse discharge conditions but in different configurations, one as a single-cell discharging into a load, and the other as part of a 4-cell parallel array. For the first time in the literature, volume rendering of the electrochemical dissolution and re-deposition of copper was accomplished without the need for disturbing the active material after a cell has been opened for analysis. The ability to analyze an anode or cathode coupon without disturbing the layers enables the direct correlation of physical effects to non-destructive testing such as

electrical data and EIS measurements. The CT data show a cell operated in parallel at high C rates will experience the effects of over-discharge without the electrical data indicating over-discharge has occurred, which is a traditional battery health management parameter. The knowledge of this phenomenon occurring will prevent catastrophic failures from occurring, as it can be further studied and additional metrics added to a battery management system.

This work has addressed the question of current sharing in a parallel cell array at high discharge rate, but there are many open questions remaining that can be addressed in future work. First, it would be highly desirable to repeat the parallel testing with EIS probes permanently attached to the experimental apparatus. The question of the effect of the changes in contact resistance and to some extend the slight changes in inductance due to the movement of the probe wires needs to be addressed to increase the confidence factor in the data obtained in this work. Additionally, the discharge experiment needs to be fully automated to avoid the extended rest periods observed in the data. Ideally access to an industrial cycler such as a MACCOR Series 4000 would also allow for automated collection of capacity, EIS, and ESR data between cycle groups.

Expansion of the f_{SoH} diagnostic to other chemistries and form factors would be a natural extension of this work. When compared to the data described in [3, 4], it appears the physical size of the cell has a direct effect on the f_{SoH} for that form factor, as the 18650 has an identified frequency of 316 Hz compared to the 158 Hz identified in this work. Further research needs to be conducted with 18650 $LiFePO_4$ and 26650 $LiCoO_2$ cells to determine the full extent of the influence of form factor versus chemistry.

Finally, expanding the X-ray computed tomography technique to more cells would provide invaluable insights. A carefully designed experiment would select a large group of closely matched cells and construct several 4P1S arrays to be discharged in the same profile as this work. At specified intervals, one of the arrays would be disassembled and the electrodes analyzed on all of the cells. Given enough parallel arrays, one could develop a model of the degradation of the copper as a function of cycle and capacity loss, potentially identifying the critical point where the array becomes unsafe to operate. If used with EIS spectra, it is possible a critical feature could be identified that would eliminate the need for destructive post-mortems and enable on-the-fly safety monitoring for batteries in parallel for this specific issue.

Bibliography

[1] R. Carter, B. M. Huhman, C. T. Love, and I. V. Zenyuk, "3D X-ray Computed Tomography Comparison of Individual and Parallel Assembled Commercial LFP Batteries at End of Life after High Rate Cycling," *Advanced Energy Letters,* Submitted for Publication.

[2] C. T. Love and K. Swider-Lyons, "Impedance Diagnostic for Overcharged Lithium-Ion Batteries," *Electrochemical and Solid-State Letters,* vol. 15, no. 4, pp. A53-A56, January 1, 2012 2012.

[3] N. S. Spinner, C. T. Love, S. L. Rose-Pehrsson, and S. G. Tuttle, "Expanding the Operational Limits of the Single-Point Impedance Diagnostic for Internal Temperature Monitoring of Lithium-ion Batteries," *Electrochimica Acta,* vol. 174, pp. 488-493, 8/20/ 2015.

[4] C. T. Love, M. B. V. Virji, R. E. Rocheleau, and K. E. Swider-Lyons, "State-of-health monitoring of 18650 4S packs with a single-point impedance diagnostic," *Journal of Power Sources,* vol. 266, pp. 512-519, 11/15/ 2014.

[5] S. S. Zhang, K. Xu, and T. R. Jow, "The low temperature performance of Li-ion batteries," *Journal of Power Sources,* vol. 115, no. 1, pp. 137-140, 2003.

[6] G. Park, H. Nakamura, Y. Lee, and M. Yoshio, "The important role of additives for improved lithium ion battery safety," *Journal of Power Sources,* vol. 189, no. 1, pp. 602-606, 2009.

[7] S.-i. Tobishima and J.-i. Yamaki, "A consideration of lithium cell safety," *Journal of Power*

Sources, vol. 81, pp. 882-886, 1999.

[8] J. P. Schmidt, T. Chrobak, M. Ender, J. Illig, D. Klotz, and E. Ivers-Tiffee, "Studies on LiFePO4 as cathode material using impedance spectroscopy," (in English), *Journal of Power Sources,* vol. 196, no. 12, pp. 5342-5348, Jun 15 2011.

[9] A. Jossen, "Fundamentals of battery dynamics," *Journal of power sources,* vol. 154, no. 2, pp. 530-538, 2006.

[10] C. Wang, A. J. Appleby, and F. E. Little, "Charge–discharge stability of graphite anodes for lithium-ion batteries," *Journal of Electroanalytical Chemistry,* vol. 497, no. 1, pp. 33-46, 2001.

[11] F. Nobili, F. Croce, B. Scrosati, and R. Marassi, "Electronic and electrochemical properties of LixNi1-yCoyO2 cathodes studied by impedance spectroscopy," (in English), *Chemistry of Materials,* vol. 13, no. 5, pp. 1642-1646, May 2001.

[12] X. Y. Qiu *et al.*, "Electrochemical and electronic properties of $LiCoO_2$ cathode investigated by galvanostatic cycling and EIS," *Phys Chem Chem Phys,* vol. 14, no. 8, pp. 2617-30, Feb 28 2012.

[13] F.-M. Wang, H.-Y. Wang, M.-H. Yu, Y.-J. Hsiao, and Y. Tsai, "Differential pulse effects of solid electrolyte interface formation for improving performance on high-power lithium ion battery," *Journal of Power Sources,* vol. 196, no. 23, pp. 10395-10400, 2011.

[14] T. Momma, M. Matsunaga, D. Mukoyama, and T. Osaka, "Ac impedance analysis of lithium ion battery under temperature control," (in English), *Journal of Power Sources,* vol. 216, pp. 304-307, Oct 15 2012.

[15] N. S. Zhai, M. W. Li, W. L. Wang, D. L. Zhang, and D. G. Xu, "The Application of the EIS in Li-ion Batteries Measurement," *Journal of Physics: Conference Series,* vol. 48, no. 1, p. 1157, 2006.

[16] S. L. Wu, H. C. Chen, and S. R. Chou, "Fast Estimation of State of Charge for Lithium-Ion Batteries," (in English), *Energies,* vol. 7, no. 5, pp. 3438-3452, May 2014.

[17] T. L. Kulova, V. A. Tarnopol'skii, and A. M. Skundin, "The impedance of lithium-ion batteries," (in English), *Russian Journal of Electrochemistry,* vol. 45, no. 1, pp. 38-44, 2009/01/01 2009.

[18] J. G. Zhu, J. G. Zhu, Z. C. Sun, X. Z. Wei, and H. F. Dai, "A new electrochemical impedance

spectroscopy model of a high-power lithium-ion battery," *RSC advances*, vol. 4, no. 57, pp. 29988-29998, 2014.

[19] M. Takahashi, S. Tobishima, K. Takei, and Y. Sakurai, "Reaction behavior of LiFePO4 as a cathode material for rechargeable lithium batteries," *Solid state ionics*, vol. 148, no. 3-4, pp. 283-289, 01/2002.

[20] G. Lindbergh, M. Klett, M. Behm, and R. Wreland Lindström, "Aging in Lithium-Ion Batteries," *Electrochimica acta*, vol. 110, p. 335, 2013.

[21] H. Oman, "Extracting pulse power from batteries," in Energy Conversion Engineering Conference, 1989. IECEC-89., Proceedings of the 24th Intersociety, 1989, pp. 1067-1071 vol.2.

[22] H. Oman, "Battery configurations for multi-megawatt pulse power," *Aerospace and Electronic Systems Magazine, IEEE*, vol. 5, no. 8, pp. 23-26, 1990.

[23] A. Attia, G. Halpert, D. Perrone, R. A. Vidas, and R. C. Miles, "The development of a sealed lead-acid battery for pulse power applications," in *Battery Conference on Applications and Advances, 1991. Proceedings of the Sixth Annual*, 1991, pp. 1-19.

[24] J. B. Cornette, "Investigation Of Battery Charged Capacitor Pulsed Power Systems for Electromagnetic Launcher Experiments," in *Pulsed Power Conference, 1991. Digest of Technical Papers. Eighth IEEE International*, 1991, pp. 782-785.

[25] T. Nagaura, *Progress in Batteries & Solar Cells*. Brunswick, OH: JEC Press Inc., 1991.

[26] V. Chaudhari et al., "Battery operated portable 300 kV pulsed power system," in Power Modulator Symposium, 2002 and 2002 High-Voltage Workshop. Conference Record of the Twenty-Fifth International, 2002, pp. 351-353.

[27] A. S. Rishi Verma, and Lakshmi Nair, "Development of battery powered 100kV dc power supply," *Review of Scientific Instruments*, vol. 77, 2006.

[28] R. J. Allen, C. N. Boyer, J. M. Neri, and M. Veracka, "Development of a 150-kW, Battery Powered, Rapid Capacitor Charger for a Small Railgun in Burst Mode Operation at 3 RPS," in *IEEE International Power Modulators and High Voltage Conference, Proceedings of the 2008*, 2008, pp. 106-108.

[29] R. J. Allen, C. N. Boyer, B. M. Huhman, J. M. Neri, and M. J. Veracka, "Progress toward a self-contained rapid capacitor charger for a small railgun in burst mode operation at 3

RPS," in *Power Modulator and High Voltage Conference (IPMHVC), 2012 IEEE International*, 2012, pp. 218-220.

[30] S. L. Holt, J. C. Dickens, J. L. McKinney, and M. Kristiansen, "A compact 5kV battery-capacitor seed source with rapid capacitor charger," in *Pulsed Power Conference, 2009. PPC '09. IEEE*, 2009, pp. 897-901.

[31] B. M. Huhman and J. M. Neri, "Investigations Into the Design of a Compact Battery-Powered Rep-Rate Capacitor Charger," (in English), *Ieee Transactions on Plasma Science*, vol. 41, no. 10, pp. 2659-2665, Oct 2013.

[32] B. M. Huhman, J. M. Neri, and D. A. Wetz, "Design of a battery intermediate storage system for rep-rated pulsed power loads," in *Electric Ship Technologies Symposium (ESTS), 2013 IEEE*, 2013, pp. 1-5.

[33] B. M. Huhman, J. M. Neri, D. A. Wetz, and L. Mili, "Development of a Rep-rated Capacitor Bank Utilizing Electrochemical Energy Storage," (in English), *2014 17th International Symposium on Electromagnetic Launch Technology (Eml)*, 2014.

[34] B. M. Huhman and D. A. Wetz, "Progress in the development of a battery-based pulsed power system," in *Electric Ship Technologies Symposium (ESTS), 2015 IEEE*, 2015, pp. 441-445.

[35] B. M. Huhman, D. A. Wetz, and L. Mili, "Development of a Rep-Rated Pulsed Power System Utilizing Electrochemical Prime Power," (in English), *Ieee Transactions on Plasma Science*, vol. 44, no. 12, pp. 3398-3408, Dec 2016.

[36] D. A. Wetz, D. A. Wetz, P. M. Novak, B. Shrestha, and J. Heinzel, "Electrochemical Energy Storage Devices in Pulsed Power," *IEEE transactions on plasma science*, vol. 42, no. 10, p. 3034, 01/2014.

[37] D. A. Wetz, D. A. Wetz, B. Shrestha, S. T. Donahue, and D. N. Wong, "Capacity Fade of 26650 Lithium-Ion Phosphate Batteries Considered for Use Within a Pulsed-Power System's Prime Power Supply," *IEEE transactions on plasma science*, vol. 43, no. 5, p. 1448, 01/2015.

[38] B. Shrestha, "Capacity fading induced on electrochemical energy storage cells as a result of high C discharge," Dissertation/Thesis, ProQuest, UMI Dissertations Publishing, 2013.

[39] Y. Y. Chen and A. Sitzman, "Testing a Lithium Ion Battery as a Pulsed Power Source," pp.

485-488: IEEE.

[40] G. Ning, B. Haran, and B. N. Popov, "Capacity fade study of lithium-ion batteries cycled at high discharge rates," *Journal of Power Sources,* vol. 117, no. 1, pp. 160-169, 2003/05/15/ 2003.

[41] N. Williard, "Degradation Analysis and Health Monitoring of Lithium-Ion Batteries," Master of Science, Mechancial Engineering, University of Maryland, College Park, MD, 2011.

[42] X. Gong, R. Xiong, and C. Mi, "Study of the Characteristics of Battery Packs in Electric Vehicles with Parallel-Connected Lithium-Ion Battery Cells," *Industry Applications, IEEE Transactions on,* vol. PP, no. 99, pp. 1-1, 2014.

[43] R. Gogoana, M. B. Pinson, M. Z. Bazant, and S. E. Sarma, "Internal resistance matching for parallel-connected lithium-ion cells and impacts on battery pack cycle life," *Journal of Power Sources,* vol. 252, no. 0, pp. 8-13, 4/15/ 2014.

[44] Z. C. Feng and Y. Zhang, "Thermal runaway due to symmetry breaking in parallel-connected battery cells," *International Journal of Energy Research,* vol. 38, no. 6, pp. 813-821, 2014.

[45] B. Han-Sik, L. Jeong-Min, M. Hyung-Soo, and C. Gyu-Ha, "Load sharing improvement in parallel-operated lead acid batteries," in *Industrial Electronics, 2001. Proceedings. ISIE 2001. IEEE International Symposium on,* 2001, vol. 2, pp. 1026-1031 vol.2.

[46] Z. Jiucai, C. Song, H. Sharif, and M. Alahmad, "Modeling Discharge Behavior of Multicell Battery," *Energy Conversion, IEEE Transactions on,* vol. 25, no. 4, pp. 1133-1141, 2010.

[47] M. Chin-Sien, N. Kong Soon, and H. Yao-Ching, "Parallel Operation of Battery Power Modules," *Energy Conversion, IEEE Transactions on,* vol. 23, no. 2, pp. 701-707, 2008.

[48] M. A. Roscher, O. S. Bohlen, and D. U. Sauer, "Reliable State Estimation of Multicell Lithium-Ion Battery Systems," *Energy Conversion, IEEE Transactions on,* vol. 26, no. 3, pp. 737-743, 2011.

[49] M. Guo and R. E. White, "Thermal Model for Lithium Ion Battery Pack with Mixed Parallel and Series Configuration," *Journal of The Electrochemical Society,* vol. 158, no. 10, pp. A1166-A1176, October 1, 2011 2011.

[50] J. Goodenough, "Rechargeable batteries: challenges old and new," (in English), *Journal of*

Solid State Electrochemistry, vol. 16, no. 6, pp. 2019-2029, 2012/06/01 2012.

[51] T. B. Reddy, *Linden's Handbook of Batteries*, 4th ed. New York, NY: McGraw-Hill Education, 2011.

[52] R. Spotnitz, "LITHIUM-ION BATTERIES The Basics," (in English), *Chemical Engineering Progress,* vol. 109, no. 10, pp. 39-43, Oct 2013.

[53] P. Singh, R. Vinjamuri, X. Wang, and D. Reisner, "Fuzzy logic modeling of EIS measurements on lithium-ion batteries," 2006, pp. 1673-1679: Elsevier.

[54] S. S. Zhang, S. S. Zhang, K. Xu, and T. R. Jow, "EIS study on the formation of solid electrolyte," *Electrochimica acta,* vol. 51, no. 8-9, pp. 1636-1640, 20/2006.

[55] A.-K. Hjelm and G. Lindbergh, "Experimental and theoretical analysis of LiMn 2O 4 cathodes for use in rechargeable lithium batteries by electrochemical impedance spectroscopy (EIS)," *Electrochimica acta,* vol. 47, no. 11, pp. 1747-1759, 2002.

[56] M. Itagaki, K. Honda, Y. Hoshi, and I. Shitanda, "In-situ EIS to determine impedance spectra of lithium-ion rechargeable batteries during charge and discharge cycle," *Journal of electroanalytical chemistry (Lausanne, Switzerland),* vol. 737, pp. 78-84, 01/2015.

[57] F. Gao and Z. Tang, "Kinetic behavior of LiFePO4/C cathode material for lithium-ion batteries," *Electrochimica acta,* vol. 53, no. 15, pp. 5071-5075, 01/2008.

[58] M. Petzl, M. Kasper, and M. A. Danzer, "Lithium plating in a commercial lithium-ion battery - A low-temperature aging study," *Journal of power sources,* vol. 275, pp. 799-807, 01/2015.

[59] P. Svens, S. Pontus, B. Mårten, and L. Göran, "Lithium-Ion Battery Cell Cycling and Usage Analysis in a Heavy-Duty Truck Field Study," *Energies (Basel),* vol. 8, no. 5, pp. 4513-4528, 01/2015.

[60] Y. Xie, Y. Y. Xie, J. Y. Li, and C. Yuan, "Mathematical modeling of the electrochemical impedance spectroscopy in lithium ion battery cycling," *Electrochimica acta,* vol. 127, pp. 266-275, 01/2014.

[61] J. Xu, C. C. Mi, B. Cao, and J. Cao, "A new method to estimate the state of charge of lithium-ion batteries based on the battery impedance model," *Journal of power sources,* vol. 233, pp. 277-284, 01/2013.

[62] E. Darcy, "Screening Li-ion batteries for internal shorts," (in English), *Journal of Power*

Sources, vol. 174, no. 2, pp. 575-578, Dec 6 2007.

[63] S. Santhanagopalan, P. Ramadass, and J. Zhang, "Analysis of internal short-circuit in a lithium ion cell," *Journal of Power Sources,* vol. 194, no. 1, pp. 550-557, 2009.

[64] W. Cai, H. Wang, H. Maleki, J. Howard, and E. Lara-Curzio, "Experimental simulation of internal short circuit in Li-ion and Li-ion-polymer cells," *Journal of Power Sources,* vol. 196, no. 18, pp. 7779-7783, 2011.

[65] G.-H. Kim, K. Smith, J. Ireland, and A. Pesaran, "Fail-safe design for large capacity lithium-ion battery systems," *Journal of Power Sources,* vol. 210, pp. 243-253, 2012.

[66] D. Lee, R. Patwa, H. Herfurth, and J. Mazumder, "Computational and experimental studies of laser cutting of the current collectors for lithium-ion batteries," *Journal of Power Sources,* vol. 210, pp. 327-338, 2012.

[67] C. Forgez, D. Vinh Do, G. Friedrich, M. Morcrette, and C. Delacourt, "Thermal modeling of a cylindrical LiFePO4/graphite lithium-ion battery," *Journal of Power Sources,* vol. 195, no. 9, pp. 2961-2968, 2010.

[68] B. M. Huhman, J. M. Neri, and D. A. Wetz, "Application of a Compact Electrochemical Energy Storage to Pulsed Power Systems," (in English), *Ieee Transactions on Dielectrics and Electrical Insulation,* vol. 20, no. 4, pp. 1299-1303, Aug 2013.

[69] B. M. Huhman, D. A. Wetz, B. Shrestha, and P. M. Novak, "Characterization of High Power Battery Cells and Analysis of Battery Module Cooling for Shipboard Pulsed Load Management," in *ASNE Day 2013*, Arlington, VA, 2013: American Society of Naval Engineers.

[70] B. M. Huhman, J. M. Heinzel, L. Mili, C. T. Love, and D. A. Wetz, "Investigation into State-of-Health Impedance Diagnostic for 26650 4P1S Battery Packs," (in English), *Journal of the Electrochemical Society,* vol. 164, no. 1, pp. A6401-A6411, January 1, 2017 2017.

[71] (2014, September 30). *NRL Commissions Small Railgun*. Available: https://www.nrl.navy.mil/media/news-releases/2014/nrl-commissions-small-railgun

[72] (2017). R44175, Navy Lasers, Railgun, and Hypervelocity Projectile: Background and Issues for Congress.

[73] Y. Kheng Tan and S. Panda, Review of Energy Harvesting Technologies for Sustainable

WSN. 2010.

[74] Y.-G., J.-S. Hu, and W. L.-J. Guo, "Nanostructured Materials for Electrochemical Energy Conversion and Storage Devices," *Advanced Materials,* vol. 20, pp. 2878-2887, 2008.

[75] D. L. Anderson. (2010) Lowering costs of lithium-ion batteries for EV power trains. *Sustainable Manufacturer Network.* Available: http://image.sustainablemfr.com/a/sage-supplier-lowering-costs-of-lithium-ion-batteries-for-ev-power-trains-cylindrical-cells-diagram.gif

[76] H. He *et al.*, "Failure Investigation of LiFePO4 Cells in Over-Discharge Conditions," *Journal of The Electrochemical Society,* vol. 160, no. 6, pp. A793-A804, January 1, 2013 2013.

[77] J. Vetter *et al.*, "Ageing mechanisms in lithium-ion batteries," (in English), *Journal of Power Sources,* vol. 147, no. 1-2, pp. 269-281, Sep 9 2005. Journal of Power Sources

[78] D. Aurbach, E. Zinigrad, Y. Cohen, and H. Teller, "A short review of failure mechanisms of lithium metal and lithiated graphite anodes in liquid electrolyte solutions," (in English), *Solid State Ionics,* vol. 148, no. 3-4, pp. 405-416, Jun 2002.

[79] V. F. Lvovich, Impedance Spectroscopy: Applications to Electrochemical and Dielectric Phenomena. Hoboken, New Jersey: John Wiley & Sons, 2012.

[80] "Basics of Electrochemical Impedance Spectroscopy," Gamry Instruments2010.

[81] M. R. Shoar Abouzari, F. Berkemeier, G. Schmitz, and D. Wilmer, "On the physical interpretation of constant phase elements," *Solid State Ionics,* vol. 180, no. 14–16, pp. 922-927, 6/25/ 2009.

[82] S. Kochowski, "Description of the frequency behaviour of metal–SiO2–GaAs structure characteristics by electrical equivalent circuit with constant phase element," *Thin solid films,* vol. 415, no. 1-2, pp. 133-137, 01/2002.

[83] M. E. Orazem and B. Tribollet, *Electrochemical Impedance Spectroscopy*. Pemmington, NJ: John Wiley & Sons, 2008.

[84] M. Dubarry, C. Truchot, and B. Y. Liaw, "Synthesize battery degradation modes via a diagnostic and prognostic model," *Journal of Power Sources,* vol. 219, pp. 204-216, 2012.

[85] M. Dubarry, V. Svoboda, R. Hwu, and B. Yann Liaw, "Incremental Capacity Analysis and Close-to-Equilibrium OCV Measurements to Quantify Capacity Fade in Commercial

Rechargeable Lithium Batteries," *Electrochemical and Solid-State Letters,* vol. 9, no. 10, p. A454, 2006.

[86] A. Devie and M. Dubarry, "Lithium Ion Battery Conditioning and Performance Testing Procedures Guidelines," Hawai'i Natural Energy Institute, Honolulu, HI2015.

[87] (2012). Evaluation of Electrode Materials for Welding of Copper Tabs for Battery Module Construction.

[88] "IPC-2221A Generic Standard on Printed Board Design," IPC, Northbrook, IL2003.

[89] T. Waldmann *et al.*, "Review—Post-Mortem Analysis of Aged Lithium-Ion Batteries: Disassembly Methodology and Physico-Chemical Analysis Techniques," *Journal of The Electrochemical Society,* vol. 163, no. 10, pp. A2149-A2164, 2016.

[90] N. Williard, B. Sood, M. Osterman, and M. Pecht, "Disassembly methodology for conducting failure analysis on lithium–ion batteries," *Journal of Materials Science: Materials in Electronics,* vol. 22, no. 10, pp. 1616-1630, 2011.

[91] N. Aguiló-Aguayo, P. Amann, P. P. Espiñeira, J. Petrasch, and T. Bechtold, "X-ray micro tomography of three-dimensional embroidered current collectors for lithium-ion batteries," *Journal of Power Sources,* vol. 306, pp. 826-831, 2016.

[92] D. P. Finegan *et al.*, "Investigating lithium-ion battery materials during overcharge-induced thermal runaway: an operando and multi-scale X-ray CT study," *Phys. Chem. Chem. Phys,* vol. 18, no. 45, pp. 30912-30919, 2016.

[93] D. P. Finegan *et al.*, "In-operando high-speed tomography of lithium-ion batteries during thermal runaway," *Nature Communications,* vol. 6, p. 6924, 2015.

[94] S. Komini Babu, A. I. Mohamed, J. F. Whitacre, and S. Litster, "Multiple imaging mode X-ray computed tomography for distinguishing active and inactive phases in lithium-ion battery cathodes," *Journal of Power Sources,* vol. 283, pp. 314-319, 2015.

[95] F. Sun, H. Markotter, I. Manke, A. Hilger, and N. Kardjilov, "Characterization of Lithium Ion Batteries with In Situ X-Ray Tomography and Radiography," *ECS Transactions,* vol. 72, no. 8, pp. 3-11, 2016.

[96] V. Yufit, P. Shearing, R. W. Hamilton, P. D. Lee, M. Wu, and N. P. Brandon, "Investigation of lithium-ion polymer battery cell failure using X-ray computed tomography," *Electrochemistry Communications,* vol. 13, no. 6, pp. 608-610, 2011.

[97] C. T. Love, K. Swider-Lyons, and C. J. Patridge, "Impedance Diagnostic for Overcharged Lithium-Ion Batteries," *Meeting Abstracts,* vol. MA2012-02, no. 10, p. 1041, June 4, 2012 2012.

[98] N. Williard, W. He, C. Hendricks, and M. Pecht, "Lessons Learned from the 787 Dreamliner Issue on Lithium-Ion Battery Reliability," *Energies,* vol. 6, no. 9, pp. 4682-4695, 2013.

[99] T. Osaka, D. Mukoyama, and H. Nara, "Review-Development of Diagnostic Process for Commercially Available Batteries, Especially Lithium Ion Battery, by Electrochemical Impedance Spectroscopy," (in English), *Journal of the Electrochemical Society,* vol. 162, no. 14, pp. A2529-A2537, 2015.

[100] M. Doube *et al.*, "BoneJ: Free and extensible bone image analysis in ImageJ," *Bone,* vol. 47, no. 6, pp. 1076-9, Dec 2010.

[101] J. Kasnatscheew *et al.*, "Lithium ion battery cells under abusive discharge conditions: Electrode potential development and interactions between positive and negative electrode," *Journal of Power Sources,* vol. 362, no. Supplement C, pp. 278-282, 2017/09/15/ 2017.